Early-age structural development and autogenous shrinkage of alkali-activated slag/fly ash cements

Siva UPPALAPATI

Examination Committee:
Prof. dr. ir. Bob Puers, Chair
Prof. dr. ir. Özlem Cizer, Supervisor
Prof. dr. ir. Lucie Vandewalle, Supervisor
Prof. dr. ir. Yiannis Pontikes
Prof. dr. ir.-arch. Koen Van Balen
Prof. dr. ir. Stéphanie Staquet
(Université Libre de Bruxelles)
Prof. dr. ir. Guang Ye
(Delft University of Technology)

Dissertation presented in partial fulfilment of the requirements for the degree of Doctor of Engineering Science (PhD): Civil Engineering

February 2021

© 2021 KU Leuven – Faculty of Engineering Science
Uitgegeven in eigen beheer, Siva Uppalapati, Kasteelpark Arenberg 40, box 2448, B-3001 Leuven (Belgium)

Alle rechten voorbehouden. Niets uit deze uitgave mag worden vermenigvuldigd en/of openbaar gemaakt worden door middel van druk, fotokopie, microfilm, elektronisch of op welke andere wijze ook zonder voorafgaandelijke schriftelijke toestemming van de uitgever.

All rights reserved. No part of the publication may be reproduced in any form by print, photoprint, microfilm, electronic or any other means without written permission from the publisher.

Acknowledgement

I would like to express my sincere gratitude to my promotor Prof. Özlem Cizer for giving me the opportunity to study this interesting research topic. In addition to her continuous assistance and guidance, she given me freedom and flexibility to pursue the research of my interest. I would like to thank her for all the professional advices and support that she has given me throughout the duration of this research.

I am also grateful to my co-promotor Prof. Lucie Vandewalle for the continuous support and feedback provided during this work. I would like to sincerely thank Prof. Yiannis Pontikes and Prof. Stephanie Staquet for their enlightening comments and fruitful discussions during the internal meetings. Thanks to the other members of examination committee, Prof. Guang Ye and Prof. Koen Van Balen for their valuable inputs during my preliminary decency.

I would like to thank my colleagues of MAT: Ahmed, Anna, Aziliz, Celine, Charlotte, Hussein, Leidy, Maura, Marcello, Naveen, Nathalie, Rutger, Shiju, Tasos, and Youen for their wonderful company and continuous support during these years. I am like to show my gratitude to the lab coordinators Stephan, Gerda, Jimmy, Jan, and Bernd for helping me with multiple experiments. Special thanks to Kristine Loonbeek, Annick, and Rita for helping me with all the administrative work and making arrangements whenever required.

I am deeply indebted to my mother for her immense moral support not only during this work, but throughout my life. She has continuously sacrificed her present for my future and made it possible for everything that I am now. I would like to convey a sincere note of thanks to my sister Kalyani and my father-in-laws Ramakrishna and Narendra babu for their support during my times of need on both academic and social issues. I would also like to thank to my cousins, Raja and Ramu for all their support and encouragement. Finally, I would like to thank my wife Rohini for her constant support and for keeping me sane over the past few months.

Siva Uppalapati

Leuven, February 2021.

Abstract

Alkali-activated cement is considered to be a promising eco-friendly alternative to Ordinary Portland Cement (OPC). In addition to its eco-friendly performance, the alkali-activated cements synthesized with blast furnace slag and fly ash offers several potential advantages as compared to OPC, including higher rate of strength development and good resistance to chemical and fire attacks. Despite these advantages, the acceptance and application of the alkali-activated slag/fly ash (AASF) cements in the construction industry is hampered by concerns related to their rapid hardening behaviour resulting in very short setting times and large autogenous shrinkage. However, the scientific reasoning and the mechanism behind quick setting process and large autogenous shrinkage remain poorly understood in the literature.

Activator type is one of the most dominant factors that influences setting and autogenous shrinkage behavior in AASF cements. Sodium silicate is the typically used activator in AASF cements due the superior or comparable strength properties to Portland Cement. However, AASF cements activated with sodium silicate have critical shortcomings such as quick setting and large shrinkage deformations which cannot secure their performant functions in concrete applications. Moreover, sodium silicate is not naturally available, and its production process is expensive with a high environmental impact. On the other hand, AASF cements activated with naturally occurring minerals like sodium carbonate and sodium sulfate generates much longer setting time and lower autogenous shrinkage than sodium silicate activation. The fundamental elements behind the setting and shrinkage mechanisms are not fully understood. The main objective of this doctoral research is to explore the setting and autogenous shrinkage behavior in AASF cements with sodium silicate, sodium carbonate and sodium sulfate solutions through an interlinked assessment of reaction kinetics, phase formations, gel structure, stiffness development, mechanical properties, and pore structure. The evolution of early-age structure development is continuously monitored using ultrasonic P-wave velocity in order to understand the setting and hardening behaviour. The pore pressure caused by self-desiccation is calculated and related to the measured autogenous shrinkage towards a better understanding of complex autogenous shrinkage behavior in AASF cements. The cracking tendency under restrained autogenous shrinkage is investigated experimentally using circular ring test. Moreover, the

influence of curing temperature at 40°C is investigated as a mitigation strategy to control the autogenous shrinkage.

Regardless of the activator type, Al substituted C-S-H gel and N-A-S-H gel are observed as the main reaction products. The partial substitution of sodium silicate with sodium carbonate and sodium sulfate significantly reduces the rate of reaction due to decrease in alkalinity (OH^- ions) of the activating solution. At equal replacement of the sodium silicate by sodium carbonate and sodium sulfate, the samples with sodium carbonate exhibits higher rate of reactivity due to the formation of calcite as a nucleation seed to the precipitation of C-A-S-H gels.

Comparative assessment of ultrasonic measurements with Vicat setting times and calorimetry heat flow curves shows that condensation reaction between the aluminosilicate units formed near the particle surface is most likely responsible for setting process in AASF cements. Research findings confirm that self-desiccation is one of the main driving forces for autogenous shrinkage in AASF cements. Besides self-desiccation, the Si-polycondensation reaction at solid-liquid interface or between adjacent aluminosilicate units during induction period of heat flow curves is also responsible for the autogenous shrinkage.

The autogenous shrinkage of sodium silicate-activated samples significantly reduces during early-ages if sodium carbonate or sodium sulfate is incorporated in the solution. The reduced autogenous shrinkage is attributed to a decrease in self-desiccation and capillary stresses in the pore fluid. The decrease in viscoelastic deformation associated to the rearrangement of C-A-S-H gels under internal stresses, on the other hand, reduces the autogenous shrinkage. Besides the self-desiccation process, reduction in the Si polycondensation reaction during induction period of the heat flow curves is also responsible for a lower autogenous shrinkage in samples activated with sodium carbonate and sodium sulfate. As a result of considerably reduced autogenous shrinkage and rarely affected tensile strength, the time of cracking under restrained condition is prolonged in case of sodium carbonate and sodium sulfate activation.

The increase in curing temperature to 40°C can effectively reduce the autogenous shrinkage in AASF cements. This is the result of suppression of the self-desiccation process due to decrease in rate of reaction, formation of a matrix with higher elastic modulus at early ages, formation of more 3D-structured N-A-S-H type gels, and considerable increase in crystallinity of C-A-S-H type gels.

Samenvatting

Alkali-geactiveerd cement wordt beschouwd als een veelbelovend milieuvriendelijk alternatief voor Portland Cement (PC). Naast de milieuvriendelijke prestaties, biedt het met hoogovenslak en vliegas gesynthetiseerde alkali-geactiveerde cement verschillende potentiële voordelen in vergelijking met PC, waaronder een snellere sterkteontwikkeling en een goede weerstand tegen chemische aantasting en brand. Ondanks deze voordelen wordt het aanvaarden en toepassen van alkali-geactiveerd slak/vliegas (AASF) cement in de bouwindustrie belemmerd door hun snelle bindingsgedrag dat resulteert in zeer korte uithardingstijden en grote autogene krimp. Tot op heden is er echter weinig literatuur beschikbaar aangaande dit snel bindingsproces en grote autogene krimp.

Het type activator is een van de belangrijkste factoren die het bindingsproces en autogene krimpgedrag in AASF-cement beïnvloeden. Natriumsilicaat is de meest gebruikte activator in AASF-cement vanwege de hogere of vergelijkbare sterkte-eigenschappen ten opzichte van Portland Cement. Met natriumsilicaat geactiveerde AASF-cementen vertonen echter kritieke minpunten, zoals een snelle binding en grote krimpvervormingen, waardoor hun toepassingen in beton niet verzekerd zijn. Bovendien is natriumsilicaat niet van natuurlijke afkomst, en het productieproces ervan is duur en heeft een grote impact op het milieu. Anderzijds zorgt AASF-cement, dat geactiveerd is met natuurlijk voorkomende mineralen zoals natriumcarbonaat en natriumsulfaat, voor een veel langere bindingstijd en een lagere autogene krimp dan met natriumsilicaat activatie. De fundamentele elementen achter het bindingproces en het krimpmechanisme zijn niet volledig gekend. Het hoofddoel van dit doctoraatsonderzoek is het onderzoek van het bindingsproces en autogene krimpgedrag in AASF-cementen met natriumsilicaat-, natriumcarbonaat- en natriumsulfaatoplossingen via een onderlinge vergelijking van reactiemechanismen, fasevormingen, gelstructuur, stijfheidsontwikkeling, mechanische eigenschappen en poriestructuur. De evolutie van de structuurontwikkeling in de beginfase wordt continu opgevolgd met behulp van de ultrasone P-golfsnelheid (UPV) om het bindings- en verhardingsgedrag te begrijpen. De poriëndruk, veroorzaakt door “zelfuitdroging” wordt berekend en gerelateerd aan de gemeten autogene krimp om zo een beter inzicht te krijgen van dit complexe autogene krimpgedrag in AASF-cement. De scheurvorming onder belemmerde autogene krimp wordt experimenteel onderzocht met behulp van een ringtest.

Bovendien wordt de gunstige invloed van de uithardingstemperatuur bij 40° C onderzocht op de beperking van de autogene krimp.

Ongeacht het type activator worden Al-vervangende C-S-H gel en N-A-S-H gel waargenomen als de voornaamste reactieproducten. De gedeeltelijke vervanging van natriumsilicaat door natriumcarbonaat en natriumsulfaat verlaagt de reactiesnelheid aanzienlijk als gevolg van de afname van de alkaliteit (OH^- ionen) van de activerende oplossing. Bij gelijke vervanging van natriumsilicaat door natriumcarbonaat en natriumsulfaat vertonen de monsters met natriumcarbonaat een hogere reactiesnelheid als gevolg van de vorming van calciet als nucleatie voor de neerslag van C-A-S-H gels.

Een vergelijking van ultrasone metingen met Vicat bindingstijden en calorimetrische metingen toont aan dat de condensatiereactie tussen de aluminiumsilicaten die nabij het deeltjesoppervlak worden gevormd, hoogstwaarschijnlijk verantwoordelijk is voor het bindingsproces in AASF-cement. Onderzoeksresultaten bevestigen dat zelfuitdroging één van de belangrijkste oorzaken is voor autogene krimp in AASF-cement. Naast zelfuitdroging is ook de Si-polycondensatiereactie op het grensvlak tussen de vaste en vloeibare fase of tussen aangrenzende aluminosilicaten tijdens de inductieperiode van de hydratatie verantwoordelijk voor de autogene krimp.

De autogene krimp van natriumsilicaat geactiveerde monsters vermindert aanzienlijk op jonge leeftijd als natriumcarbonaat of natriumsulfaat in de oplossing wordt opgenomen. De verminderde autogene krimp wordt toegeschreven aan een afname van zelfuitdroging en capillaire spanningen in de porievloeistof. Anderzijds is het zo dat de afname van de visco-elastische vervorming als gevolg van de herschikking van C-A-S-H gels onder interne spanningen de autogene krimp vermindert. Naast het zelfuitdroging mechanisme is ook de vermindering van de Si polycondensatiereactie tijdens de inductieperiode van de hydratatie verantwoordelijk voor een lagere autogene krimp in monsters die met natriumcarbonaat en natriumsulfaat zijn geactiveerd. Als gevolg van de aanzienlijk verminderde autogene krimp en de nauwelijks verminderde treksterkte, zal het tijdstip van scheuren onder belemmerde vervorming op een latere leeftijd plaatsvinden in het geval van activering met natriumcarbonaat en natriumsulfaat.

De verhoging van de verhardingstemperatuur tot 40° C kan de autogene krimp in AASF-cement effectief verminderen. Dit is het gevolg van de onderdrukking van het zelfuitdroging mechanisme als gevolg van de afname van de reactiesnelheid, de vorming van een matrix met

een hogere elasticiteitsmodulus op jonge leeftijd, de vorming van meer 3D-gestructureerde N-A-S-H type gels, en een aanzienlijke toename van de kristalliniteit van C-A-S-H type gels.

Contents

Acknowledgement ..... **i**

Abstract ..... **iii**

Samenvatting ..... **v**

Contents ..... **ix**

List of Figures ..... **xv**

List of Tables ..... **xxiii**

List of symbols ..... **xxv**

1 **Introduction** **1**

1.1 Problem statement 1

1.2 Research aims and objectives 2

1.3 Research methodology 3

1.3.1 Early age structural development 3

1.3.2 Reaction kinetics of AASF binder 4

1.3.3 Characterization of solid phases and pore structure 4

1.3.4 Autogenous shrinkage 5

1.3.5 Cracking tendency 5

1.4 Research outline 5

2 **State of the art** **9**

2.1 Introduction 9

2.2 Alkali-activated cements (AACs) 9

2.2.1 Definition and classifications 9

2.2.2 Raw materials 10

2.2.3 Alkaline activators 12

2.2.4 Carbon footprint 14

2.3 Reaction mechanisms and reaction products 15

2.3.1 Alkali-activated slag (AAS) 15

2.3.2 Alkali-activated fly ash (AAF) 17

2.3.3 Alkali-activated slag/fly ash blends (AASF) 19
2.4 Early age reaction process from ultrasonic measurements 20
2.5 Setting process of AAS cements 22
2.6 Chemical shrinkage 23
2.7 Autogenous shrinkage and its mechanisms 24
2.8 Measurement methods of autogenous shrinkage 28
2.9 Current understanding of autogenous shrinkage in AACs 30
2.9.1 Autogenous shrinkage of alkali-activated slag (AAS) 30
2.9.2 Autogenous shrinkage of alkali-activated fly ash (AAF) 32
2.10 Factors influencing autogenous shrinkage in AAS cements 32
2.11 Cracking tendency 36
2.12 Mitigation of autogenous shrinkage in AAS cements 37
2.13 Conclusions 38
3 **Materials and experimental methods 41**
3.1 Introduction 41
3.2 Materials 41
3.2.1 Raw materials 41
3.2.2 Alkaline activators 44
3.3 Mix compositions and mixing procedure 45
3.3.1 Mix compositions 45
3.3.2 Carbon footprint 46
3.3.2 Mixing procedure and curing conditions 47
3.4 Experimental methods 47
3.4.1 Setting and hardening behavior 47
3.4.2 Characterization of solid phases and pore structure 51
3.4.3 Modelling autogenous shrinkage caused by self-desiccation mechanism 53
3.4.4 Restrained ring test 56
3.5 Conclusion 57
4 **Setting and hardening behavior 59**
4.1 Introduction 59
4.2 Reaction process 59
4.2.1 Heat of hydration 59

4.2.2 Evolution of ultrasonic P-wave velocity on paste 62
4.2.3 Ultrasonic measurements on paste samples 66
4.3 Setting behavior 68
4.3.1 Vicat setting times 68
4.3.2 Comparison between Vicat setting times and ultrasonic measurements 69
4.3.3 Comparison between Vicat setting times and calorimetric measurements 72
4.4 Strength and stiffness development 74
4.4.1 Compressive strength 74
4.4.2 Flexural strength 76
4.4.3 Splitting tensile strength 78
4.4.4 Static E-modulus 79
4.4.4 Ultrasonic measurements on mortar samples 81
4.4.6 Elastic properties from ultrasonic measurements 83
4.4.5 Ultrasonic measurements versus compressive strength development 85
4.5 Conclusions 86
5 **Characterization of solid phases and pore structure 89**
5.1 Introduction 89
5.2 Thermogravimetry analysis (TGA) 89
5.2.1 Bound water content 90
5.3 XRD analysis 93
5.4 FT-IR analysis 96
5.5 Pore solution composition 101
5.5.1 Concentration of OH^- ions versus dissolved Si, Na, Al ions 106
5.5.2 Concentration of OH^- ions versus reaction kinetics 107
5.6 Microchemistry of the reaction products 109
5.7 Pore structure 112
5.7.1 Mercury Intrusion Porosimetry (MIP) 113
5.7.2 Nitrogen absorption test 116
5.8 Conclusions 119
6 **Autogenous shrinkage 121**
6.1 Introduction 121
6.2 Chemical shrinkage 121

6.3 Autogenous shrinkage 124
6.3.1 Time-Zero (t_0) 124
6.3.2 Autogenous shrinkage V_s chemical shrinkage 129
6.3.3 Autogenous shrinkage V_s cumulative heat release 130
6.4 Internal relative humidity 131
6.5 Surface tension 134
6.6 Modelling autogenous shrinkage caused by self-desiccation 135
6.7 Predication of autogenous shrinkage in AASF cements 143
6.7.1 Predication from compressive strength and bound water content 143
6.7.2 Prediction from ultrasonic P-wave velocity (UPV) measurements 147
6.7.3 Prediction from existing models of OPC-based materials 149
6.8 Conclusions 149
7 **Autogenous shrinkage cracking tendency 153**
7.1 Introduction 153
7.2 Restrained ring test 154
7.3 Time-dependent properties 156
7.3.1 Tensile strength 156
7.3.2 Static elastic modulus 157
7.3.3 Free autogenous shrinkage 157
7.4 Measured inner steel ring strains 159
7.5 Quantitative analysis of the restrained ring test 161
7.5.1 Determination of the actual residual tensile stress 161
7.5.2 Determining the theoretical elastic stress 163
7.5.3 Degree of restraint 166
7.5.4 Stress relaxation 167
7.5.5 Cracking potential 169
7.6 Conclusions 170
8 **Mitigation of autogenous shrinkage by elevated curing temperature 173**
8.1 Introduction 173
8.2 Compressive strength 174
8.3 Vicat setting time and autogenous shrinkage 175
8.4 Reaction kinetics 177

8.4.1 Isothermal calorimetry....177
8.4.2 Thermogravimetric analysis....178
8.5 Characterization of reaction products....180
8.5.1 XRD analysis....180
8.5.2 FT-IR analysis....181
8.5.3 Pore solution composition....183
8.6 Characterization of pore structure....186
8.6.1 MIP....186
8.6.2 Nitrogen absorption test....187
8.7 Internal relative humidity....189
8.8 Elastic modulus....191
8.9 Effect of curing temperature on autogenous shrinkage....192
8.10 Prediction of autogenous shrinkage....198
8.11 Conclusion....199
9 **Conclusion....201**
9.1 General conclusions....201
9.2 Recommendations for future research....208
Appendix A....211
Appendix B....215
Appendix C....225
Appendix D....227
Bibliography....229
Curriculum vitae....261
List of publications....263

List of Figures

Figure 1.1: Cement production and forecast by regions, based on United states Geological survey data [1].....1

Figure 1.2: Outline of the PhD thesis.....7

Figure 2.1: Effect of alkali-modulus on 28-days strength of alkali-activated slag [63]. 13

Figure 2.2: Reaction process of the alkali-activated slag [82].....16

Figure 2.3: Model for the reaction mechanism in alkali-activated fly ash [13].....18

Figure 2.4: Stability of N-A-S-H type gel in hybrid systems as a function of pH value and Ca content [30]. 19

Figure 2.5: The UPV evolution of sodium silicate activated AAS cements [110]. 21

Figure 2.6: Chemical shrinkage and autogenous shrinkage during hydration [a] and their relationship [b] in Portland cement paste [135, 136]. 24

Figure 2.7: Capillary tension mechanism in cementitious materials. 27

Figure 2.8: An illustration of volumetric method (buoyancy method) to measure autogenous shrinkage [156]. 28

Figure 2.9: Setup for measuring linear autogenous shrinkage using corrugated tube method [149]. 29

Figure 2.10: Effect of substituting slag by metakaolin on the autogenous shrinkage of AAS cements [133]. 33

Figure 2.11: Effect of alkali-content (Na_2O) and alkali-modulus (M_s) on the autogenous shrinkage of AAS cement mortars [163]. 34

Figure 2.12: Micro-cracking of the sodium silicate activated slag cement at 7 days. 36

Figure 3.1: X- ray diffraction analysis of slag and fly ash.....42

Figure 3.2: Particle size distribution of slag and fly ash measured with Laser diffraction analysis. 43

Figure 3.3: Particle size distribution of river sand 0/4. 43

Figure 3.4: Ultrasonic pulse wave transmission unit of the measurement equipment.....48

Figure 3.5: Device [a] and cyclic loading [b] for determination of static E-modulus. 50

Figure 3.6: Dilatometry method for determination of chemical shrinkage on paste samples. 54

Figure 3.7: Corrugated tube method for determination of autogenous shrinkage on mortar samples. 54

Figure 3.8: The apparatus for internal RH measurement. 55

Figure 3.9: A basic experimental setup for pendant drop tensiometry [a]; a typical drop image as acquired by a camera [b] [221]. 55

..... 57

Figure 3.10: Circular restrained ring test. 57

Figure 4.1: Heat evolution rate with an inset showing the first minutes of AASF pastes. 60

Figure 4.2: Cumulative heat release of AASF pastes. 61

Figure 4.3: Typical ultrasonic P-wave velocity curve of AASF pastes [SS-1.0]; first 4 hours [a], up to 24 hours [b]. 63

Figure 4.4: Derivative of the P-wave velocity in AASF pastes [SS-1.0]; first 4 hours [a], up to 24 hours [b]. 63

Figure 4.5: First derivative of ultrasonic P-wave velocity V_s heat evolution curve from isothermal calorimetry, for SS-1.0. 65

Figure 4.6: Temperature evolution curve from ultrasonic measurement V_s heat evolution curve from isothermal calorimetry, for SS-1.0. 65

Figure 4.7: Ultrasonic P-wave velocity curves of AASF pastes; first 4 hours [a], up to 48 hours [b]. 67

Figure 4.8: Vicat setting times of AASF pastes. 68

Figure 4.9: Comparison between the ultrasonic measurements and Vicat setting times of AASF cements. 70

Figure 4.10: Expoential fitting model of cumulative heat release curve of SS-1.0. 73

Figure 4.11: Compressive strength of AASF mortar samples. 75

Figure 4.12: Comparison between compressive strength and cumulative heat release, up to 7 days. 76

Figure 4.13: Flexural strength of AASF mortar samples. 77

Figure 4.14: Comparison between flexural tensile strength and compressive strength of AASF. 77

Figure 4.15: Splitting tensile strength of AASF mortar samples. 78

Figure 4.16: Comparison between compressive strength and tensile strength of AASF. 78

Figure 4.17: Static E-modulus of AASF mortar samples. 79

Figure 4.18: Comparison between static E-modulus and square root of compressive strength, up to 28 days. 80

Figure 4.19: Comparison between static E-modulus and cumulative heat release, up to 7 days. 81

Figure 4.20: Evolution of the ultrasonic P-wave velocity [a] and derivative of the P-wave velocity in AASF mortar samples [SC-0.7]. 81

Figure 4.21: Ultrasonic P-wave velocity curves of the AASF mortar samples. 82

Figure 4.22: Elastic properties derive from ultrasonic measurements; Assumed Poisson's ratio [a], dynamic E-modulus [b], bulk modulus [c], and shear modulus [d]. 84

Figure 4.23: Comparison between dynamic E-modulus from ultrasonic measurements and experimentally measured static E-modulus of AASF mortar samples, up to 7 days. 85

Figure 4.24: Comparison between ultrasonic measurements and compressive strength of AASF mortar samples, up to 7 days 86

Figure 4.25: Comparison between dynamic E-modulus from ultrasonic measurements and compressive strength of AASF mortar samples, up to 7 days. 86

Figure 5.1: DTG curves of AASF cement pastes after curing for 7 days. 90

Figure 5.2: Bound water content in AASF pastes, calculated based on the weight loss between 30 °C-600 °C. 91

Figure 5.3: Comparison between bound water content and cumulative heat release, up to 7 days. 92

Figure 5.4: Comparison between bound water content and compressive strength, up to 28 days. 92

Figure 5.5: XRD patterns of AASF pastes activated with sodium silicate (SS – 1.0) at different curing ages. Key: Ht- Hydrotalcite, Cs – calcium aluminate silicate hydrate gel, M – Mullite, Q – Quartz. 94

Figure 5.6: XRD patterns of AASF pastes activated with sodium carbonate (SC – 0.6) at different curing ages. Key: Ht- Hydrotalcite, Cs – calcium aluminate silicate hydrate gel, C – Calcite, S – Hydroxysodalite, G – Gaylussie, P – Pirssonite, M – Mullite, Q – Quartz. 94

Figure 5.7: XRD patterns of AASF pastes activated with sodium carbonate (SC – 0.6) at different curing ages. Key: Ht- Hydrotalcite, Cs – calcium aluminate silicate hydrate gel, M – Mullite, Q – Quartz. 95

Figure 5.8: FTIR spectrum of slag and fly ash raw materials. 96

Figure 5.9: FTIR spectrum of AASF paste samples; (a) SS-1.0, (b) SC-0.7 (c) SC-0.6 (d) Su-0.7, and (e) Su-0.6. 97

Figure 5.10: Peak intensity of main Si-O-Si (Al) band in FTIR spectrum of AASF paste samples; (a) SS-1.0, (b) SC-0.7 (c) SC-0.6 (d) Su-0.7, and (e) Su-0.6. 99

Figure 5.11: Deconvolution FTIR spectrum of SS-1.0 sample after 1 day of curing. 100

Figure 5.12: Peak of N-A-S-H type gels centered at around 1035 cm^{-1} in FTIR spectrum of AASF paste samples at; 1 day (a), and 28 days (b). 100

Figure 5.13: Concentration of Na ions in the pore solution of AASF cements. 102

Figure 5.14: Concentration of OH^- ions in the pore solution of AASF cements. 103

Figure 5.15: Concentration of Ca ions in the pore solution of AASF cements. 104

Figure 5.16: Concentration of Si in the pore solutions of AASF cements. 105

Figure 5.17: Concentration of Al in the pore solutions of AASF cements. 105

Figure 5.18: Concentration of Na, Si and Al ions as a function of OH^- ions in the pore solution. 107

Figure 5.19: Comparison between concentration of OH^- ions in the pore solution with the cumulative heat release, up to 7 days 108

Figure 5.20: Comparison between concentration of OH^- ions in the pore solution with the bound water content, up to 7 days. 108

Figure 5.21: Pore size distribution of AASF paste samples activated with: (a) SS-1.0, (b) SC-0.7 (c) SC-0.6 (d) Su-0.7, and (e) Su-0.6, derived from MIP test. 114

Figure 5.22: N_2 absorption isotherms of the AASF pastes activated with: (a) SS-1.0, (b) SC-0.7 (c) SC-0.6 (d) Su-0.7, and (e) Su-0.6, derived from N_2 adsorption test. 117

Figure 5.23: Pore size distribution of AASF pastes activated with: (a) SS-1.0, (b) SC-0.7 (c) SC-0.6 (d) Su-0.7, and (e) Su-0.6, derived from N_2 adsorption test. 118

Figure 5.24: Total pore volume derived from MIP method V_s compressive strength [a] and static E-modulus [b] of AASF samples at 7 days. 119

Figure 6.1: Chemical shrinkage of AASF paste, derived from the dilatometry method (negative values indicates shrinkage). 122

Figure 6.2: Comparison between chemical shrinkage and cumulative heat release, up to 7 days. 123

Figure 6.3: Autogenous shrinkage of AASF mortar samples, from the time of mixing.....124

Figure 6.4: Autogenous shrinkage of AASF mortar samples, plotted as from Vicat final setting time. 125

Figure 6.5: Comparison between autogenous shrinkage and ultrasonic P-wave velocity measurements SS-1.0 [a], SC-0.7 [b], SC-0.6 [c], Su-0.7 [d], and Su-0.6 [e]. 128

Figure 6.6: Comparison between autogenous shrinkage and chemical shrinkage of AASF samples, after Vicat final setting time or time-zero. 129

Figure 6.7: Comparison between autogenous shrinkage and cumulative heat release of AASF samples. 130

Figure 6.8: Measured internal relative humidity (RH) of AASF mortar samples. 131

Figure 6.9: Calculated autogenous RH (RH_k) of AASF mortar samples. 133

Figure 6.10: Autogenous shrinkage as a function of autogenous RH (RH_k) or self-desiccation. 134

Figure 6.11: Surface tension of the pore solutions extracted from AASF mortars. 134

Figure 6.12: Calculated capillary tension in the pore fluid of AASF samples. 138

Figure 6.13: Comparison between calculated capillary tension in the pore fluid and measured autogenous shrinkage. 138

Figure 6.14: Degree of saturation in the AASF mortar samples. 140

Figure 6.15: Comparison between calculated shrinkage and measured autogenous shrinkage SS-1.0 [a], SC-0.7 [b], SC-0.6 [c], Su-0.7 [d], and Su-0.6 [e]. 141

Figure 6.16: Comparison between compressive strength and measured autogenous shrinkage for AASF samples. 144

Figure 6.17: Comparison between bound water content and measured autogenous shrinkage for AASF samples. 144

Figure 6.18: Predicted autogenous shrinkage from compressive strength and bound water content in AASF samples activated with SS-1.0 [a], SC-0.7 [b], SC-0.6 [c], Su-0.7 [d], and Su-0.6 [e]. 146

Figure. 6.19: Correlation between the measured autogenous shrinkage and ultrasonic P-wave velocity of mortar samples. 147

Figure 6.20: Predicted autogenous shrinkage from ultrasonic measurements in AASF samples activated with SS-1.0 [a], SC-0.7 [b], SC-0.6 [c], Su-0.7 [d], and Su-0.6 [e]. 148

Figure 6.21: Predicted autogenous shrinkage from Eurocode 2 [a] and ACI 209 [b]. 149

Figure 7.1: Restrained ring test: Stress distribution based on the boundary conditions; autogenous condition and/or drying from top and bottom [a], drying from outer circumference [b] [327, 328]. 155

Figure 7.2: Calculated direct tensile strength of AASF mortar samples. 156

Figure 7.3: Time-dependent direct tensile strength. 157

Figure 7.4: Time-dependent static elastic modulus of the AASF mortar samples. 158

Figure 7.5: Early-age free autogenous shrinkage of AASF mortar samples. 158

Figure 7.6: Measured strains in the restrained inner steel ring. 159

Figure 7.7: Age of macro-cracking or visible crack in AASF mortar samples. 160

Figure 7.8: Measured strains in the restrained steel ring against cumulative heat release. ...161

Figure 7.9: Scheme of restraint ring test [327]. 162

Figure 7.10: Actual residual stresses developed in AASF mortar rings. 163

Figure 7.11: Scheme of the ring to determine the theoretical-elastic stress; initial condition without shrinkage [a]; allowing mortar to shrinkage without restraint [b]; elastic deformation to satisfy boundary conditions [c]. 164

Figure 7.12: Predicted theoretical elastic stresses in the restrained AASF mortar ring. 165

Figure 7.13: Calculated degree of restraint. 166

Figure 7.14: Estimated relaxed stress in AASF mortar rings. 167

Figure 7.15: Estimated relaxed stress for OPC mortars with water-to-binder ratio of 0.5 [327] 168

Figure 7.16: Creep factor up to the age of 24 hours. 169

Figure 7.17: Cracking potential of AASF mortar samples. 170

Figure 8.1: Compressive strength of AASF mortar samples at 20°C and 40°C. 174

Figure 8.2: Vicat setting times of AASF pastes at 20°C and 40°C. 175

Figure 8.3: Autogenous shrinkage starting from the Vicat final setting time for SS-1.0 [a], SC-0.7 [b], SC-0.6 [c], Su-0.7 [d], and Su-0.6 [e] at both 20°C and 40°C. 176

Figure 8.4: Heat flow curves of the AASF paste samples at 20°C [a] and 40°C [b]. 177

Figure 8.5: Cumulative heat release of the AASF paste samples at 20°C [a] and 40°C [b]. .178

Figure 8.6: Comparison between the compressive strength and cumulative heat release of the AASF samples at 40°C, up to 7 days. 178

Figure. 8.7: Comparison of the bound water content of the AASF paste samples cured at 20°C and 40°C, calculated based on the weight loss between 30 °C-600 °C. 179

Figure 8.8: Comparison between the cumulative heat release and bound water content of the AASF samples at 40°C, up to 7 days. 179

Figure 8.9: Comparison between the compressive strength and bound water content of the AASF samples at 40°C, up to 28 days. 180

Figure 8.10: XRD patterns of the AASF samples after 1-day cured at 20°C and 40°C, Key: Ht-Hydrotalcite, Cs – calcium silicate hydrate type gels, C – Calcite, S – Hydroxysodalite, G – Gaylussie, P – Pirssonite, M – Mullite, Q – Quartz. 181

Figure 8.11: FTIR spectrum of AASF paste samples after: (a) 1 day, and (b) 28 days curing at 40ºC. 182

Figure 8.12: Deconvolution FTIR spectra of SS-1.0 sample after 1 day of curing at 20ºC [a] and 40ºC [b]. 183

Figure 8.13: Comparing the concentration of (a) Na, (b) OH^- (c) Al, (d) Si, (e) CO_3^{2-}, and (f) S ions in pore solutions of AASF cured at 20ºC and 40ºC; initial concentration values are from alkaline-solutions. 186

Figure 8.14: Pore size distribution of AASF pastes at 3 days [a] and 7 days [b]. 187

Figure 8.15: N_2 absorption isotherms (left) and differential curves (right) of the AASF pastes activated with SS-1.0 [a], SC-0.7 [b], SC-0.6 [c], Su-0.7 [d], and Su-0.6 [e]. 189

Figure 8.16: Measured internal relative humidity of AASF mortar samples at 40°C. 190

Figure 8.17: Calculated autogenous relative humidity *(RH_k)* of AASF mortar samples at 20°C [a] and 40°C [b]. 191

Figure 8.18: Measured static elastic modulus of AASF mortar samples cured at 20°C and 40°C. 191

Figure 8.19: Calculated capillary tension in pore fluid of AASF mortar samples cured at 40°C. 195

Figure 8.20: Comparison between calculated capillary tension in the pore fluid and measured autogenous shrinkage. 195

Figure 8.21: Comparison between calculated shrinkage and measured autogenous shrinkage SS-1.0 [a], SC-0.7 [b], SC-0.6 [c], Su-0.7 [d], and Su-0.6 [e]. 197

Figure 8.22: Comparison between measured autogenous shrinkage and bound water content [a] and compressive strength [b]. 198

Figure 8.23: Comparison between measured and predicted autogenous shrinkage SS-1.0 [a], SC-0.7 [b], SC-0.6 [c], Su-0.7 [d], and Su-0.6 [e]. 199

Figure 9.1: Schematic outline of the reaction mechanism involved in studied AASF systems based on UPV and heat flow measurements. 202

Figure B.1: A bottom-up approach for developing optimal mix compositions. 215

Figure B.2: Effect of slag/fly ash ratio on Vicat setting times. 216

Figure B.3: Heat evolution rate of AASF pastes. 216

Figure B.4: Cumulative heat release of AASF pastes. 217

Figure B.5: Compressive strength development of AASF mortar samples. 217

Figure B.6: Autogenous shrinkage of AASF mortar samples. 218

Figure B.7: Effect of type and concentration on Vicat setting times of AASF pastes. 220

Figure B.8: Effect of type and concentration on heat evolution of AASF pastes. 222

Figure B.9: Effect of type and concentration on compressive strength of AASF pastes. 223

Figure C.1: Repeatability of the isothermal calorimetry heat flow curves. 225

Figure C.2: Repeatability of the autogenous shrinkage of AASF mortar samples. 226

List of Tables

Table 2.1: CO_2-equivalent for 1kg production of materials (GWP value ranges). 15

Table 3.1: Chemical composition of slag and fly ash measured with XRF [%]. 41

Table 3.2: Physical properties of slag and fly ash. 43

Table 3.3: Mix proportions of alkali-activated slag/fly ash blends. 46

Table 3.4: CO_2 equivalent per mortar mix (kg/m^3) and compared to traditional OPC. 46

Table 4.1: Ultrasonic P-wave velocity corresponding to Vicat setting times of studied AASF. 70

Table 4.2: Parameters of the expoential fitting model for AASF. 73

Table 4.3: Comparing setting times with reaction degree. 74

Table 5.1: Concentration of CO_3^{2-} ions in the pore solutions of AASF cements, in $mmol.L^{-1}$. 109

Table 5.2: Concentration of S ions in the pore solutions of AASF cements, in $mmol.L^{-1}$. 109

Table 5.3: Atomic ratios in the reaction products of AASF pastes by EPMA point analysis. 110

Table 5.4: Pore size proportions for AASF pastes at 3, 7, and 28 days, derived from MIP. 115

Table 6.1: Comparison between the Vicat final setting time and knee point of the autogenous shrinkage curves. 126

Table 6.2: RHs [%] of pore solutions extracted from AASF mortar samples, measured by using Rotronic station probes. 132

Table 6.3: Calculated Kelvin radius (nm) for the studied AASF samples. 136

Table 6.4: Parameters of the exponential fitting model for compressive strength and bound water content in the studied AASF samples. 145

Table 8.1: Pore size proportions for AASF pastes at 3 and 7 days, derived from MIP. 187

Table 8.2: Measured RHs [%] of pore solutions extracted from AASF samples cured at 40°C. 190

Table 8.3: Calculated Kelvin radius [nm] for AASF samples cured at 40°C. 194

Table 8.4: Saturation degree [-] for AASF samples cured at 40°C. 196

Table B.1: Mix proportions of alkali-activated slag/fly ash blends. 219

List of symbols

Abbreviations

AACs	Alkali-activated cements
AAF	Alkali-activated fly ash
AAS	Alkali-activated slag
AASF	Alkali-activated slag/fly ash
AASHTO	American Association of State Highway Transportation Officials
ASTM	American Society for Testing and Materials
EA	Expansive Agents
EC	Eurocode
EN	European Norm
FA	Fly ash
GGBFS	Ground Granulated Blast Furnace Slag
GHG	Greenhouse gas
GWP	Global Warming Potential
HM	Hydraulic Modulus
LWA	Light Weight Aggregates
PC	Portland clinker
OPC	Ordinary Portland cement
SAP	Superabsorbent Polymers
SCM	Supplementary cementitious material
SRA	Shrinkage reducing Agents
SS	Sodium silicate
SC	Sodium carbonate
Su	Sodium sulfate

Analytical techniques

BET	Brunauer-Emmett-Teller
BTJADE	Beton au jeune age, mesure de la deformation endogene

DSC	Differential Scanning Calorimetry
DFT	Density Function Theory
DTG	Differential Thermogravimetric analysis
FEM EPMA	Field Emission Gun Electron Probe Micro Analyzer
FTIR	Fourier Transform Infra-Red spectroscopy
ICP-OES	Inductively Coupled Plasma Optical Emission Spectrometry
LVDT	Linear Variable Differential Transformer
LOI	Loss of Ignition
MIP	Mercury Intrusion Porosimetry
NMR	Nuclear Magnetic Resonance
SEM	Scanning Electron Microscopy
TGA	Thermogravimetric Analysis
TSTM	Temperature Stress Testing Machine
UPV	Ultrasonic P-wave Velocity
WDS	Wavelength Dispersive Spectrometers
XRD	X-ray Diffraction
XRF	X-ray Fluorescence

Cement chemistry notations and minerals

C-S-H	$CaO\text{-}SiO_2\text{-}H_2O$	Calcium silicate hydrate
C-A-S-H	$Cao\text{-}Al_2O3\text{-}SiO_2\text{-}H_2O$	Calcium aluminium silicate hydrate
N-A-S-H	$Na_2O\text{- }Al_2O_3\text{-}SiO_2\text{-}H_2O$	Sodium aluminosilicate hydrate
(N,C)-A-S-H	$Na_2O/CaO\text{- }Al2O_3\text{-}SiO_2\text{-}H_2O$	Sodium/calcium aluminosilicate hydrate
C	$CaCO_3$	Calcite
G	$Na_2Ca(CO_3)_2.\ 5H_2O$	Gaylussie
H_t	$Mg_6Al_2CO_3(OH)16.4H_2O$	Hydrotalcite
H_y	$Na_8Al_6Si_6O_{24}(OH)_2(H_2O$	Hydroxysodalite
M	$3Al_2O_32SiO_2$	Mullite
P	$Na_2Ca(CO_3)_2.\ 2H_2O$	Pirssonite
Q	SiO_2	Quartz

Symbols

E_d	GPa	Dynamic Elastic modulus
E_s	GPa	Static Elastic modulus
f_c	MPa	Compressive strength
$f_{c,\infty}$	MPa	Ultimate compressive strength
$f_{ct,sp}$	MPa	Splitting tensile strength
f_{ct}	MPa	Direct tensile strength
$f_{ct,\infty}$	MPa	Ultimate direct tensile strength
f_{ft}	MPa	Flexural strength
G_d	GPa	Dynamic shear modulus
K_d	GPa	Dynamic bulk modulus
K_p	GPa	Static bulk modulus
K_s	GPa	Bulk modulus of the solid skeleton
M_d	GPa	P-wave modulus
P_{cap}	MPa	Capillary pressure
Q	[J]	Heat of hydration
Q_∞	[J]	Ultimate heat of hydration
r	nm	Kelvin radius
R	J/mol k	Universal gas constant
RH	%	Relative humidity drop
RH_s	%	Relative humidity drop due to dissolved slats
RH_k	%	Relative humidity drop due to menisci formation
S	-	Saturation fraction
S_c	-	Chemical shrinkage ratio
T	K	Absolute temperature
t_o	min	Time-Zero; Final setting time
V_c	ml/g	Volume of cement before mixing
V_m	cm^3/mol	Molar volume of the pore solution
V_p	m/s	Ultrasonic P-wave velocity
V_w	ml/g	Volume of water before mixing
V_{ew}	ml/g	Evaporable water content
V_{rc}	ml/g	Volume of reacted cement
V_{rp}	ml/g	Volume of reaction products formed

V_{rw}	ml/g	Volume of water reacted with cement
V_{tp}	ml/g	Total permeable pore
W_b	%	Bound water content
$W_{b,\infty}$	%	Ultimate bound water content
W/B	-	Water-to-binder ratio
α	[%]	Degree of hydration
τ	-	Time parameter
β	-	Shape parameter
υ	-	Poisson's ratio of mortar
ρ	Kg/ m^3	Density
γ	mN/m	Surface tension
ε_{auto}	με	Total autogenous shrinkage
ε_e	με	Elastic deformation
ε_c	με	Time-dependent deformation

Quantitative analysis of restrain ring test

E_{st}	GPa	Elastic modulus of steel ring
P_{act}	MPa	Actual Pressure
P_{ela}	MPa	Elastic stress of mortar ring
R_{im}	mm	Inner radius of mortar ring
R_{om}	mm	Outer radius of mortar ring
R_{is}	mm	Inner radius of steel ring
R_{os}	mm	Outer radius of steel ring
U_{free}	mm	Radial displacement of mortar ring
U_m	mm	Elastic deformation of mortar ring
U_{st}	mm	Elastic deformation of steel ring
ε_{st}	με	Restrained inner ring strains
υ_s	-	Poisson's ratio of steel ring
$\sigma(r)$	MPa	circumferential or hoop stress at any radius (r)
$\sigma_{act,max}$	MPa	Maximum actual residual stress in mortar ring
$\sigma_{els,max}$	MPa	Maximum Elastic stress in mortar ring
φ	%	Degree of restraint
σ_{rel}	MPa	Stress relaxation

ø	-	Creep factor

Chapter 1

Introduction

1.1 Problem statement

Concrete is an important construction material in infrastructure development and with its ease of production and use, local availability, low cost and versatile applications, globally its usage is second to water. Due to rising population, continuous urbanization and development of infrastructure with it, the global cement production, an essential constituent of concrete, is expected to continuously increase in the future. The total annual cement consumption in 2016 is around 4.10 Gt [1] and it is expected to increase up to 4.68 Gt/year by 2050 [1, 2]. Fig. 1.1 shows the expected cement production up to 2050 by regions.

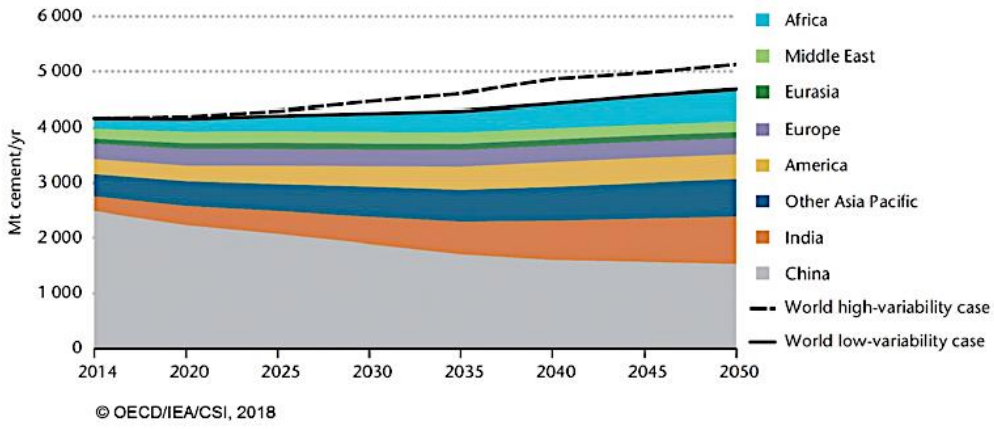

Figure 1.1: Cement production and forecast by regions, based on United states Geological survey data [1].

Such an enormous volume of cement production is accompanied with a significant amount of CO_2 emission and energy consumption due to physical and chemical processes involved in the conversion of limestone into Portland cement clinker [3, 4, 5]. Today, the cement industry is responsible for about 6-10% of total global anthropogenic CO_2 emission, or about 6% of total anthropogenic greenhouse gas (GHG) emission [6, 7]. In addition to this, the production of

cement requires large quantities of natural resources, particularly limestone. Therefore, the biggest challenge of the cement industry nowadays is to develop low-carbon or eco-efficient cements [8]. The well-established way to do so, is using supplementary cementitious materials (SCMs) such as fly ash and blast furnace slag as partially substitution of Portland clinker (PC) [9]. While the maximum allowable limit of usage of SCMs in blended cements is limited due to their lower performance compared to Ordinary Portland Cement (OPC), using alkalis offers a promising solution to enhance their reactivity. This can be achieved in two ways: 1) by adding alkalis in blended cements, where PC is partially replaced with SCMs, which is called as hybrid cements [10] and 2) by alkali-activation of SCMs that fully replace PC, which is termed as alkali-activated cements (AACs) [11].

Alkali-activated cement as a sustainable binder, is developed by completely replacing PC with industrial residues, which do not require any further processing and are inherently rich in calciumsilicates and aluminosilicates that are the main chemical components found in PC sources [12, 13, 14, 15]. Alkali-activated cements (AACs) are reported to generate nearly 55-80% lower CO_2 emission than PC [16, 17]. In addition to its eco-friendly performance, alkali-activated cements, developed with blast furnace slag and fly ash, are reported to show various advantages over OPC, including lower heat release during hydration reaction, higher rate of strength development at early ages, excellent resistance to fire and chemical attacks due to a refined pore structure and improved interface transition zones in concrete [18, 19, 20, 21]. Overall, the alkali-activated slag/fly ash (AASF) cements are considered to be promising binder systems with reduced environmental footprints and comparable or even better performance to OPC. However, the use of AASF cements in engineering practice and structural applications is limited due to critical shortcomings such as quick setting time, low workability and large volume instability [19, 22, 23, 24, 25, 26, 27]. However, the scientific and comprehensive reasoning behind the quick setting time and large autogenous shrinkage in AASF cements is still remaining a crucial research gap in the literature. Therefore, an integrated research approach is essential to study and understand the early age structural development associated with the setting behavior and the causes for large autogenous shrinkage behavior.

1.2 Research aims and objectives

The above stated problems and research gaps led to the definition of these research questions. The main objectives of this research are: (1) to study the early-age structural development and (2) to understand the complex autogenous shrinkage behavior in alkali-activated slag/fly ash

cements (AASF). Detailed analysis on the reaction kinetics, reaction chemistry and microstructure development are essential to explore the basic mechanism of autogenous shrinkage and to develop mitigation strategies in AASF cements. To reach this aim, the following objectives are defined:

- Analyzing the setting and hardening behavior of AASF cements continuously by using ultrasonic measurements.
- In-depth understanding of the mechanism of autogenous shrinkage in AASF cements through an interlinked assessment of reaction kinetics, reaction products, and microstructure development.
- Developing predictive tools to assess the autogenous shrinkage accurately in AASF cements.
- Understanding the cracking risk of AASF cements under restrained autogenous shrinkage conditions.
- Developing a mitigating strategy against autogenous shrinkage, based on the new knowledge on mechanisms of autogenous shrinkage in AASF cements.

The research will deliver new scientific and comprehensive knowledge beyond the state-of-the-art and will contribute to the scientific underpinning of AASF cements with respect to setting and autogenous shrinkage behaviour.

1.3 Research methodology

In this study, different alkali-activated slag/fly ash cements at 80:20 vol% of slag/fly ash ratio were formulated by varying type and concentrations of the alkaline solution. This will deliver various binder systems with different chemistry, reaction kinetics, and reaction products. In this way, the impact of solidification process and microstructure development on autogenous shrinkage is well explored. Due to the availability of various activators in different combinations, a bottom-up approach is followed in this study, meaning that a screening test is adopted based on heat release, setting time and strength development. Most ideal activator combinations are selected for further studies including, early-age structural development, autogenous shrinkage, cracking and shrinkage mitigation strategies.

1.3.1 Early age structural development

Early-age structural development of the compositions is characterized using the ultrasonic P-wave velocity method, a non-classical method, which provides more reliable results than the

classical methods such as Vicat test. This ultrasonic method is widely used in OPC-based materials for continuously monitoring the setting process by studying P-wave transmission velocity, energy or frequency content and S-wave reflection coefficient. Longitudinal wave (P-wave) velocity is sensitive to the formation of hydrates and characterizes very early age microstructure changes associated with the setting.

1.3.2 Reaction kinetics of AASF binder

Hydration kinetics, which describe the rate of reaction products formation, is studied by means of isothermal conduction calorimetry (TAM Air device TA Instruments), where heat generation by the exothermic hydration reaction is used as an indication of the reaction progress. The degree of reaction can be computed as a function of heat release at any time (t) and the heat release when complete hydration is reached, which is determined by using expoential fitting function. Applicability of this model for AASF cements is investigated and adjusted according to the parameters involved. Another commonly used method for determining the degree of reaction is the Thermogravimetric analysis (TGA) with a principle proportion to chemical bound water. In this study, TGA is performed at the age of 1, 3, 7, 28, 90 and 180 days and the chemical bound water at the age of 180 days is considered as the ultimate value for determining the degree of reaction. Pore solution is another essential tool used in this study to determine the dissoution kinetics of precursors, which controls the reaction kinetics and the amount of reaction products formation over time.

1.3.3 Characterization of solid phases and pore structure

Due to the fact that reaction phases formed in the studied AASF cements are mainly X-ray amorphous, we aim here to identify the formation of possible crystalline phases while we have sulfate and carbonate ions in the activating solutions. Thermogravimetric analysis (TGA) will support the XRD results and will deliver the time-dependent evolution of the reaction products. The final physical, chemical and mechanical properties of the binder structure are controlled by the nanostructure arrangement of the silicon and aluminum in the hydrated gel, which significantly depends on the nature and type of activator and curing conditions. Binder structure evolution is characterized by using a combination of sophisticated analytical techniques. Attenuated total reflectance Fourier transform infrared (ATR-FTIR) spectroscopy is able to monitor structural formation in the binders and to identify the chemistry of the phase assemblages. By using Electron Probe Micro Analyzer (EPMA) point analyses, the elemental ratios of the hydration phases are evaluated. Characterization of the pore structure is performed

using mercury intrusion porosimetry and Nitrogen sorption tests. The in-depth understanding of the reaction chemistry of the hydration products and microstructure development of the studied AASF cements and relating this knowledge to the autogenous shrinkage behavior will deliver the novel contribution to the relevant scientific domain.

1.3.4 Autogenous shrinkage

The notion autogenous shrinkage (ε_{as}) is defined as the combination of chemical shrinkage (ε_{cs}), self-desiccation (ε_{sd}) and self-induced thermal deformation (ε_{td}). The autogenous shrinkage is tested on mortar scale, whereas the chemical shrinkage measurements were performed using the paste samples of the same composition as the binder phase of mortar. Autogenous shrinkage on mortar scale is tested via Auto-shrink digital dilatometer which is typically used for cement research. The chemical shrinkage is measured by using dilatometry method in paste scale. At a certain point of time (so-called time-zero), the stiffness of the matrix is high-enough to restrain the volume changes caused by chemical shrinkage and changes the autogenous shrinkage from the function of chemical shirnkage to self-desiccation. To investigate the self-desiccation process after 'time-zero', both internal relative humidity and surface tension of the pore solution were measured as inputs. Due to the fact that heat release during the hydration process in alkali-activated cements is quite low compared to OPC-based materials, the thermal deformation is ignored in this study. Based on the new knowledge on mechanisms of autogenous shrinkage, a mitigation strategy to control the autogenous shrinkage in AASF cements is developed.

1.3.5 Cracking tendency

Cracking tendency of AASF cements under restrained autogenous shrinkage conditions is experimentally studied using circular ring test.

1.4 Research outline

The outline of the thesis and the interaction between different chapters are illustrated in Fig. 1.2.

Chapter 1 describes the problem statement, the objective of this work, research methodology and the outline of this thesis.

Chapter 2 gives a literature overview of the alkali-activated cements with main focus on reaction mechanisms, reaction products, nano-and microstructure development. The overview

of autogenous shrinkage mechanisms and crucial factors affecting the autogenous shrinkage in alkali-activated cements (AACs) are discussed.

Chapter 3 describes the mix compositions and various experimental techniques used in this study.

Chapter 4 focusses on the early age structural development of alkali-activated cements. By combining ultrasonic measurements and isothermal calorimetry heat flow curves, the reaction process is discussed. The setting behaviour is studied by using traditional Vicat needle tests, as well as the ultrasonic measurements. The mechanical strength and stiffness development are discussed, and their correlations are investigated. Furthermore, these experimentally measured strengths and elastic properties are compared with ultrasonic measurements and correlations are formulated to predict mechanical properties from ultrasonic measurements in alkali-activated cements.

Chapter 5 gives the comprehensive description of solid phases and pore structure of the investigated alkali-activated cements. The dominant reaction products formed in the studied compositions, their chemical compositions and atomic ratios were investigated. The pore structure characterization was done using Mercury Intrusion Porosimetry (MIP) and Nitrogen absorption test.

Chapter 6 describes the autogenous shrinkage behaviour in the studied alkali-activated cements. The capillary tension caused by self-desiccation process is evaluated, in order to to elucidate the relationship between the capillary tension in the pore fluid and the autogenous shrinkage. Based on the obtained results, different parametrized models are developed to predict autogenous shrinkage in alkali-activated cements.

Chapter 7 assesses the stress development and cracking tendency under restrained autogenous conditions for the studied alkali-activated cements.

Chapter 8 describes the effect of elevated curing temperature (40°C) as a mitigation strategy for autogenous shrinkage. The influence of the curing temperature on the reaction kinetic, reaction chemistry, and microstructure development, respectively, is investigated first and then interlinked to the measured autogenous shrinkage.

Chapter 9 summarizes the main conclusions and proposes research perspectives for future studies.

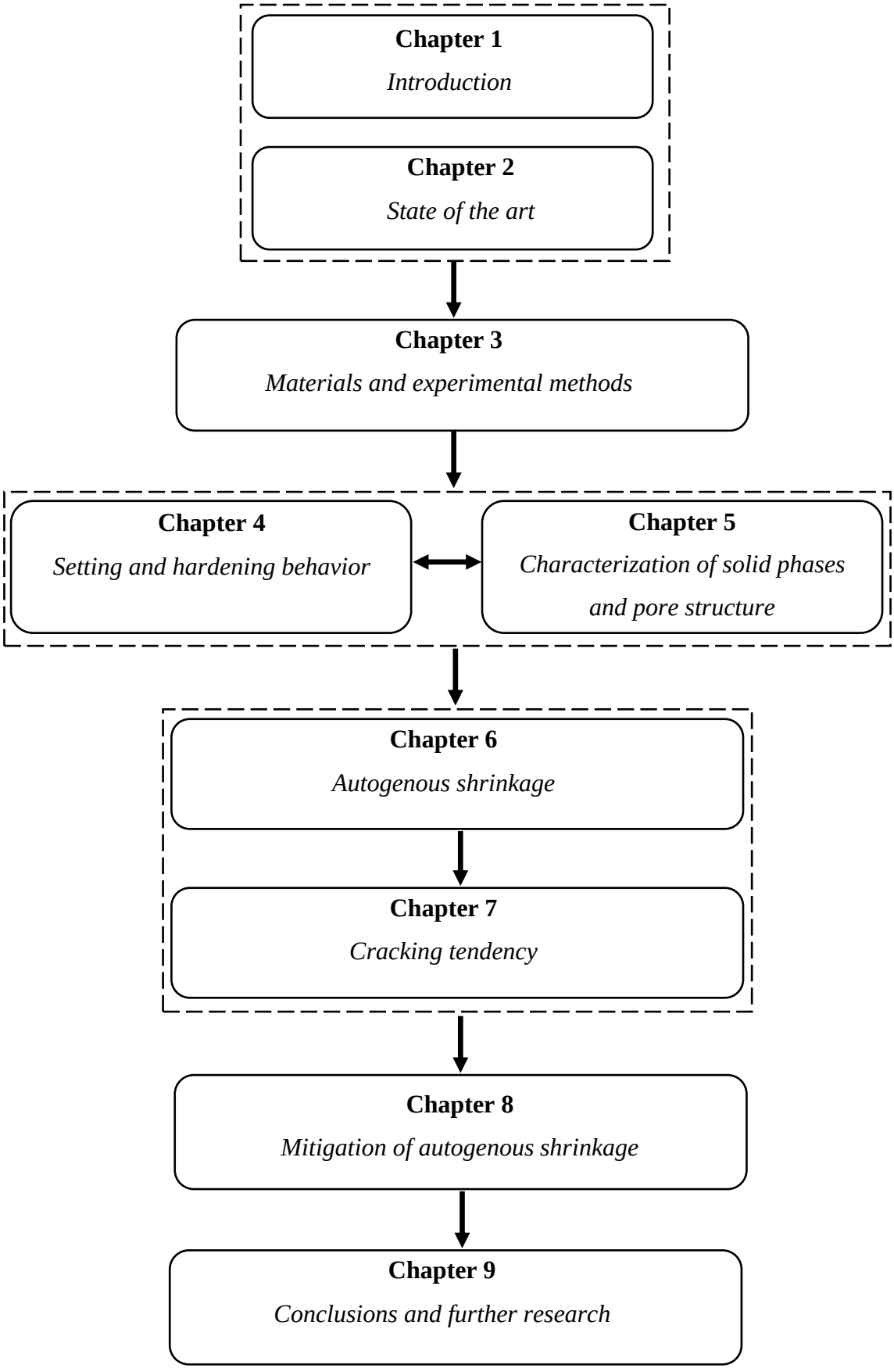

Figure 1.2: Outline of the PhD thesis.

Chapter 2

State of the art

2.1 Introduction

In this chapter, the current state of the art on the alkali-activated cements with focus on reaction mechanisms, microstructure development and autogenous shrinkage mechanisms is reviewed. First, the general classification of alkali-activated cements is defined, and the commonly used raw materials and the alkaline solutions are discussed. Then, the environmental benefits of using alkali-activated cements developed with different source materials and alkaline solutions are given and compared with the traditional Portland cement. Secondly, the basic reaction mechanisms, reaction products, nano-and microstructure of the hydrated gels formed in alkali-activated cements are presented with respect to the current literature findings. In the third part, the proposed mechanisms for autogenous shrinkage in alkali-activated slag cements (AAS) and its influencing factors are briefly discussed. Furthermore, the mitigation strategies to control autogenous shrinkage are emphasized. Finally, the research gaps and the key questions regarding reaction process and complex autogenous shrinkage behavior of AAS are addressed.

2.2 Alkali-activated cements (AACs)

2.2.1 Definition and classifications

Alkali-activated cements (AACs) are defined as the new class of cementitious materials that are produced from the reaction between the alkali sources (i.e. concentrated alkaline solutions) and the fine solid reactants rich in calcium-silicate and aluminosilicate sources [28, 29, 30]. Similar to OPC-based materials, the mechanical and durability properties of the alkali-activated cements are primarily dependent on the phase assemblages and microstructure development [31, 32, 33, 34, 14], which can be modified by using different raw materials and alkaline solutions. Based on the chemical composition of the raw materials used, the alkali-activated cements can be classified into three different systems:

1. High calcium systems: alkali-activation of calcium-silicate rich materials (Ca + Si >70%) like blast furnace slag. In this case the main reaction product is calcium silicate hydrate (C-S-H) type gels, which differ slightly from the gel formed in cement hydration, in that it has low C/S ratio of range around 0.9-1.2 [35, 36, 37]. Previous studies [38, 39, 40, 41] proposed that aluminium (Al) is taken up in this gel to form C-A-S-H gel, in which aluminium tetrahedra replace silicon tetrahedra in bridging positions to give rise to Q^1, Q^2, and Q^2 (IAI) units.
2. Low calcium systems: alkali-activation of aluminosilicates rich materials like Class F fly ash and metakaolin, result in a three-dimensional inorganic alkaline polymer N-A-S-H gel as the main reaction product [42, 43, 44].
3. Hybrid systems: alkali-activation of materials with CaO, SiO_2, and Al_2O_3 content > 20% (blending both calciumsilicate and aluminosilicate materials), comprising a mix of cementitious gels (C-A-S-H + N-A-S-H gels) [45, 46, 47, 48]. For examples, the alkali-activation of slag/fly ash (AASF) cement is the most commonly used hybrid system.

2.2.2 Raw materials

Blast Furnace slag: A number of studies have reported that slags from different origins yield cementitious reaction products with alkali-activation [49, 50]. Among them, ground granulated blast furnace slag (GGBFS) is the commonly used source material for alkali-activated cements due to its high reactivity. However, the use of blast furnace slag as the source material in alkali-activated cements mainly depends on the amount of its vitreous phase, which contains a network of depolymerized calcium and silicates as hydraulically activity components. Previous studies have suggested that slag with a vitreous phase of 85-95% is usable for alkali-activated cements. The hydraulic activity of blast furnace slag can be obtained by calculating the basicity coefficient using wt% of oxides, Eq. 2.1.

$$K_b = \frac{CaO + MgO}{SiO_2 + Al_2O_3} \tag{2.1}$$

$$HM = \frac{CaO + MgO + Al_2O_3}{SiO_2} \tag{2.2}$$

Based on the basicity coefficient, the blast furnace slag is classified into three types: acidic (K_b <1), basic (K_b >1) and neutral (K_b =1) slags. Both neutral and basic type slags are preferred for alkali-activated cements. Moreover, in order to achieve good hydration properties, the

hydraulic modulus (HM) of the slag, calculated using Eq. 2.2, should exceed 1.4, as suggested in previous study [51]. In addition to the chemical composition of blast furnace slag, the physical properties like particle size distribution also influences its rate of reactivity. It is recommended to use slag with a specific surface area of around 400-600 m^2/Kg [30].

Fly ash: Fly ash (FA), an industrial by-product from coal fired thermal power plants, is another source material that is commonly used for preparing alkali-activated cements. Depending on the coal type and combustion furnace, the chemical composition of fly ash varies widely. It is generally classified into two categories based on the lime content: (1) Class F or Siliceous fly ash, in which the majority oxides are SiO_2 and Al_2O_3 and it contains CaO<10% and (2) Class C or Calcareous fly ash, in which the CaO content is >10%, usually in between 15-30% [52]. Among these two types, Class F fly ash is commonly used for alkali-activated materials due to high amounts of amorphous aluminosilicates and low CaO content. In Class C type fly ash, the presence of a high Ca content accelerates the rate of reaction and leads to a quick setting time and low workability, which makes it unsuitable for concrete applications that require longer setting time [53]. EN 450-1 [52] suggests some specification for siliceous Class F fly ash to produce good binder as below:

- Reactive CaO ≤ 10%
- $SiO_2 + Al_2O_3 + Fe_2O_3 \geq 70\%$, in which Fe_2O_3 should be <10%
- Unburnt carbon or LOI < 5%
- $SO_3 \leq 3\%$
- Free lime < 1%
- High vitreous content (>85-95%)

Besides the chemical composition, the fineness of the fly ash is another important factor that affects the setting time and mechanical strength properties of alkali-activated cements [54]. It was reported that, fly ash with a maximum of 80-90% particles having a seize size under 45µm is preferred for alkali-activated cements [30]. One previous study has reported that the surface charge on the fly ash particle also influences the setting behavior in fly ash-based alkali cements [55].

Similar to Class F fly ash, metakaolin is an amorphous and highly reactive aluminosilicate-rich source material used in the production of alkali-activated cements. Nevertheless, the use of metakaolin in alkali-cements is limited due to its high fineness and specific surface area causing high demand of solution in producing a good workable concrete.

2.2.3 Alkaline activators

The alkaline activator is the second essential component in alkali-cements, that strongly affects the reaction kinetics, formation of reaction products and microstructure development [56]. The activation of calciumsilicate and aluminosilicate rich materials is a chemical process with several steps that starts with breaking the Si-Al bonds of the source materials in a high alkaline environment [29, 30]. According to the chemical composition, the alkaline activators can be classified in to six groups as given below [57]:

1) Caustic alkalis (MOH)
2) Weak acid slats (M_2CO_3, M_2SO_4, M_3PO_4, MF)
3) Silicates ($M_2O.nAl_2O_3$)
4) Aluminates ($M_2O.\ nAl_2O_3$)
5) Aluminosilicates ($M_2O.\ Al_2O_3.(2\text{-}6)SiO_2$) and
6) Strong acid slats (M_2SO_4)

M stands for Na and K.

Nevertheless, in literature, Na-based activators are widely used compared to K-based activators. This is because, the Na^+ cations have smaller ionic size or lower charge density compared to K^+ cations. This enhances the dissolution process of the materials (i.e. more active) [58]. On the other hand, the hydroxides, silicates, carbonates, and sulfates are often used anions in alkali-cements.

Sodium silicate: A majority of studies have reported that slag activated with sodium silicate or a mixture of sodium silicate and sodium hydroxide gave superior or comparable strength properties to OPC-based materials [56, 59]. Sodium silicate in alkali-cements is generally expressed as a ratio between the silica oxide and the sodium oxide, termed as alkali-modulus ($M_s=SiO_2/Na_2O$) [28]. Two important factors that need to be considered when sodium silicate is used as activator are: (1) silica content and (2) alkali-modulus ratio [29]. In slag activation, the soluble silicates react with dissolved calcium ions from the slag and forms silica-rich C-A-S-H type gels [59]. An increase in silica content leads to the formation of more densely packed C-A-S-H type gels with a higher degree of silica polymerization or longer silicate chains [60, 39]. Similarly, in fly ash activation, the silica content plays an important role in the reaction degree as well as in the composition and structure of N-A-S-H gels. The presence of silicates in solution favors the early formation of silica-rich gels and leads to quick setting and poor workability [61, 54]. Moreover, the increase in silica content reduces the pH value and raises

the viscosity of the alkaline solution, which can affect the reaction degree of the materials [62]. Based on the type of slag, the optimum value of alkali-modulus various between 0.75-1.50 as shown in Fig. 2.1.

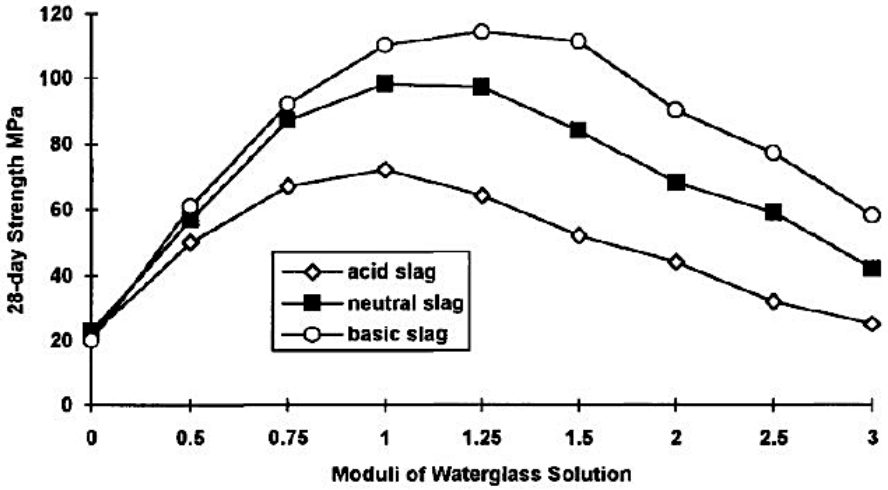

Figure 2.1: Effect of alkali-modulus on 28-days strength of alkali-activated slag [63].

Sodium carbonate and sodium sulfate: The use of sodium carbonate and sodium sulfate in alkali-activation of slag (AAS) has gained interest by many researchers, since they are less expensive and their production process has a less environmental impact compared to sodium silicate and sodium hydroxide solutions [64, 65, 66, 67, 68, 69]. However, these activators are not that much attractive for the construction industries as they generate longer setting times (>3 days) and slower strength development [67, 68].

In order to counterbalance the disadvantages of each activator, many researchers are interested in hybrid or blended activators in AAS cements. The effect of different hybrid activators on hydration and strength behavior of AAS have been studied and reported that the hybrid activation results AAS cements with a good balance between mechanical properties, production cost and environmental footprint [70]. Recently, Bernal et al. [71] demonstrated that slag activated with hybrid sodium carbonate and sodium silicate enhanced reaction kinetics and setting times compared to a solely carbonate-activated slag. The authors also suggest that this hybrid activator can be used effectively for the development of high strength AAS materials. On the other hand, the combination of sodium carbonate and sodium sulfate with sodium hydroxide also improved the reactivity at early ages and consequently results in a higher rate of strength development [72, 73]. Nevertheless, the research with a main focus on

setting behaviour and autogenous shrinkage of AAS activated with hybrid alkaline solutions does not exist.

The alkalinity (pH value) of the activating solution is another important factor that affects the activation process. It has been reported that high alkalinity (OH^- ions) is required to activate the aluminosilicate rich materials like fly ash and metakaolin, since the solubility of silicate and aluminate increases with the concentration of OH^- ions (pH value) in the pore solution [74]. In contrast, the use of high alkalinity is not favorable in calcium-silicate rich materials like blast furnace slag since the calcium becomes less soluble with increasing pH value of the solution [74]. Besides the pH value, the alkali-content (Na_2O) in the activating solution can also affect the properties of alkali-cements. Most studies [63, 75] have reported that a Na_2O concentration between 4% to 5.5% is the most ideal concentration for the activation of slag. However, elsewhere, a Na_2O concentration of 8% is reported as ideal for sufficient strength properties in alkali-activated slag [19]. On the other hand, for fly ash-based activated cements, a Na_2O concentration of 14% is recommended to achieve good mechanical properties [54]. It has been reported that an increasing concentration of activator can result in a higher strength development. However, an increase in concentration behind the optimum range has negative influences and decreases the strength values [76].

2.2.4 Carbon footprint

Many studies [77, 17] have been conducted to compare the environmental benefits of using this new alkali-activated cements over Portland cement since it is the main motivation for developing the alternative binder options. In this study, one particular aspect of environmental impact, namely Global Warming Potential (GWP) is reported, which is an indicator of global warming due to the emission of greenhouse gases. The GWP of a material is expressed in CO_2-equivalent (CO_2-e) greenhouse gas (GHG) emission. The GWP values of OPC, blast furnace slag, fly ash and various alkaline solutions are presented in Table. 2.1. Although slag and fly ash are industrial by-products, the milling and grinding of these materials demand a certain amount of energy, thus the CO_2-e for these materials is nonzero as given in Table. 2.1. However, compared to OPC, the difference in CO_2-e is enormous. Yet, for preparing mortar or concrete with OPC, water is the main source for hydration. While in alkali-activated cements, a highly alkaline activating solution is required to hydrate the slag and fly ash materials. Hence the environmental impact of the activating solutions needs to be taken into account. As observed, the production of sodium hydroxide and sodium silicate have very high environmental impact, as these solutions have to be chemically prepared. While the sodium

carbonate and sodium sulfate occur naturally and can also be obtained as by-products from various industrial activities [67, 68]. However, the mining and processing of these materials require certain energy and have environmental footprints.

Table 2.1: CO_2-equivalent for 1kg production of materials (GWP value ranges).

Materials	**CO_2-e**	**Avg CO_2-e**	**References**
	(Kg/ Kg production)	(Kg/ Kg production)	
OPC	0.94-1.00	0.97	[77, 17, 16]
Slag	0.019-0.026	0.022	[78, 16]
Fly ash	0.019-0.027	0.022	[17, 16]
Sodium hydroxide	1.25-1.90	1.55	[17, 16]
Sodium silicate	1.54-2.12	1.83	[79, 17]
Sodium carbonate	0.12-0.59	0.35	[80, 81]
Sodium sulfate	0.22-0.47	0.34	[78, 80]

2.3 Reaction mechanisms and reaction products

2.3.1 Alkali-activated slag (AAS)

As explained above, blast furnace slag is a typically used high calcium source material, which contains larger amounts of calcium and a low content of silicates and aluminates in glassy phase. A recent study [82] describes the complex reaction mechanism of alkali-activated slag with four main stages: (1) hydrolysis and destruction of the slag bonds, (2) releasing Al and Si monomers and Ca^{2+} ions surrounded by OH^- ions with continuous dissolution of slag, (3) condensation between the dissolved ions and monomers to form C-A-S-H type gels, and (4) ongoing reaction over time via solid-state mechanism, as shown in Fig. 2.2. These authors confirm that the reaction process of alkali-activated slag is similar to OPC-based materials with a dissolution followed by a precipitation of reaction products at early ages and later followed by solid-state reaction.

Other researchers [83, 84, 36] also suggested a similar reaction mechanism with four stages including the dissolution of source materials, formation of initial reaction products, interaction between this newly formed reaction products or condensation reaction and formation of more reaction products (C-A-S-H gels) with continuous reaction.

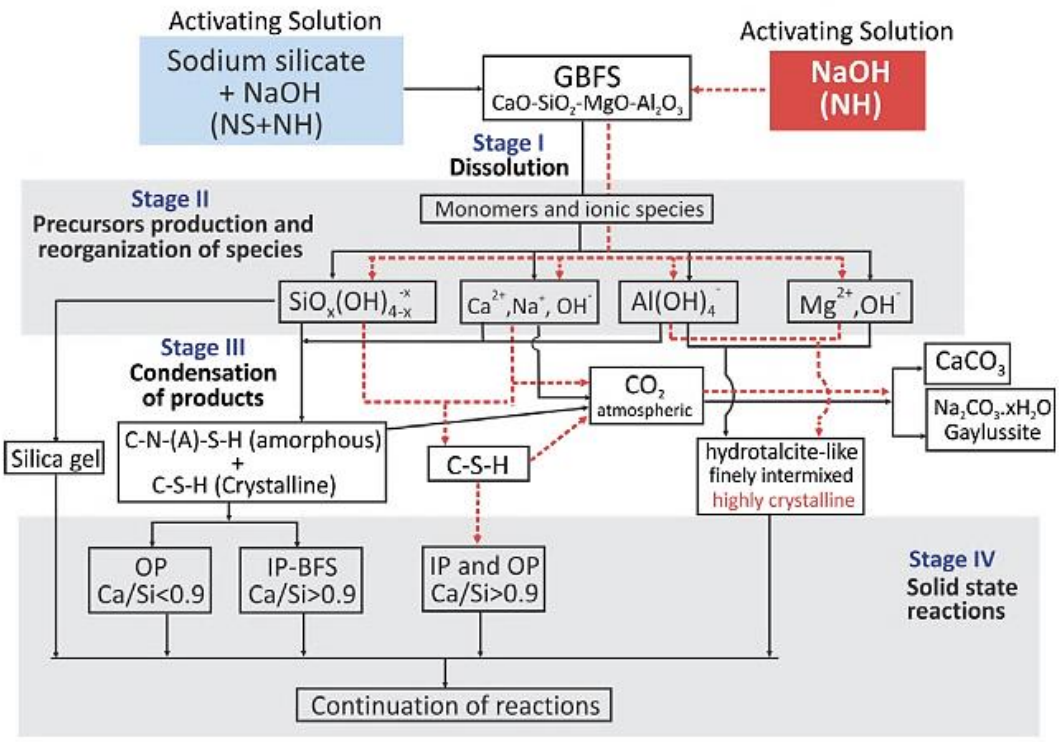

Figure 2.2: Reaction process of the alkali-activated slag [82].

In this system, calcium-alumina-silicate-hydrate (C-A-S-H) is identified as the main reaction product, which is similar to the reaction product formed in cement hydration [31, 35, 85]. Some authors [86, 87] also demonstrated that Na^+ can replace some of the chemically bounded Ca^{2+} ions in C-A-S-H gel with a decrease in Ca/Si ratio, leading to the formation of (N,C)-A-S-H gels. The nano-and microstructure of this C-A-S-H type gels mainly depends on the type and concentration of the activator and curing conditions [60]. The C-A-S-H type gels formed in sodium hydroxide have a lower degree of crosslinking structure with only a small amount of Q^3 units [60, 88], while in sodium silicate activation, the C-A-S-H gel forms with a higher degree of crosslinking structure having more Q^2 and Q^3 units [60, 59, 89, 90]. Moreover, the sodium silicate activation also affects the chemical composition of C-A-S-H gel by providing extra silicates from the activating solution, i.e. the Ca/Si formed in sodium silicate is lower than in the sodium hydroxide activation [91]. The C-A-S-H gel formed in sodium carbonate activation shows a higher degree of crosslinking structure with more Q^3 sites compared to sodium hydroxide, but lower than the sodium silicate-activated slag systems [60]. Also, curing at elevated temperature forms more uniform C-A-S-H gel with lower degree of crosslinking (or no Q^3 units observed) [29].

The formation of secondary products in slag activation depends on the activator type, chemical composition of slag and curing conditions [37, 34, 36]. The main secondary product identified in slag activation with sodium hydroxide and sodium silicate is hydrotalcite ($Mg_6Al_2CO_3(OH)_{16}.4H_2O$), which is a Mg-Al layered double hydroxide with interstitial CO_3^{2-} ions and water molecules [36, 89, 92]. Also, the silica containing AFm phases such as strätlingite are likely to form in sodium silicate activation [91, 18]. However, these AFm phases cannot be identified from XRD patterns, as they are intermixed with C-A-S-H type gels [93]. In samples activated with sodium carbonate and sodium sulfate, calcite and ettringite are observed as the main secondary reaction products, respectively. The early age reaction in sodium carbonate favors the formation of carbonate phases like calcite and gaylussite ($Na_2Ca(CO_3)_2.5H_2O$), as CO_3^{2-} ions in the activating solution react with dissolved Ca^{2+} and Na^+ ions [64]. The formation of this carbonate phases and the low pH value (11-12) of the sodium carbonate solution explain the reason for longer setting times and slower strength development in sodium carbonate activated slag cements at early ages [67]. As sodium sulfate is a neutral salt, a neutral pH (~7.0) will be obtained when combined with water. Just like with sodium carbonate, the SO_4^{2-} ions from the activating solution react with the dissolved Ca and Al ions from the slag to form sulfate phases like ettringite [68]. The formation of ettringite, an expansive sulfate phase, can benefit the alkali-activated cements by reducing shrinkage at early-ages [94, 95].

2.3.2 Alkali-activated fly ash (AAF)

Both fly ash and metakaolin are the two commonly used low calcium source materials in alkali-activated cements. Although the chemical composition and particle size distribution differ significantly, the amorphous aluminosilicate in these two materials is identified as the main reactivity phase. Thus, the same reaction model is suggested by many researchers for fly ash or metakaolin or other aluminosilicate rich activated materials. In fly ash-based alkali-cements, the complex chemical reactions can be divided into three stages as described below [30]:

- **Dissolution-coagulation:** This stage includes the destruction of Si-O-Si bonds in the fly ash and the formation of negatively charged silanol ($Si-OH^-$) and sialate ($Si-O^-$) species. The alkali-cations (Na^+) in the activating solution neutralize this negatively charged species and yield $Si-O-Na^+$, which hinders the reversion of this reaction to form Si-O-Si. In the same way, the Al-O-Si bonds in the fly ash are impact and result in $Al(OH)_4$ anions.

- **Coagulation-condensation:** The silicate and aluminate species accumulate to form a coagulated structure and starts the polycondensation reaction.
- **Condensation-crystallization:** Solid phases are gradually formed and crystalline.

Many researchers [96, 13] subsequently modified the above described model and reported that the formation of the main reaction product N-A-S-H in alkali-activated fly ash includes four main stages as shown in Fig. 2.3. During the first stage, when the source material fly ash comes into contact with the alkaline activator, it dissolves silicate and aluminate species as monomers. During second stage, these monomers accumulate to form dimers, which then interact with another monomer to form trimers and so on, and forms aluminosilicate gel (Stage III). This initial formed gel is rich in Al (called as Gel 1, Si/Al ratio is around 1). The formation of this Al-rich gel (Gel 1) can be explained by the fact that the aluminum dissolved more quickly than silicon as Al-O bonds are weaker than Si-O bonds [97]. As the reaction proceeds (Stage IV), more Si species are dissolved from the source material and this increases the Si concentration in the N-A-S-H gel (named Gel 2, Si/Al ratio is around 2). Afterwards, a polymerization reaction occurs between the Gel 2 units to form large molecular structural units (N-A-S-H gels).

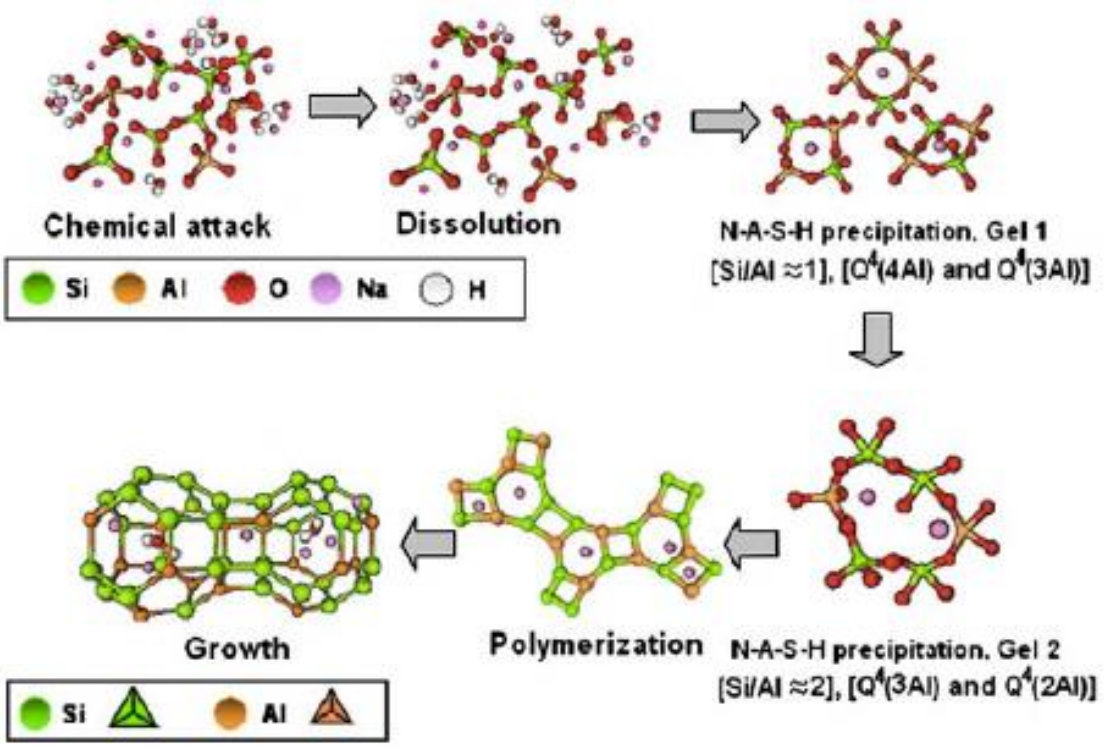

Figure 2.3: Model for the reaction mechanism in alkali-activated fly ash [13].

In this system, a three-dimensional inorganic polymer network (N-A-S-H type gels) is identified as the major final reaction product [31, 42]. Nevertheless, the gel structure can vary

significantly depending on the curing condition and the activator type or presence of soluble silicates in the activating solutions. Sodium silicate is more effective than sodium hydroxide activation in fly ash-based systems, as the dissolved Al ions react with silicates that are initially present in the activating solution to form aluminosilicate gels [97]. The N-A-S-H type gel formed in sodium hydroxide activation is predominated with Q^4(nAl) units [42]. On the other hand, the main secondary reaction products formed in fly ash-based systems are zeolite phases like hydroxysodalite ($Na_4Al_3Si_3O_{12}OH$) and herschelite ($NaAlSi_2O_6.3H_2O$) [76].

2.3.3 Alkali-activated slag/fly ash blends (AASF)

Recently, many researchers have been focused on developing hybrid systems by mixing both calciumsilicate and aluminosilicate rich materials as it counterbalances the disadvantage of each sole activated system. For instance adding a moderate amount of fly ash in alkali-activated slag cements increases the setting time, workability, longterm mechanical strength development and durability properties [98, 99]. Previous studies have suggested that both C-A-S-H and N-A-S-H type gels form simultanelouly in this hybrid systems [47, 100]. On the other hand, some studies argue that both these reaction products do not develop as two separate gels, but they interact and undergo continious structural and compositional changes [101]. Few studies [102, 46] have been conducted to explore the compatibility of these two gels and reported that the stability of N-A-S-H gel in hybrid systems mainly depends on the alkalinity (pH value) and the calcium content, as shown in Fig. 2.4. At pH > 12 and with sufficient calcium content, the formation of C-A-S-H type gel is favoured over N-A-S-H gel [46].

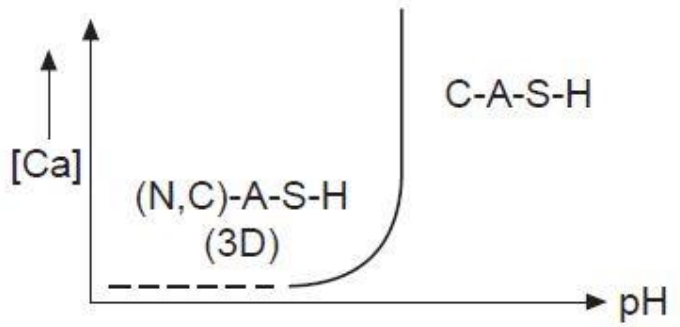

Figure 2.4: Stability of N-A-S-H type gel in hybrid systems as a function of pH value and Ca content [30].

The presence of dissolved calcium ions in the pore solution destroys N-A-S-H type gels, with partial replacement of Na with Ca ions via ion exchange reaction to form (N,C)-A-S-H type

gel. As the reaction proceeds, the calcium ions degenertes N-A-S-H type gels by releasing the aluminum ions due to polarising effect of the Ca^{2+} ions to form less polymerized C-A-S-H gels. From litertaure, it can be summarized that co-precipitaion of C-A-S-H and N-A-S-H type gels is visible in hydrib systems at early ages, however, over time, this mix evolves towards a single C-A-S-H type gel. It is also reported that the continious structural and compositional changes in gels have no impact of the mechanical strength properties of the material [30].

2.4 Early age reaction process from ultrasonic measurements

Similar to hydrating Portland cements, the early-age reaction of AAS cements is critical to the formation of reaction products and internal microstructure development. This affects the setting and hardening process and shrinkage deformation, particularly the early-age autogenous shrinkage. Therefore, it is of great importance to explore the early-age reaction process of AAS cements. Nevertheless, there are only limited studies focusing on the early-age reaction process of AAS cements due to its complexity and difficulties. Among them, most of the studies have used isothermal calorimetry to monitor the early-age reaction process of AAS cements due to its convenience [28, 37, 68, 84, 103, 104]. However, this characterization method could not provide the information about the microstructure evolution of the material. Recently, some advanced characterization techniques like ^{29}Si NMR and ^{27}Al NMR were used to study the early reaction process of AAS cements [105, 106]. This method has become an accepted and preferred approach to study the complex reaction process of alkali-cements, but the economic constraints (its high-cost) and prolonged measuring time have limited the application of this innovate method. Besides, various analyzing methods including Thermogravimetric and Differential Scanning Calorimetry (TG/DSC), X-ray Diffraction, Fourier Transform Infrared Spectroscopy (FTIR), and Scanning Electron Microscopy (SEM), are applied to understand the reaction process and reaction chemistry of AAS cements. Fig. 2.2 illustrates the reaction process of the alkali-activated slag cements monitored using SEM analysis and ^{29}Si NMR and ^{27}Al NMR.

On the other hand, ultrasonic wave measurement is a non-destructive and continuous method that has been successfully applied to monitor the early-age reaction process of cement-based materials [107, 108]. Nevertheless, there are few studies [109, 110] that have been carried out on the AAS cements to characterize the early-age microstructure evolution by using the ultrasonic wave measurements. Recently, Cao et al. [110] investigated the reaction process during the first 24 hours in AAS cements activated with sodium silicate by using an embedded

piezoelectric transducer based ultrasonic monitoring system. Based on the UPV evolution curve, the reaction process during the first 24 hours in AAS cements activated with sodium silicate is divided into five different stage: (1) dissolution stage, (2) acceleration stage, (3) deceleration stage, (4) secondary acceleration stage, and (5) secondary deceleration stage (Fig. 2.5) [110].

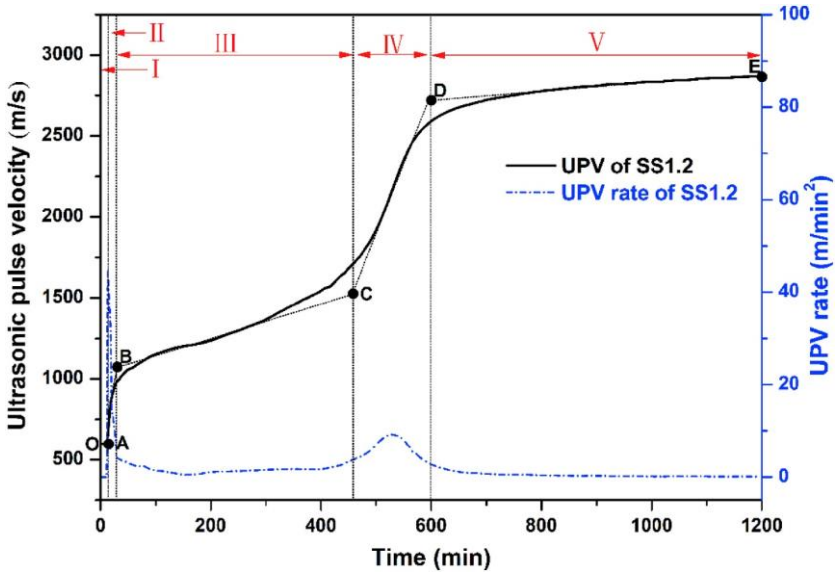

Figure 2.5: The UPV evolution of sodium silicate activated AAS cements [110].

Stage 1: Corresponds to the formation of initial reaction products near un-hydrated slag particles, from the chemical reaction between the dissolved ionic species and SiO_4^{4-} ions from the sodium silicate activating solution.

Stage 2: The ultrasonic velocity increases rapidly due to a significant increase in the formation of reaction products, resulting gradually densified matrix.

Stage 3: The ultrasonic velocity increases slowly due to the temporary suppression of slag hydration as a result of the barrier effect that arises from the formation of initial reaction products around the un-hydrated slag particles.

Stage 4: The ultrasonic velocity increases again rapidly due to the formation of massive reaction products. Once the alkalis penetrate through the wrapped layer formed by the initial reaction products, the concentration of Ca^{2+} and SiO_4^{4-} ions dissolved form the slag increases and contributes to the formation of further reaction products.

Stage 5: The ultrasonic velocity tends to level off. During this stage, the dissolution process and chemical reaction reach equilibrium, the reaction rate decreases gradually.

This study demonstrated that an increase in silica content or alkali-modulus of the activating solution speed up the reaction process during II and increases the reaction degree of AAS cements at early hours. In samples activated with sodium hydroxide, however, only first three stages are observed. Besides, these authors reported that the hydrated gel formed in samples activated with sodium silicate is denser than with sodium hydroxide and affects the ultrasonic velocity evolution, particularly at early hours. Nevertheless, much more research is needed in this area to provide a better understanding on the early-age reaction process of AAS cements by using ultrasonic measurements.

2.5 Setting process of AAS cements

It is well-known that the setting of slag activated with sodium silicate occurs very quickly and makes it unsuitable for applications that require longer setting time [23, 27, 19]. As explained above, the AAS cements are transformed progressively from a liquid precursor to a solid gel as a result of complex chemical reactions composed of dissolution, gelation, polycondensation and densification. The rate of these reactions determines the setting time that is significantly controlled by the solid precursor, type and concentration of the alkaline solution. Co-activation of calcium-rich slag and aluminosilicate-rich fly ash has shown to control the setting process and to counterbalance the tendency of quick setting in sole alkali-activated slag (AAS) and retards setting [111]. Many studies have reported that the setting time of AAS cements is increased with increasing fly ash content [112, 113, 114, 98].

Previous studies have reported that the type and concentration of the activator are the most dominant parameters that influence the setting process of AAS cements [115, 72]. High activator concentration is often necessary to achieve the desired strength, but this can lead to prohibitively short setting times (as short as 60 minutes) due to the acceleration effect of the highly alkaline activator [115, 116]. Some researchers have shown that the nature of anions in the activator significantly affect the setting time of alkali-activated slag, as the anions in the solution can react directly with the ions dissolved from the source materials to form stable reaction products, resulting in setting [34, 56, 72].

Until now, conventional methods such as Vicat needle test on paste (EN 196-3) and the penetration test (ASTM C403) on mortar are mostly used to monitor the setting time of AAS. However, both methods destroy the microstructure at the point of penetration and do not allow monitoring the setting and hardening processes continuously. Evolution of ultrasonic wave velocity in cement and concrete has been commonly used to continuously monitor the

percolation of the solid phases which cause dramatic changes in the ultrasonic wave behavior [107, 108]. Longitudinal wave (P-wave) velocity is sensitive to the formation of hydrates and can characterize very early microstructural changes associated with setting.

A few studies have recently used the ultrasonic wave reflection method to monitor the setting time of metakaolin-based geopolymers [117, 118, 119]. They found that geopolymers show a wide range of setting times depending on the chemical parameters including geopolymer composition (Si/Al ratio), type and concentration of the activator used. Nevertheless, not much research has been carried out to investigate the setting process of AAS cements using ultrasonic measurements.

2.6 Chemical shrinkage

Chemical shrinkage, also called as Le Chatelier contraction, is defined as the volume reduction caused by the formation of reaction products with lower volume compared to the combined volume of reactant particles (cement) and consumed water [120]. The chemical shrinkage can be described by the following equation [121]:

$$S_c = \frac{(V_{rc} + V_{rw}) - V_{rp}}{V_c + V_w} \tag{2.3}$$

Where S_c is chemical shrinkage ratio, V_{rc} (ml/g) is the volume of reacted cement, V_{rw} (ml/g) is the volume of water that reacted with cement, V_{rp} (ml/g) is the volume of reaction products formed, V_c (ml/g) is the volume of cement before mixing, and V_m (ml/g) is volume of water before mixing. Chemical shrinkage results both from the formation of the main reaction products and also from the secondary reaction products such as ettringite [122]. By using molecular weights and densities of the hydration products and reactants, the chemical shrinkage at complete hydration of traditional Portland cement is estimated in the range of 0.065-0.08 ml/ g of cement [123]. In alkali-activated slag cements, quantifying chemical shrinkage is a complex phenomenon, since different reaction products are formed with its own volume stoichiometry by varying the type and concentration of the activating solution. Nevertheless, recent studies [124, 125, 103] have reported that the theoretical value of chemical shrinkage at complete hydration of slag with sodium silicate activation is in the range of 0.107-0.140 ml/g of slag, which is twice the chemical shrinkage of traditional Portland cement.

2.7 Autogenous shrinkage and its mechanisms

Autogenous shrinkage refers to the macroscopic volume reduction of cementitious materials under sealed conditions without any moisture exchange with the surrounding environment [126]. It has been reported that autogenous shrinkage is one of the main causes for early-age cracking in concrete, which forms serious threat to structural durability through service life [127, 128]. AAS cements are known to have considerably higher autogenous shrinkage that is 6-10 times higher than that of the Portland cement [129, 130, 131, 132, 133, 134, 25], hereby inducing a higher risk to early age micro-cracking. Therefore, in recent years, much attention has been given to understand the causes and mechanism behind this large autogenous shrinkage behavior in AAS.

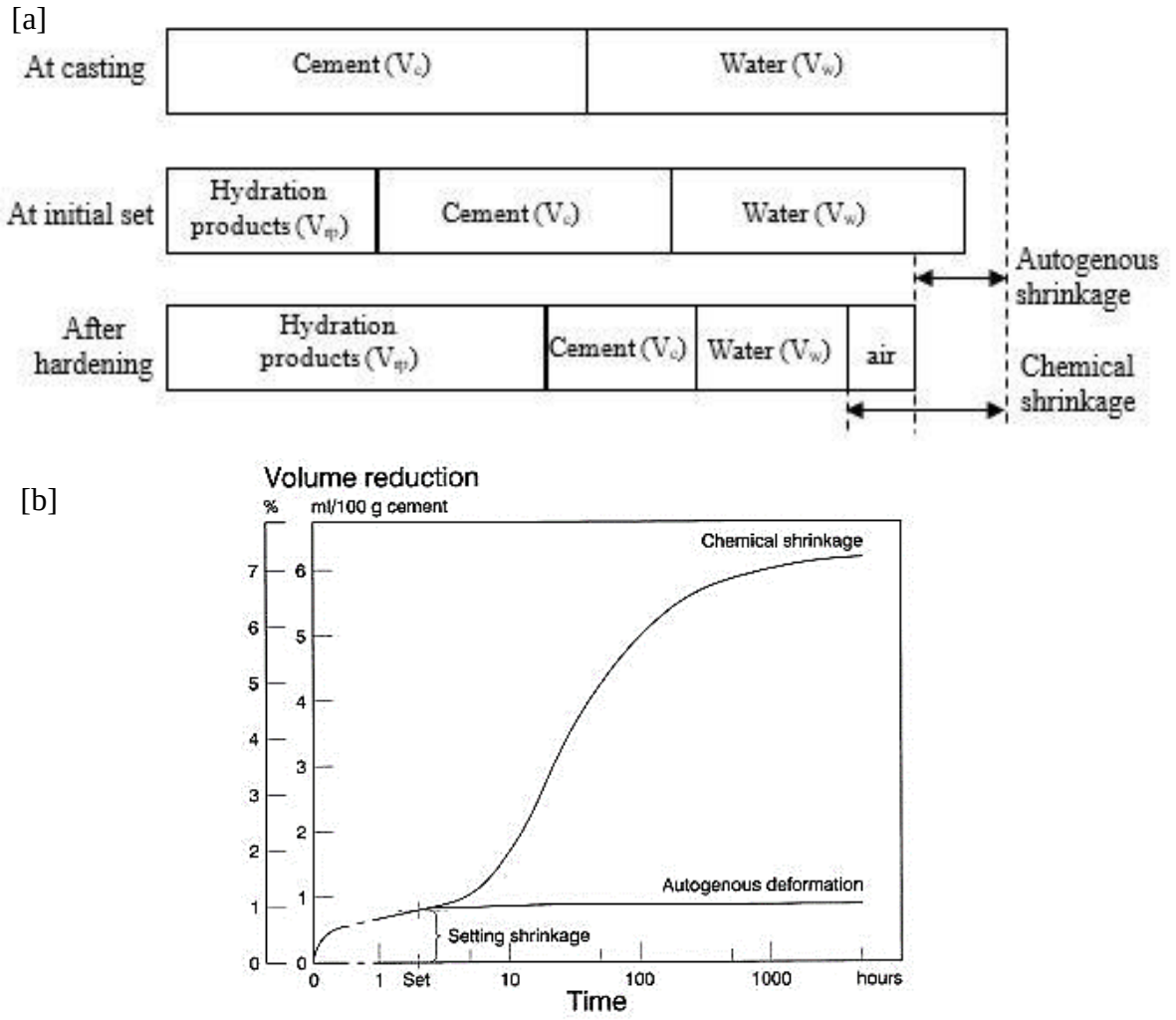

Figure 2.6: Chemical shrinkage and autogenous shrinkage during hydration [a] and their relationship [b] in Portland cement paste [135, 136].

Chemical shrinkage, occurring due to the negative balance between the reaction products and reactants, is considered as the basic driving force for autogenous shrinkage in cementitious materials [122, 136]. Fig. 2.6 shows the reactions causing internal chemical shrinkage and external autogenous shrinkage, and their relationship in traditional Portland cement paste [135, 136]. When cement paste is still in fluid state, the autogenous shrinkage is in the same order of magnitude as the chemical shrinkage. As the reaction proceeds, all the solid phases or grains get into contact and start forming an interconnected solid skeleton (setting). Consequently, the stiffness of the matrix increases and restraints the further volume reduction caused by chemical shrinkage. As a result, a number of empty voids are created in capillary pores and air-solution menisci occur. With a reaction going on, the bigger pores empty first to supply solution for the hydration process and the radius of air-solution menisci decrease, accompanied with an internal relative humidity drop (called as self-desiccation). The decrease in menisci radius leads to the development of hydrostatic tensile stresses in the pore solution and causes bulk volume reduction also known as self-desiccation shrinkage [122, 126, 137]. Meanwhile, both the disjoining pressure and the surface tension of the solid particles change with internal RH drop [138, 139, 137, 140].

Thus, the autogenous shrinkage due to change in internal RH, namely self-desiccation can be explained by three principal mechanisms [139]:

1. Change in surface tension of the solid particles
2. Disjoining pressure
3. Capillary tension in the pore fluid

Surface tension: Solid particles have surface tension as a result of asymmetric attractive forces acting on molecules near the solid surface or at the interface with other materials. Change in surface tension of the cement gel hydrates could result in expansion or shrinkage of the cement paste. The magnitude of the surface tension depends on the thickness of the adsorbed water layer, which is related to the change in internal RH [141]. With increase in thickness of the adsorbed water layer, the surface tension of the cement gel hydrates decreases and results in expansion. However, removing the absorbed water layers increases the surface tension of cement gel hydrates and results in bulk shrinkage. This mechanism is significant in case of lower RH (< 40%) [142, 143] and can be neglected for RH >75% [122], since only the first three layers of adsorbed water strongly affect the surface tension of the solid particles while the outer layers (4th, 5th etc..) have almost negligible effect.

Disjoining pressure: Disjoining pressure represents the interaction between two solid surfaces (like C-S-H gel layers) whose distance is smaller than two times the thickness of the absorbed layer. This mechanism is a combined effect of van der Waals forces, double layer repulsion, and structural forces. Among these forces, the van der Waals forces are attractive, while double layer repulsion and structural forces are repulsive. When the relative humidity increases and more water molecules are adsorbed, the repulsive forces increase and the van der Waals attractive forces decrease, resulting in a swelling pressure known as disjoining pressure [122]. If the relative humidity continuously drops, the disjoining pressure decreases and causes shrinkage [122, 139, 137]. Nevertheless, the relative humidity range responsible for this disjoining pressure mechanism is still under debate [144].

Capillary tension: The capillary tension in the pore solutions is related to the formation of air-solution in partly emptied pores. As explained above, once the solid skeleton is formed, the chemical shrinkage creates an internal empty void in bigger pores and causes air-solution menisci, accompanied with a drop of internal RH. As the solution is continuously consumed from bigger pores to smaller pores during the hydration process, the radius of menisci decreases gradually and develops a capillary pressure in the pore fluid. This capillary tension in the pore solutions puts the surrounding solids in compression and causes shrinkage, as illustrated in Fig. 2.7. The capillary tension in the pore solution can be described by relating to the radius of menisci, using Laplace equation:

$$P_c = -\frac{2\gamma_w}{a} = -\frac{2.\gamma_w.\cos\theta}{r} \tag{2.4}$$

Where γ_w [N/m] is the surface tension of pore solution, θ [-] is the contact angle between the pore solution and solids, a [m] is the radius of menisci (also known as Kelvin radius), and r [m] is the radius of capillary, which is related to the internal relative humidity of the matrix (Kelvin's law):

$$\ln(RH) = \frac{2.\gamma_w.\mathrm{V_w}.\cos\theta}{r.R.T} \tag{2.5}$$

Where V_w [18.02 10^{-6} m^3/mol] is the molar volume of the solution, R [8.314 J/(mol.K) is the ideal gas constant, and T [273+curing temperature (°C) K] is the temperature. By combining these two equations, the relationship between the capillary tension in the pore fluid and the internal RH can be calculated using Kelvin-Laplace equation:

$$P_c = -\frac{RT.\rho_w}{M_w}.\ln(RH) \quad (2.6)$$

This equation assumes the menisci formation in circular cylinder pores and consumption of solution starts first from big pores to small pores. As a consequence, all the pores with a radius smaller than the Kelvin radius or menisci radius is filled with solution, while the pores with a radius bigger than the menisci radius are consumed first [145, 122].

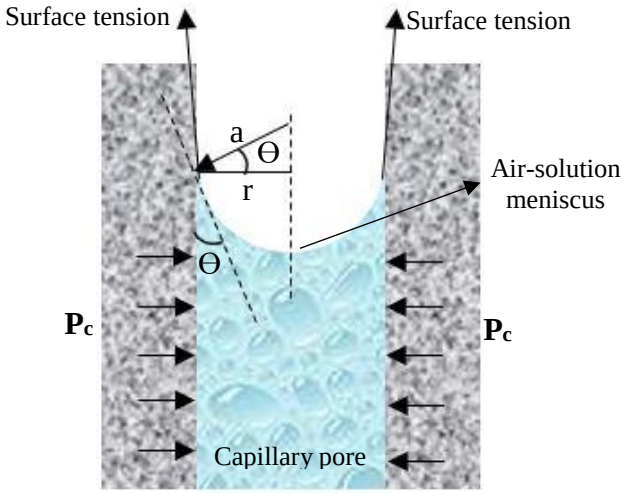

Figure 2.7: Capillary tension mechanism in cementitious materials.

Time-zero definition: Time-zero (t_0) is defined as the transition time when the cement pastes changes from fluid to solid state or the time at which the self-supporting skeleton starts to form and residual tensile stress in the matrix begin to develop. This transition time corresponds to the time when the autogenous shrinkage changes from the function of chemical shrinkage to self-desiccation shrinkage. It is important to accurately define the time-zero (t_0) and separate the self-desiccation shrinkage that induces cracking potential inside the material, from the free chemical shrinkage.

Different approaches have been suggested in literature to define 'time-zero' for cementitious materials, such as the time where the shrinkage rate reaches a maximum value [146], or the time when the hydration heat release increases [147], or the time when an ultrasonic P-wave velocity reaches a specific value [148]. ASTM C1698-09 [149] standard and other researchers [150] have suggested the final setting time obtained from Vicat needle test as 'time-zero' for cementitious materials. However, some studies [151, 152, 153] argue the reliability of using Vicat final setting time as time-zero. Recent studies have defined time-zero using some specific approaches such as: (1) by monitoring the stress development inside the materials using

Temperature Stress Testing Machine (TSTM) [154], and (2) by monitoring the moisture change or internal RH change [155].

2.8 Measurement methods of autogenous shrinkage

In the literature, two methods are commonly reported to measure the autogenous shrinkage on paste, mortar and concrete scale: (1) volumetric method, and (2) linear method.

Volumetric method: In this method, the volume of autogenous shrinkage is measured by casting the fresh cement paste into a tight membrane that is immersed in a liquid (paraffin oil) as shown in Fig. 2.8 [156]. The volume of autogenous shrinkage is continuously monitored by measuring the change in weight (buoyancy weight) of the submerged sample.

The main advantage of using this method is that the measurements can start immediately after casting. However, the lack of stable contact between the cement paste and membrane makes this method inefficient. The formation of entrapped air and bleeding water on the surface of cement pastes obstruct this contact significantly. Moreover, the bleeding water could be reabsorbed into the cement paste as a consequence of chemical shrinkage and this overestimates the measured autogenous shrinkage. Additionally, the water absorption tendency of the membrane and the elastic-pressure from membrane are also reported as considerable shortcoming for this method.

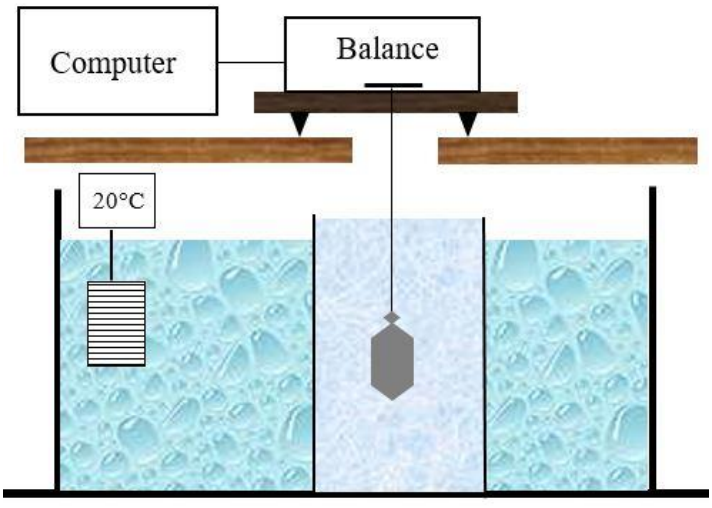

Figure 2.8: An illustration of volumetric method (buoyancy method) to measure autogenous shrinkage [156].

Linear method: The linear measurements of autogenous shrinkage are carried out by casting cement, mortar, or concrete specimens in rigid steel molds and recording the change in free

length of the specimen from one end or both ends using Linear Variable Differential Transforms (LVDT's) or displacement transducers [157]. Based on the displacement direction, this method is classified into vertical or horizontal methods. However, the horizontal method is commonly used as it reduces the influences of gravity on the measurement.



Figure 2.9: Setup for measuring linear autogenous shrinkage using corrugated tube method [149].

Different testing set-ups and testing methods have been developed for measuring the linear autogenous shrinkage and they can generally be classified into contact methods and non-contact methods, as reported in [158]. In the contact method, the sensors or gauges are embedded into the specimen or kept in direct contact with the specimen for measuring the linear autogenous shrinkage. However, in the non-contact method, a laser displacement sensor is used to measure the linear autogenous shrinkage. A major disadvantage of these linear displacement methods is the risk of restraining displacements at the very first hours due to the friction with the rigid steel molds. However, this problem can be minimized by lubricating the molds. Additionally, the bleeding water may reabsorb into the specimen as a consequence of chemical shrinkage and this affects the early age autogenous shrinkage measurements.

In order to avoid the difficulties in sealing or controlling the moisture loss in prism specimens, a corrugated tube method was developed by Jensen and Hansen [159] and standardized as ASTM C1698 [149]. In this standard method, fresh cement paste/mortar is casted into a thin polyethylene corrugated tube having a length of 420 ± 2 mm and outer diameter of 29 ± 0.5 mm under vibration and sealed with tight-fitting plugs to avoid moisture loss. The linear deformations of the cement paste casted in the corrugated tube are simply measured using

LVDT's or dial gauges attached at one end as shown in Fig. 2.9. This method allows transformation of volumetric shrinkage into linear shrinkage due to higher stiffness in the radial direction compared to the longitudinal direction of the corrugated tube. By rotating this corrugated tube in longitudinal direction, the blending problem can be eliminated in this method. The corrugated tube method could also be extended to the measurement of the linear autogenous shrinkage for concrete mixes with large size aggregates, under controlled temperature conditions, using BTJADE device as described in [160].

2.9 Current understanding of autogenous shrinkage in AACs

Alkali-activated cements (AACs) are known to have a high autogenous shrinkage and high sensitivity to early-age cracking, which imposes limits for their application in structures [161, 162, 27]. Therefore, much attention has been given towards understanding the complex mechanism of autogenous shrinkage and to develop mitigation strategies in AACs. A brief review on the current understanding of autogenous shrinkage in AACs is given below.

2.9.1 Autogenous shrinkage of alkali-activated slag (AAS)

Despite having favorable properties, such as higher rate of strength development, excellent resistance to fire and chemical attacks, and eco-friendly performance compared to the traditional Portland cement, the application of alkali-activated slag (AAS) cements has been hindered partly by concerns related to their high volume instability and early-age cracking risk [129, 130, 132, 134]. The large autogenous shrinkage at early ages has been reported as one of the major causes of immature cracking in AAS cement, and thus many efforts have been made in recent years to explore the autogenous shrinkage behavior in AAS cements. Despite research efforts [163, 164, 165, 24] there is still no consensus on the complex mechanism of autogenous shrinkage behavior in AAS.

Many researchers [166, 167, 168, 131] have reported that the development of a high capillary tension in the pore fluid due to formation of a finer pore structure is the main driving force for large autogenous shrinkage in AAS cements. Collins and Sanyayan [166] experimentally found that slag activated with sodium silicate has around 82% of mesopores (2nm to 25 nm) in the total pore volume, while OPC has only around 35% of mesopores and large volume of macropores (>25 nm). With the formation of denser microstructure, the chemical shrinkage occurring due to continuous reaction results in air-solution menisci with smaller Kelvin radius and the development of high capillary tension in the pore fluid, resulting in larger autogenous

shrinkage. Besides the formation of denser microstructure, the pore solution chemistry which is related to the type and concentration of the activator affects the magnitude of autogenous shrinkage in AAS cements [163, 134]. Due to the presence of more ions in the pore solution, which were mainly sourced from the alkaline solution, the surface tension of the partially filled pores increases. Consequently, the capillary tension in the pore fluid increases and thus the autogenous shrinkage. Ballekere.et al. [163] reported that the surface tension of the pore solution in sodium silicate-activated slag cements is 25% higher than that of OPC system. A higher degree of saturation, lower elastic modulus, and higher chemical shrinkage also contribute to the high autogenous shrinkage in AAS cements compared to that of OPC systems [25].

A recent study [165] reported that, besides the capillary tension caused by self-desiccation, also the reduction in steric-hydration forces due to consumption of ions from the pore solution, particularly during the acceleration period of the heat flow curve, also causes autogenous shrinkage in AAS cements.

On the other hand, some authors [132, 169, 24] argue that the visco-elastic or visco-plastic behavior associated to the rearrangement and reorganization of the C-A-S-H particles under internal stress is attributed to the high magnitude of autogenous shrinkage in AAS cements. In sodium silicate-activated samples, the Na^{+} ions present in C-A-S-H gels to compensate the charge imbalance created by substitution of Si^{4+} by Al^{+3} at tetrahedral bridging position, reduce the stacking regularity of (Na)-C-A-S-H gel and make it easier to collapse and redistribute under capillary pressure than the C-S-H gel formed in OPC-based systems. Some other authors [170, 130] also suggested that the high autogenous shrinkage in AAS cements is due to the formation of silica-rich gel or C-A-S-H gel with low Ca/Si.

Fang et al. [171] has reported that the autogenous shrinkage of AAS cements in fluid state is equivalent to the chemical shrinkage, which is similar to the OPC-based systems. While after the formation of a solid skeleton or setting time, the autogenous shrinkage in AAS cements is attributed to capillary tension caused by self-desiccation and also partly from the rearrangement of the reaction products. Another finding of this research is that around 70% of the autogenous shrinkage during the first 24 hours is contributed to chemical shrinkage. This is in contrast to the finding of [167], which reported that the autogenous shrinkage is mainly attributed to self-desiccation in hardened state rather than volume changes occurring due to chemical shrinkage in fresh state. Due to these controversial finding and opinions, it is still not clearly understood which mechanism causes the large autogenous shrinkage in AAS cements.

2.9.2 Autogenous shrinkage of alkali-activated fly ash (AAF)

Contrary to alkali-activated slag (AAS) systems, only a few studies have reported the shrinkage behavior of alkali-activated fly ash (AAF) systems, particularly the autogenous shrinkage at early ages. Ma.et. all [172] performed a comprehensive study on the autogenous shrinkage of AAF systems at 40°C. These authors reported that continuous reorganization and polymerization of N-A-S-H gel is more likely to cause autogenous shrinkage in AAF systems, rather than the self-desiccation process that occurs in OPC-based systems and also in AAS systems.

In sol-gel systems, the morphology of the reaction products depends strongly on the reversibility degree of the condensation reaction [173, 174]. A porous, space-filling gel will be formed when the condensation reaction is nearly irreversible. If the condensation reaction is reversible, or if the rate of bond breaking is higher compared to the rate of condensation, the molecules restructure and reorganize themselves, creating a more stable and cross-linking/denser structure, which occupies only a small fraction of the original gel volume. Under intermediate condensation reaction, highly cross-linked clusters grow until they are large enough to settle out of the suspension in the form of precipitates [173, 174].

In fact, the reaction in AAF systems corresponds to the sol-gel process [175], the morphology of the N-A-S-H type gel seems to be dependent on the reversibility degree of the condensation reaction. Based on the BSE images, Ma.et. all [172] revealed that the N-A-S-H gels formed at early ages have lower density than the original fly ash particles but undergo continuous polymerization reaction over time and transform into the denser gel (brightness increases). This continuous reorganization and polymerization reaction is supported by the formation of two types of gel in AAF systems: Al-rich gel at early ages and Si-rich or denser gel over time [97].

2.10 Factors influencing autogenous shrinkage in AAS cements

As explained above, the autogenous shrinkage is the macroscopic volume reduction resulting from the effect of chemical shrinkage and self-desiccation. Consequently, the factors affecting the hydration process (i.e. chemical shrinkage) and pore structure, as well as the macro-mechanical properties like strength and stiffness development can influence the autogenous shrinkage of AAS cements. Some factors which can affect the autogenous shrinkage of AAS cements are:

1. Incorporation of other precursors like fly ash and metakaolin
2. Type and concentration of the activator
3. Curing temperature
4. Water-to-binder ratio
5. Fineness and chemical composition of the slag

Incorporation of other precursors:

Alkali-activation of slag with fly ash, another commonly utilized industrial by product, counterbalances the disadvantages of sole alkali-activated slag (AAS) systems such as quick setting process, poor workability, and large volume instability. It has been expensively reported that incorporating fly ash effectively reduces the autogenous shrinkage of AAS cements [176, 171, 167, 177, 178, 162]. For example, substituting 30% and 50% of slag by fly ash can reduce the autogenous shrinkage to around 15% and 40%, respectively [178]. These authors demonstrated that incorporating fly ash retards the hydration process and consequently reduced the chemical shrinkage and coarser the pore structure. As a result, the capillary tension in the pore fluid decreases and results in lower autogenous shrinkage.

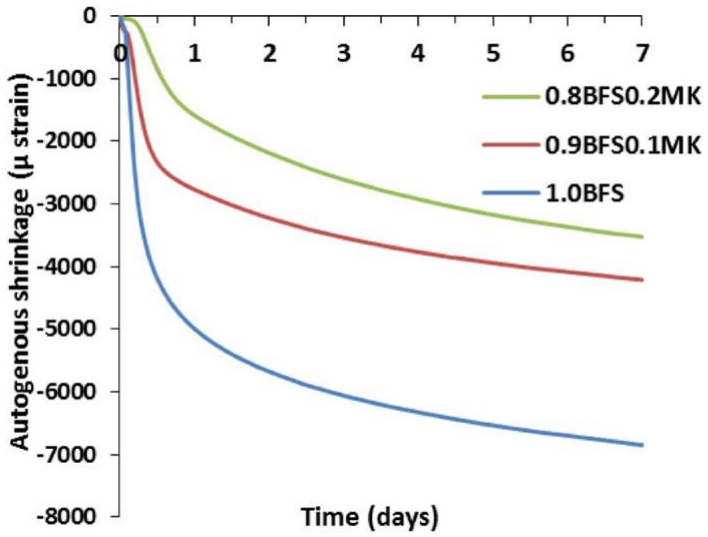

Figure 2.10: Effect of substituting slag by metakaolin on the autogenous shrinkage of AAS cements [133].

Recent study [133] also reported that substitution of 10% and 20% slag by metakaolin can lead to around 40% and 50% reduction of the autogenous shrinkage, respectively. Nevertheless, the use of metakaolin as partial substitution of slag seems to be less attractive than fly ash, since incorporating metakaolin increases the demand of water/solution for a better workability. Another study reported that replacing slag with limestone up to 30% can increase the

autogenous shrinkage of AAS cements, but further increase in limestone causes reduction in autogenous shrinkage due to dilution effect [131].

Type and concentration of the activator:

Since the type and concentration of the activator strongly influence both the micro-physical-chemical properties, such as rate of chemical reaction, reaction products, and pore structure, as well as the macro-mechanical properties [34, 103, 179], they affect the rate and magnitude of the autogenous shrinkage. In sodium silicate activation, both the concentration of alkali-content (Na_2O) and alkali-modulus or silica content have a significant influence on the autogenous shrinkage of AAS cements. It has been reported that increasing the alkali-content of the sodium silicate solution enhances the early age reaction rate and causes higher chemical shrinkage and autogenous shrinkage [180, 163, 167, 164, 25]. However, this finding seems to contradict with the results of [177], which found that samples activated with higher alkali-content (Na_2O) exhibited larger chemical shrinkage, but lower magnitude of autogenous shrinkage. On the other hand, samples activated with higher silica content indicate enhanced reaction and pore refinement, resulting in a substantial increase in the pore pressure, and thus autogenous shrinkage related to self-desiccation [163, 167].

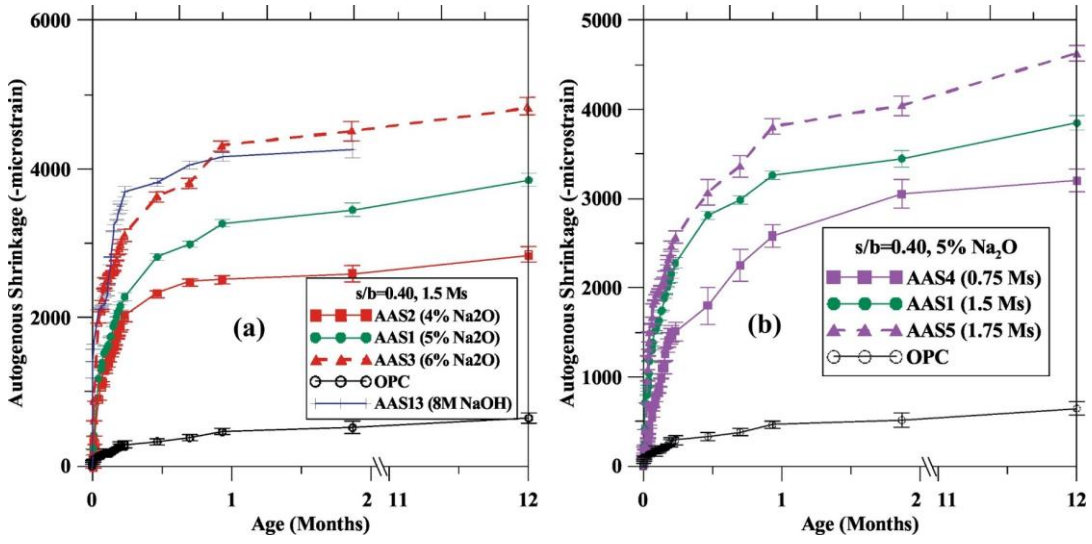

Figure 2.11: Effect of alkali-content (Na_2O) and alkali-modulus (M_s) on the autogenous shrinkage of AAS cement mortars [163].

Samples activated with sodium carbonate and sodium sulfate resulted in a lower autogenous shrinkage compared to the samples activated with sodium silicate [181]. However, it should be remarked that research on sodium carbonate and sodium sulfate activated slag systems is very limited, especially with regards to the early-age autogenous shrinkage behavior. Yuan et al.

[95] reported that blending sodium carbonate and sodium sulfate solution reduces the shrinkage of AAS cements by modifying the reaction products with the formation of expansive phases like ettringite at early ages.

Curing temperature:

As explained above, some authors [132, 24] have attributed the large autogenous shrinkage behavior in AAS cements to visco-plastic or visco-elastic compliance of the reaction products. Meanwhile, curing samples at elevated temperature was reported to reduce the deformability of C-A-S-H gels by improving its stability through strengthening the bonds between adjacent C-A-S-H nanoparticles [132, 182, 19]. Therefore, increasing curing temperature is suggested to considerably reduce the autogenous shrinkage of AAS cements. Nevertheless, the effect of curing temperature on the autogenous shrinkage and how it is connected to the reaction kinetics, reaction chemistry and microstructure development is still remaining as a crucial research gap in the literature.

Water-to-binder ratio:

Like in OPC-based systems, water-to-binder has been considered as one the factors that influences the autogenous shrinkage in AAS cements. Samples with low water-to-binder ratio show higher autogenous shrinkage. The large autogenous shrinkage in samples with low water-to-binder ratio can be attributed to the development of high capillary tension in the smaller pores (i.e. high self-desiccation). In alkali-activated materials, water content refers to the amount of water added, and water originally presented in the activating solution.

Chemical composition and fineness of the slag:

The rate and magnitude of the autogenous shrinkage are both dependent on the hydration rate and microstructure development, which are strongly affected by chemical composition of the original raw material. In literature, the influence of varying the chemical composition of the slag with different content of MgO, Al_2O_3, TiO_2 and Ca/Si ratio on the hydration properties of AAS cements was investigated. However, the number of studies focusing on the influence of slag chemistry on the autogenous shrinkage is rather limited.

It has been reported that increasing the MgO content in slag can reduce the shrinkage of AAS cements [183, 184]. This reduction in shrinkage may be related to various factors:

- Formation of C-M-S-H type gels, having more polymerized units and stronger bonds [185].

- High MgO content appeared to reduce the Al substitution into the C-A-S-H gel due to formation of more Mg-Al hydrotalcite [92].
- Formation of magnesium silicate hydrate and expansive hydrotalcite-like phases [186].

Similarly, the increase in Al_2O_3 content in the slag can reduce the shrinkage of AAS cements due to decrease in its reactivity [187]. The results from ^{29}Si NMR demonstrated that the rise in chain length of the C-A-S-H gel by incorporating more Al species at tetrahedral bridging position causes a reduction in the degree of reaction [188]. TiO_2 content in the slag however has only minor influence on reactivity of AAS cements and thus on their shrinkage deformations [188].

In addition to the chemical composition of the slag, the physical properties like fineness can also affect the autogenous shrinkage of AAS cements. It has been reported that increasing the fineness of the slag accelerates the rate of reaction and pore refinement that result in greater autogenous shrinkage [184].

2.11 Cracking tendency

Due to a higher autogenous shrinkage, the alkali-activated slag (AAS) cements tend to have high cracking risk compared to OPC-based materials. However, the cracking potential of AAS cements under restrained autogenous shrinkage conditions is not well reported in the literature. Meanwhile, it has been reported that AAS cements have lower elastic modulus [25], higher rate of tensile strength development [25], and higher creep effect [189, 190], which may affect the cracking tendency of AAS cements. Nevertheless, the combined effects of these on cracking potential of AAS cements is not well understood with the results reported in the literature.

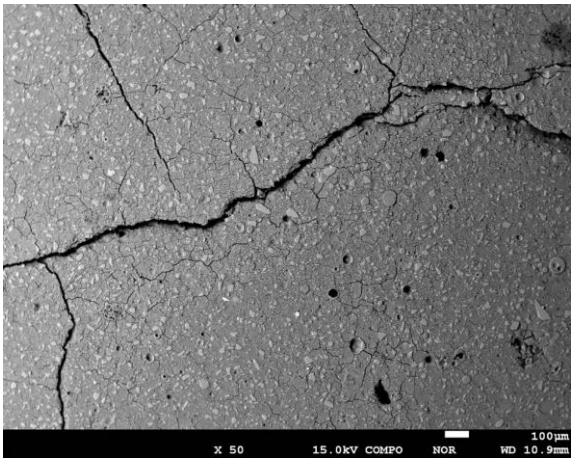

Figure 2.12: Micro-cracking of the sodium silicate activated slag cement at 7 days.

For example, Collins and Sanjayan [189] found that incorporating a shrinkage reducing chemical admixture (SR) reduced the shrinkage of AAS cements. However, the time of cracking for both samples with and without SR is close to each other. This is attributed to a lower rate of tensile strength development in samples with SR [189].

2.12 Mitigation of autogenous shrinkage in AAS cements

Since the alkali-activated slag (AAS) cements suffer from large autogenous shrinkage and high cracking risk, which imposes limits for their application in structures, developing mitigation strategies for autogenous shrinkage has interested many researchers, recently. Based on the mechanism, the mitigation strategies can be divided in to three types:

1. Reducing the impact of main driving forces
2. Adding an expansive agent
3. Internal restraint

Reducing the impact of main driving forces:

Considering that capillary tension caused by the self-desiccation process is the main driving force for the autogenous shrinkage in AAS cements [167], mitigation strategies can be developed to reduce the self-desiccation process by internal curing and/or reducing the surface tension of the pore solution by shrinkage reducing agents (SRA).

Internal curing by superabsorbent polymers (SAP) and light weight aggregates (LWA) can effectively reduce the autogenous shrinkage in AAS cements [134, 163, 176]. For example, adding 0.3wt% of SAP reduced the autogenous shrinkage by around 75% and 60% in AAS cements activated with sodium silicate and sodium carbonate, respectively [191]. By introducing SAP into the system, a solution/water reservoir is created which provides extra solution during hydration to compensate for the solution consumption. As a result, the capillary tension induced by the self-desiccation process is reduced and results in a lower autogenous shrinkage [192, 193]. It has been reported that using 0.3% of SAP is sufficient to fully compensate the autogenous shrinkage in Portland cement [194, 137]. However, adding SAP, regardless of their content, cannot completely eliminate the autogenous shrinkage of AAS cements, suggesting the existence of other mechanism(s) that contribute to the autogenous shrinkage rather than self-desiccation [194, 193]. On the other hand, lower rate of strength development at early ages is reported as the main drawback of this method [191, 192].

Shrinkage-reducing admixtures (SRA) are also found to be effective to reduce the autogenous shrinkage of AAS cements [130, 163]. For example, adding 2wt% of SRA reduced the autogenous shrinkage of sodium silicate-activated slag cement by around 85% [130]. The reduction in autogenous shrinkage with SRA is primarily associated with a decrease in surface tension of the pore solution [132, 195]. The addition of SRA also creates a coarser pore structure and results in lower autogenous shrinkage related to the self-desiccation [130].

Adding expansive agents:

In literature, the effect of using various expansive agents (EA) on the autogenous shrinkage of AAS cements are reported. For example, the addition of CaO-based expansive agents can remarkably reduce the autogenous shrinkage of AAS cements due to the formation of voluminous portlandite ($Ca(OH_2)$) and hydrated C-A-S-H gel with high Ca/Si ratio [196, 195]. This is in contrast to the finding of [132], who reported that the shrinkage of AAS cements increases due to refinement in the pore structure with incorporating CaO-based expansive agent. Another study reported the influence of adding anhydrite ($Ca(SO_4)$) and quick lime expansive agents on shrinkage behavior of AAS cements [94]. They found that adding these EA reduced the shrinkage of AAS cements due to the formation of residual crystal $Ca(OH_2)$ as the main expanding source rather than AFt phases. However, Bakharev et al [197] evaluated the effect of adding gypsum as expansive agent and found that shrinkage of AAS is significantly reduced due to the compensating effect of AFm and AFt phases.

Internal restraint:

Introducing sand/aggregates and other high-stiffness particles into the systems can serve as an internal restraint to reduce the shrinkage deformation of cementitious materials. It is well known that AAS mortar/concrete shows less autogenous shrinkage than AAS paste.

2.13 Conclusions

In this chapter, the current state of the art regarding the alkali-activated cements was discussed. Firstly, the various source materials and the activating solution used in AACs were addressed, together with their environmental impact. Ground granulated blast furnace slag activated with sodium silicate was reported as a suitable alternative binder offering comparable or even superior properties to the traditional Portland cements. However, the rapid reaction in sodium silicate-activated slag cements at early hours due to the presence of soluble SiO_4^{4-} results in a quick setting time and large autogenous shrinkage at early ages. On the other hand, the

production process of sodium silicate solution is expensive with high environmental impact. The use of naturally occurring minerals like sodium carbonate and sodium sulfate, on the contrary, shows a much longer setting time (>3 days) and lower autogenous shrinkage. The use of hybrid or a blended activator appears to be a promising alternative in order to counterbalance the shortcoming of each activator and to create a good balance between mechanical properties, production cost and environmental footprints. Nevertheless, the effect of using hybrid activators on the early-age properties (i.e. setting process, mechanical strength and stiffness development, autogenous shrinkage) of AAS cements has not been investigated yet.

Secondly, the reaction mechanisms, reaction products, nano-and microstructure of the hydrated gels formed in AAS cements were discussed. Both type and concentration of the activator strongly control the early-age reaction process, phase assemblage, molecular structure of the hydrated gels and microstructure development, which significantly influence the setting and hardening behavior and early-age autogenous shrinkage of AAS. In order to understand and explain the influence of using hybrid activators on early-age properties, it is therefore of major importance to first understand the influence of using hybrid activators on the reaction process, reaction products, reaction chemistry and microstructure development.

Thirdly, the current understanding of the mechanism for large autogenous shrinkage behavior in AAS cements was discussed. Nevertheless, the scientific and comprehensive reasoning behind the larger autogenous shrinkage of AAS is still remaining a crucial research gap in the literature. Moreover, the effect of using hybrid activators on the autogenous shirnkage of AAS cements has not been investigated yet.

Although the AAS cements show higher autogenous shrinkage, its cracking tendency under restraint condition is not well explained with the results reported in the literature.

Finally, the mitigation strategies to control the autogenous shrinkage of AAS cements were addressed. Considering the visco-elastic/visco-plactic behaviour of the reaction products as the main contribution for large autogenous shrinkage, the elevated curing temperature may be effective in reducing the autogenous shrinkage of AAS cements. However, the research on cuirng temperature effect on autogenous shrinkage and how it is connected to the reaction kinetics, reaction chemistry and microstructure development is limited/non-existent.

Considering the state of the art, the main research gaps and the key question asked are:

- What is the influence of using hybrid activating solutions on reaction process and how does this affect the setting and hardening behavior?

- How do the changes in micro-chemical properties (rate of reaction, phase assemblage, reaction chemistry of hydrated gels, and pore structure) and macro-mechanical properties (strength and stiffness development) influence the autogenous shrinkage of AAS cements activated with hybrid alkaline solutions?
- How is the cracking risk under restraint autogenous shrinkage conditions?
- Will increasing curing temperature act as a mitigation strategy for autogenous shirnkage in AAS cements?

The next chapters aim to provide answers for these questions.

Chapter 3

Materials and experimental methods

3.1 Introduction

In this chapter the material properties, mix compositions and testing methods/analytical techniques are introduced. The first section describes the chemical and mineralogical compositions and physical properties of the materials, the second section describes the mix compositions and mixing procedures for pastes and mortars, curing conditions, and the third section includes various testing methods and analytical techniques that have been applied in the present study.

3.2 Materials

3.2.1 Raw materials

Ground granulated blast furnace slag from ORCEM, the Netherlands, and siliceous fly ash from BauMineral, Germany, were used as the primary materials in this study. Their chemical compositions, determined from X-ray fluorescence (XRF) spectrometry and quantified using Super-Q software, and the loss of ignition (LOI), determined according to EN 196-2 [198], are given in Table 3.1.

Table 3.1: Chemical composition of slag and fly ash measured with XRF [%].

Materials	SiO_2	Al_2O_3	Fe_2O_3	CaO	MgO	SO_3	MnO	K_2O
Slag	36.19	12.41	0.60	39.80	8.25	-	0.32	0.49
Fly ash	57.44	26.13	6.29	2.43	1.49	0.83	0.05	2.90
Materials	TiO_2	V_2O_5	SrO	ZrO_2	Na_2O	S	BaO	LOI
Slag	1.07	0.01	0.09	0.04	-	1.53	0.06	-0.98
Fly ash	1.34	0.04	0.13	0.05	0.45	-	0.13	1.58

The slag is neutral with basicity coefficient K_b= (CaO+MgO)/(SiO_2+Al_2O_3) equal to 0.99. The calculated hydraulic modulus HM = (CaO+MgO+Al_2O_3)/SiO_2 of slag is 1.65, which is greater than the required value of 1.4 for good hydration properties, as reported in Chapter 2. The fly ash used in this study complies Class F since it has a lower CaO content (≤10%) and SiO_2 + Al_2O_3 + Fe_2O_3 ≥ 70% [199]. The negative LOI value in slag is associated to the oxidation of sulfur rich compounds. The LOI value in fly ash is associated to the unburnt carbon. The technical sheet of the raw fly ash is given in Appendix A. From BSE image of raw fly ash shown in Appendix A, it is clear that the fly ash particles are spheres with different sizes, in which most of them are hollow known as cenospheres [200].

The mineralogical composition of slag and fly ash was identified by powder X-ray diffraction (XRD) analysis using a Philips Analytical X-ray diffractometer with CuKα radiation (λ = 1.54 Å) operating at 45 kV and 35 mA. The samples were scanned over a range of 5°-55° 2theta and measured in step scan mode at 2s per 0.02° 2theta. The slag is mainly amorphous with broad diffraction hump centered around 30° 2theta, while fly ash contains some crystalline phases like mullite (9.5%), quartz (3.5%) and hematite (0.5%) along with the amorphous phase (83.7%) (Fig. 3.1).

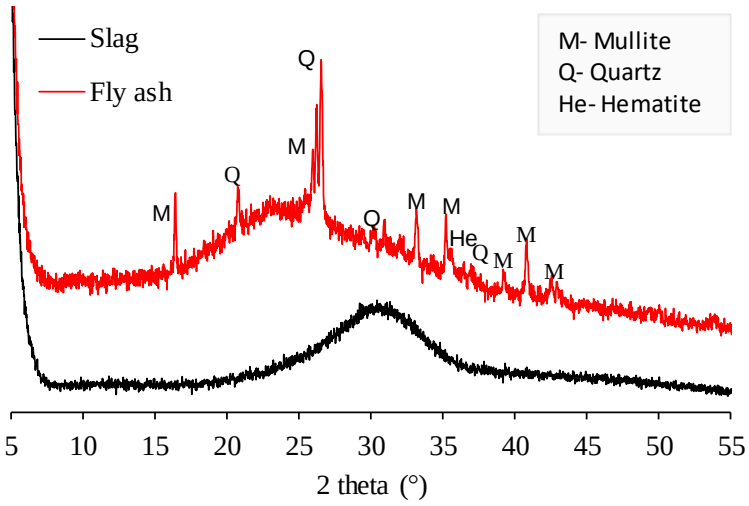

Figure 3.1: X- ray diffraction analysis of slag and fly ash.

The physical properties of slag and fly ash are given in Table 3.2. The BET (Brunauer-Emmett-Teller) specific surface area was determined using Nova 2200e Surface Area Analyzer, Quantachrome Instruments. Blaine fineness of the materials was determined using Blaine apparatus as per EN 196-6 [201]. The particle density values were determined using glass pycnometers with white spirit as the measurement liquid in accordance with EN 1097-5 [202].

The specific surface area and density of slag are higher than that of the fly ash. The particle size distributions determined by wet laser diffraction (Malvern Mastersizer) are given in Fig. 3.2. River sand 0/4 having a specific gravity of 2.60 g/cm^3 and water absorption of ≤0.5% is used as a fine aggregate, complying with the European standard EN 12620 [203]. The particle size distribution of river sand 0/4, determined according to EN 9336-1 [204] is shown in Fig. 3.3.

Table 3.2: Physical properties of slag and fly ash.

Material	BET [m^2/g]	Blaine [cm^2/g]	Density [Kg/m^3]
Slag	2.903	5200	3350
Fly ash	2.160	3686	2485

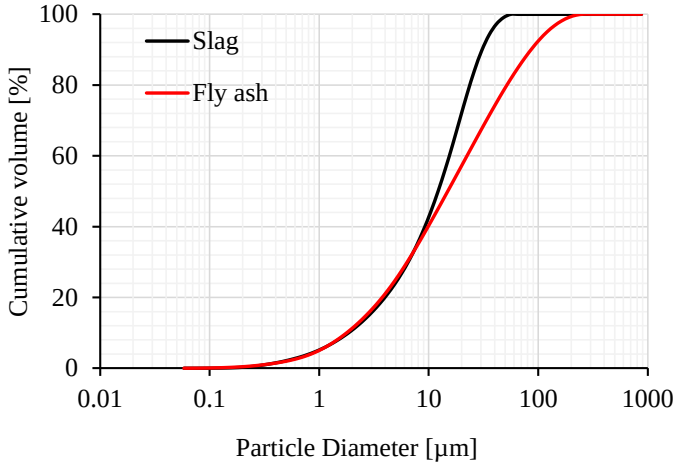

Figure 3.2: Particle size distribution of slag and fly ash measured with Laser diffraction analysis.

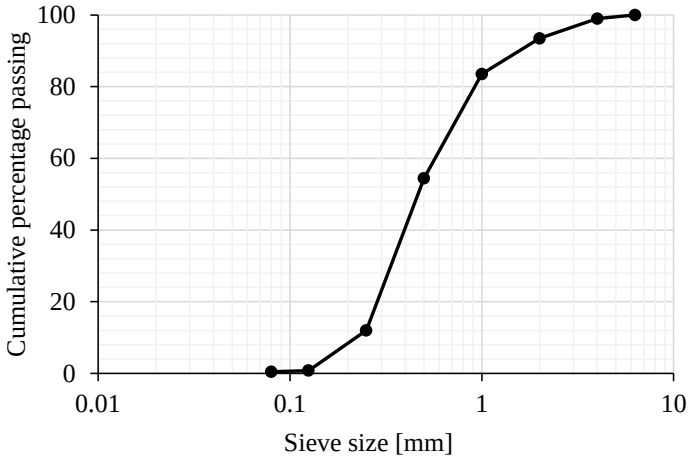

Figure 3.3: Particle size distribution of river sand 0/4.

3.2.2 Alkaline activators

As explained in Chapter 2, the most commonly used activator in alkali-activated cements is sodium silicate or a combination of both sodium silicate and sodium hydroxide. However, these activators are not naturally available, and its production process is expensive with a high environmental impact [77]. Therefore, the use of naturally occurring minerals like sodium carbonate and sodium sulfate have become an attractive alkaline source to develop more cost effective and greener alkali-activated cements [70]. Nevertheless, the sole activation of slag with sodium carbonate and sodium sulfate generates longer setting (>3 days) and slower strength development when compared to the sodium silicate activation [67, 68]. Therefore, in order to counterbalance the shortcoming of each activator, hybrid activators are suggested in this study to create a good balance between mechanical properties, production cost and environmental footprints. Due to availability of various activators with different concentrations and possibility of developing different combinations of hybrid activators, screening is adopted with bottom-up approach based on the setting times, heat of hydration, and strength results (Appendix B).

The concentration of activator in terms of alkali-content (Na_2O) is defined as the ratio of Na_2O content in the activating solution to the total binder weight. The alkali-modulus is defined as the ratio of SiO_2 to Na_2O content in the activating solution. From literature [28, 29, 30], it is known that both the alkali-content (Na_2O) and the alkali-modulus (M_s= SiO_2/Na_2O) have significant influence on properties of the alkali-activated cements. Alkali-content (Na_2O) in between 5.5 to 8.0% is reported as the ideal concentration for alkali-activated slag cements [19]. For neutral slag, however, an alkali-modulus of 0.75-1.5 is reported as the optimum activator modulus for sodium silicate solution [63]. Therefore, the sodium silicate solution with an alkali-modulus (M_s= SiO_2/Na_2O) of 1.0 and an alkali-content (Na_2O) of 8.0% was set as a reference activator in this study.

The effect of type and concentration of the activator on Vicat setting times, strength development and heat of hydration is investigated in Appendix B. Based on this screening test results given in Appendix B, two different combinations of hybrid activators, including sodium silicate + sodium carbonate and sodium silicate + sodium sulfate were selected with the aim to reduce sodium silicate solution, which is more expensive and less environmentally friendly. The screening test results, given in Appendix B, reveal that incorporating sodium carbonate and sodium sulfate significantly delay the final setting time and reduce the reaction rate of sodium silicate-activated samples. However, they show comparable or even better strength

properties to sole sodium silicate-activated samples with elapse of time. Moreover, the partially substituting of sodium silicate with the less expensive (~2-3 times) and more environmentally friendly alternative activators like sodium carbonate and sodium sulfate can reduce the environmental impact, as explained below in section 3.3.2.

These hybrid activators were prepared by partially substituting (50 wt%) sodium silicate solution of alkali-modulus 1.0 with sodium carbonate and sodium sulfate solutions. A solution-to-binder ratio of 0.6 was used in all mixes. The powder sodium carbonate and sodium sulfate are dissolved in de-ionized water at least 24h before use and were cooled down to room temperature.

3.3 Mix compositions and mixing procedure

3.3.1 Mix compositions

In addition to the activator type and concentration, the effect of slag/fly ash ratio on setting behavior, rate of reaction, strength development and autogenous shrinkage is investigated in Appendix B. From screening test results given in Appendix B, it is clear that the setting time and workability increased significantly with increasing fly ash content in the alkali-activated slag (AAS) cements. Moreover, it is observed that increasing fly ash content effectively reduced the autogenous shrinkage of AAS cements. However, since the availability of fly ash is declining in central Europe, only a slag-fly ash ratio of 80-20 vol% was chosen in this study. Adding this moderate amount of fly ash (20 vol%) can sufficiently increase the workability and setting time of AAS cement to cast samples without any defects (such as voids that effect the strength and shrinkage properties).

Five types of alkali-activated slag/fly ash (AASF) blends were developed at 80:20 vol% of slag/fly ash ratio by varying the type and concentration of the alkaline solution as listed in Table 3.3. Based on screening mix composition (Appendix B), the sodium silicate solution with alkali modulus 1.0 was partially substituted (50 wt%) by two sodium carbonate and sodium sulfate concentrated solutions (~0.6M and 0.9M) in order to obtain the molar ratios (SiO_2/Na_2O) of 0.7 and 0.6, respectively. A water-to-binder ratio of 0.5 is fixed to all mixes. The water in this study refers to the amount of water originally presented in sodium silicate solution and the water added to dissolve the sodium carbonate or sodium sulfate activators. The concentration of OH^- ions (Table. 3.3) in the alkaline solutions was measured by titration

against hydrochloride (0.1M HCL) acid using phenolphthalein and methyl orange as the indicators.

Table 3.3: Mix proportions of alkali-activated slag/fly ash blends.

Mix ID	Sodium Silicate		Sodium Carbonate	Sodium Sulfate	Modulus M_s= (SiO_2/Na_2O)	OH^- ions [mmol.L-1]
	SiO_2 [%]	Na_2O [%]	Na_2O [%]	Na_2O [%]		
SS-1.0	8.0	8.0	-	-	1.0	5000±100
SC-0.7	4.0	4.0	1.75	-	0.7	2500±100
SC-0.6	4.0	4.0	2.75	-	0.6	2500±100
Su-0.7	4.0	4.0	-	1.75	0.7	2500±100
Su-0.6	4.0	4.0	-	2.75	0.6	2500±100

3.3.2 Carbon footprint

Since environmental issues promote the demand of using alkali-activated cement as an alternative binder to Portland cement, it is essential to investigate the environmental benefits of alkali-cements developed (Table. 3.3) in this study.

Table 3.4: CO_2 equivalent per mortar mix (kg/m^3) and compared to traditional OPC.

Mix	**$CO_{2\text{-}e}$ (kg)**	**Relative to OPC**
OPC	0.43	1.00
SS-1.0	0.270	0.65
SC-0.7	0.133	0.31
SC-0.6	0.160	0.36
Su-0.7	0.153	0.33
Su-0.6	0.156	0.36

By considering the average CO_2 equivalent value of the source materials and alkaline activators given in Table 2.1, the CO_2 equivalent GHG emission for each mix composition was calculated and compared to the traditional OPC (Table. 3.4), per unit volume of mortar (i.e. binder content of 450 Kg/m^3). From Table. 3.4, the AASF sample activated with sodium silicate (SS-1.0) has

a $CO_{2\text{-}e}$ value of 0.65 to that of OPC, indicating that it has 35% lower CO_2 equivalent GHG emission than traditional OPC sample. However, when sodium silicate is partial substituted with natural occurring minerals like sodium carbonate and sodium sulfate, the CO_2 equivalent GHG emission is 65% to 70% lower than OPC samples. This difference in $CO_{2\text{-}e}$ values indicates the clear benefit of using sodium carbonate and sodium sulfate as alternative activators in sustainable development.

3.3.2 Mixing procedure and curing conditions

Alkali-activated slag/fly ash paste was prepared according to EN-196-3 [205], using a HOBART cement mixer. After pouring the alkaline solution and slag/fly ash source materials into the mixing bowl, two mixing periods of 90 sec at low speed followed. In between these two mixing periods, paste adhering to the wall and the bottom part of the bowl was removed by using a rubber or plastic scraper for 30 sec.

The mortar samples at 1:3 binder-to-sand ratio by weight were prepared according to the standard procedure given in EN 196-1 [206]. For testing the mechanical strength properties, all mortar samples after demoulding were triple wrapped in thin plastic sheets and then in alumina foil to prevent the evaporation of water. Afterwards, the sealed mortar samples were stored at 20°C, ~93% RH (moist curing room) and 40°C, ~75% RH until the age of testing.

To characterize the reaction products using analytical techniques (e.g. for TGA and XRD) and pore size distribution, a small amount of paste was prepared using an overhead mixer at 750 rpm for 2 min, then it was poured into 2ml plastic vessels and sealed with a lid. Afterwards the sealed bottles were put in an oven at the required curing temperatures (20°C and 40°C) until the age of testing.

3.4 Experimental methods

3.4.1 Setting and hardening behavior

Vicat setting time

The initial and final setting times were measured using an automatic recording Vicat needle apparatus according to EN 196-3 [205]. According to the standard, the initial setting is determined as the elapsed time between “zero time” (the time when the activating solution is mixed with the binder system) to the time at which the distance between the needle and the baseplate is 4±1 mm. The final setting time is the elapsed time, measured from the “zero-time”

to the time at which the needle penetrates less than 0.5 mm into the specimen. The reported results are the average values of three measurements. Since the standard consistency was not used in the preparation of alkali-activated paste samples, the setting time derived in this study could not be termed as standard setting times.

Ultrasonic pulse velocity (UPV) measurements

A non-destructive ultrasonic wave transmission test is a well-established method to monitor the setting and hardening behavior of cementitious materials. An ultrasonic P-wave transmission test, according to EN 12504-4 [207], was performed by using a commercially available IP-8 ultrasonic measuring instrument, manufactured from UltraTest, Germany. The device consists of a PC-connected controller unit allowing up to eight measuring cells. Each measuring cell is composed of a high damping silicon mould, with an ultrasonic transmitter and receiver pair and a temperature sensor (Fig. 3.4). Four sound absorbers embedded in the silicon mould help to reduce the influence of waves travelling through the mould, by passing the paste/mortar samples. Two measuring cells with a volume of 98 mL and 195 mL were used to monitor the setting and hardening behavior of pastes and mortar samples, respectively. An ultrasonic pulse wave was transmitted every minute using a 30 kHz transducer in order to study the setting and hardening behavior of alkali-activated slag/fly ash cements. By measuring the propagation time 't' of the pulse wave over a path length 'l' or distance between transmitter and receiver, the P-wave transmission velocity ($v=l/t$) through paste and mortar samples was computed.

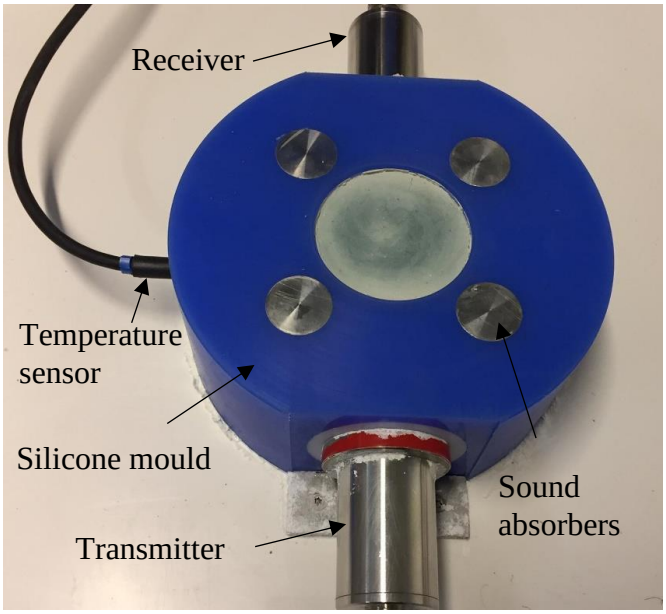

Figure 3.4: Ultrasonic pulse wave transmission unit of the measurement equipment.

Isothermal calorimetry

Isothermal calorimetry is a convenient technique to measure the heat evolution during hydration of cementitious materials as a function of time. In this study, the rate of heat evolution in alkali-activated slag/fly ash cements was measured using TA Instruments TAM Air Calorimetry at 20°C and 40°C. The raw materials were first mixed with the alkaline solutions externally using an overhead mixer at 750 rpm for 2 min and then around 8±0.5 g of the mixed paste sample was transferred into a small ampoule and loaded into the calorimeter channels. The heat evolution results are normalized by mass of the binder (slag + fly ash) materials. The reported results are an average of two measurements. The repeatability of the isothermal heat flow curves for studied AASF paste samples is given in Appendix C.

Mechanical properties

The mechanical strength and elastic properties were tested on hardened mortar samples according to the European standards. Three specimens were tested for each mix composition and the average values were reported with standard deviations.

The flexural strength was measured on 40 x 40 x 160 mm^3 mortar prisms by standard three-point bending test according to the EN 196-1 [206]. Two halves of the broken prism were then used for testing compressive strength by using Schenck press with a displacement rate of 2 mm/min. The flexural strength and compressive strength of the mortar samples are calculated using Eq. 3.1 and Eq. 3.2, respectively.

$$f_{ft} = \frac{1.5.F_{ft}.l}{b^3} \tag{3.1}$$

$$f_c = \frac{F_c}{A} \tag{3.2}$$

with f_{ft} [N/mm^2] the flexural strength, F_{ft} [N] the maximum load applied at fracture, l [mm] the distance between supports in flexural test, b [mm] the width of the sample, f_c [N/mm^2] the compressive strength, F_c [N] the measured maximum load, and A [mm^2] the area of sample (40 x 40 mm^2).

The splitting tensile strength tests were performed on cylinder specimens with dimensions of 100 x 100 mm^2, respectively. The applied loading rate was similar to the loading rate of the compressive test, i.e. 2 mm/min. A bearing strip of a width less than 8% of the cylinder

dimension is used for the splitting test in order to achieve a line load, as suggested in [208]. The splitting tensile strength $f_{ct,sp}$ [N/mm^2] can be calculated using Eq. 3.3.

$$f_{ct,sp} = \frac{2.F_s}{\pi.D.L} \tag{3.3}$$

with F_s [N] the measured maximum load, D [mm] the diameter of the sample and L [mm] the sample length. According to the EN 1992-1-1 [209], the direct tensile strength (f_{ct}) can be derived from the splitting tensile strength using equation 3.4.

$$f_{ct} = 0.9.f_{ct,sp} \tag{3.4}$$

Static Elastic modulus

The quasi-static elastic modulus (E_s) of AASF mortar samples were measured using duplicate 100 x 200 mm cylinders in sealed conditions under compression. A device consisting of two aluminum rings attached to the cylinder with screws was used to monitor the elastic properties of AASF mortar samples. Three strain gauges coupled to the aluminum rings with a spacing of 120°C in circular direction were used to measures the displacement in the sample subjected to the compression by cyclic axial loading suggested in EN 12390-13 [210] (Fig. 3.5). The static E-modulus was then calculated as:

$$E_s = \frac{\Delta\sigma}{\Delta\epsilon} \tag{3.5}$$

with Δσ the difference in applied stress between the start and the end of the cycle and Δε the difference in measured stains.

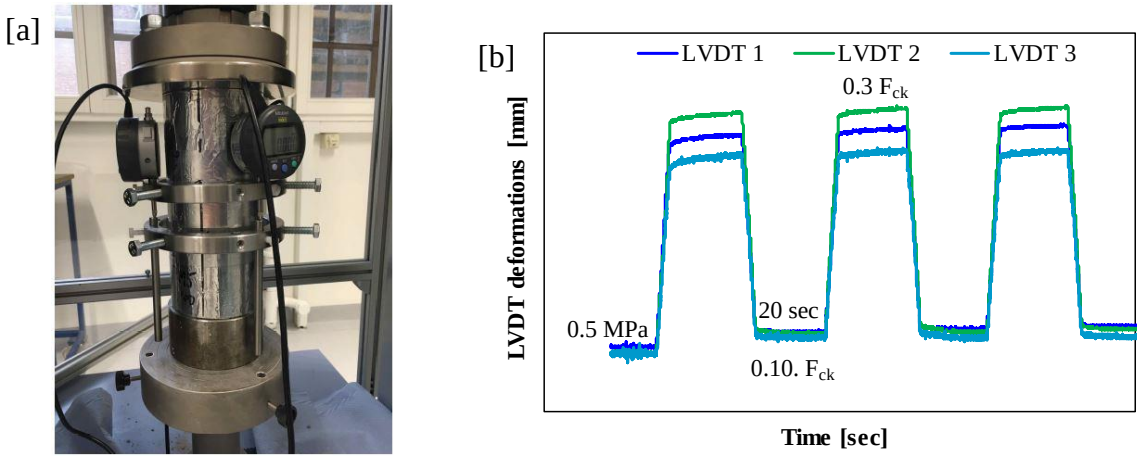

Figure 3.5: Device [a] and cyclic loading [b] for determination of static E-modulus.

Dynamic Elastic modulus

The dynamic elastic modulus of mortar samples was measured using ultrasonic pulse velocity, according to EN 12504-4 [207] and B 15-229 [211]. By measuring ultrasonic P-wave velocity (V_p in m/s) and the density of the mortar samples (ρ in g/cm^3), the dynamic modulus of elasticity (E_d in GPa) is calculated using Eq. 3.6.

$$E_d = V_p^2 . \rho . \left[\frac{(1+\vartheta)(1-2\vartheta)}{(1-\vartheta)}\right] \quad (3.6)$$

with υ the Poisson ratio and a constant value of 0.15 is adopted in this study [208].

3.4.2 Characterization of solid phases and pore structure

In order to better understand the performance of alkali-activated slag/fly ash cements, an extensive characterization of the reaction products is performed using five analytical techniques: thermogravimetric analysis (TGA), pore solution composition using ICP-OES, X-ray diffraction (XRD), Fourier transform infrared spectroscopy (FTIR), and Electron probe micro-analyzer (EPMA).

Thermogravimetric Analysis

The thermogravimetric analysis (TGA) was performed on the paste samples cured at both 20±1°C and 40±1°C under sealed conditions. A Netzsch STA 409 PC DSC-TGA equipment in a through flow N_2 atmosphere (60 mL/min) over a temperature range of 20-1000°C and at a controlled rate of 10°C/min was used. This analysis was performed on crushed paste samples after vacuum drying at 0.023 mbar for 2h to remove the free water [212]. The weight loss between 30°C and 600°C, which represents the total bound water content (both physical and chemical), is used as a relative measure of the reaction degree.

Pore solution chemistry and pH measurement

A high-pressure device was used to extract the pore solution from the mortar samples, similar to the one described in [213]. An axial pressure of around 350 MPa was applied to the samples in a confined volume, developing tri-axial compression with the aim to remove the pore solution from the mortar samples. After extraction, the pore solution was immediately filtered using syringe type filters. One part of filter solution was diluted with nitric acid (0.3 vol%) to measure the concentration of Na, Si, Al, Ca ions in the pore solution. Another part of filter solution is diluted in sodium hydroxide solution (0.1 mol/L) instead of nitric acid to measure

the concentration of sulfur (S) in the pore solution, as described in [214]. The diluted solutions were analyzed using Inductively Coupled Plasma Optical Emission Spectrometry (ICP-OES). The concentration of OH^- ions the pore solutions was measured on the non-diluted pore solution by titration against hydrochloride acid (0.1M HCL) using phenolphthalein and methyl orange as the indicators.

X-ray diffraction analysis (XRD)

XRD data were collected on powder samples using a Bruker D2 Phaser with CuKα radiation (λ = 1.54 Å) operating at 30 kV and 10 mA. The samples were scanned over a range of 5°-70° 2θ and measured in step scan mode at 2s per 0.02° 2θ. Since the crystalline phase like ettringite will decompose during hydration stoppage with solvent exchange and/or freeze-drying techniques [215, 216, 217], XRD measurements were performed on powder paste samples without any hydration stoppage in this study.

Fourier transform infrared (FTIR) spectroscopy

Attenuated Total Reflectance FTIR spectrometry was used to monitor the structural formation in binder and to identify the chemistry of the reaction products. The analysis was carried out on vacuum-dried powdered samples. Spectrums were acquired on a Bruker Alpha-P with diamond crystal, in a region of 4000-500 cm^{-1} at a spectral resolution of 2 cm^{-1} with 64 scans; the measurements were supported by OPUS software.

Electron probe micro-analyzer (EPMA)

Microchemistry of AASF was investigated by using JEOL Hyperprobe JXA-8530F field emission gun electron probe micro-analyzer (FEM EPMA) with five wavelength dispersive spectrometers (WDS). The EPMA was operated at 15kv and 15nA, using Ka crystals as follows: PETH for Ca, PETJ for Si, TPA for Al and Mg, and TAPH for Na. The analysis was performed on the paste samples impregnated using a low-viscosity epoxy resin, polished with SiC paper and then coated with platinum. At least 20-25 points were measured on each sample surface. By comparing the chemical compositions of slag/fly ash particles derived from XRF and EPMA point analysis, the atomic ratios of the hydrated gel reported in this study by excluding the unreacted particles.

Pore size distribution

Pore structure analysis was conducted using the Mercury Intrusion Porosimetry (MIP) method by assuming the contact angle and surface tension of mercury was 130°C and 0.485 N/m,

respectively. The measurements were performed on paste samples casted in 2 ml plastic vials and stored at controlled temperature of 20±1°C and 40±1°C, respectively. At the required age (3, 7 and 28 days), a slice of the hardened paste sample was cut and submerged in isopropanol for one week, to stop the reaction without inducing significant changes on the pore structure [218]. Afterwards they were kept under low vacuum in a desiccator for 4-5 days to remove the isopropanol.

Nitrogen adsorption test was also implemented to characterize the gel pores that are beyond the detection range of the mercury intrusion method. Nitrogen adsorption tests were performed using Nova 2200e Surface Area Analyzer, Quantachrome Instruments. Pore size distributions were calculated using the Density Function Theory (DFT) method [219] from absorption branches over a relative pressure of 0.005-0.98 range and the surface area was calculated by Brunauer-Emmett-Teller (BET) method. The reaction was stopped similar to MIP samples and were ground to 65-100 μm using a centrifugal mill. As for pre-treatment, powder samples were degassed under vacuum flow for 24 hours at a constant temperature of 20±1°C.

3.4.3 Modelling autogenous shrinkage caused by self-desiccation mechanism

Chemical shrinkage

Dilatometry method, according to ASTM C1608-17 [220] was used to monitor the chemical shrinkage of pastes at a constant curing temperature of 20±1°C (Fig. 3.6). Immediately after mixing, about 10±2g of AASF paste was placed at the bottom of a small glass vial, with a diameter of 50 mm and a height of about 65 mm. Then the remaining space of the vial was filled with distilled water and closed with the lid encasing a graduated tube with total volume of 10 ml and an accuracy of 0.1 ml (Fig. 3.6). Three parallel tests were carried out for each mixture and the average value was used as the chemical shrinkage. The principle of this method is that the water above the paste is sucked into the samples to compensate the chemical shrinkage.

Autogenous shrinkage

The linear autogenous shrinkage behavior was investigated on mortar samples using Auto-shrink digital dilatometer as suggested by ASTM C1698-09 [149]. Three corrugated polyethylene tubes of 29 mm in diameter and 420 mm in length (Fig. 3.7) were casted for each mix composition and tested at both 20±1°C and 40±1°C, respectively. The change in length

was continuously monitored by means of linear variable differential transformers (LVDTs). This corrugated tube method effectively prevents moisture loss to the environment and minimizes restrain to shrink during hardening, i.e. it allows the specimen to shrink freely. The repeatability results of the autogenous shrinkage are given in Appendix C.



Figure 3.6: Dilatometry method for determination of chemical shrinkage on paste samples.

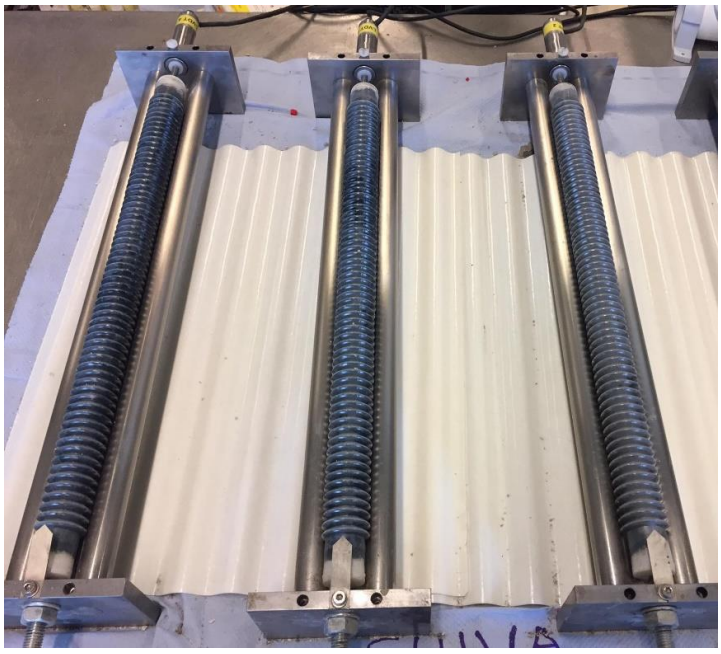

Figure 3.7: Corrugated tube method for determination of autogenous shrinkage on mortar samples.

Internal relative humidity (RH) measurements

Internal relative humidity (RH) of mortar samples was measured by means of Rotronic HC2-AW-USB RH station probes (Fig. 3.8). Before starting the measurements, the probes were calibrated using standard salt solutions of known constant RH in the range of 65-95%. After calibration, the freshly mixed mortar was cast in a plastic container (Rotronic PS-40) and then put into the measuring chamber. The RH in the samples was recorded at an interval of one minute up to 14 days, at a constant temperature of 20±1°C and 40±1°C, respectively.



Figure 3.8: The apparatus for internal RH measurement.

Surface tension of extracted pore solutions

The surface tension of the pore solution was measured using the Pendant drop test (Fig. 3.9). This method measures the surface tension of a liquid based on the shadow image of the liquid drop suspended from the end of a tube, using drop shape analysis by Young-Laplace equation [221].

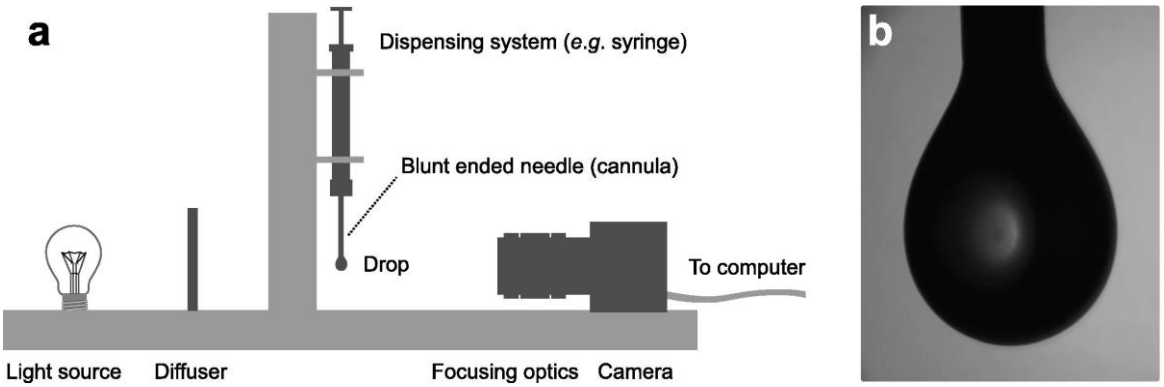

Figure 3.9: A basic experimental setup for pendant drop tensiometry [a]; a typical drop image as acquired by a camera [b] [221].

Degree of saturation

The degree of saturation is defined as the ratio between the evaporable water content and the total permeable pore space in the mortar. The evaporable water content was measured by oven-drying the samples at 105°C until constant mass was achieved. The mortar was then placed in a vacuum desiccator attached with a pressure gage and water line, to measure the total amount of open porosity by vacuum saturation technique, following the procedure described in ASTM C642-13 [222].

3.4.4 Restrained ring test

The circular ring test was conducted to investigate the cracking behavior of alkali-activated slag/fly ash cements under restrained autogenous conditions. The geometry of the steel ring specimens used in this study are shown in Fig. 3.10. The inner ring had a wall thickness (t_s) of 6.1 mm and an outer diameter ($R_{o,is}$) of 161.75 mm, and a height (h) of 75 mm. While the outer steel ring had an inner diameter ($R_{i,os}$) of 186.75 mm, resulting in a mortar ring thickness (t_m) of 25 mm. The base plate is made of plywood and coated with non-absorptive substance to prevent moisture loss from mortar into the base. Freshly mixed AASF mortar was casted into the steel ring in two layers and compacted with a rod and some additional hammering on the sides to ensure proper consolidation. After completion of the casting process, the top surface of the ring was immediately sealed with an inner layer of plastic and an outer layer of aluminum foil. This top surface was then covered with a wooden plate to avoid drying shrinkage. After removing the outer ring at the final setting time, the outer surface of the mortar ring is wrapped in aluminum tape in order to avoid the moisture loss to the environment. Friction between the steel ring and mortar as well as between the mortar and the base plate was minimized by applying grease.

The autogenous shrinkage of AASF mortars causes the mortar ring to shrink. This resultant deformation imposed on the inner steel ring was measured by four strain gauges attached at the mid-height of the inner steel ring. The strain gauges were connected to data acquiring systems in half-bridge configuration to continuously monitor the inner ring strains, up to the time of cracking. The ring specimens were stored in a climate room with 20±1°C, ~65% relative humidity. The average of two ring test measurements was presented for each mixture.

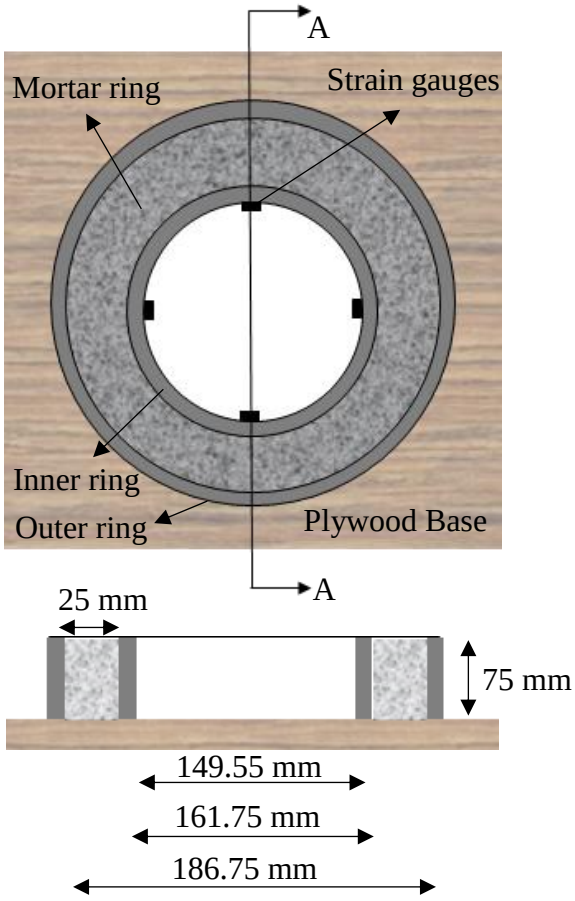

Figure 3.10: Circular restrained ring test.

3.5 Conclusion

In this chapter, all the source materials, alkaline activators and the various experimental methods/techniques used in this study were described thoroughly, in order to allow meaningful interpretation of the experimental results in the following chapters.

Moreover, the environmental issues mainly related to Global Warming Potential (GWP), which is expressed in CO_2 equivalent greenhouse gas emission (GHG) was discussed for the mix compositions investigated in this research. The mix with sodium silicate as a sole activating solution show around 35% lower CO_2 emission compared to that of traditional OPC. However, the partial substitution of sodium silicate with sodium carbonate and sodium sulfate solution significantly reduces the $CO_{2\text{-}e}$ (around 65-70%) and is suggested as a promising route to develop less expensive and more environmentally friendly AAS cements.

Chapter 4

Setting and hardening behavior

4.1 Introduction

In this chapter, the influence of the substitution of sodium silicate by sodium carbonate and sodium sulfate on the setting and hardening behavior of alkali-activated slag/fly ash cement is studied. First, the reaction process of alkali-activated slag/fly ash cements (AASF) is investigated using isothermal calorimetry and ultrasonic measurements. The heat evolution from calorimetry, which reflects the chemical process and the ultrasonic P-wave velocity evolution, which is directly related to the microstructure, are closely related to each other. Therefore, by relating heat evolution and ultrasonic P-wave velocity, the reaction process of AASF cements is interpreted in this chapter. Afterwards, the setting behavior of AASF cements is studied, by performing Vicat Needle test and ultrasonic measurements. The mechanical strength and stiffness development of AASF mortar are described and correlated with the heat evolution curves and ultrasonic measurements on mortar samples. Finally, the main conclusions are summarized.

4.2 Reaction process

4.2.1 Heat of hydration

Fig. 4.1 shows the heat evolution curves during the first 72h of the AASF pastes. They show two peaks: (1) an initial dissolution peak formed during the first few minutes with a significant amount of heat release, and (2) an acceleration peak at relatively low intensities at 6-20 hours. Similar trend of calorimetry heat flow curves were observed for slag/fly ash blends activated with sole sodium silicate [223, 224], sodium carbonate [65, 64] and sodium sulfate solutions [68, 69]. The first peak corresponds to the initial wetting/dissolution of slag and fly ash particles and coagulation of the resulting dissolved species [225, 84]. The second peak corresponds to

the formation of reaction products as a result of reaction between the dissolved ions and/or the anions present in the activator [84].

The time of occurrence of the initial dissolution peak is independent from type and concentration of the activator. However, the magnitude of this dissolution peak is slightly higher for sodium silicate activation (SS-1.0) due to a higher concentration of OH^- ions (see Table 3.3), resulting in rapid dissolution of slag and consequently formation of more aluminosilicate complexes or C-A-S-H type gels with low Ca/Si ratio. The initial dissolution peak is followed by an induction period with a very low amount of heat release due to the barrier effect of the initial reaction products layer [226, 227]. Consequently, the induction period is attributed to the time required to reach a critical concentration of the dissolved ions to form reaction products.

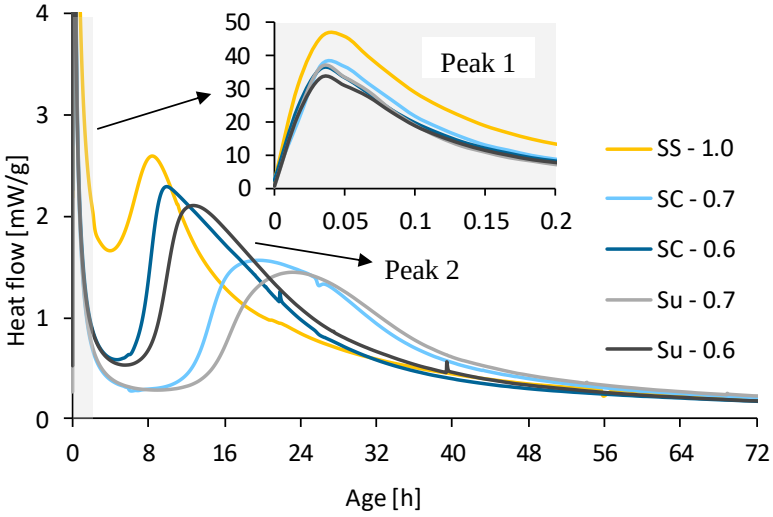

Figure 4.1: Heat evolution rate with an inset showing the first minutes of AASF pastes.

The duration of the induction period seems to depend mainly on the concentration of OH^- ions and Na_2O content of the activator (Fig. 4.1). The sample activated with SS-1.0 having a higher concentration of OH^- ions (see Table. 3.3) indicate a shorter induction period. This suggests that an increase in OH^- ions concentration enhances the dissolution of slag and precipitation of the reaction products. This is in agreement with the previous studies, which have reported that an increase in pH value of the activator leads to a more rapid dissolution of slag and increases the solubility of silicates and aluminates [74]. On the other hand, in samples with sodium carbonate and sodium sulfate having same concentration of OH^- ions, the duration of the induction period decreases, and an intense and sharp acceleration peak occurs with increase in concentration (Na_2O) of the activator. These results suggest that the increase in alkali-content

(Na_2O) of the activator also accelerates the formation of the reaction products. In other words, the alkali (Na^+) provided by sodium carbonate and sodium sulfate can expedite the depolymerization of Si-Al structure of slag and increase the concentration of dissolved ions required for hydration reaction.

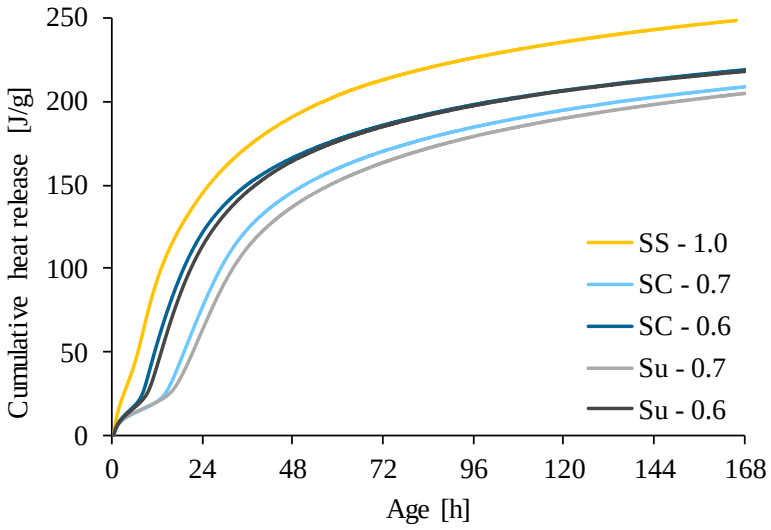

Figure 4.2: Cumulative heat release of AASF pastes.

The cumulative heat release during the first 7 days of AASF pastes is shown in Fig. 4.2. It can be seen that the partial substitution of sodium silicate with sodium carbonate and sodium sulfate significantly reduce the rate of reaction due to decrease in alkalinity (OH^- ions) of the solution. The longer induction period in samples with sodium carbonate and sodium sulfate is represented by a relatively slow increase in the heat release between initial rise (dissolution period) and later rise (acceleration period). By comparing the cumulative heat release in samples with sodium carbonate (SC) and sodium sulfate (Su), it can be seen that the concentration (Na_2O) of the activator has a more significant influence on the reaction rate than the nature of anion (CO_3^{2-} and SO_4^{2-}) present in the activator. At the same concentration (Na_2O), the samples with sodium carbonate have somewhat higher cumulative heat release during acceleration period compared to samples with sodium sulfate. This implies that sodium carbonate activation forms more reaction products than the sodium sulfate at the same concentration. This is mainly attributed to the formation of calcite at early ages (see Chapter 5: TGA and XRD results), which can act as nucleation sites for the precipitation of more C-A-S-H type gels [228, 229]. In other words, as the saturation limit of calcite is much lower than that of $CaSO_4$ and C-A-S-H type gels, the formation of calcite in samples with sodium carbonate is faster and accelerate the further dissolution of slag to provide more dissolved Ca^{2+} ions, thereby

faster and accelerate the further dissolution of slag to provide more dissolved Ca^{2+} ions, thereby promoting the formation of C-A-S-H type gels. This is supported from pore solution analysis data (Fig. 5.15), where the concentration of Ca^{2+} ions is slightly higher for samples with sodium carbonate than samples with sodium sulfate at the same concentration.

4.2.2 Evolution of ultrasonic P-wave velocity on paste

Typical ultrasonic P-wave velocity (UPV) curve and its first derivative (acceleration) curve of AASF paste (SS-1.0) are illustrated in Fig. 4.3 and Fig. 4.4, respectively. By relating UPV curves with isothermal calorimetry heat flow, the UPV curve can be divided into five characteristic stages as follows: dissolution stage (stage I), condensation stage (stage II), induction stage (stage III), acceleration stage (stage IV), and the deceleration stage (stage V). Immediately after mixing and moulding, the measured ultrasonic velocity of the fresh paste is lower than the velocity of the alkali solution (1450-1600 m/s) and air (340 m/s). Since fresh paste is a liquid suspension of slag and fly ash particles, the solution/air phase acts as a dominating factor that determines the ultrasonic velocity. Although a fully connected pore solution isolates the suspended solid particles from each other, the ultrasonic velocity in the fresh paste is lower than the velocity of the solution. The initial value of the P-wave velocity in AASF pastes is around 300 m/s (Fig. 4.3a). A similar value is reported for OPC in the literature [230, 231, 232, 233]. It is suggested that the presence of air bubbles in the mixing solution and tiny air-bubbles entrapped into the paste during mixing can result in a lower value of ultrasonic velocity [234, 235, 236]. Additionally, the dispersion of solid particles in the solution can lead to a lower ultrasonic velocity, as the travel time of the ultrasonic wave increases with an increase in the elongated length of the wave-path due to suspended grains [237].

As clearly observed in Fig. 4.3a, the ultrasonic velocity during the first dissolution stage decreases at a very slow rate. This stage corresponds to the pre-induction period of heat flow curves, which is assigned to the wetting and dissolution of slag and fly ash particles, hydrolysis of silicate and aluminate species and subsequent formation of either aluminosilicate oligomers or monomers in solution and their complexation with calcium and sodium [238, 97, 82]. By correlating the ultrasonic velocity curve with the isothermal calorimetry heat flow curves, the first dissolution stage in UPV curves can be explained as follows: the decrease in the ultrasonic velocity during the first dissolution stage can be attributed to the formation of aluminosilicate oligomers with cavities that accommodate alkaline cations as charge imbalance generated by replacing Al^{3+} with Si^{4+} ions [239, 76]. Simultaneously, the hydrolysis of dissolved

aluminosilicate oligomers results in the formation of more smaller aluminosilicate oligomers and/or monomers in solution can also lower the ultrasonic velocity. In other words, the presence of more Si-Al units with cavities and their reaction complexes with dissolved Ca^{2+} and Na^{+} ions in the solution [240], in suspension, creates less space for the waves to propagate and lowers the value of ultrasonic velocity during the first dissolution stage. It is obvious that the reaction mechanism during the first hours in AASF is a 'through-solution' precipitation that contrasts with the 'topotactic' growth of C-S-H gel in OPC-based materials [35]. Additionally, the decrease in the ultrasonic velocity may also partially result from un-reacted hollow fly ash, after the dissolution of small fly ash particles that are trapped inside the larger hollow fly ash particles [241].

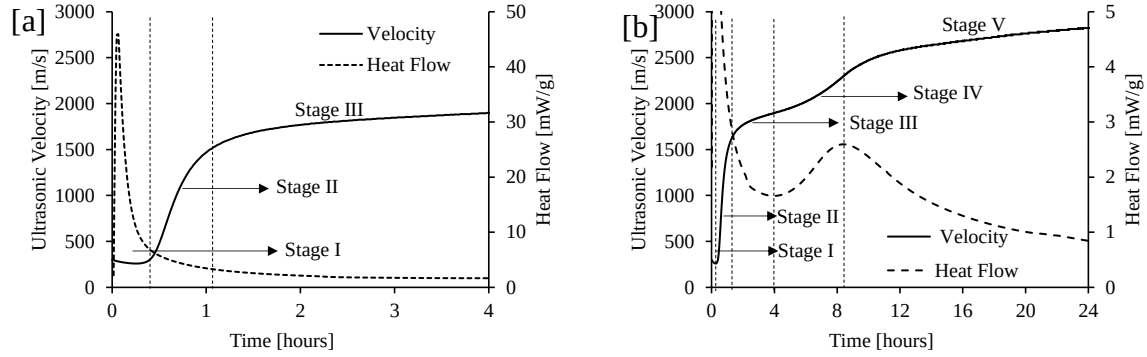

Figure 4.3: Typical ultrasonic P-wave velocity curve of AASF pastes [SS-1.0]; first 4 hours [a], up to 24 hours [b].

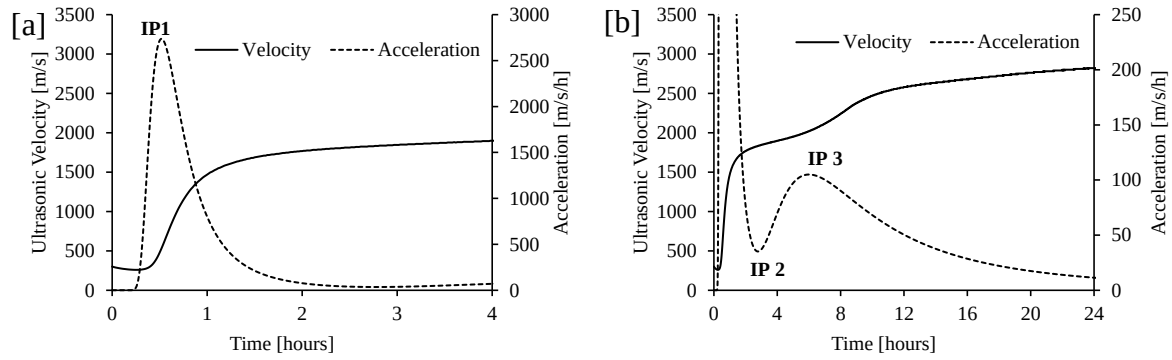

Figure 4.4: Derivative of the P-wave velocity in AASF pastes [SS-1.0]; first 4 hours [a], up to 24 hours [b].

After a certain time (around 15-25 minutes) the solid percolation path starts to develop and leads to the propagation of wave through the solid phase instead of through liquid phase, which leads to a sudden increase in ultrasonic velocity, as shown in Fig. 4.3a. In other words, the propagation of the ultrasonic velocity is considered to increase when the system changes from

the suspension state to the solid network frame, defined by the first inflection point IP1 (maximum of first derivative curve) in this study (Fig. 4.4a). It can be seen clearly from Fig. 4.3b that the ultrasonic velocity already starts to increase rapidly in the pre-induction period of heat flow curves. This remarkable acceleration of ultrasonic velocity in the pre-induction period can be explained by two phenomena. Firstly, the previously formed aluminosilicate oligomers and/or monomers in solution may undergo continuous condensation reactions and form large aluminosilicate structural units near the slag/fly ash particle surface [117], which leads to the development of interconnected solid phases and increase in ultrasonic velocity. Secondly, the formation of reaction products upon contact with the dissolved Ca^{2+} ions from slag and the anions of the activator, changes the material from liquid suspension to a porous solid state [110]. The formation of the reaction products fills the pore spaces originally occupied by the alkaline solution and increases the solid volume fraction which contributes to the significant rise in ultrasonic velocity during the second stage. This reaction and corresponding reaction products formed in the pre-induction period plays an important role in the initial setting behaviour of the AASF. This rapid increase in ultrasonic velocity during the condensation stage of UPV curves and per-induction period of heat flow curve indicates that the reaction mechanism of AASF systems is composed of dissolution followed by precipitation and rapid condensation between initially formed aluminosilicate oligomers and/or monomers. This early increase of the ultrasonic velocity in the pre-induction period can also be partially explained by some physical phenomena: air bubble migration to the surface, workability loss due to intake of solution by initial chemical reactions and densification of the internal structure by settling of the particles due to gravity, causing a mechanical bounding between particles [233].

During the third stage, only a small increase in ultrasonic velocity can be observed, corresponding to the induction period of heat flow curves, as shown in Fig. 4.3b. Previous studies have reported that the induction period in AASF systems could be due to the dilution effect caused by the formation of Si-Al rich layer on the surface of unreacted particles or the time needed to rise to a critical concentration of ions in order to form more reaction products [225, 104]. Therefore, the gradual increase in ultrasonic velocity during the induction period can be attributed to the formation of more interconnected network structure by polycondensation reaction at solid-liquid interface and/or between initial reaction products. In other words, two functional silicate groups attached to the adjacent aluminosilicate structural units or low Ca/Si ratio C-A-S-H gels can be brought into contact to form a more interconnected

solid-phase network. As a result, the ultrasonic velocity increases slowly until the end of the induction stage, defined by the second inflection point (IP2) in this study as shown in Fig. 4.4b. After that, the ultrasonic velocity increases gradually up to the third inflection point (IP 3), which is associated to the end of the acceleration period in heat flow curve (Fig. 4.3b). As more reaction products are formed and linked to the connected solid phases, the total solid volume fraction increases and leads to a gradual increase in the ultrasonic velocity during the acceleration stage (stage IV). During the de-acceleration stage, a slight increase in the ultrasonic velocity is recorded and it reaches a plateau (Fig. 4.3b). The heat flow curves correspond well with the first derivative of ultrasonic P-wave velocity and temperature measurement by the ultrasonic device as shown in Fig. 4.5 and Fig. 4.6, respectively.

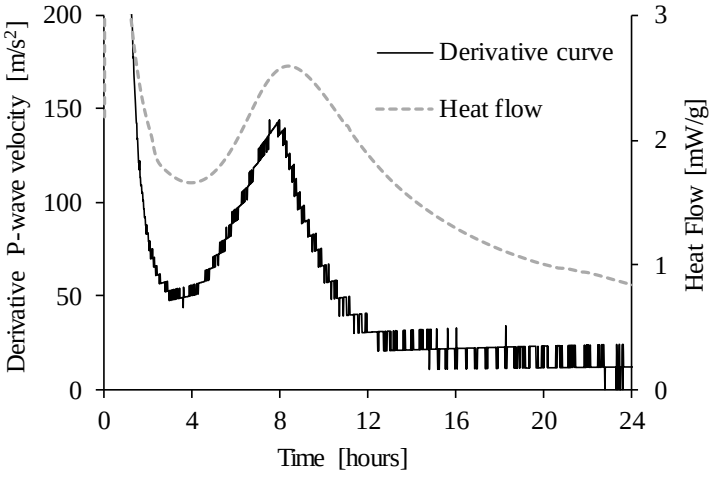

Figure 4.5: First derivative of ultrasonic P-wave velocity V_s heat evolution curve from isothermal calorimetry, for SS-1.0.

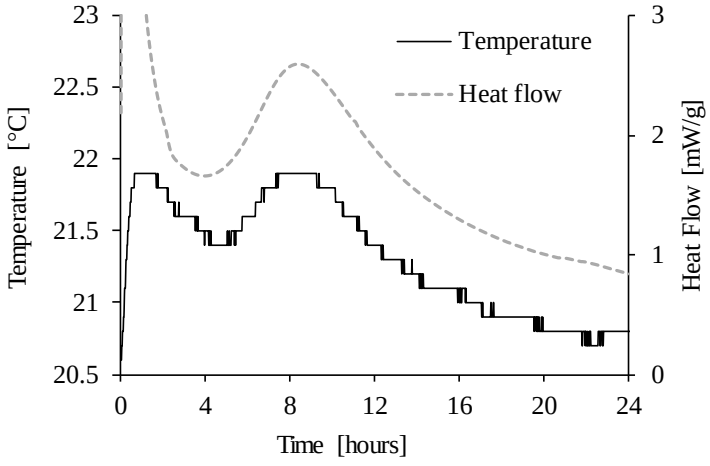

Figure 4.6: Temperature evolution curve from ultrasonic measurement V_s heat evolution curve from isothermal calorimetry, for SS-1.0.

Based on the evolution of ultrasonic velocity curves, the reaction process of AASF can be described as a combination of four stages: dissolution-hydrolysis (stage A), precipitation-condensation (stage B), polycondensation (stage C), and further reaction with advantaged time of curing (stage D). Stage A represents the initial stage of reaction, in which the dissolution and hydrolysis of dissolved species occur simultaneously and form aluminosilicate oligomers and monomers in solution. Stage B starts with a condensation reaction between the aluminosilicate species to form large units near the surface of slag/fly ash particles. Simultaneously, the formation of initial reaction products due to the reaction between dissolved Ca^{2+} from slag and the anions from the activator increases the connected solid volume fraction. Stage C is assigned to the polycondensation reaction at solid-liquid interface and/or between the previously formed reaction products, as the aluminosilicate units formed near the surface of slag/fly ash particles act as a barrier and temporarily suppress the further dissolution to form new reaction products. Stage D corresponds to the further growth of the reaction products, with an increase in the concentration of the dissolved ions in the pore solution.

4.2.3 Ultrasonic measurements on paste samples

The ultrasonic P-wave velocity (UPV) curves of AASF pastes are shown in Fig. 4.7. It can be observed that all samples show a similar trend in ultrasonic curves with five stages. During the first dissolution stage, the ultrasonic velocity gradually decreases in all samples. This indicates that, irrespective of anions present in the activator, an aluminosilicate oligomer with cavities is favored at early hours of reaction. Since the pH value of all alkaline solutions used in this study is greater than 14.0 (see Table. 3.3), the concentration of dissolved Al and Si increases, and the concentration of Ca ions decreases in the pore solution [74]. In sodium silicate activation (SS-1.0), the SiO_4^{4-} anions present in the activator solutions react more readily with the dissolved Al ions to forms aluminosilicate oligomers and/or monomers at early hours. The samples with sodium carbonate (SC) also favour the formation of aluminosilicate structural units within the first few minutes of reaction as the concentration of dissolved calcium ions in the solution is very low to precipitate carbonate phases like calcite. While in samples with sodium sulfate (Su), the decrease in the ultrasonic velocity associated with the formation of aluminosilicate units indicates that the dissolved Al ions react with SiO_4^{4-} ions in the pore solution rather with the SO_4^{2-} anions provided from the activating solutions.

During the condensation stage, there is a steep increase in the P-wave velocity in all samples, regardless of anions present in the activating solution. This is mainly attributed to the condensation reaction between the initially formed aluminosilicate units as explained above.

Moreover, this behavior is assigned to the formation of reaction products like low Ca/Si ratio C-A-S-H gels [242, 59], calcite [243, 71, 65], and ettringite [244, 68] when the dissolved Ca^{2+} ions reacts with the activator anions SiO_4^{4-}, CO_3^{2-} and SO_4^{2-} respectively. However, no clear diffraction peaks corresponding to the formation of these reaction products are found in the XRD patterns (See Chapter 5, Fig. 5.7-5.9) after 5 hours of reaction in studied AASF. These results suggest that a sufficient amount of Ca^{2+} ions has not been released yet by the slag to form these reaction products, due to its low solubility in high alkaline conditions (pH>14). On the other hand, some studies on sodium sulfate activation [245, 246, 247, 248] have reported that the presence of high amounts of OH^- ions (high pH value) affects the morphology and crystallinity of ettringite phases formed at early hours. At high pH value (pH > 13.2), the ettringite formed is almost X-ray amorphous and difficult to identify in the XRD patterns [249]. Further investigation using scanning electron microscopy and ^{27}Al NMR is necessary here to elucidate the presence of ettringite in the studied AASF compositions.

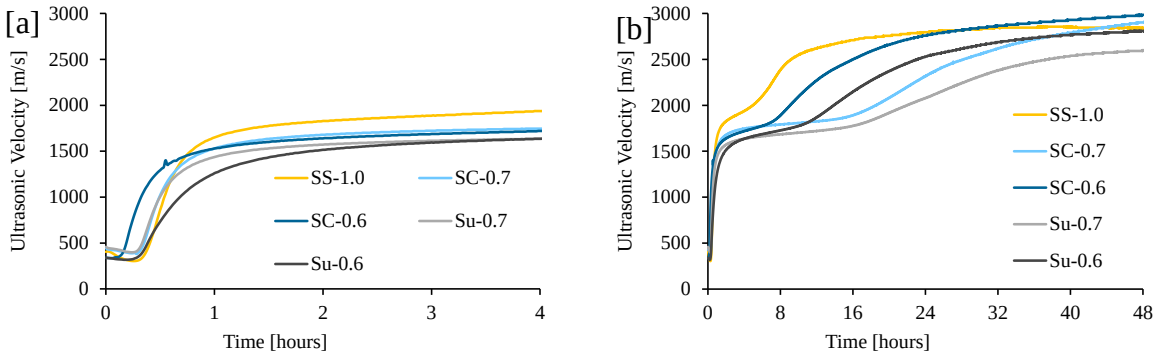

Figure 4.7: Ultrasonic P-wave velocity curves of AASF pastes; first 4 hours [a], up to 48 hours [b].

During induction stage, the ultrasonic velocity increases rapidly for the sample activated with sodium silicate (SS-1.0). Since the increase in the ultrasonic velocity is associated to the connected solid volume fraction, the solid network seems to develop faster with higher SiO_2 content in the activator. This behavior can be attributed to a high degree of silica condensation reaction, forming a Si-rich gel and subsequently reacting with the dissolved Ca^{2+} ions to form more C-A-S-H gel with an increased connected solid volume fraction. While in samples with sodium carbonate and sodium sulfate, a longer induction stage is observed due to the low concentration of OH^- ions (Fig. 4.7), resulting in lower rate of reaction. An increase in concentration (Na_2O) of sodium carbonate and sodium sulfate, results in a more rapid evolution of ultrasonic velocity during acceleration stage. This suggest that an increase in alkali-content enhances the dissolution of slag and consequently increases the reaction products precipitation.

These results correspond to the calorimetry heat flow results (Fig. 4.1). In the samples activated with sodium silicate (SS-1.0), a decrease in ultrasonic velocity was noticed over time. This is likely due to a greater autogenous shrinkage in SS-1.0 (see Chapter 6), which leads to the loss of contact between ultrasonic probes and paste sample.

4.3 Setting behavior

4.3.1 Vicat setting times

The Vicat setting times of the studied AASF pastes are shown in Fig. 4.8. In OPC-based materials, the setting time is defined as the time required to completely lose its plasticity or stiffening of paste without significant development of strength, which usually occurred at around 6-10 hours. However, for sodium silicate activated AASF, it lasts only 1.5 hour. With the incorporation of sodium carbonate and sodium sulfate, the initial setting time of sodium silicate-activated samples only slightly increases, while the final setting time notably increases. Both initial and final setting of AASF cements increase with increase in concentration of sodium carbonate (SC-0.6) and sodium sulfate activators (SS-0.6). These results are inconsistent with the calorimetry results, where the rate of reaction increases with increase in concentration (Na_2O) of activators and they are expected to show lower setting times. This contrast behavior can be well explained by relating the setting process with the ultrasonic velocity measurements (see section 4.3.2). Samples with sodium sulfate have longer setting times compared to those with sodium carbonate with same concentration or alkali-content (Na_2O). This suggests that the nature of anions present in the activator also affects the setting behavior of AASF cements.

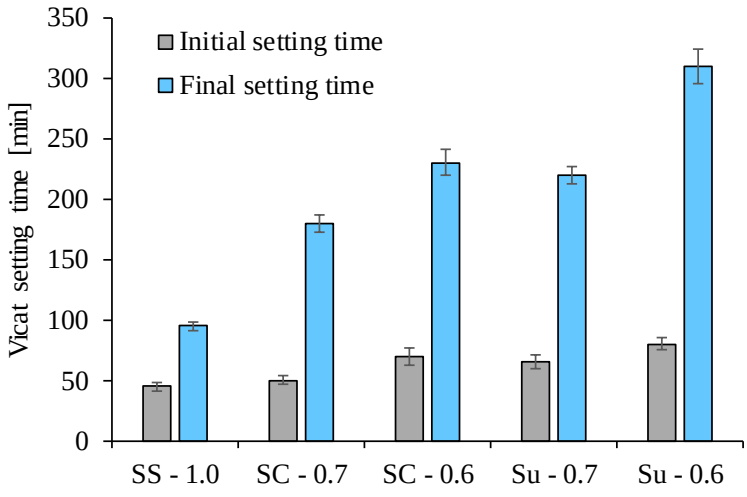

Figure 4.8: Vicat setting times of AASF pastes.

4.3.2 Comparison between Vicat setting times and ultrasonic measurements

Two strategies are often used to analyze the setting behavior of cementitious materials by using ultrasonic velocity measurement. The first one is based on the time to reach a specific value or range of ultrasonic velocity. The second approach adopts identification of the characteristic points or inflection points in the ultrasonic curves, corresponding to the district change in microstructure development. In order to accurately determine the inflection points on the ultrasonic curves, smoothing of the curves is recommended by using mathematical modelling. Among the different mathematical models available in the literature [250, 233, 108], a tri-exponential function (Eq. 4.1) is the most appropriate function for fitting the ultrasonic P-wave curves at early ages in AASF cements.

$$V_p(t) = \sum_{i=1}^{3} a_i \cdot \exp\left(-\left(\frac{b_i}{t}\right)^{c_i}\right) + d \qquad (4.1)$$

With a_i the amplitude, b_i the time parameter, c_i the shape parameter and d the baseline parameter.

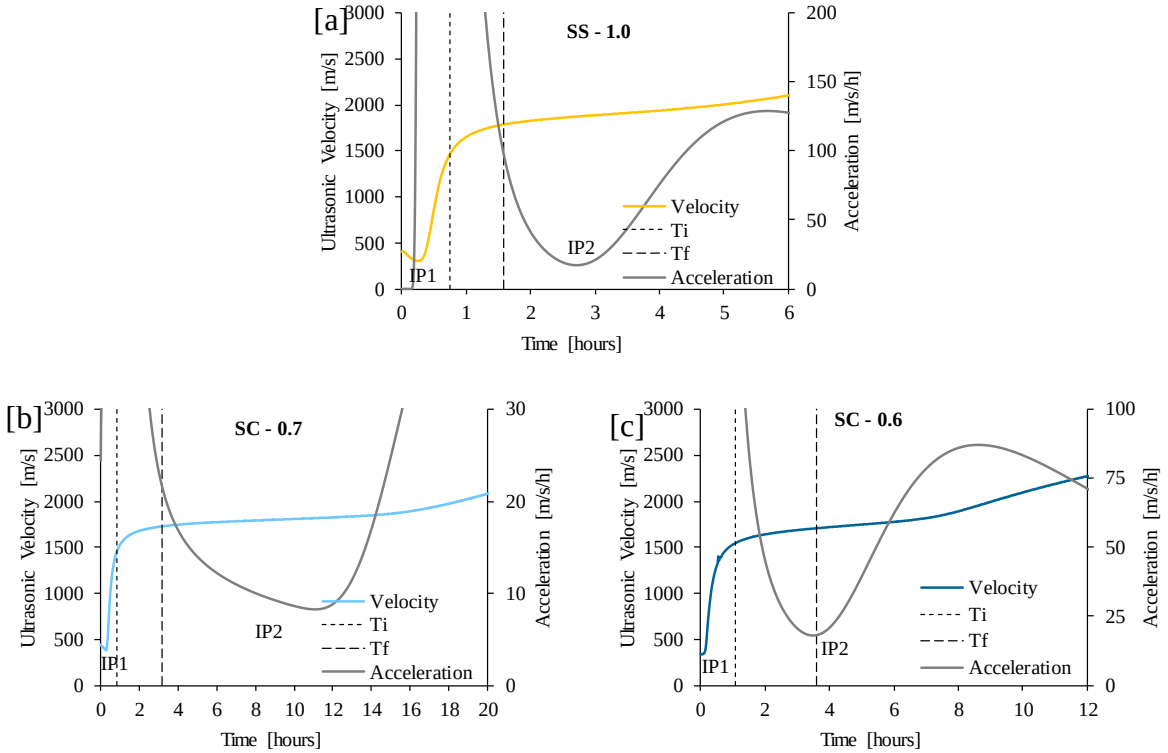

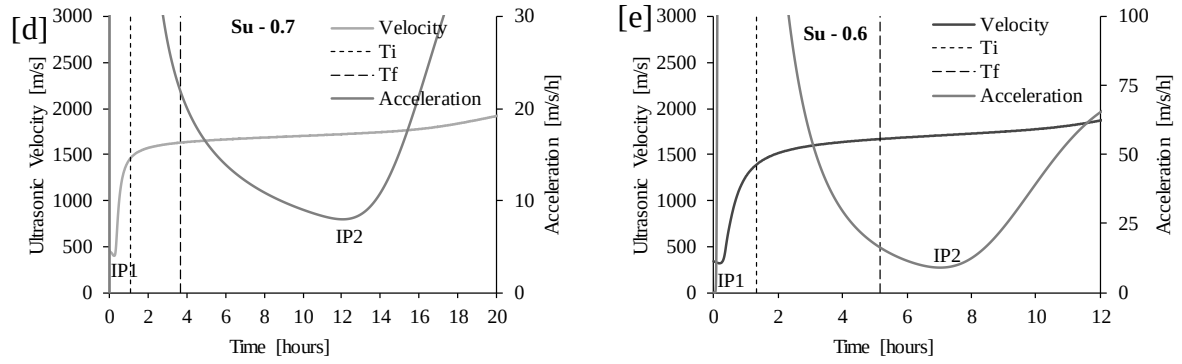

Figure 4.9: Comparison between the ultrasonic measurements and Vicat setting times of AASF cements.

By comparing Vicat setting times with ultrasonic velocity curves (Fig. 4.9), it can be seen that the initial setting time corresponds quite well to the end of the condensation stage of the ultrasonic velocity curves, where a rigid framework of connected solid phases is formed as a result of continuous condensation reaction between initial formed aluminosilicate units. However, the final setting time cannot be determined from the inflection point approach in the same way as described for OPC-based materials in [251, 233, 237]. An alternative approach based on ultrasonic P-wave velocity can be used to define the initial and final setting time of AASF as illustrated in Table. 4.1. The initial and final setting times of studied AASF can be determined by the velocity ranges: 1450-1550 m/s, 1650-1750 m/s, respectively. Similar velocity ranges have been proposed in literature to estimate the initial and final setting time of the cement paste with water-to-binder ratio of 0.5 [237, 252].

Table 4.1: Ultrasonic P-wave velocity corresponding to Vicat setting times of studied AASF.

Mix	Ultrasonic P-wave velocity at initial setting time [m/s]	Ultrasonic P-wave velocity at final setting time [m/s]
SS – 1.0	1465	1650
SC – 0.7	1525	1725
SC – 0.6	1550	1715
Su – 0.7	1460	1650
Su – 0.6	1440	1680

Results show that both initial and final setting time of AASF occur before the formation of massive reaction products in the acceleration stage of the ultrasonic measurements (Fig. 4.9). This is in contrast to Portland cement pastes where the initial and final setting time appear in the acceleration period, where C_3S hydrates to C-S-H and portlandite. This implies that the setting process in AASF cannot be solely attributed to the formation of C-A-S-H type gel, like in Portland cements.

Initial setting time:

With regard to the ultrasonic measurements, the initial setting time was found to appear in the condensation stage (Fig. 4.9), corresponding to the pre-induction period of heat flow curves. As explained above, the condensation stage in ultrasonic measurement can be attributed to the continuous condensation reaction between the aluminosilicate units and formation of initial reaction products with no or little influence on setting process. From Fig. 4.7, it can be seen that by incorporating sodium carbonate and sodium sulfate, no significant change was observed during the condensation stage of the ultrasonic measurements. This would explain the marginal differences in the initial setting time between the sodium silicate-activated sample and those with sodium carbonate and sodium sulfate (Fig. 4.8). In other words, regardless of anions present in the activator, all samples favour the formation of aluminosilicate units during the first hours of reaction and leads to initial setting process as a result of condensation reaction.

Final setting time:

Vicat final setting time of AASF occurs during the induction period of ultrasonic measurements, where the velocity increases slowly due to the polycondensation reaction at solid-liquid interface and/or between adjacent aluminosilicate structural units (Fig. 4.9). The Vicat test results reveal that final setting of sodium silicate-activated samples are significantly delayed with incorporating sodium carbonate and sodium sulfate solutions (Fig. 4.8). This is mainly attributed to the decrease in concentration of SiO_4^{4-} ions in the activating solution (Table. 3.3). Also, the partial substitution of sodium silicate with sodium carbonate and sodium sulfate solutions reduces the pH value (OH^- ions) of the activating solution (Table. 3.3) and consequently decreases the concentration of dissolved Si ions in pore solution due to decrease in its solubility at lower pH value. The decrease in concentration of Si ions in the pore solution suppresses the degree of Si polycondensation and results to longer setting time in samples with sodium carbonate and sodium sulfate. In Fig. 4.8, it is observed that the final setting time increases with increasing concentration of sodium carbonate and sodium sulfate solutions (SC-

0.6 and SSu-0.6). The presence of more CO_3^{2-} and SO_4^{2-} ions in the pore solution, which are likely not involved in the formation of reaction products, is assumed to decelerate the polycondensation reaction between the adjacent aluminosilicate structural units and lead to longer setting times. Further study is needed to support this assumption. At equal replacement of sodium silicate with sodium carbonate (SC-0.6) and sodium sulfate (SSu-0.6), the final setting is faster for samples with sodium carbonate (Fig. 4.9). This can be explained by the lower induction time and faster precipitation of reaction products in samples with sodium carbonate (SC-0.6) than samples with sodium sulfate (Su-0.6), as observed in Fig. 4.7b.

4.3.3 Comparison between Vicat setting times and calorimetric measurements

Setting generally occurs when a specific microstructural development or reaction degree start to occur [253]. Therefore, the comparison between Vicat setting times and reaction degree is meaningful. In general, the degree of reaction can be represented by the ratio of the cumulative heat release at a time "*t*" of reaction process to the total heat release at infinite time Q_∞ (Eq. 4.2) [107]. The main advantage of using the cumulative heat release to determine the reaction degree is that it is a continuous measurement starting from the mixing time. However, measuring the ultimate heat release Q_∞ is virtually impossible since the accuracy of the measuring heat release is uncertain at this point. Previous studies [109] have compared the ultrasonic velocity curves with isothermal calorimetry of alkali-activated slag by relating the ultimate heat release Q_∞ to the total heat release after 7 days. Another study [254] assumes that the ultimate heat release is equal to the heat release that occurs at a heat flow of 0.3 W/g, which is not always the case. Therefore, the mathematical modelling is adopted in this study in order to accurately determine the ultimate heat release Q_∞. An exponential function (Eq. 4.3) was concluded to be the best fitting function for the multi-curvature heat flow curves [107]. The ultimate heat release can be found by adding the parameter 'Q_i' (i = number of peaks in the heat flow curves) (Eq. 4.4).

$$\alpha(t) = \frac{Q(t)}{Q_\infty} \tag{4.2}$$

$$Q(t) = \sum \left[Q_i \,.\, \exp\left(\left[\frac{-\tau_i}{t} \right]^{\beta_i} \right) \right] \tag{4.3}$$

$$Q_\infty = \sum Q_i \tag{4.4}$$

In the above exponential equations, $\alpha(t)$ is the degree of reaction at equivalent age t, $Q(t)$ is the cumulative heat release at time t, Q_∞ is the ultimate heat release at infinite time, τ and β are the time and shape parameters, respectively. Fig. 4.10 illustrates the expoential fitting model of the cumulative heat release curves of sodium silicate-activated slag/fly ash blend (SS-1.0). Parameters of the this model for the studied AASF mixes are given in Table. 4.2. It can be noticed that the ultimate heat of hydration values and other parameters from this fitting model correspond well with the isothermal calorimetry results (Fig. 4.2).

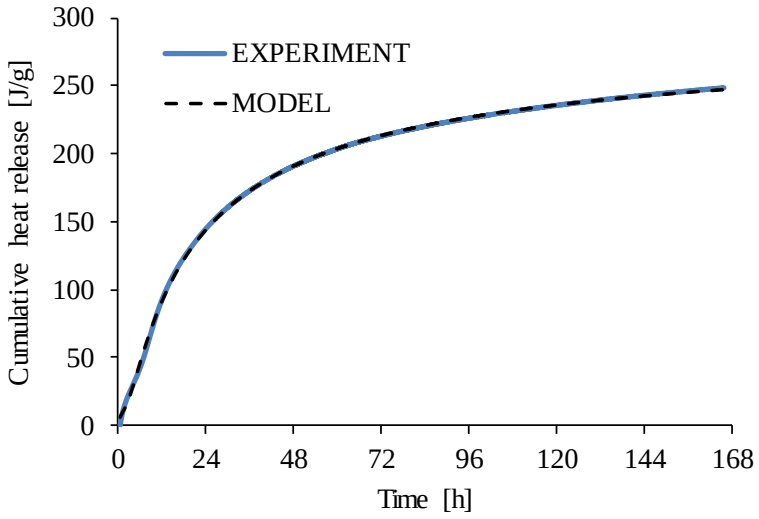

Figure 4.10: Expoential fitting model of cumulative heat release curve of SS-1.0.

Table 4.2: Parameters of the expoential fitting model for AASF.

Mix	Q_1	Q_2	τ_1	τ_2	β_1	β_2	Q_∞
SS-1.0	34.50	262.0	2.30	17.00	0.37	0.75	296.5
SC-0.7	22.70	207.5	2.25	26.90	0.19	1.33	230.2
SC-0.6	16.80	228.0	2.77	17.95	0.18	1.00	245.0
Su-0.7	23.20	207.1	1.80	30.50	0.22	1.30	230.3
Su-0.6	16.50	227.0	1.32	20.00	0.19	1.08	243.5

The relation between the calculated reaction degree and the Vicat setting times of AASF pastes is summarized in Table. 4.3. A reaction degree of around 2.1-3.2% and 3.5-4.5% corresponds to the formation of a critical volume fraction of reaction products, resulting to initial and final

setting times for AASF, respectively. Previous studies predict the initial and final setting time of OPC-based materials with w/b of 0.5 at a reaction degree of around 7.5 % and 13% respectively [255, 233]. This significant difference in reaction degree corresponding to the Vicat setting times is mainly attributed to the polycondensation reaction between the aluminosilicate units, formed near the surface of slag/fly ash particles in AASF. Nevertheless, further study is needed to validate this model using techniques like ^{29}Si NMR and scanning electron microscopic with EDS analysis.

Table 4.3: Comparing setting times with reaction degree.

Mix	Reaction degree at initial setting time or end of condensation stage [%]	Reaction degree at final setting time or end of induction stage [%]
SS – 1.0	2.5	3.8
SC – 0.7	3.0	4.0
SC – 0.6	2.1	3.5
Su – 0.7	3.2	4.5
Su – 0.6	2.4	4.2

4.4 Strength and stiffness development

4.4.1 Compressive strength

The compressive strength of the studied AASF mortar samples at different curing ages is shown in Fig. 4.11. Samples activated with sodium silicate (SS-1.0) have higher compressive strength compared to the samples with sodium carbonate and sodium sulfate solutions. This can be explained by a higher rate of reaction in samples activated with SS-1.0 (Fig. 4.1) and consequently formation of denser microstructure. At 1 day, the compressive strength values for samples with sodium carbonate and sodium sulfate are around 10-20 MPa, and 7.5-14 MPa, respectively. These strength values are considerably lower than that of OPC mortar samples (around 25 MPa) with w/b ratio of 0.5 [10]. These finding suggest that incorporating sodium carbonate and sodium sulfate solutions lower the strength development as compared to that of sole sodium silicate activated samples and traditional OPC-based materials, at early hours. However, after 3 days, the compressive strength of samples with sodium carbonate and sodium sulfate strongly increased and are comparable to the sodium silicate-activated sample (SS-1.0).

Regardless of anions present in the activator, the compressive strength increases with increase in concentration (Na_2O) of the activator. This is attributed to the higher rate of reaction with increase in concentration or alkali-content of the activator (as explained in sec 4.2.1). Although no significant change in reaction rate was found between the samples activated with sodium carbonate and sodium sulfate with the same concentration (Na_2O), the samples with sodium carbonate show higher compressive strength at given curing ages (Fig. 4.11). This implies that other factors such as pore size distribution and phase assemblage influence the compressive strength development.

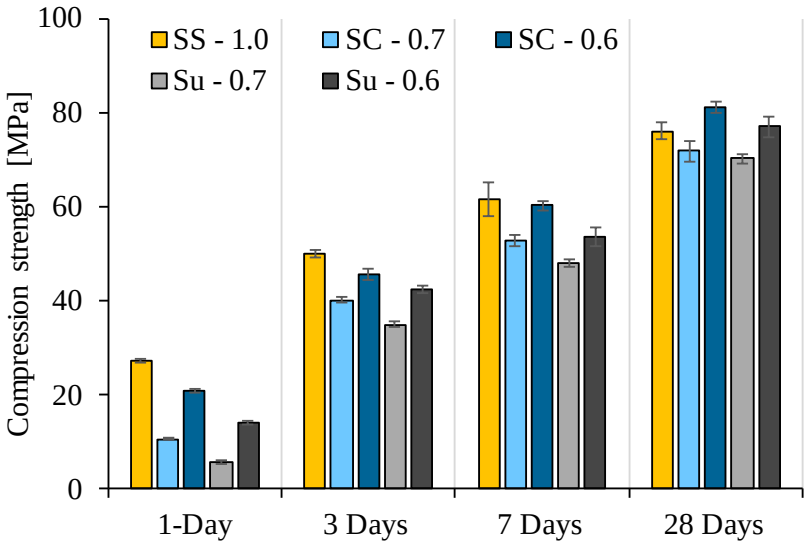

Figure 4.11: Compressive strength of AASF mortar samples.

It is interesting to notice that the samples activated with SC-0.6 and Su-0.6 have higher compressive strength values compared to the samples activated with sodium silicate (SS-1.0) at 28 days. This is likely due to the microcracking induced by larger autogenous shrinkage in SS-1.0 (see Chapter 6 and Chapter 7).

Previous studies have demonstrated a good correlation between cumulative heat release and compressive strength for OPC-based materials [256, 10]. To verify this correlation for studied AASF cements, the relationship between the cumulative heat release, normalized by binder content and compressive strength up to 7 days is shown in Fig. 4.12. A good correlation was found between the heat release and the compressive strength, indicating that the mechanical strength development during early-ages in studied AASF can be determined from isothermal calorimetry heat release, similar to OPC-based materials.

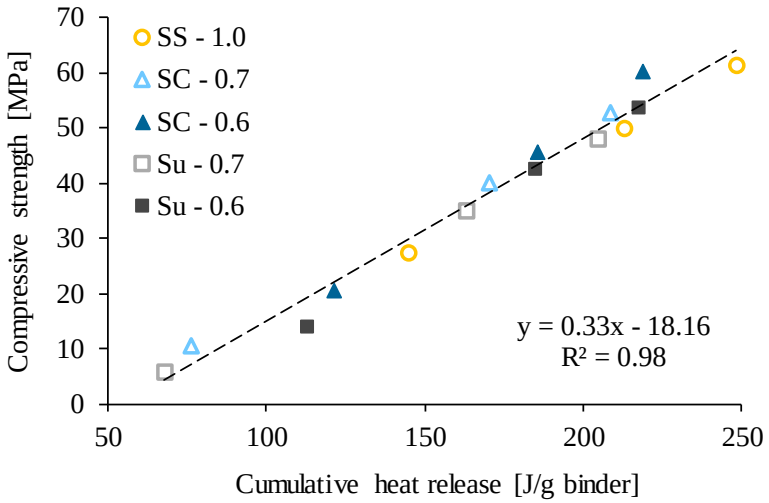

Figure 4.12: Comparison between compressive strength and cumulative heat release, up to 7 days.

4.4.2 Flexural strength

The flexural strength of AASF mortar samples at different curing ages is shown in Fig. 4.13. Similar to the compressive strength development, samples activated with sodium silicate have higher rate of flexural strength development during the first 24 hours, while the samples with sodium carbonate and sodium sulfate have slow development of flexural strength. However, after 3 days, the flexural strength of samples with sodium carbonate (SC) and sodium sulfate (Su) greatly improved, becoming equal to the flexural strength of sodium silicate-activated samples (SS-1.0).

In fact, the compressive strength is mainly dependent on the porosity or microstructure development, while the flexural strength is much more sensitive to micro-cracking of the matrix. Although the mortar samples are not under real restrained condition, the unreacted slag/fly ash particles and the presence of inert materials like sand in mortars can act as the local restraint to shrinkage and lead to micro-cracking in the matrix. It is clear from autogenous shrinkage results presented in Chapter 6, that the partial substitution of sodium silicate with sodium carbonate and sodium sulfate significantly reduced the autogenous shrinkage of sodium silicate-activated samples. As a result, the samples activated with sodium silicate (SS-1.0) having larger autogenous shrinkage can form more microcracks which reduced the flexural strength, while samples with sodium carbonate and sodium sulfate result in less micro-cracking and improve the flexural strength.

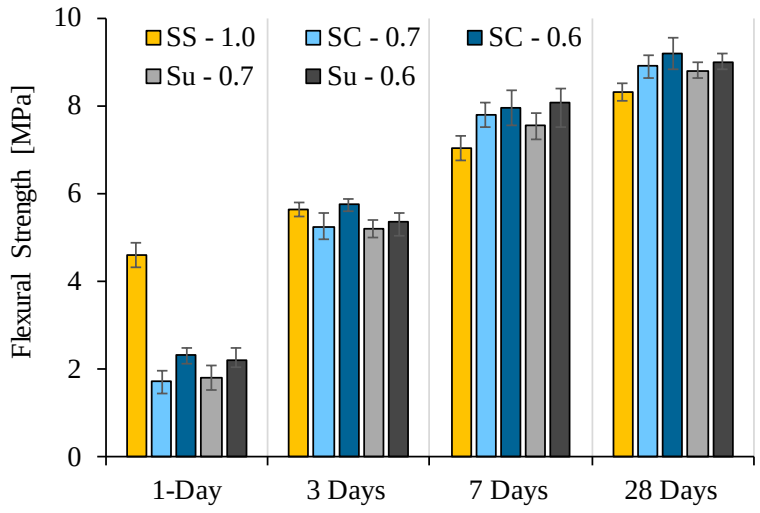

Figure 4.13: Flexural strength of AASF mortar samples.

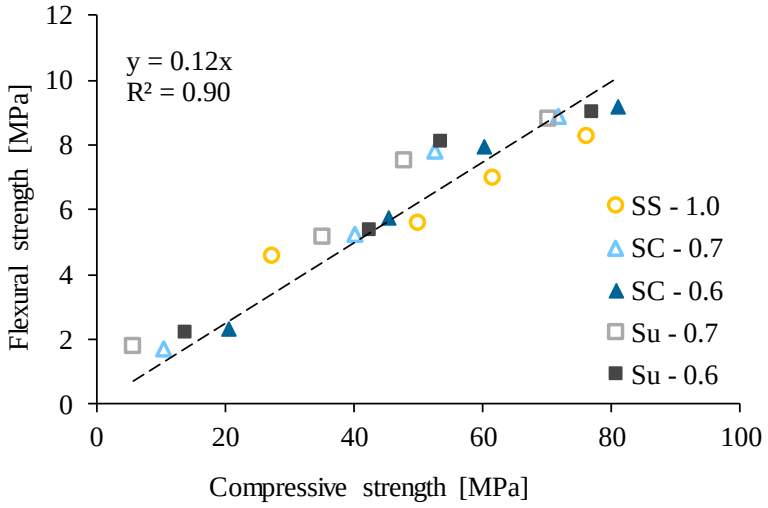

Figure 4.14: Comparison between flexural tensile strength and compressive strength of AASF.

According to Eurocode 2 [209], there exists a good correlation between the compressive strength and flexural strength for OPC-based materials, given as:

$$f_{ft} = 0.201.\, f_c \tag{4.5}$$

Where f_{ft} is the average flexural tensile strength and f_c is the average compressive strength. A similar correlation is deduced for alkali-activated slag/fly ash cements as shown in Fig. 4.14. The multiplication factor is found to be smaller (0.12) for AASF cements compared to the one reported in Eurocode 2 (0.201) for OPC-based materials. This can be attributed to the presence of more micro-cracks induced by large autogenous shrinkage as shown in Fig. 6.4 (Chapter 6).

4.4.3 Splitting tensile strength

The results of the splitting tensile strength at different curing ages are shown in Fig. 4.15. At 1 day, the splitting tensile strength of samples activated with sodium silicate (SS-1.0) is higher than that of samples with sodium carbonate and sodium sulfate. However, at 3 days and beyond, there is only a marginal decrease in tensile strength with incorporating sodium carbonate (SC) and sodium sulfate (Su).

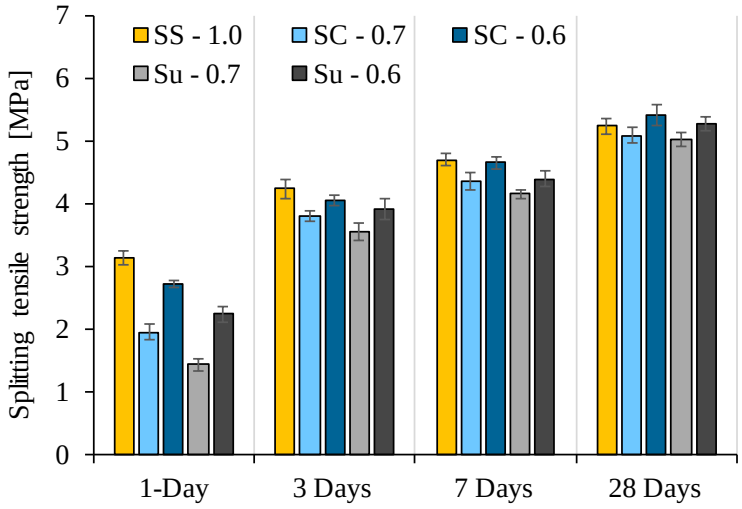

Figure 4.15: Splitting tensile strength of AASF mortar samples.

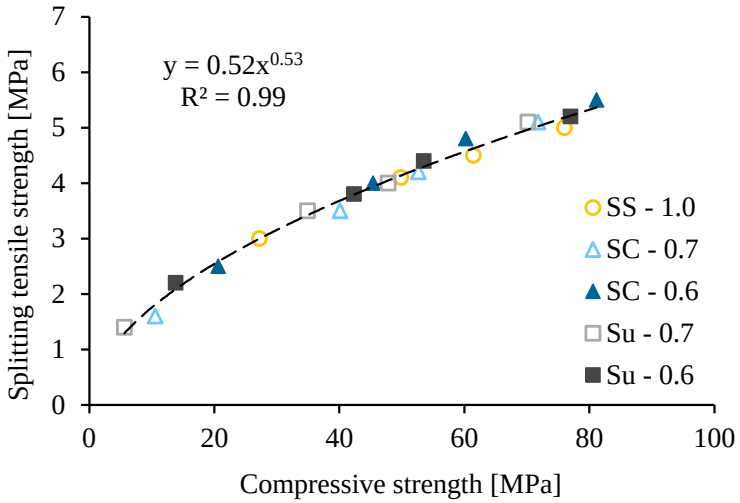

Figure 4.16: Comparison between compressive strength and tensile strength of AASF.

These results suggest that partial substitution of sodium silicate with sodium carbonate and sodium sulfate solutions has minimal influence on the splitting tensile strength development of AASF mortar samples. It is worth noting that this marginal difference in splitting tensile

strength and the significant decrease in autogenous shrinkage due to incorporation of sodium carbonate and sodium sulfate is beneficial for reducing the cracking potential of AASF cements. This will be discussed further in Chapter 7. Similar to OPC-based materials [257], there exists a good relationship between the compressive strength and splitting tensile of studied AASF mortar samples (Fig. 4.16). A similar correlation is reported for sodium silicate-activated fly ash/slag blends with the constant factor of 0.45 in [98].

4.4.4 Static E-modulus

The static elastic modulus of AASF mortar samples at different curing ages is shown in Fig. 4.17. Samples activated with sodium silicate having a higher concentration of OH^- ions (Table. 3.3) result in a higher rate of reaction and consequently formation of denser matrix with higher stiffness. The partial substitution of sodium silicate with sodium carbonate and sodium sulfate significantly reduces the elastic modulus during the first 24 hours. The elastic modulus at 1 day is reduced by around 60% when low concentrated sodium carbonate (SC-0.7) and sodium sulfate (Su-0.7) is used. However, the level of decrease in elastic modulus is much lower with increasing concentration of sodium carbonate and sodium sulfate activator at later ages as shown in Fig. 4.17.

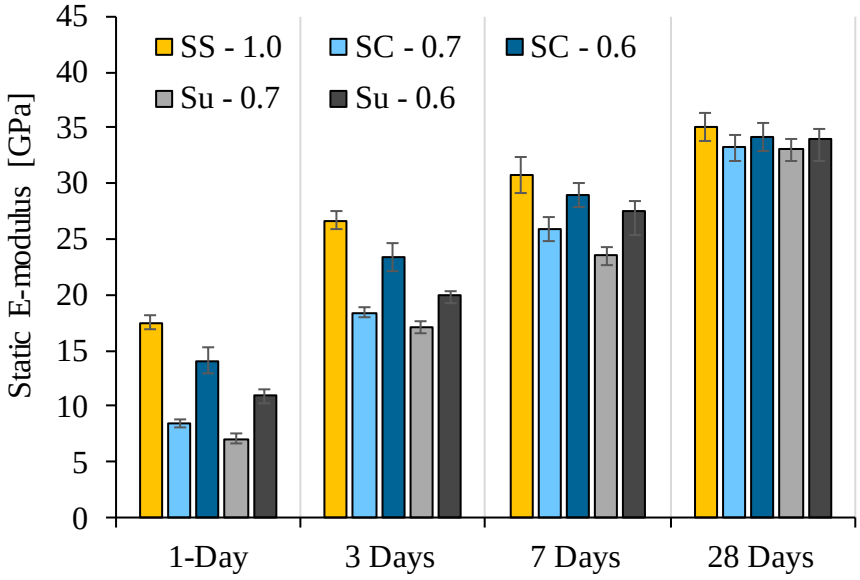

Figure 4.17: Static E-modulus of AASF mortar samples.

At the same concentration (Na_2O), samples with sodium carbonate have higher elastic modulus compared to that of samples with sodium sulfate. This can be explained by the higher rate of reaction due to formation of calcite, which acts as a nucleation seed for the precipitation of

more reaction products. At 28 days, the level of difference in elastic modulus between all studied AASF mortars is within the band width of the standard deviation (Fig. 4.17). This implies that both concentration and nature of anions present in the activator have less influence on the stiffness development at later ages.

In the serviceability limit state, the elastic modulus is one of the key parameters to design concrete structural elements and it is generally expressed in terms of compressive strength development. Fig. 4.18 shows the static elastic modulus of the studied AASF mortar samples as a function of the compressive strength development, up to 28 days. It is obvious that the relation between static elastic modulus and compressive strength in AASF cements is adequately represented by Eq. 4.6, with a determination coefficient (R^2) of 0.91. This indicates that there is a strong correlation between the static elastic modulus and the compressive strength development in AASF cements.

$$E_s = 0.48.\, f_c \tag{4.6}$$

E_s is the static elastic modulus in GPa and f_c is the compressive strength in MPa. Moreover, a good linear correlation is found between the experimentally measured static E-modulus and isothermal calorimetry heat release (Fig. 4.19). This implies that the stiffness development is mainly associated to the rate of reaction in AASF cements.

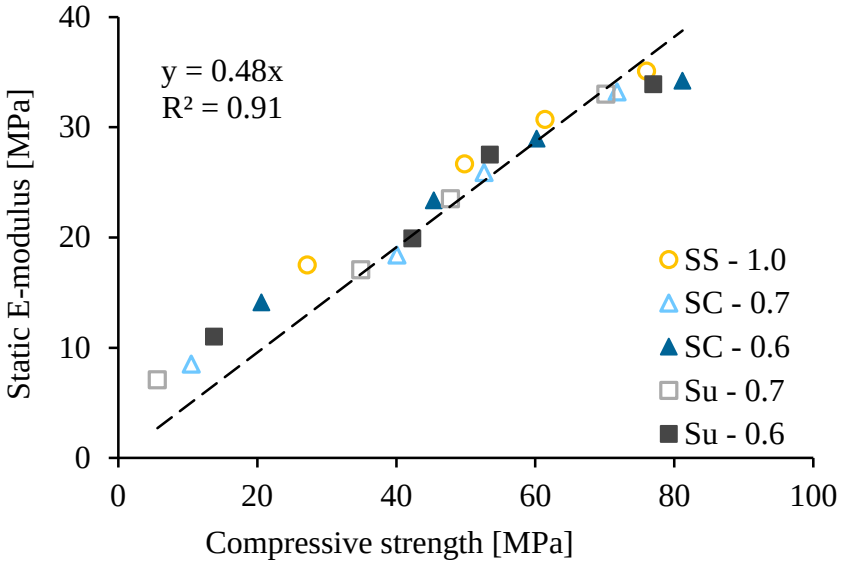

Figure 4.18: Comparison between static E-modulus and square root of compressive strength, up to 28 days.

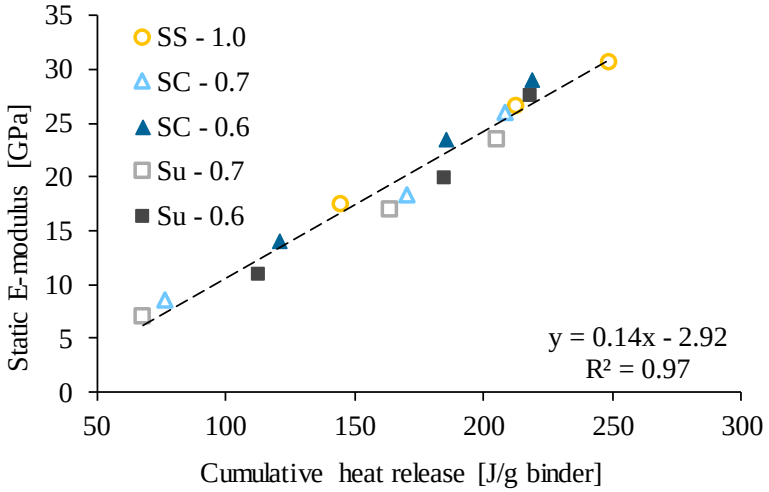

Figure 4.19: Comparison between static E-modulus and cumulative heat release, up to 7 days.

4.4.4 Ultrasonic measurements on mortar samples

The ultrasonic P-wave velocity curves on mortar samples are shown in Fig. 4.20. The P-wave velocity curve of the AASF mortar samples composed of two S-shaped functions, results in two peaks in the derivative of the P-wave velocity curve (Fig. 4.20b). This is in contrast with the evolution of the P-wave velocity curve in OPC mortar samples, which only show one S-shaped curve [107].

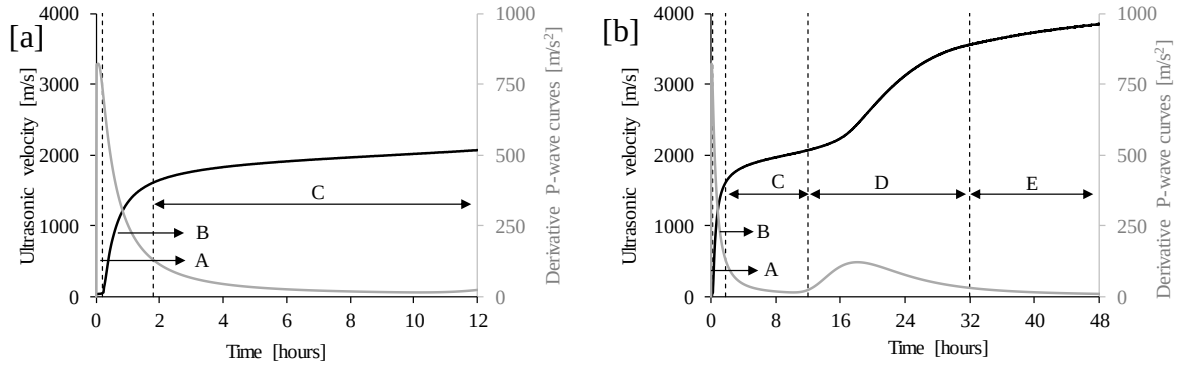

Figure 4.20: Evolution of the ultrasonic P-wave velocity [a] and derivative of the P-wave velocity in AASF mortar samples [SC-0.7].

The P-wave velocity curve of the AASF mortar samples follows similar evolution as the paste samples with five characteristic stages: (A) dissolution stage, (B) condensation stage, (C) induction stage, (D) acceleration stage, and (E) deceleration stage, as described in Section 4.2.2.

Stage A: In the dissolution stage, the initial P-wave velocity of the AASF mortar samples is around 35-50 m/s, which is substantially lower than the value in alkaline solution (1450-1550 m/s) and in air (340 m/s). This is mainly due to the air bubbles entrapped during mixing or due to a lot of tiny air bubbles in the mixing alkaline solution. The P-wave velocity during the dissolution stage of AASF mortar samples increases slightly (Fig. 4.20a). This is in contrast to the P-wave velocity evolution in the paste samples, where the P-wave velocity decreases due to the formation of aluminosilicate units with cavities in suspension. This can be explained by considering mortar samples as a solution-saturated porous solid rather than a suspension and having elastic granular frame before starting reaction of slag/fly ash particles [233].

Stage B: In the condensation stage, the P-wave velocity starts to increase rapidly (Fig. 4.20). This steep increase in P-wave velocity is primarily attributed to the formation of initial reaction products and continuous condensation reaction between them. Compared to the paste samples (Fig. 4.7), this initial increase in P-wave velocity in mortar samples is much steeper. This can primarily be explained by slightly increase in early-age reaction kinetics due to the formation of an interfacial transition zone (ITZ), resulting in a higher solution-to-binder in this zone and lower solution-to-binder ratio in bulk paste zone [108].

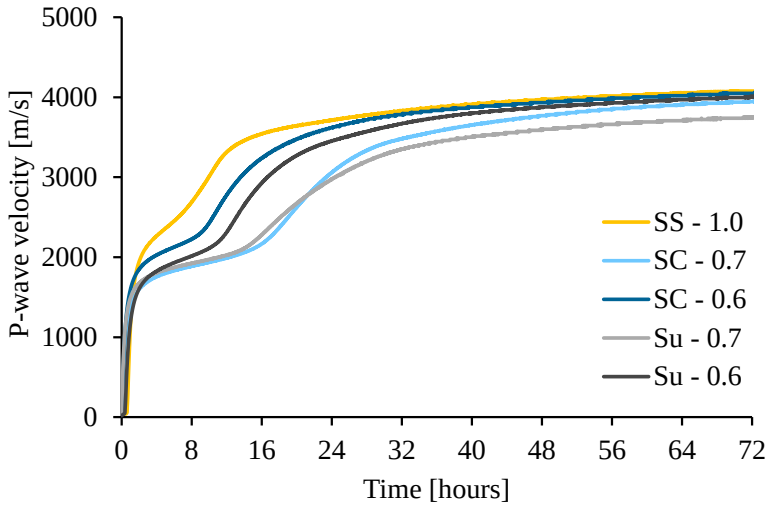

Figure 4.21: Ultrasonic P-wave velocity curves of the AASF mortar samples.

Stage C: In the induction stage, the P-wave velocity increases slowly. Because of the formation of initial reaction products around the unreacted slag/fly ash particles, the dissolution process is temporary suppressed to form further reaction products.

Stage D: In the acceleration stage, the P-wave velocity increases significantly. This stage corresponds to a period of intense hydration and rapid formation of C-A-S-H type gels that could occupy capillary pores and increases the interconnected solid volume fraction.

Stage E: In the deceleration stage, the increase in P-wave velocity slow down. This stage corresponds to the ongoing reaction at advanced times of curing.

The P-wave velocity of the studied AASF mortar samples is shown in Fig. 4.21. Regardless of type and concentration of the activator, the evolution of P-wave velocity shows similar trend in all AASF mortar samples. During early ages (dissolution and condensation stage) the difference in P-wave velocity between the studied AASF mortar samples is marginal. However, from the starting of the induction stage, the mortar samples activated with high silica content (SS-1.0) and high alkali-content (SC-0.6 & Su-0.6) reaches higher P-wave velocity. The P-wave velocity in mortar samples correspond well with the P-wave velocity results in paste samples (Fig. 4.7). It should be notice that after 24 hours, the P-wave velocity in SS-1.0 increases in slower rate due to its large shrinkage behavior (Chapter 6), causing loss of contact between the ultrasonic probes and mortar samples. Moreover, the formation of more micro-cracks/voids in SS-1.0 due to the restraining effect of sand particles on autogenous shrinkage, can affect the propagation of ultrasonic waves.

4.4.6 Elastic properties from ultrasonic measurements

From ultrasonic P-wave velocity measurements, the dynamic elastic modulus (E_d), shear modulus (G_d) and bulk modulus (K_d) of cementitious materials can be calculated using Eq. 4.7-4.10 [107]. V_p is the ultrasonic P-wave velocity, M_d is the P-wave modulus, ρ is the density of mortar, υ is the Poisson ratio for which a constant value of 0.15 is adopted in this study [208]. The calculated results for AASF mortar samples are shown in Fig. 4.22. At same concentration, samples with sodium carbonate have higher elastic properties compared to the samples with sodium sulfate at early ages. However, after 48 days, no significant change is observed in the elastic properties of samples with sodium carbonate and sodium sulfate. The influence of alkali-content or concentration (Na_2O) of the activator is also visible in the results of elastic properties (Fig. 4.22).

$$M_d = V_p^2 \, \rho \tag{4.7}$$

$$E_d = M_d \left[\frac{(1+\vartheta)(1-2\vartheta)}{(1-\vartheta)}\right] \tag{4.8}$$

$$G_d = \frac{E_d}{2.(1+\vartheta)} \tag{4.9}$$

$$K_d = \frac{E_d}{3(1-2\vartheta)} \tag{4.10}$$

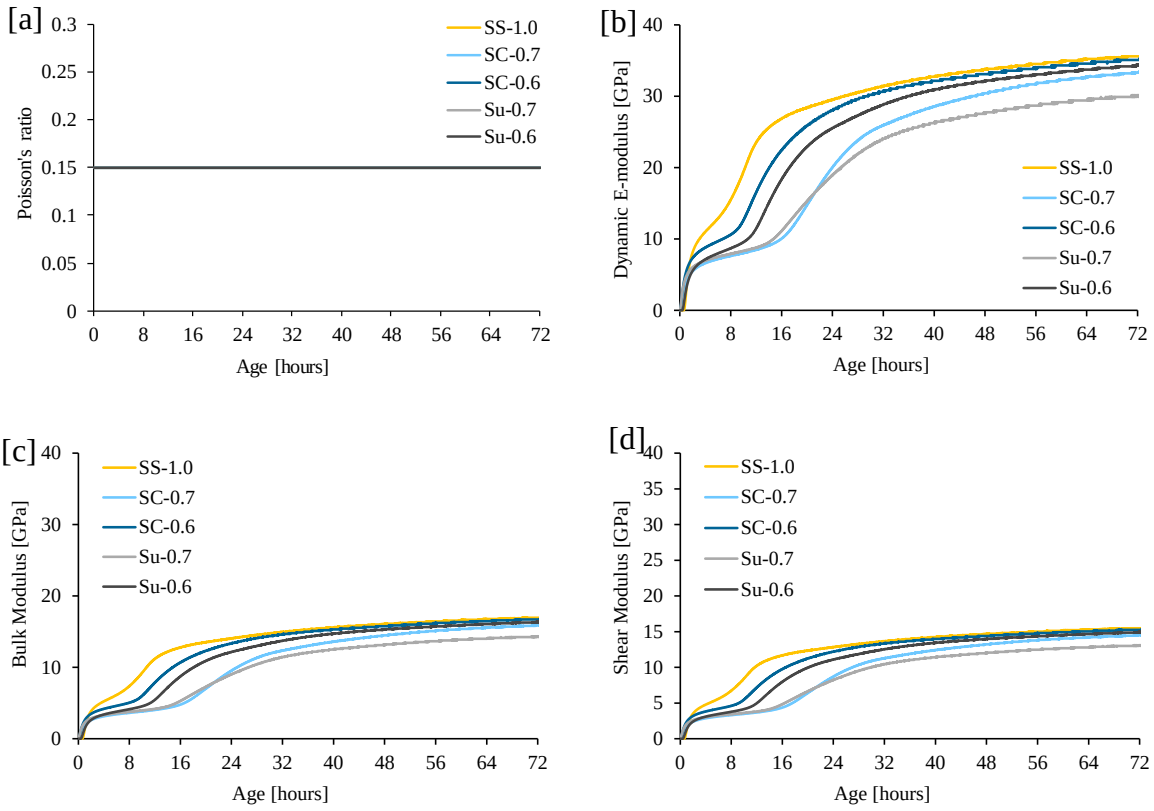

Figure 4.22: Elastic properties derive from ultrasonic measurements; Assumed Poisson's ratio [a], dynamic E-modulus [b], bulk modulus [c], and shear modulus [d].

Many researchers [107, 108] and standard codes [209] suggested a linear relationship between static and dynamic elastic modulus for OPC-based materials. A similar correlation between calculated dynamic E-modulus and experimentally measured static modulus for AASF mortar samples is shown in Fig. 4.23. A negative intercept value of 16.45 of the linear equation (Eq. 4.11) is mainly attributed to the lack of very early age data on the static elastic modulus. The relationship between the dynamic (E_d) and static (E_s) elastic modulus of the studied AASF mixes can be described by the following formula:

$$E_s = 1.15.E_d - 16.45 \quad (4.11)$$

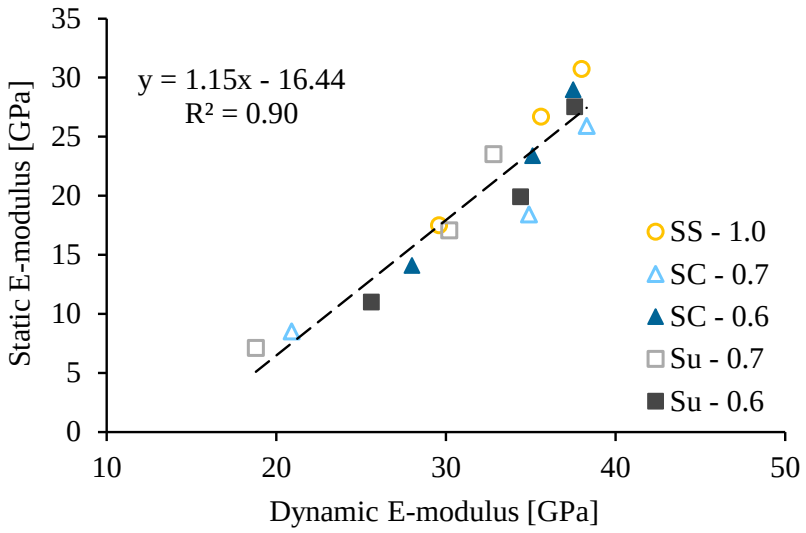

Figure 4.23: Comparison between dynamic E-modulus from ultrasonic measurements and experimentally measured static E-modulus of AASF mortar samples, up to 7 days.

4.4.5 Ultrasonic measurements versus compressive strength development

Previous studies [258, 259, 108] have reported that ultrasonic P-wave velocity and dynamic elastic modulus derived from ultrasonic measurements can be correlated with compressive strength development in OPC-based materials. The results of the correlations of the compressive strength with ultrasonic P-wave velocity and dynamic elastic modulus for the studied AASF mixes are shown in Fig. 4.24 and Fig. 4.25, respectively. An exponential function was fitted to the results. This allows continuous prediction of the compressive strength development at early ages by using ultrasonic measurements, according to the following relationships:

$$f_c = 0.27.\exp(0.001.V_p) \quad (4.12)$$

$$f_c = 0.88.\exp(0.11.E_d) \quad (4.13)$$

F_c is the compressive strength [MPa], V_p is the ultrasonic P-wave velocity, and E_d is the dynamic elastic modulus derived from P-wave velocity measurements.

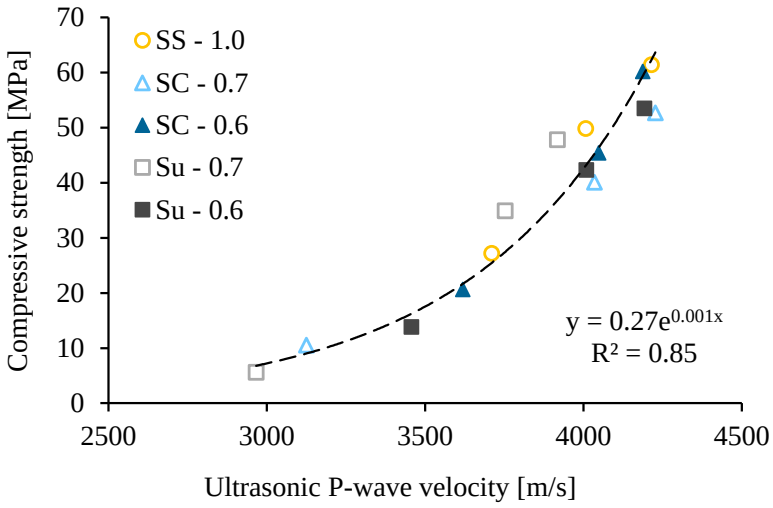

Figure 4.24: Comparison between ultrasonic measurements and compressive strength of AASF mortar samples, up to 7 days.

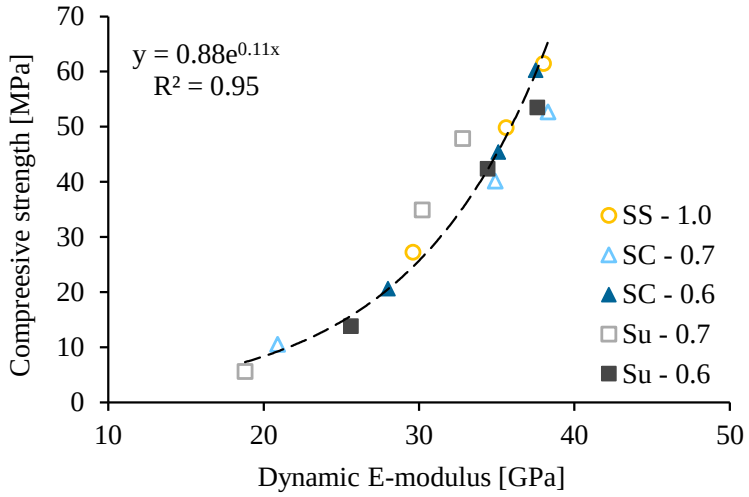

Figure 4.25: Comparison between dynamic E-modulus from ultrasonic measurements and compressive strength of AASF mortar samples, up to 7 days.

4.5 Conclusions

In this chapter, the early age reaction process of AASF cements was monitored by correlating the isothermal calorimetry heat flow curves and ultrasonic P-wave measurements. The effect of incorporating sodium carbonate and sodium sulfate on the setting and hardening behavior of sodium silicate-activated slag/fly ash cement was investigated. Based on the results presented, the following conclusions can be drawn:

- Incorporating sodium carbonate and sodium sulfate lower the rate of reaction of sodium silicate-activated samples. Increase in alkali-content or concentration (Na_2O) of the sodium carbonate and sodium sulfate solution accelerates the reaction of AASF cements.
- Samples with sodium carbonate shows better reactivity than samples with sodium sulfate at same concentration.
- Based on the evolution of ultrasonic P-wave velocity, the complex chemical reactions in studied AASF cements composed of dissolution followed by precipitation and rapid polycondensation, and densification by forming more reaction products.
- The partial substitution of sodium silicate with sodium carbonate and sodium sulfate has no significant influence on initial setting time, while the final setting time increases significantly.
- The setting in AASF cements is mainly associated to the condensation reaction between the aluminosilicate units precipitated near the particle surface.
- The ultrasonic P-wave velocity range of around 1450-1550 m/s and 1650-1750 m/s corresponds well with the initial and final setting of studied AASF, respectively.
- The strength and stiffness development of the sodium silicate-activated cements significantly decreases during the first 24 hours with incorporation of sodium carbonate and sodium sulfate solutions. However, after 3 days, the strength and stiffness development in samples with sodium carbonate and sodium sulfate strongly increases and shows comparable or even higher strength values than the sole sodium silicate-activated sample.
- Correlations between calorimetry results, ultrasonic results and strength results were also investigated. From there correlations it can be concluded that the early age compressive strength ($\leq$ 7days) and elastic modulus of AASF cements can be predicted from isothermal calorimetry heat flow curves. Moreover, an exponential relationship is proposed between the strength development and the ultrasonic P-wave velocity measurements for the studied AASF cements.

Chapter 5
Characterization of solid phases and pore structure

5.1 Introduction

This chapter gives a comprehensive description on solid phases and pore structure of the investigated AASF cement pastes. Firstly, the solid phases of AASF cements are characterized using a complementary set of analytical methods, including thermogravimetry (TG), X-ray diffraction (XRD), Attenuated Total Reflectance FTIR spectrometry, pore solution chemical composition analyzed using ICP-OES, and field emission gun electron probe micro-analyzer (FEM EPMA). The reaction degree of AASF cements, quantified using bound water content measured from thermogravimetry analysis (TGA), is compared with the isothermal calorimetry results and also with the dissolution kinetics measured from pore solution analysis, which control the reaction kinetics in cementitious materials. The strength results shown in Chapter 4 are correlated to TGA results and discussed in this chapter. Due to the fact that the reaction phases formed in AASF cements are mainly X-ray amorphous, the XRD analysis is used to identify the formation of possible crystalline phases due to the presence of carbonate and sulfate anions in the activating solutions. The FT-IR analysis is performed to investigate the gel molecular structure of the reaction products formed in the studied AASF cements. EPMA point analysis is performed to obtain the atomic ratios of the main reaction products formed in AASF. The second part examines the pore structure of AASF cements using mercury intrusion porosimetry (MIP) and nitrogen adsorption test. Finally, the main conclusions are summarized.

5.2 Thermogravimetry analysis (TGA)

Fig. 5.1 illustrates the DTG spectrum of AASF pastes at 7 days. The first peak below 275 °C in DTG curves is assigned to the loss of chemically bound water from the hydrated gel

structures, including C-A-S-H and N-A-S-H (zeolite like) type gels [260]. The second peak observed at 275 °C-400 °C is due to the decomposition of hydrotalicte [92]. The mass loss between 400 °C and 600 °C could be due to either the dehydroxylation of calcium rich C-A-S-H type phases [261] or dehydration of silica gel, condensed from the unreacted sodium silicate solution [82] or obtained from the carbonation of C-A-S-H phases in samples with sodium carbonate [262]. A very small peak observed at 600 °C-800 °C in samples with sodium carbonate could be due to formation of carbonate phases [183]. From DTG curves (Fig. 5.1), no significant change in the phase assemblage is observed in sodium silicate-activated samples with incorporation of sodium carbonate and sodium sulfate.

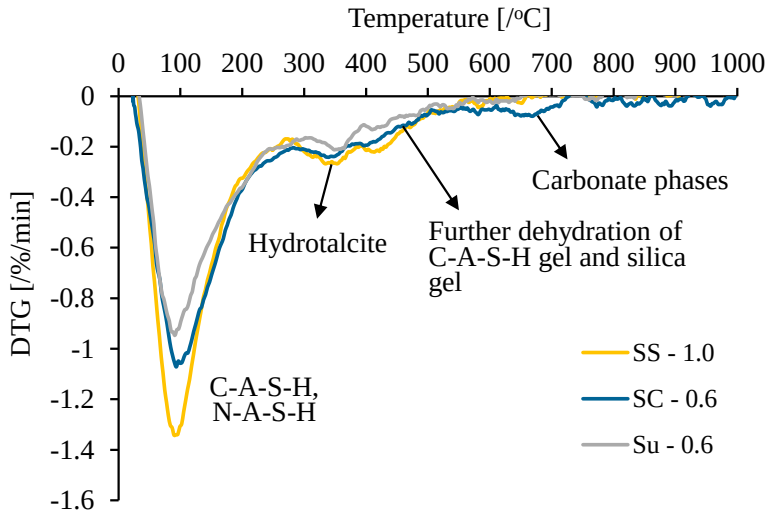

Figure 5.1: DTG curves of AASF cement pastes after curing for 7 days.

5.2.1 Bound water content

In this study, the weight loss between 30 °C-600 °C is used as a relative measure of the reaction degree for AASF cements. Fig. 5.2 shows the bound water content, derived from TGA by measuring the weight loss between 30 °C-600 °C, for AASF pastes at different curing ages. The samples activated with sodium silicate (SS-1.0) have the higher bound water content compared to the other samples, at all ages. This corresponds to the higher reactivity with sole sodium silicate activation, which is consistent with the calorimetry heat flow curves explained in Chapter 4 (Fig. 4.2). The higher bound water content in SS-1.0 can also be partly explained by the incorporation of more structural water into the reaction products due to higher amounts of alkalis (Na^+) as a charge imbalance created by the substitution of tetrahedral Al in the bridging position of silicate chain. Skibsted et al. [263] demonstrated that the samples activated with a high silica content in activator results in C-A-S-H with higher Al content in tetrahedral

bridging position, which leads to the presence of more alkalis (Na^+) in the interlayer of C-A-S-H phases and bound more water. Further study is required to support this observation.

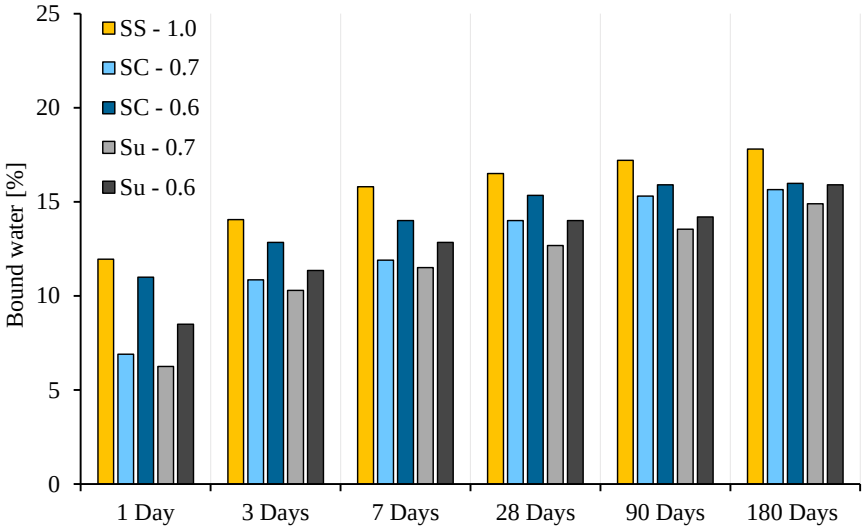

Figure 5.2: Bound water content in AASF pastes, calculated based on the weight loss between 30 °C-600 °C.

Bound water content of sodium silicate-activated samples is significantly decreased during the first 24 hours with incorporation of sodium carbonate and sodium sulfate solutions, indicating the reduction in reactivity (Fig. 5.2). This is due to the fact that incorporating sodium carbonate and sodium sulfate reduces the alkalinity (OH^- ions) of the sodium silicate activator (Table. 3.2) and consequently results in lower dissolution kinetics of slag, and thus lower reactivity. However, with increasing the concentration (Na_2O) of the sodium carbonate (SC-0.6) and sodium sulfate (Su-0.6) solutions, the bound water content increases significantly at early hours (Fig. 5.2). These results confirm that increasing alkali-content in the activating solution accelerates the reactivity, although it does not induce any changes in alkalinity (OH^- ions) of the solution (Table. 3.3). In other words, the Na^+ cations itself provided by the activating solution enhance the dissolution process and increases the reactivity of AASF cements. Nevertheless, the impact of concentration of the activator shows very limited influence on reactivity at later ages (≥28 days).

At the same concentration, samples incorporated with sodium carbonate have higher bound water content compared to the samples with sodium sulfate. This implies that sodium silicate-activated samples with incorporation of sodium carbonate have better reactivity than those with sodium sulfate due to formation of calcite which act as nucleation seeds for the precipitation

of more C-S-H type gels. This observation is consistent with isothermal calorimetry heat flow curves. Fig. 5.3 shows the relationship between the cumulative heat release and the measured bound water content from 30 °C-600 °C, until 7 days. A positive intercept value of 3.75 of the linear regression equation is attributed to the omission of heat release in the initial 30 minutes. Moreover, a correlation between the bound water content and the compressive strength until 28 days is shown in Fig. 5.4.

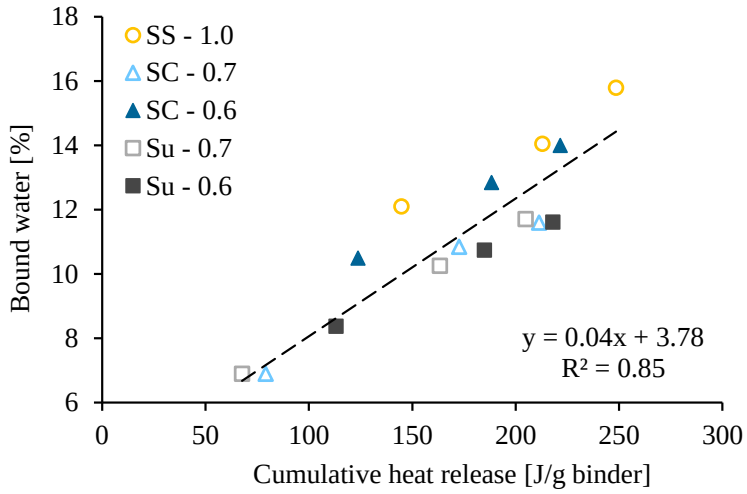

Figure 5.3: Comparison between bound water content and cumulative heat release, up to 7 days.

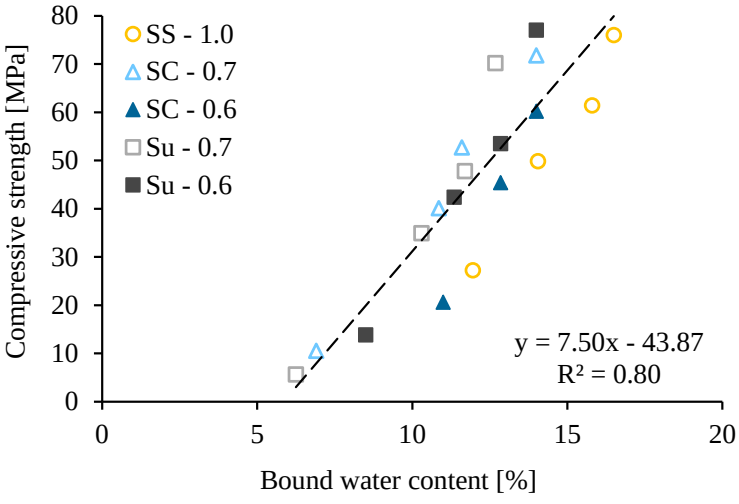

Figure 5.4: Comparison between bound water content and compressive strength, up to 28 days.

5.3 XRD analysis

The XRD diffractograms of AASF pastes activated with different activator studied in this work are shown in Fig. 5.5 to Fig. 5.7. The XRD patterns indicates that the reacted AASF pastes are highly amorphous. After 1 day of curing, a strong peak at around 2θ=29º is observed in samples activated with sodium silicate (Fig. 5.5). It is similar to the peak related to the formation of Al-substitute C-S-H type gels [264, 265, 60, 37, 88]. From XRD patterns, no change was observed in the position or d-spacing value of this C-S-H type gels with the incorporation of sodium carbonate and sodium sulfate solutions. This implies that the partial substitution of sodium silicate with sodium carbonate and sodium sulfate has limited influence on the gel structure of the main reaction product (C-A-S-H). However, the peak of this C-S-H type gel in sodium silicate activation (SS-1.0) is sharper and more intense during the first 24 hours compared to the samples with sodium carbonate and sodium sulfate. This indicates that a larger amount of C-A-S-H type gels is formed during early hours in samples activated with SS-1.0 having higher silica content. In other words, the presence of aqueous silicates contributes to the formation of more Si-Al units during early hours of reaction and subsequently forms more C-A-S-H type gels by reacting with the dissolved Ca^{2+} ions. This is supported by TGA bound water content results, which show that the samples activated with sodium silicate (SS-1.0) have higher reactivity at early ages. The decrease in the peak intensity associated to the formation of C-A-S-H type gels may partly explain the reduction in early age strength of sodium silicate-activated samples with incorporation of sodium carbonate and sodium sulfate solutions. With increase in curing time, the intensity of C-A-S-H type gel peak increases for all mixes, indicating the formation of larger amounts of C-S-H type gels. These results are consistent with calorimetry heat flow curves and TGA bound water content results, where they show that the rate of reaction increases with curing time. Similarly, the intensity of another peak at 2θ=49º that also attributed to the formation of C-A-S-H type gels [266], increases over time in all AASF samples.

In addition to the formation of non-crystalline reaction products (C-A-S-H type gels), the amorphous fraction as noticed with a board hump around 25° to 35° 2θ in XRD patterns of AASF pastes can also be strongly contributed to the glassy unreacted slag/fly ash materials (see Chapter 3, Section 3.2) and silica gel condensed from the unreacted sodium silicate activator. Regardless of the type of anions present in the activator, the peak corresponding to hydrotalcite (Mg-Al layered double hydroxide) is observed as the main secondary reaction product after 1 day in all AASF mixes, which is in agreement with previous studies [264, 92].

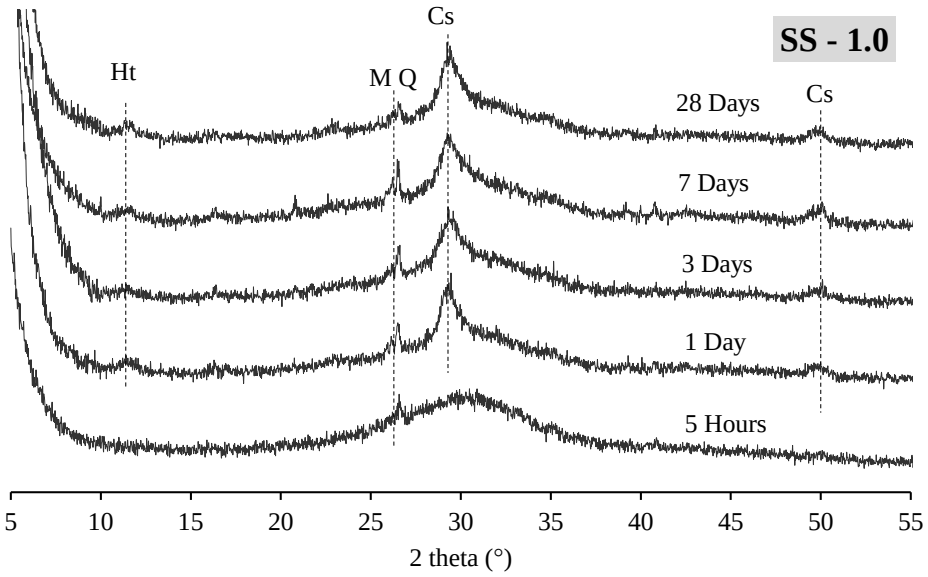

Figure 5.5: XRD patterns of AASF pastes activated with sodium silicate (SS – 1.0) at different curing ages. Key: Ht- Hydrotalcite, Cs – calcium aluminate silicate hydrate gel, M – Mullite, Q – Quartz.

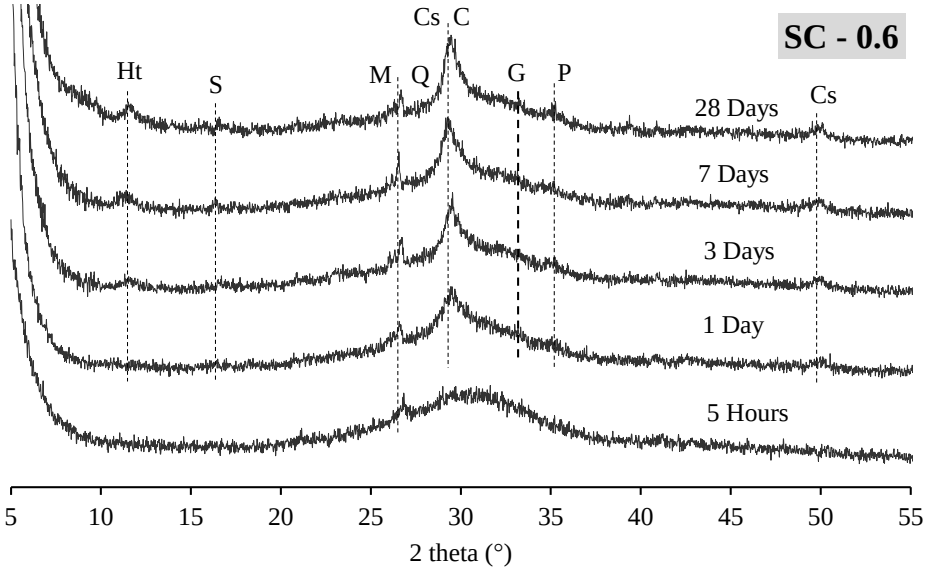

Figure 5.6: XRD patterns of AASF pastes activated with sodium carbonate (SC – 0.6) at different curing ages. Key: Ht- Hydrotalcite, Cs – calcium aluminate silicate hydrate gel, C – Calcite, S – Hydroxysodalite, G – Gaylussie, P – Pirssonite, M – Mullite, Q – Quartz.

In the samples activated with sodium carbonate (SC), the formation of carbonate phases is expected due to the presence of a high amount of CO_3^{2-} ions in the solution. This is supported by the TGA results, where a small peak in the temperature range of 600°C-800°C, associated

with the formation of carbonate phases, is observed in DTG curves (See Fig. 5.1). From XRD analysis, both calcium carbonate phase calcite and sodium-calcium carbonate phases gaylussite ($Na_2Ca(CO_3)_2$. $5H_2O$) and pirssonite ($Na_2Ca(CO_3)_2$. $2H_2O$) are identified in samples with sodium carbonate (Fig. 5.6). Previous studies [67, 64] on sodium carbonate activated slag have reported that the formation of phases like sodium aluminosilicate zeolite (NaA) are favored, as dissolved Ca^{2+} ions from slag react with CO_3^{2-} ions present in the activator to form carbonate phases. However, samples activated with hybrid sodium silicate and sodium carbonate (SC) form hydroxysodalite ($Na_8Al_6Si_6O_{24}(OH)_2(H_2O)$ rather than zeolite (NaA) (Fig. 5.6).

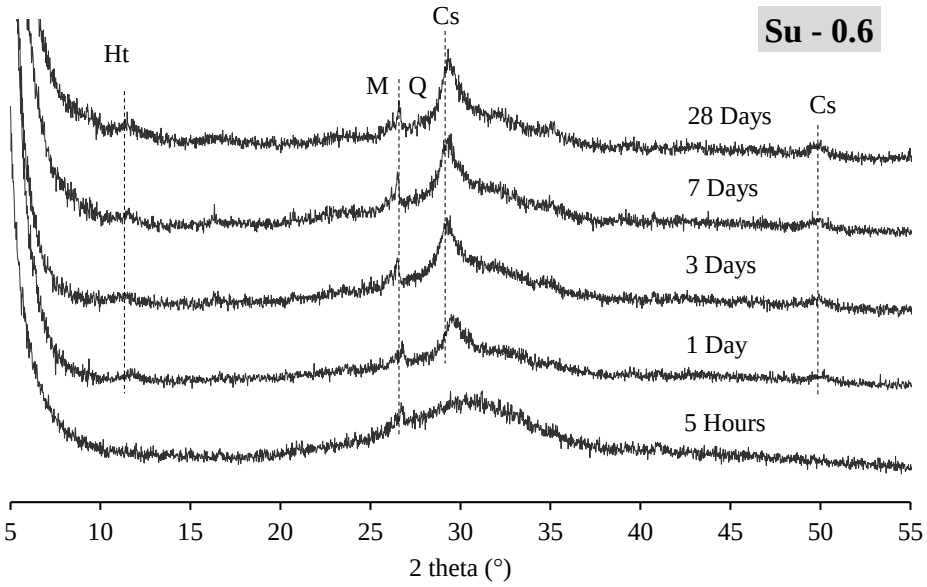

Figure 5.7: XRD patterns of AASF pastes activated with sodium carbonate (SC – 0.6) at different curing ages. Key: Ht- Hydrotalcite, Cs – calcium aluminate silicate hydrate gel, M – Mullite, Q – Quartz.

Previous studies have manifested that the presence of sulfate ions in the solution would lead to the formation of ettringite in both OPC-based systems [10] and alkali-activated systems [69, 68]. However, no diffraction peak corresponding to ettringite was found in the XRD patterns of samples with sodium sulfate (Fig. 5.7). This is most likely due to the high alkalinity of activator (pH>14.0) used in this study compared to previous studies (pH~7.0) [69, 68]. Ye et al. [132] reported that the presence of sulfate ions in alkali-activated slag cements promotes the formation of sodium calcium aluminum sulfate hydrate ((N)-C-A-S-H) rather than ettringite, because ettringite is unstable at high pH environment. However, the peaks related to the formation of a sulfate-bearing phase (N)-C-A-S-H is not observed in XRD patterns for the studied hybrid sodium silicate and sodium sulfate activating systems. Also, no other crystalline

sulfate phases are observed from XRD patterns in samples with sodium sulfate (Su). Thus, it can be concluded that no evident chemical reaction occurs between the sulfate ions provided from the activating solution and the dissolved Ca and Al ions in the pore solution to form reaction products. In other words, the XRD analysis suggests that the sulfate ions provided from the activating solution have limited contribution to the formation of crystalline reaction products. This is further supported from the pore solution chemical analysis explained in Section 5.5.

5.4 FT-IR analysis

Fig. 5.8 shows the FTIR spectra for the unreacted slag and fly-ash. The band centered at 914 cm^{-1} in slag and 1014 cm^{-1} in fly-ash is associated with the asymmetric stretching vibration mode of Si-O-T bonds (T represents the tetrahedral Si or Al units). The difference in the location of this band is consistent with the structural difference in the amorphous phases present in the individual materials. A small band at around 650 cm^{-1} is also observed in unreacted slag, which corresponds to the asymmetric stretching of tetrahedral T-O groups. An absorption band at around 745 cm^{-1} in unreacted fly-ash indicates the presence of quartz.

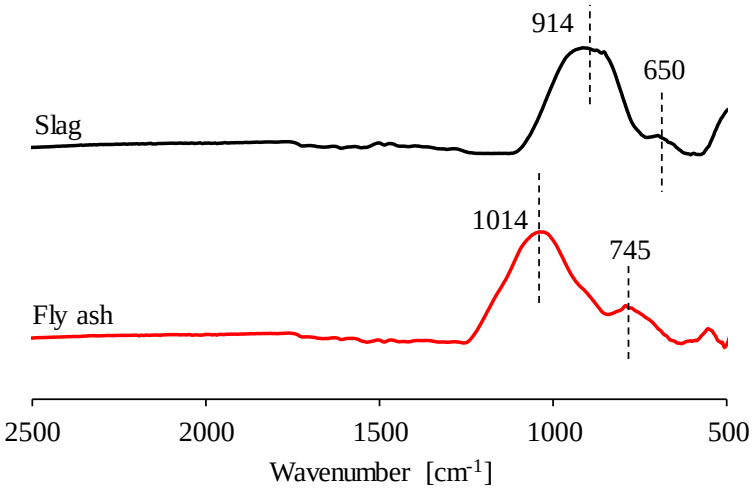

Figure 5.8: FTIR spectrum of slag and fly ash raw materials.

Fig. 5.9 shows the FTIR spectrum of the reacted AASF pastes at different curing ages. Regardless of the type and concentration of activator, all studied AASF pastes exhibit similar location bands. Two characteristic bands in the 3700-2400 cm^{-1} region and in the 1640 cm^{-1} region are assigned to the bending and stretching vibration of [OH] groups existing in various reaction products, respectively [267, 268]. These bands in AASF cements imply the presence

of hydration products with water tightly bounded to the gel structures. The small band at 1420 cm^{-1} corresponding to the asymmetric stretching of O-C-O bonds of CO_3^{2-} groups [269] is observed in samples with sodium carbonate may be due to formation of carbonate phases. This supports the DTG results and XRD results explained above.

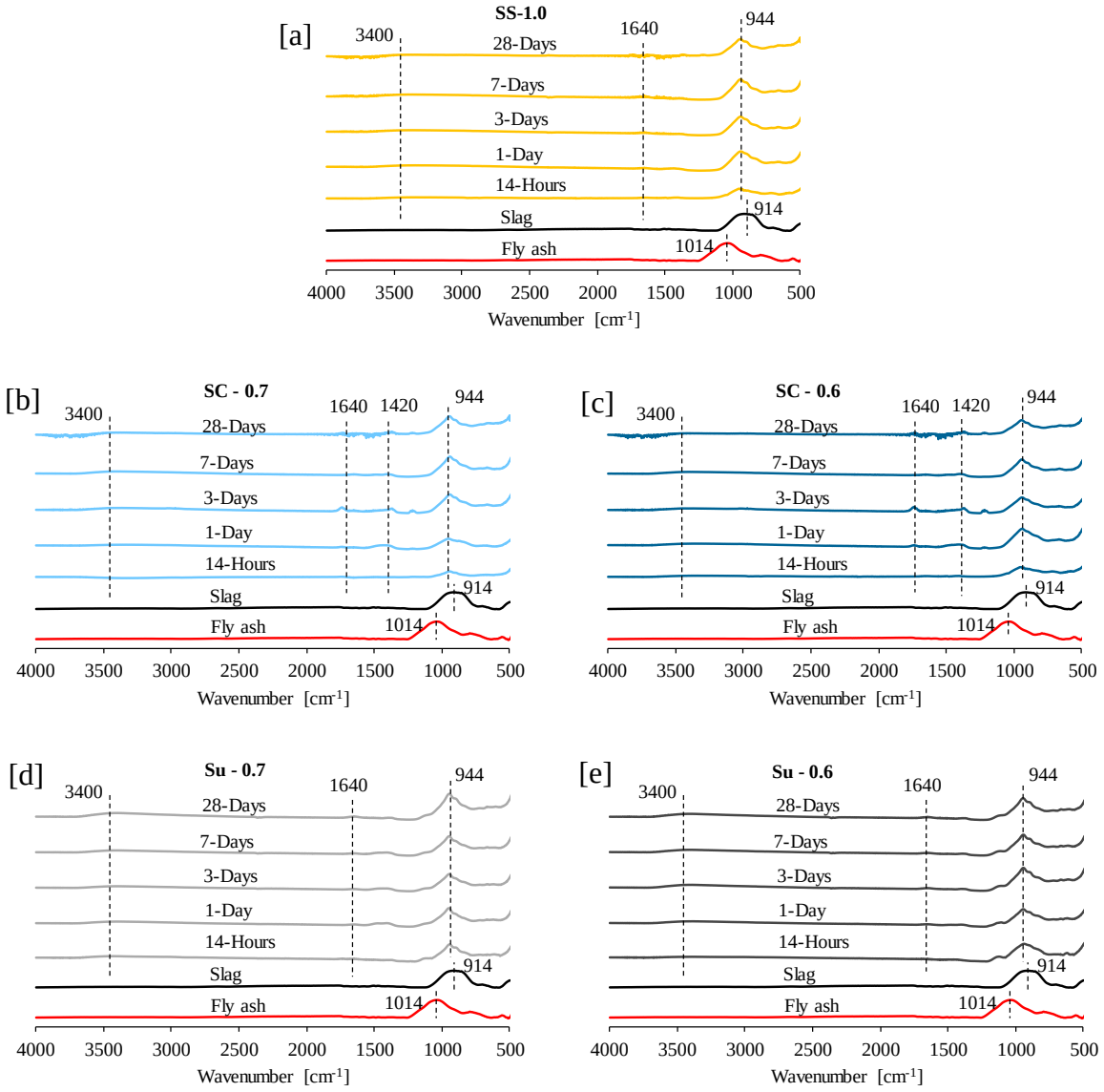

Figure 5.9: FTIR spectrum of AASF paste samples; (a) SS-1.0, (b) SC-0.7 (c) SC-0.6 (d) Su-0.7, and (e) Su-0.6.

The main band of Si-O-T bonds in slag narrows to a much sharper peak and slightly shifted to 944 cm^{-1} after alkali-activation (Fig. 5.9). It has been reported that a shift of this main band to a higher wavenumber indicates the formation of more silica poly-condensation, while a decrease in the wavenumber represents a substitution of tetrahedral Al in the reaction products [270, 46]. Therefore, the main Si-O-T band shifting to a higher wavenumber can be attributed

to the formation of new reaction products (C-A-S-H gels) with a higher degree of silica poly-condensation and increase the chain lengths of Si-O-T structure at early ages [271, 39].

As observed in Fig. 5.9, there is no significant change in the position of the main Si-O-T band with curing age, which suggests that the structure formed is relatively stable or the main reaction process (poly-condensation) may have already finished at early hours. This finding is in good agreement with the previous studies [272, 273, 274] which report that poly-condensation of reaction products C-A-S-H formed in AASF systems (with low fly ash content) is limited by its chain structure (Q^2 units). Regardless of the type and concentration of activator used in this study, the wavenumber of this main Si-O-T bonds stays almost at 944 cm^{-1}, indicating that the nature and the concentration of the activator have no significant effect on the gel structure of the main reaction products (C-A-S-H type gels).

Use of FTIR spectrum to quantify the gel structure of AASF paste is not meaningful since the intensities of the spectrum are largely affected by the used amount of powder samples that absorbs the infrared electromagnetic radiation. Nevertheless, for the sake of comparison, the peak intensity of the main Si-O-T band centered at 944 cm^{-1} is shown in Fig. 5.10.

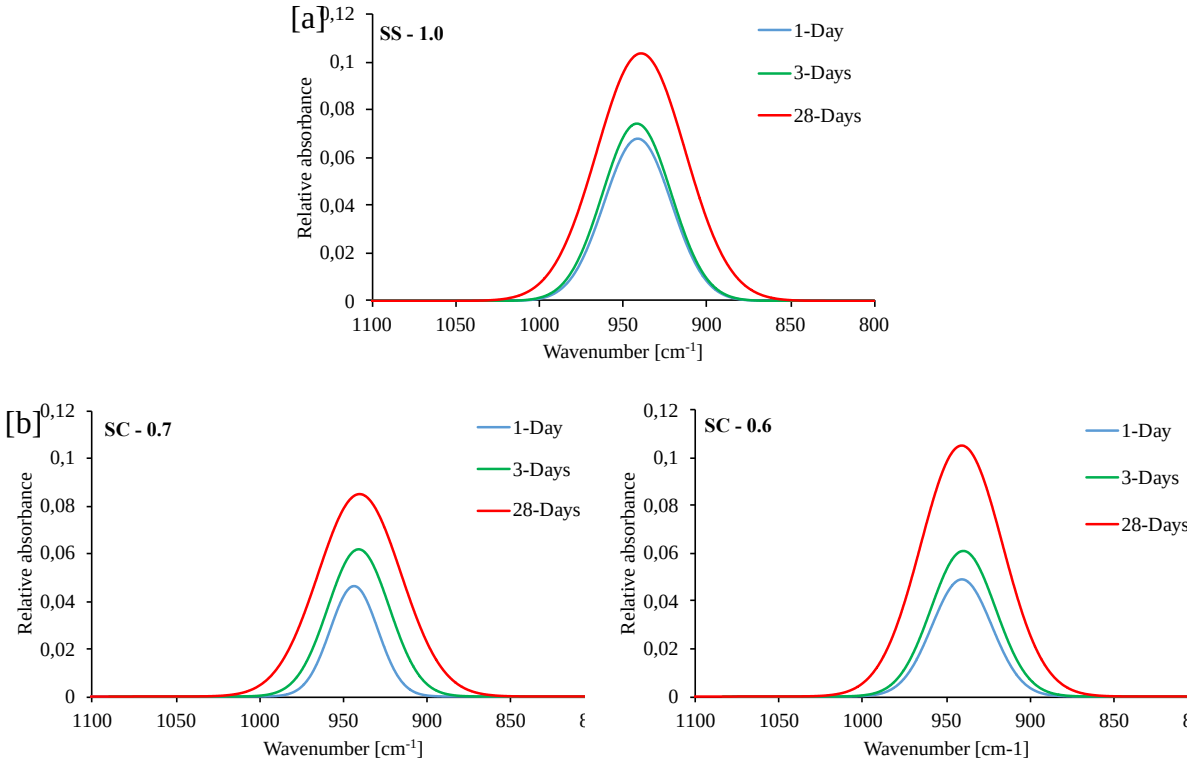

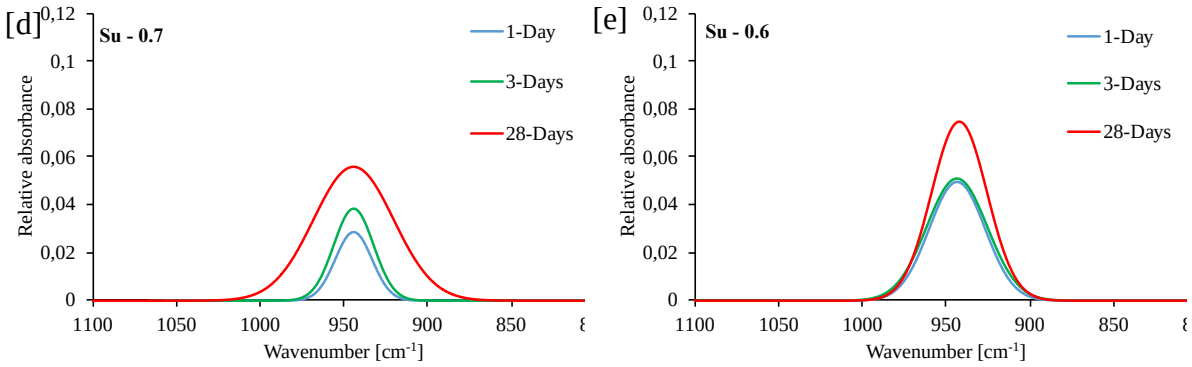

Figure 5.10: Peak intensity of main Si-O-Si (Al) band in FTIR spectrum of AASF paste samples; (a) SS-1.0, (b) SC-0.7 (c) SC-0.6 (d) Su-0.7, and (e) Su-0.6.

With increase in curing time, the intensity of the main Si-O-T band increases for all studied AASF pastes, indicating the formation of larger amounts of reaction products over time. The intensity of the main band in sodium silicate-activated samples decreased significantly with incorporation of sodium carbonate and sodium sulfate. This implies that the amount of reaction products formed in sodium silicate-activated samples decreases with the incorporation of sodium carbonate and sodium sulfate solutions. These results are in agreement with isothermal calorimetry heat flow curves and TGA bound water content results.

The band associated with Si-O-Si (Al) centered at 944 cm^{-1} indicates the formation of different gel molecular structures based on the position of silicate groups as shown in Appendix D. To obtain a better understanding of the gel structure formed in the studied AASF pastes, a detailed study on FTIR spectrum was conducted by focusing on the main Si-O-Si (Al) band region. Fig. 5.11 shows the deconvoluted FTIR spectra in the range of 800-1200 cm^{-1} using Origin software with Gaussian peak fitting as the preferred curve. Most of the peaks identified in the 800-1200 cm^{-1} region of FTIR spectra are associated to Si-O-T bonds [275, 276, 277, 273]. The small band located at 835 cm^{-1} can be related to the symmetric stretching vibration of Si-O (Q^1) bonds [278, 273]. The band at around 944 cm^{-1} is assigned to the asymmetric stretching vibration of non-bridging oxygen sites or Si-O terminal bonds (Si-O-Na type structures) [279]. The bands centered at 895 cm^{-1} and 977 cm^{-1} are derived from the asymmetric bending vibration and asymmetric stretching vibration of the Si-O-T bonds generated by Q^2 units, respectively [278, 280, 46]. These results indicate that the main reaction product in the studied AASF cements is C-A-S-H gel with more Q^2 Si-O-Si (Al) chain units. A small shoulder at 1035 cm^{-1} can be assigned to the asymmetric stretching vibration Si-O-T bonds with increased Al substitution in the silicate network (N-A-S-H type gels) [281]. This confirms the coexistence of C-A-S-H and

N-A-S-H type gels in the studied AASF pastes. Previous studies [282, 47, 48] also manifested the coexistence of C-A-S-H and N-A-S-H type gels in alkali-activated slag cements with inclusion of moderate fly ash. The broad band appearing at around 1130 cm^{-1} is related to T-O vibrations of quartz in the fly ash.

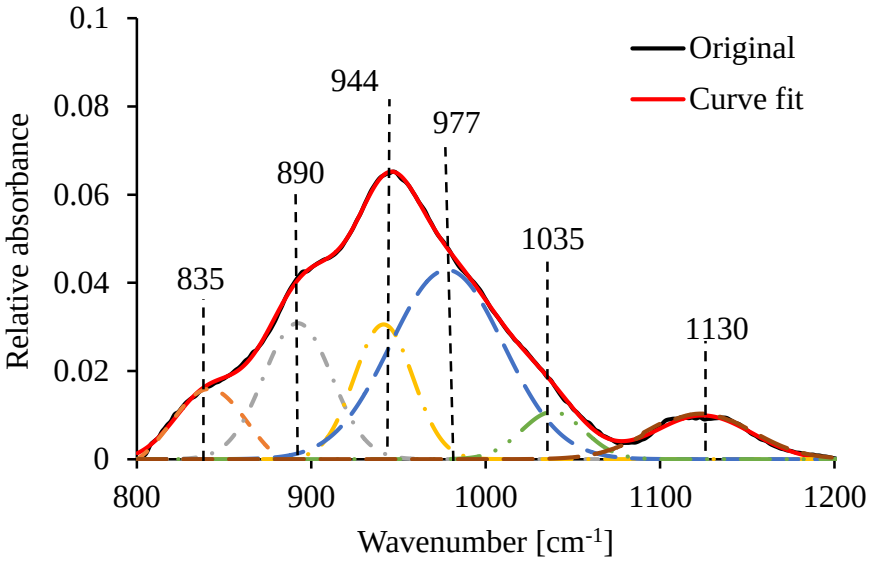

Figure 5.11: Deconvolution FTIR spectrum of SS-1.0 sample after 1 day of curing.

The peak intensity of Si-O-Si (Al) bonds in three-dimensionally structured N-A-S-H type gels, centered at 1035 cm^{-1} in FTIR spectrum, of AASF cements is shown in Fig. 5.12.

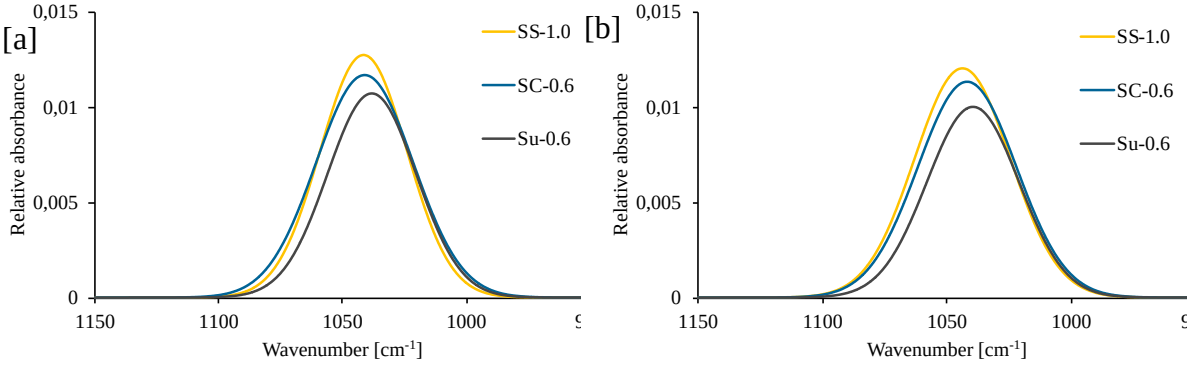

Figure 5.12: Peak of N-A-S-H type gels centered at around 1035 cm^{-1} in FTIR spectrum of AASF paste samples at; 1 day (a), and 28 days (b).

No significant change is observed in wavenumber and peak intensity of N-A-S-H type gels over time. This implies that the N-A-S-H gel structure formed during early hours is stable in studied AASF pastes, until 28 days. This results are inconsistent with Li et al. [133] who reported that the N-A-S-H gel formed in sodium silicate-activated slag cements is not stable

and gradually converts into (N,C)-A-S-H gel until a minimum Ca/Si or maximum Al/Si ratio is reached in C-A-S-H gel composition. This is most likely due to lower alkalinity of activator used in this study compared to previous studies [133]. Nevertheless, further study using ^{29}Si and ^{27}Al NMR spectroscopy is needed to confirm this observation.

5.5 Pore solution composition

The concentrations of Na, OH^-, Si, Al and Ca in the pore solution of the AASF cements up to 7 days are given in Fig. 5.13 to Fig. 5.17. The concentration of Mg in the pore solution is not presented in this study, since the values were below the detection limit of ICP-OES (less than 0.005 mmmol.L^{-1}). The low concentration of Mg in the pore solution is attributed to the formation of Mg containing phases like hydrotalcite, as observed from XRD results. The pore solution composition is mainly dominated by Na^+ and OH^- ions, and a small amount of Si, Al and Ca ions were observed. The concentration of Si, Al, and Ca is in order of Si>Al>Ca. In contrast to OPC-based materials, which have a higher Ca/(Si+Al) ratio, the AASF cements show a low Ca/(Si+Al) ratio in the pore solution and consequently this leads to the formation of reaction products with low Ca/Si ratio (see section 5.6).

Fig. 5.13 shows the concentration of Na ions in the pore solution, which were mainly sourced from the alkaline solutions (Initial values in Fig. 5.13). As observed, the initial concentration of Na ions in the pore solution decreases with curing age for all the studied AASF cements. This decrease in Na concentration is mainly attributed to intake of Na^+ cations into the calcium aluminosilicate hydrates (C-A-S-H) to compensate the charge imbalance created by substitution of Si^{4+} by Al^{+3} at tetrahedral bridging position [283, 284, 161] and formation of alkali-aluminosilicate (N-A-S-H) type gels in presence of fly ash [282, 46, 48]. The formation of N-A-S-H type gels during early ages is confirmed from the FTIR results, as explained above. The level of decrease in the Na ion concentration is higher for samples activated with only sodium silicate (SS-1.0) than those of samples with sodium carbonate and sodium sulfate (Fig. 5.13). This can be explained by the fact that samples with a high silica content in solution form longer Si-O-Si dreierketten chain units with more tetrahedral bridging sites for Si^{4+} substitution by Al^{3+}. Consequently, larger amount of sodium ions is incorporated into the gel structures to compensate the charge imbalance created by the substitution of Si^{4+} by Al^{3+} and this results into a lower concentration of Na ions in the pore solution. This is consistent with EPMA results (Section 5.6), where a higher Na/Ca and Na/Si ratio is obtained in sodium silicate (SS-1.0) compared to samples with sodium carbonate and sodium sulfate. Meanwhile, the samples

activated with SS-1.0, having a higher silica content, enhance the reactivity of fly ash during early ages [172] and form more N-A-S-H type gels, resulting in a lower concentration of Na ions in the pore solution.

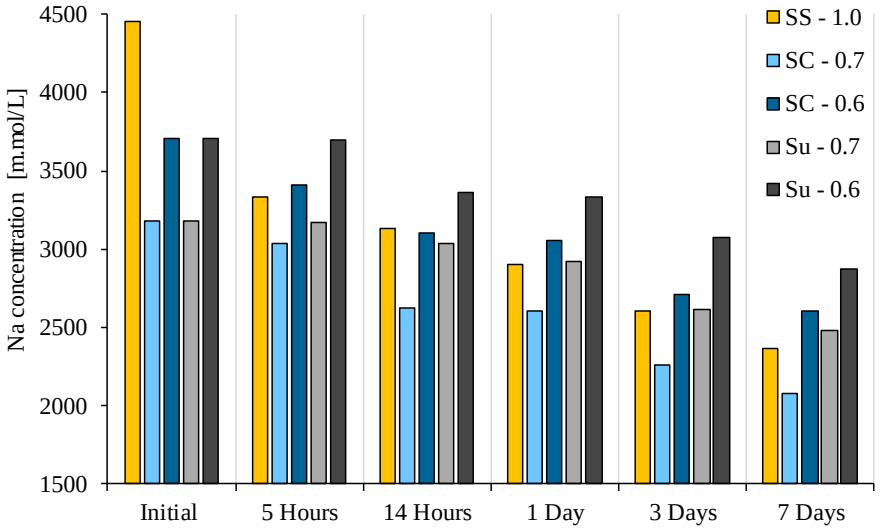

Figure 5.13: Concentration of Na ions in the pore solution of AASF cements.

By comparing the samples with sodium carbonate and sodium sulfate with same concentration or alkali-content, it can be seen that the concentration of Na ions in the pore solution decreases more significantly in samples with sodium carbonate than in samples with sodium sulfate. This is most likely due to the formation of sodium-calcium carbonate phases like gaylussite ($Na_2Ca(CO_3)_2.5H_2O$) and pirssonite ($Na_2Ca(CO_3)_2.\ 2H_2O$) and hydroxysodalite ($Na_8Al_6Si_6O_{24}(OH)_2(H_2O)_2$ by consuming Na ions in the pore solution in samples with sodium carbonate. The formation of these hydrated phases is supported from the XRD results (Fig.5.6).

The concentration of OH^- ions in the pore solution of AASF cements is shown in Fig. 5.14. Comparing the concentration of OH^- ions, it can be seen that the partial substitution of sodium silicate with sodium carbonate and sodium sulfate significantly reduces the initial concentration of OH^- ions in the sodium silicate activating solution. This is mainly attributed to the lower concentration of sodium hydroxide (OH^- ions) in the activating solutions partially substituted with sodium carbonate and sodium sulfate, as explained in Chapter 3. As can be noticed, there is a strong decrease in concentration of OH^- ions during early hours, and then a continuous gradual decrease with time for all investigated AASF cements. Previous studies reported that the reduction of OH^- ions in the pore solution is detrimental to the dissolution of slag/fly ash particles and consequently formation of reaction products [285, 214]. Therefore, the significant

decrease in concentration of OH^- ions during early hours in the studied AASF cements implies that most of the reactions occur during the initial period (<24 hours) by consuming OH^- ions in the dissolution of slag/fly ash particles. These results are consistent with calorimetry heat flow curves (Fig. 4.1), which show that the acceleration peak associated with the formation of massive reaction products occurs during the first 24 hours in all mixes.

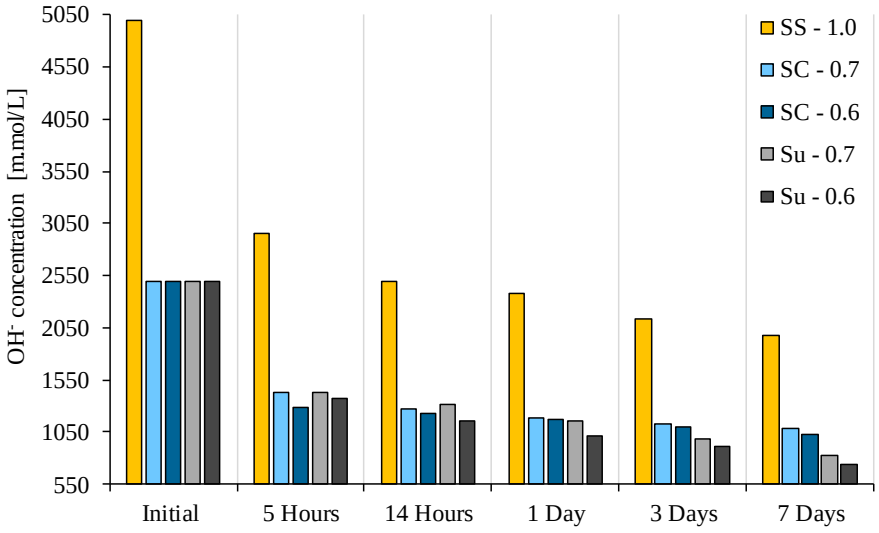

Figure 5.14: Concentration of OH^- ions in the pore solution of AASF cements.

The level of decrease in the concentration of OH^- ions is higher for samples activated with only sodium silicate (SS-1.0), implying the higher rate of reactivity compared to the samples with sodium carbonate and sodium sulfate. The concentration of OH^- ions is slightly lower in samples activated with high alkali-content (SC-0.6 and Su-0.6) (Fig. 5.14). This implies that the rate of reaction increases with increase in alkali-content or concentration of the activator, which is in agreement with the calorimetry and TGA bound water content results. Since it is evident from calorimetry results that samples with sodium carbonate show slightly higher reactivity compared to the samples with sodium sulfate with the same concentration (Na_2O), it is expected to have lower concentration of OH^- ions in samples with sodium carbonate (SC). However, the ICP-OES results show that samples with sodium carbonate have higher concentration of OH^- ions (after 14 hour of reaction) compared to the samples with sodium sulfate. Although the reason for this is not completely understood, it is currently thought that this may be related to the release of OH^- ions during the formation of carbonate salts such as calcite and gaylussite in sodium carbonated activated samples, by the chemical reaction between dissolved Ca^{2+} ions from slag and CO_3^{2-} ions from the activator [286].

The measured OH^- ions in the pore solution of all investigated samples indicates a pH value of around 13.5-14.4 from 1-7 days. Due to this higher alkalinity in the pore solution, the concentration of Ca ions remains at very low level (Fig. 5.15), since the solubility of Ca ions decreases with increase in alkalinity of the activating solution [74]. The concentration of Ca ions in the pore solution of samples activated with SS-1.0 is much lower compared to samples with sodium carbonate and sodium sulfate. This is may be due to the high alkalinity (OH^- ions) of SS-1.0, which lower the dissolution of Ca ions and/or more rapid consumption of dissolved Ca ions in the formation of reaction products.

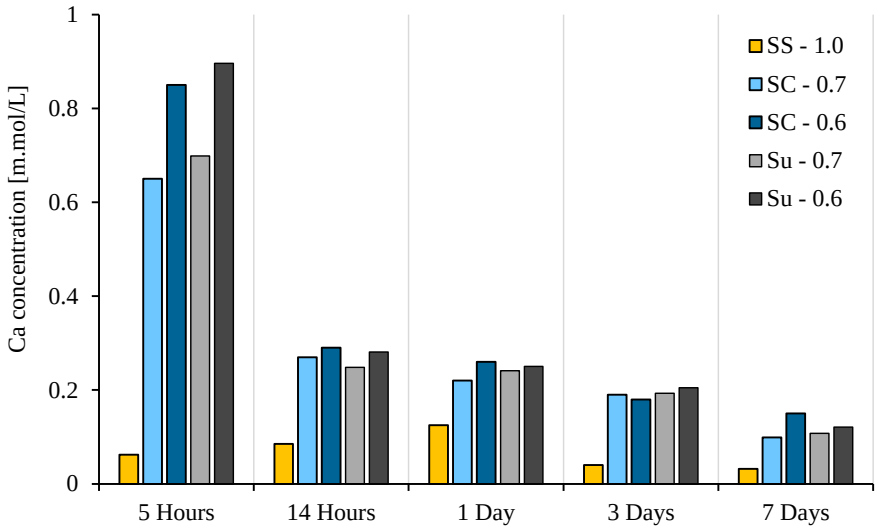

Figure 5.15: Concentration of Ca ions in the pore solution of AASF cements.

Similarly, the concentration of Si ions strongly decreases during the first 24 hours, followed by gradual decrease with time as shown in Fig. 5.16. The concentration of Si ions in the pore solution is much higher for samples activated with sodium silicate (SS-1.0) due to the presence of more soluble silicates in the activating solution. The results show that with an increase in concentration (Na_2O) of the activator, the concentration of Si ions in the pore solution decreases. The lower concentration of Si ions in the pore solution of samples activated with a high alkali-content (SC-0.6 and Su-0.6) indicates either retarded dissolution of source materials or faster precipitation of the reaction products C-A-S-H by consuming the Si ions. The latter seems to be the case here according to calorimetry and TGA results, which confirm that increase in concentration of the activator enhances the reactivity and forms more reaction products. Samples with sodium sulfate results in a lower concentration of Si ions in the pore solution compared to the samples with sodium carbonate at the same concentration (Fig. 5.16). This is probably due to lower rate of dissolution in samples with sodium sulfate.

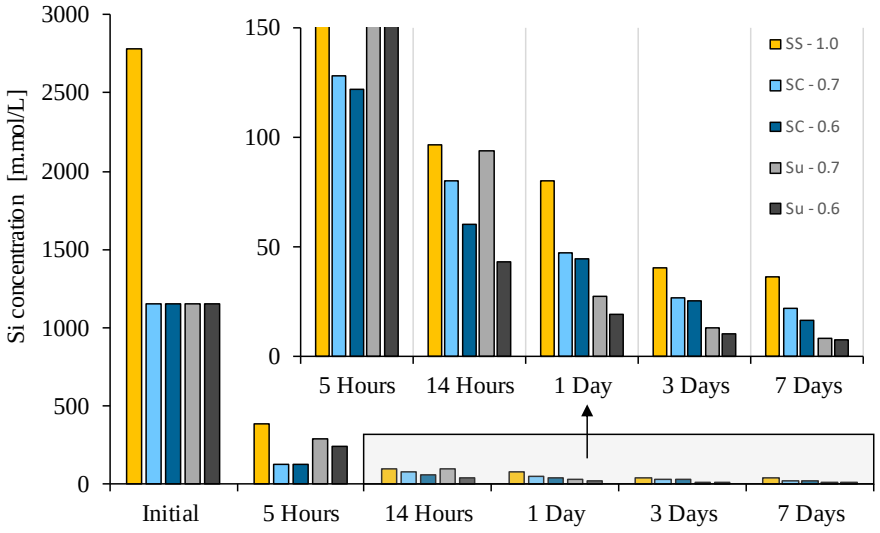

Figure 5.16: Concentration of Si in the pore solutions of AASF cements.

In samples activated with sodium silicate (SS-1.0), the concentration of Al ion in the pore solution decrease slightly with time up to 3 days and then significantly increase at 7 days. In samples with sodium carbonate (SC) and sodium sulfate (Su), the Al ions in the pore solution increased gradually over time as shown in Fig. 5.17. As expected, the concentration of Al ions in the pore solution increases with increase concentration (Na_2O) of the activator due to higher rate of dissolution.

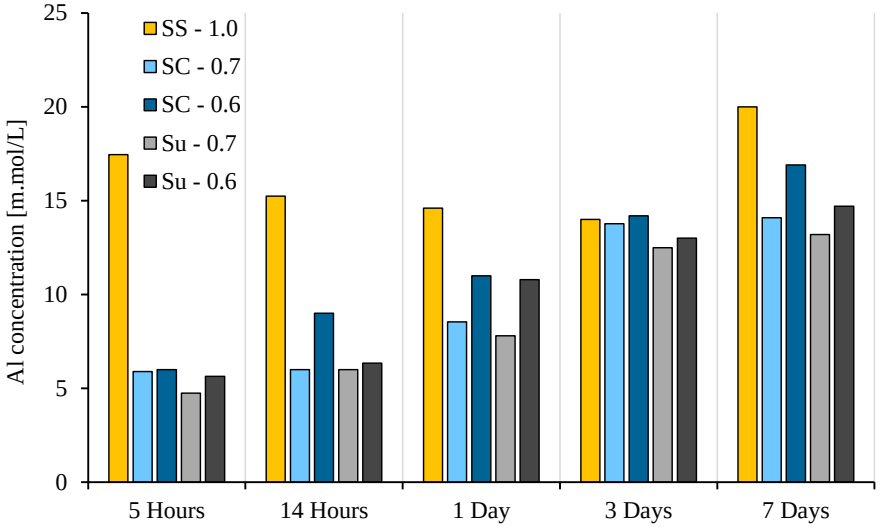

Figure 5.17: Concentration of Al in the pore solutions of AASF cements.

5.5.1 Concentration of OH^- ions versus dissolved Si, Na, Al ions

The concentration of Na, Si, and Al ions as a function of OH^- ions in the pore solution is shown in Fig. 5.18. The concentration of Na ions in the pore solution linearly decreases with the decrease in OH^- ions, regardless of the type of activator. This suggests that negatively charged hydroxide ions are well balanced with the positively charged sodium ions in the pore solution, which is consistent with the literature [214]. The concentration of Si ions decreases with the decrease in OH^- ions in the pore solution due to the formation of more reaction products by consuming Si and OH^- ions in the pore solution.

In samples activated with only sodium silicate (SS-1.0), the concentration of Al ions in the pore solution decreases with decrease in OH^- ions, up to 3 days. However, in samples with sodium carbonate and sodium sulfate, the concentration of Al ions in the pore solution increases with decrease in OH^- ions (Fig. 5.18c). This difference can be attributed to the difference in calcium aluminate silicate hydrates (C-A-S-H gels). Previous studies using ^{27}Al and ^{29}Si NMR [40, 41, 60] demonstrated that samples activated with a high silica content form C-S-H type gels with low Ca/Si ratio and intake more Al at tetrahedral bridging positions. Sampled activated with SS-1.0, having a higher silica-content, result in a C-A-S-H type gel with low Ca/Si and this could lead to an increase in aluminum presence at tetrahedral bridging positions, which leads to a decrease in the concentration of Al ions in the pore solution. This finding is supported from EPMA point explained in Section 5.6, which confirms that the samples activated with SS-1.0 have low Ca/Si and high Al/Si ratio. Nevertheless, further studies using advance techniques like NMR are required to understand the influence of this hybrid activators on the binding capacity of Al into calcium-aluminosilicate hydrates (C-A-S-H).

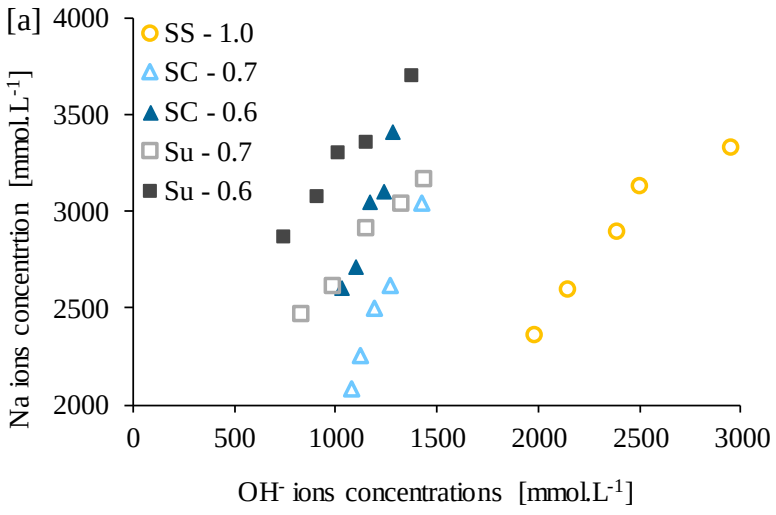

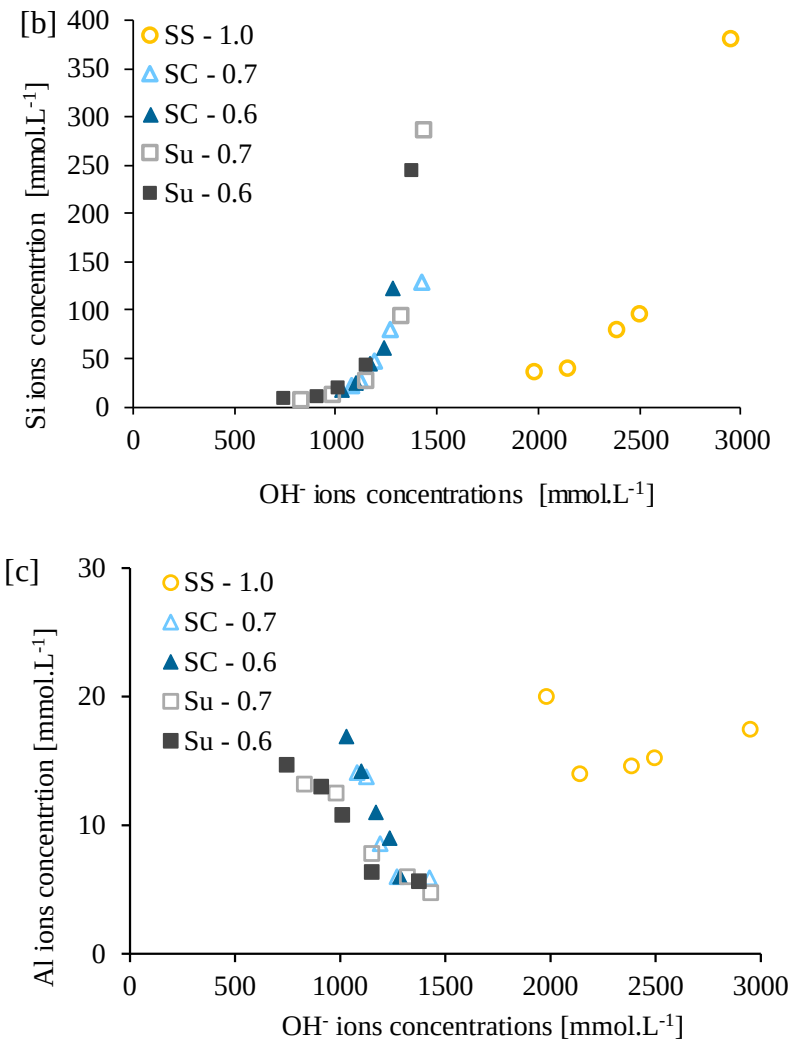

Figure 5.18: Concentration of Na, Si and Al ions as a function of OH^- ions in the pore solution.

5.5.2 Concentration of OH^- ions versus reaction kinetics

It is well-known that the concentration of OH^- ions or alkalinity of solution controls the dissolution kinetics of the slag, which effects the degree of reaction or amount of reaction products with time. For this reason, it is meaningful to compare the concentration of OH^- ions in the pore solution and reaction kinetics measured from isothermal calorimetry and TGA bound water content (Fig. 5.19-5.20). Both cumulative heat release and bound water content measured from TGA analysis linearly increase with the decrease in OH^- ions in the pore solution. These results suggest that the decrease in concentration of OH^- ions is correlated to the dissolution kinetics of slag and consequently the formation of reaction products.

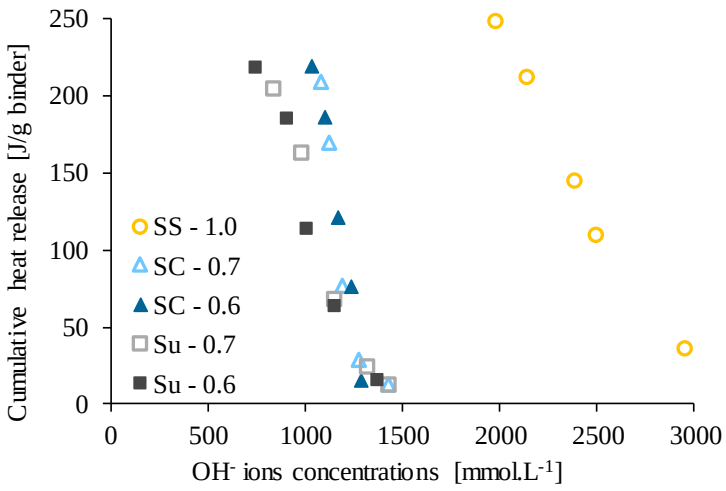

Figure 5.19: Comparison between concentration of OH^- ions in the pore solution with the cumulative heat release, up to 7 days

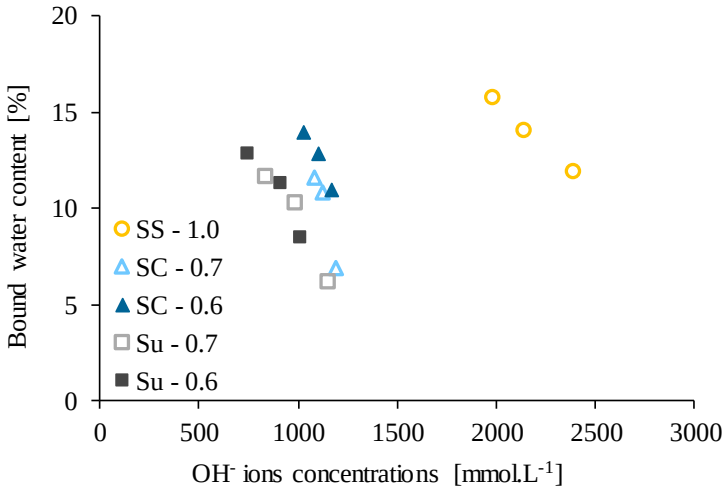

Figure 5.20: Comparison between concentration of OH^- ions in the pore solution with the bound water content, up to 7 days.

The concentration of CO_3^{2-} ions in the pore solution of samples activated with sodium carbonate (SC) at different curing ages is given in Table. 5.1. It should be noticed that the concentration of CO_3^{2-} ions in the pore solution at early hours (<24 hours) is much higher than the initial concentration in the activating solution (Table. 5.1). This is likely due to the higher rate of water molecules consumption in the reaction process than of the CO_3^{2-} ions, which leads to an increase in the concentration of the pore solution and resulted in higher CO_3^{2-} ions per liter. From XRD results, it is obvious that no clear peaks corresponding to the formation of carbonate phases are observed after 5 hours of reaction in samples with sodium carbonate (Fig. 5.6). This confirm that most of the CO_3^{2-} ions provided by the activating solution remain in the

pore solution during early hours of reaction in the studied samples with sodium carbonate (SC). However, after 1 days of curing, the concentration of CO_3^{2-} ions gradually decreases over time (Table. 5.1) due to the formation of carbonate phases by reacting with the dissolved Ca^{2+} ions. This is in agreement with XRD and DTG curves, which show the formation of carbonate phases after 1 day of reaction. In other words, the formation of carbonate phase is favored with time when the concentration of dissolved Ca^{2+} ions increase and reacts with the CO_3^{2-} ions in the pore solution.

Table 5.1: Concentration of CO_3^{2-} ions in the pore solutions of AASF cements, in mmol.L^{-1}.

Mix	Initial	5 hours	14 hours	1 Day	3 Days	7 Days
SC – 0.7	600	645	905	635	415	325
SC – 0.6	900	935	1055	860	585	565

Table 5.2: Concentration of S ions in the pore solutions of AASF cements, in mmol.L^{-1}.

Mix	Initial	5 hours	14 hours	1 Day	3 Days	7 Days
SC – 0.7	600	740	785	880	1075	1334
SC – 0.6	900	1085	1195	1375	1655	1775

Similarly, the concentration of sulfur (S) in the extracted pore solutions is higher than the initial content in the alkali-solutions (Table. 5.2). The raw materials slag and fly ash contains around 1.53% and 0.83% of sulfur, respectively (see Chapter 3, Table. 3.1). Even if this S in the raw materials is completely dissolved into the solutions, the concentration of S ions in the pore solutions should be much lower than the measured values at early ages (740-1775 mmol.L^{-1}). The much higher concentration of S in the pore solution is also attributed to the decrease in volume of solution or water molecules and increase in the concentration of the solution, i.e. S ions per liter. It is apparent from XRD results that the no crystalline sulfate phases are formed in samples with sodium sulfate. The pore solution data, together with XRD results confirm that sulfate ions provided from the activating solution have limited contribution to the formation of reaction products and mostly remain as free sulfate ions in the pore solution.

5.6 Microchemistry of the reaction products

The wavelength dispersion spectroscopy (WDS) microanalysis of AASF pastes, presented in Table. 5.3, shows that the nature of anion present in the activator have significant influence on

the chemical composition of the reaction products. The FTIR results confirm that the investigated AASF pastes exhibit both C-A-S-H and N-A-S-H type gels as main reaction products, as suggested by other studies [46, 133]. However, it is very difficult to identify these two gels independently in EPMA analysis. On the other hand, some studies [101, 46] have reported that both C-A-S-H and N-A-S-H type gels do not remain independent on the length scale probed by SEM/EDX, but intermixed towards the formation of hybrid phase (N,C)-A-S-H gel. Therefore, it is assumed that the atomic ratios presented in Table. 5.3 are assigned to the hybrid binding phases (N,C)-A-S-H.

Table 5.3: Atomic ratios in the reaction products of AASF pastes by EPMA point analysis.

Mix	No. of point analysis	**Ca/Si**	**Al/Si**	**Mg/Si**	**Na/Si**	**Na/Ca**
SS - 1.0_7D	19	0.62	0.27	0.29	0.68	1.35
		(±0.009)	(±0.006)	(±0.018)	(±0.017)	(±0.15)
SS - 1.0_28D	20	0.70	0.35	0.22	0.45	1.70
		(±0.012)	(±0.013)	(±0.009)	(±0.017)	(±0.13)
SC – 0.6_7D	26	0.84	0.24	0.20	0.01	0.01
		(±0.01)	(±0.002)	(±0.021)	(±0.000)	(±0.000)
SC – 0.6_28D	20	0.95	0.27	0.15	0.02	0.05
		(±0.03)	(±0.006)	(±0.004)	(±0.000)	(±0.000)
Su – 0.6_7D	23	0.88	0.23	0.23	0.02	0.02
		(±0.02)	(±0.003)	(±0.013)	(±0.000)	(±0.000)
Su – 0.6_28D	21	1.00	0.26	0.17	0.03	0.04
		(±0.06)	(±0.002)	(±0.015)	(±0.000)	(±0.000)

The Ca/Si ratio in (N,C)-A-S-H gel of sodium silicate activated samples (SS-1.0) at 7 days is 0.62 and it increases to 0.7 at 28 days. Similar Ca/Si atomic ratios were reported in previous studies on sodium silicate activated slag systems [92, 53]. With incorporation of sodium carbonate and sodium sulfate, the Ca/Si ratio of sodium silicate activated samples increases at a given curing time. This increase in Ca/Si ratio can reflect the relative high concentration of Ca ions and/or low concentration of Si ions in the pore solution. The pore solution data in Section 5.5 have demonstrated that increase in alkalinity or OH^- ions in the pore solution increases the dissolution of Si and Al and decreases the Ca solubility. In this respect, the samples activated with only sodium silicate (SS-1.0), having a higher concentration of OH^- ions, results in a lower dissolution of Ca ions into the pore solution compared to the samples with sodium carbonate and sodium sulfate. Moreover, it is known that samples activated with SS-1.0 have more aqueous silicate that contributes to the formation of (N,C)-A-S-H gel with a high silica polymerization structure. This explains the low Ca/Si atomic ratio in the samples activated with SS-1.0. It is also observed that the Ca/Si ratio increases over time, regardless of the activator type. This implies that the dissolution of slag increases over time, up to 28 days, in all studied AASF samples.

In samples activated with sodium silicate (SS-1.0), it observed that the Al/Si ratio of (N,C)-A-S-H gel increases from 0.27 to 0.34 with increasing curing time from 7 days to 28 days. The reason for this is that more Al will be incorporated into (N,C)-A-S-H with low Ca/Si ratio (as bridging tetrahedral) over time, as reported in thermodynamic studies on alkali-activated slag systems [287, 91]. This finding is also supported from pore solution results, where the concentration of Al ions in the pore solution decreases over time for samples activated with only sodium silicate (SS-1.0) (Fig. 5.17). Also, it should be noticed that the Al/Si ratio in SS-1.0 is around 0.35 at 28 days, which is significantly high for either a pure chain structure C-A-S-H (Al/Si < 0.2) [67] or considerable degree of crosslinking C-A-S-H structure ($0.19 \leq$ Al/Si ≤ 0.26) [288]. This is probably due to the intermixing of hydrotalcite ($Mg_6Al_2(OH)_{16}CO_3\ 4H_2O$) with C-A-S-H gel, as hydrotalcite with net positive charge acts as a charge-balancing of C-A-S-H gel having a net negative charge [289]. The results of the Mg/Si ratio suggest that some reaction products consisting Mg, such as hydrotalcite are intermixed with the C-A-S-H gel [92, 53]. However, in samples with sodium carbonate (SC) and sodium sulfate (Su), no significant change in Al/Si ratio is observed with change in curing time. The measured Al/Si ratios (0.24-0.27) in samples with sodium carbonate and sodium sulfate are consistent with results which have previously been reported in the literature [282, 37].

Samples activated with SS-1.0 have a high Na/Si and Na/Ca ratio at a given curing time compared to ratios in samples with sodium carbonate and sodium sulfate (Table. 5.3). It is generally known that sodium is incorporated into the structure of reaction products (C-A-S-H gel) to compensate the charge imbalance created by substitution of Si^{4+} by Al^{+3} at the tetrahedral bridging position [161]. Our results imply that the degree of Al substitution for Si is enhanced with increase in the silica content (SS-1.0). This is also supported by the fact that samples activated with higher silica content have a longer Si-O-Si chain with more tetrahedral bridging sites for Si^{4+} substitution by Al^{3+}. Thus, higher amounts of sodium are present in reaction products of samples activated with a high silicate content (SS-1.0). This is further supported from the pore solution results in Fig. 5.13, where the concentration of Na ions in the pore solution significantly decreases over time in the samples activated with SS-1.0. Additionally, the essential distribution of sodium along with silica, from the original sodium silicate alkaline solution, in the reaction products may also be responsible for higher sodium contents in sodium silicate sample.

5.7 Pore structure

Besides the solid phases discussed above, the pore structure is another important factor that can strongly influence the mechanical strength and stiffness development of the AASF cements. Additionally, it has been reported that the pore size distribution is a key parameter that determines the potential of autogenous shrinkage in cement-based materials and also in alkali-activated cements. Thus, investigating the pore structure is essential to understand the mechanical properties and the autogenous shrinkage behavior in the studied AASF cements.

In this study, two experimental techniques including Mercury Intrusion Porosimetry (MIP) and Nitrogen absorption test were used to characterize the pore structure in the studied AASF cements. The MIP test method was used to determine the pores in the range of 6 nm to 100 µm. While the N_2 absorption test was performed to characterize the pores in the range of 1.4 nm to 30 nm, which gives more detail information about the gel pores in studied AASF cements. Combining these two techniques helps to understand the pore size distribution ranging from 1.4 nm to 100 µm.

Due to the formation of much denser microstructure (very fine pores), it has been suggested that the N_2 absorption method is more efficient for studying the pore structure in alkali-activated slag cements. Moreover, the N_2 absorption method is less destructive for the pore

structure characterization of silica-rich or N-A-S-H type gels. Therefore, it is essential to have information on the pore structure measured from both MIP and N_2 absorption tests.

5.7.1 Mercury Intrusion Porosimetry (MIP)

The pore size distribution and differential pore size distribution curves of the studied AASF pastes at different curing ages are shown in Fig. 5.21. Generally, for OPC-based materials, two main peaks at around 10-0.1 µm and 0.5-0.01 µm are observed in the differential curves, corresponding to the formation of capillary pores and gel pores, respectively [290]. In contrast to OPC-based materials, the differential curves of the investigated AASF pastes show only one main peak with higher amplitude in the range of 0.005-0.06 µm. These findings indicate that the studied AASF cements have higher amount of mesopores compared to OPC-based materials, which is in agreement with previous studies [166]. With increasing curing ages, from 3 days to 7 days, the pore volume curves of the studied AASF cements shift towards a smaller diameter, indicating the formation of a denser microstructure over time.

The pore size proportions, derived from the MIP device, are given in Table. 5.4. The studied AASF pastes show a mesopore volume of around 81.20-85.10% of the total volume at 3 days which slightly increases to 83.0-85.50% at 7 days. This implies that most of the reaction in AASF pastes occurs at early ages (≤3 days) and results in a denser matrix with refined pore structure. From Fig. 5.21 and Table. 5.4, it can be clearly seen that the mesopore volume and total pore volume are noticeably reduced at 28 days for all investigated AASF samples. This can be attributed to the formation of a much denser matrix with pore sizes that are beyond the detecting range of the mercury intrusion method (< 6nm).

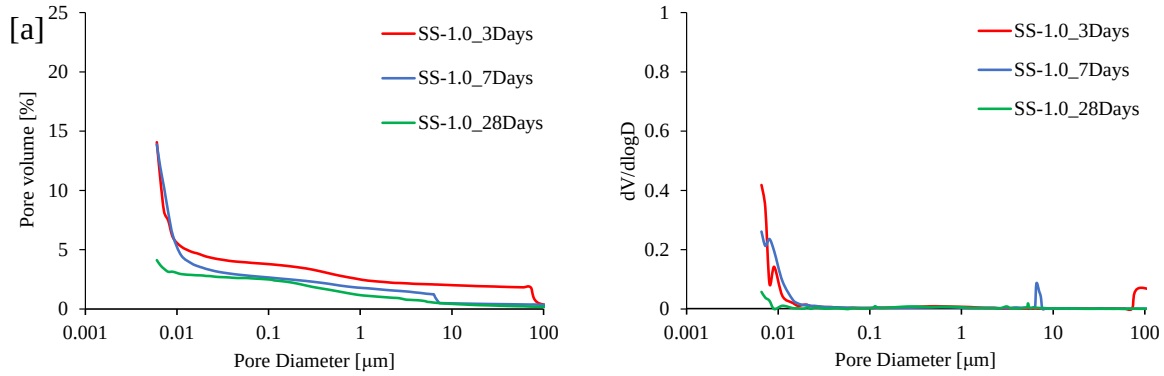

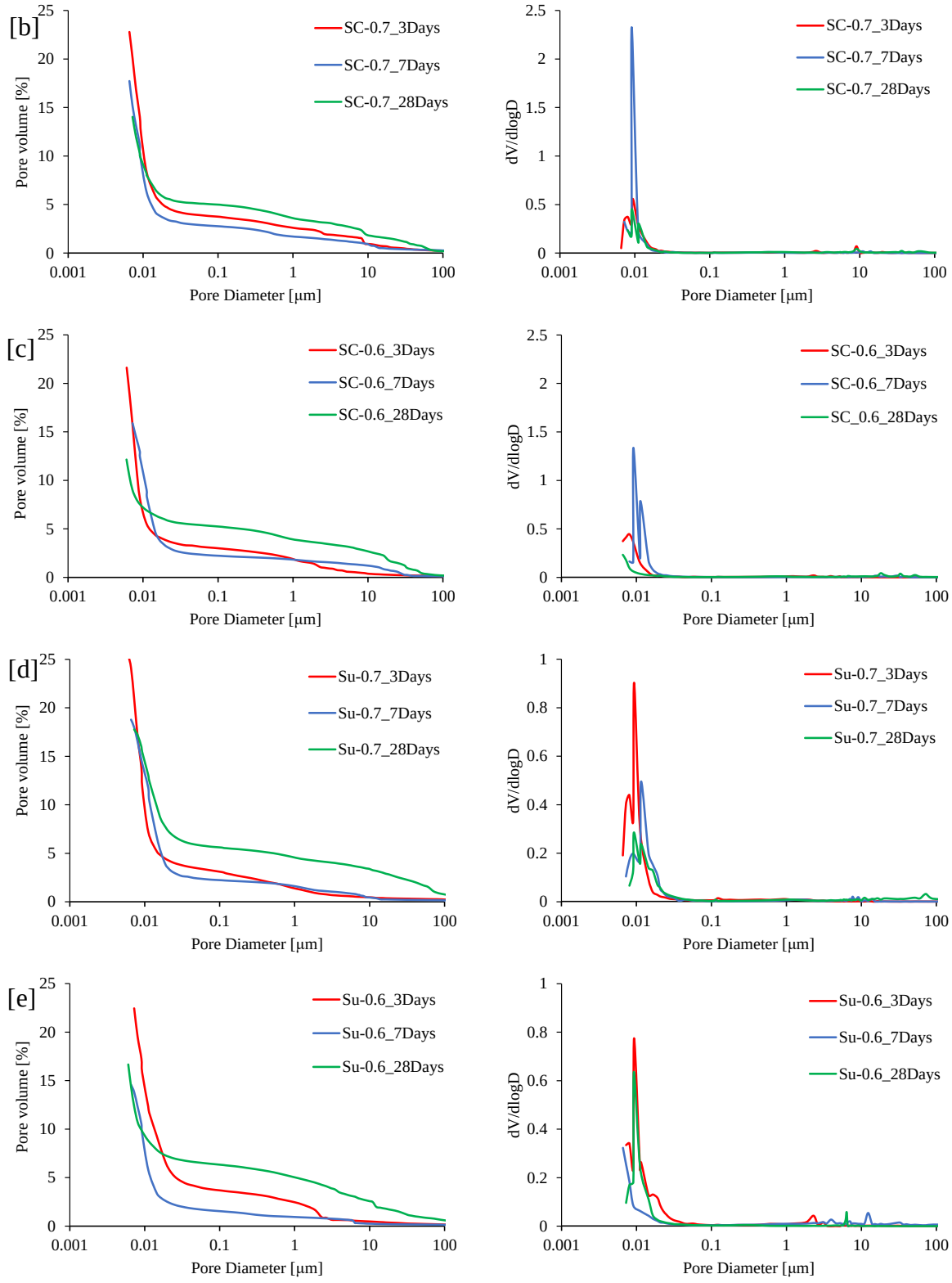

Figure 5.21: Pore size distribution of AASF paste samples activated with: (a) SS-1.0, (b) SC-0.7 (c) SC-0.6 (d) Su-0.7, and (e) Su-0.6, derived from MIP test.

Table 5.4: Pore size proportions for AASF pastes at 3, 7, and 28 days, derived from MIP.

Mix ID	Mesopore volume/Total volume [%]			Total Pore volume [%]		
	[<50 nm]			**[100µm-6nm]**		
	3 Days	7 Days	28 Days	3 Days	7 Days	28 Days
SS-1.0	84.35	84.80	47.20	14.0	13.15	3.53
SC-0.7	81.60	83.60	63.75	23.15	17.75	14.50
SC-0.6	85.15	85.40	55.55	21.60	15.90	12.15
Su-0.7	81.20	83.05	69.50	25.45	18.70	17.20
Su-0.6	82.40	83.75	60.90	22.45	16.60	14.00

The MIP test results reveal that the partial substitution of sodium silicate with sodium carbonate and sodium sulfate slightly reduces the mesopore volume at a given curing age. This is explained with the decreased reactivity in sodium silicate-activated samples when sodium carbonate and sodium sulfate are incorporated. It is interesting to notice that sample activated with SC-0.6 have a higher mesopore volume, although its reactivity is lower than with sodium silicate activation (SS-1.0). This finer pore structure in the SC-0.6 samples may be attributed to the formation of a hydroxysodalite phase, which is a microporous and mesoporous crystalline zeolite [291]. Also, the results show that the mesopore volume increases with increase in concentration of incorporated sodium carbonate and sodium sulfate solution. This confirms that the activator with higher concentration (Na_2O) is beneficial for a higher reactivity and densification of the microstructure.

By comparing the total pore volume given in Table. 5.4, it can be seen that the incorporation of sodium carbonate and sodium sulfate coarser the pore structure of sodium silicate-activated samples. The difference in total porosity between samples activated with only sodium silicate and samples with sodium carbonate and sodium sulfate is more significant at 3 days. However, at 7 days, this difference is substantial reduced. These results imply that the incorporation of sodium carbonate and sodium sulfate significantly decreases the rate of reactivity at early ages, but strongly accelerates the reaction at later ages and densifies the microstructure. These results are in agreement with TGA bound water content results explained in section 5.1 (Fig. 5.2). The total pore volume decreases with increasing curing age, indicating the formation of a denser microstructure.

5.7.2 Nitrogen absorption test

N_2 absorption test is further used to determine the pores that are beyond the detection limit of the mercury intrusion method (< 6nm). The pore sizes in between 1.4 nm to 30 nm are detected using N_2 absorption method. Fig. 5.22 shows the N_2 absorption isotherms of the studied AASF paste samples.

According to the International Union of Pure and Applied Chemistry Systems [292, 290], the shape of N_2 absorption isotherms shows type V classification, indicating that the studied AASF cements are highly micro-mesoporous materials. The results show that the isotherms of sodium silicate-activated samples change, implying the pore structure modification, with incorporation of sodium carbonate and sodium sulfate solutions (Fig. 5.22). The quantity of absorbed N_2, corresponding to the volume of gel pores, increases with increasing curing age for all the AASF samples. This confirms that the pore structure of AASF pastes becomes finer over time. Comparing the quantities of absorbed N_2 indicates that the samples activated with a higher concentration of sodium carbonate and sodium sulfate (SC-0.6 & Su-0.6) have higher gel pore volumes compared to the samples activated with SC-0.7 & Su-0.7. This result is expected, since the increase in concentration of the activator increases the reactivity and consequently the formation of more reaction products, causing an increase in gel pores in the matrix. Similarly, at the same concentration (Na_2O), samples with sodium carbonate show a higher gel porosity compared to the samples with sodium sulfate. The isothermal calorimetry and TGA results manifested that samples activated with only sodium silicate (SS-1.0) have higher reactivity and are expected to show a higher volume of gel pores. However, the samples activated with only sodium silicate (SS-1.0) show a lower gel porosity at given age compared to the samples with sodium carbonate and sodium sulfate. Although the reason for this is not clear, it is assumed that C-A-S-H gel formed in SS-1.0 activation has much denser atomic structure and creates low accessibility to the nitrogen molecules for assessing the gel pores in the system. Previous studies have reported that an increase in silica content of the activator leads to form more densely packed and more polymerized C-A-S-H gels [60, 39]. Nevertheless, further studies using ^{29}Si NMR are required to confirm this explanation. Moreover, the low quantity of N_2 absorption in SS-1.0 may also be partly attributed to the closing/collapse of some gel pores by higher capillary tension stress (see Chapter 6), resulting in N_2-inaccesible regions.

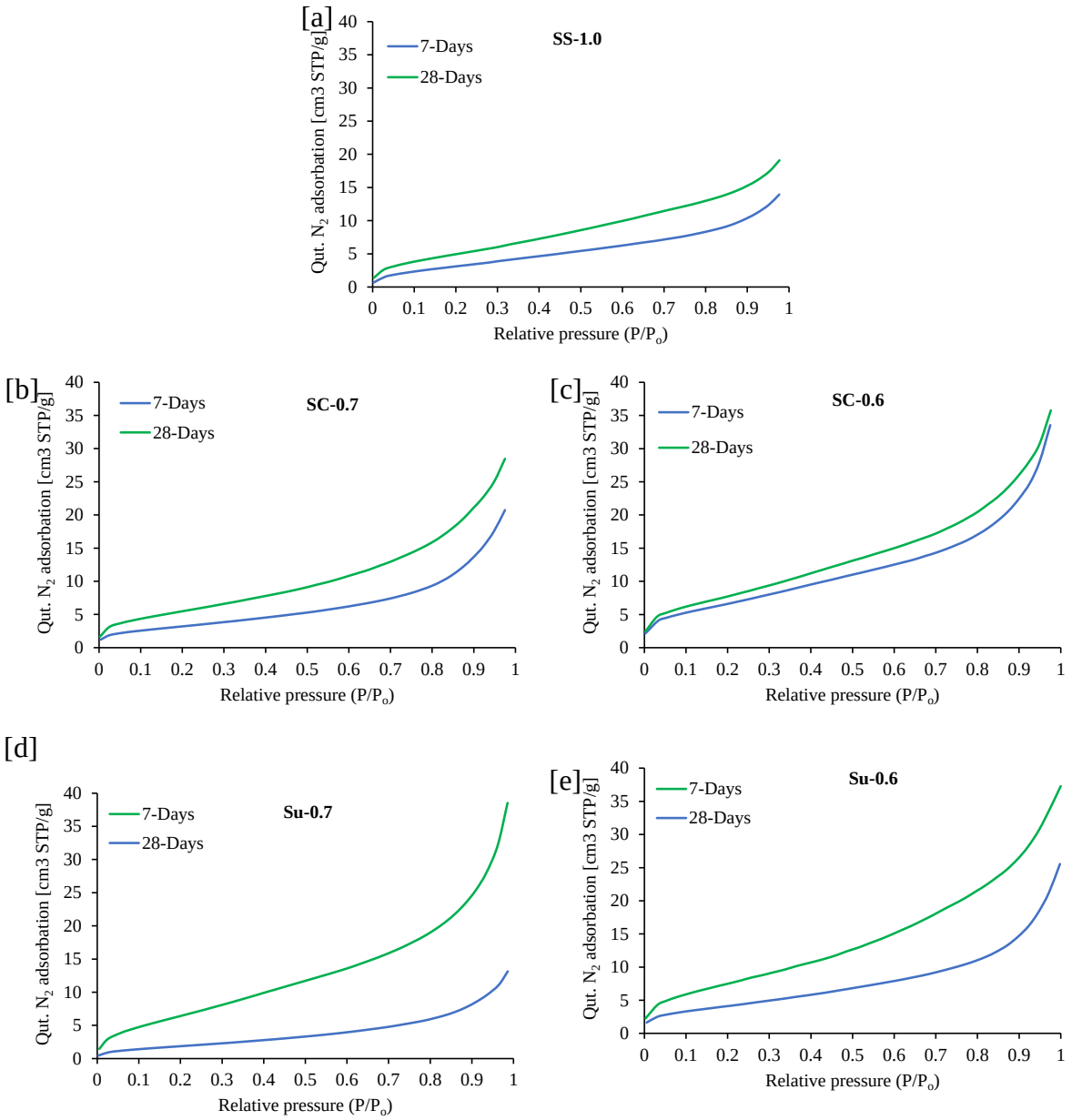

Figure 5.22: N_2 absorption isotherms of the AASF pastes activated with: (a) SS-1.0, (b) SC-0.7 (c) SC-0.6 (d) Su-0.7, and (e) Su-0.6, derived from N_2 adsorption test.

Fig. 5.23 shows the differential pore size distribution curves of the studied AASF cements at 7 days and 28 days. A large volume of pores is observed within the range of 1.4 nm to 6 nm, corresponding to the gel pores of C-A-S-H [293]. Also, very small peaks at the pore diameters between 5 nm and 15 nm are observed for all studied AASF samples. A large volume of gel pores in the samples activated with SC-0.6 and Su-0.6 confirms that the reactivity of AASF samples is enhanced with increase in concentration of the activator.

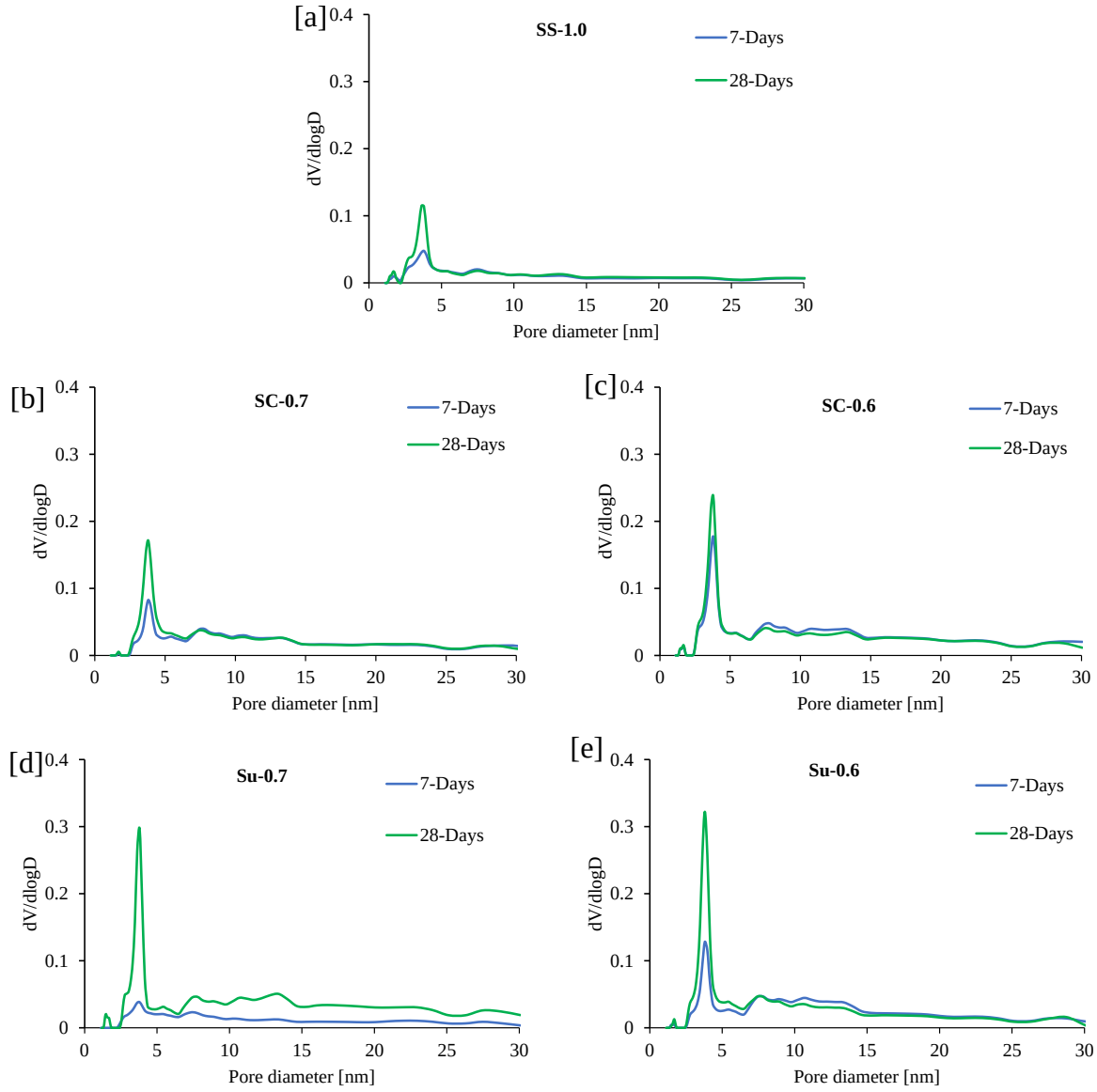

Figure 5.23: Pore size distribution of AASF pastes activated with: (a) SS-1.0, (b) SC-0.7 (c) SC-0.6 (d) Su-0.7, and (e) Su-0.6, derived from N_2 adsorption test.

Fig. 5.24 illustrates the relationship between the total pore volume, obtained from MIP results, and the compressive strength and static E-modulus of AASF samples at 7 days. The figure shows that both the compressive strength and static E-modulus of AASF samples increase linearly with a decrease in total pore volume.

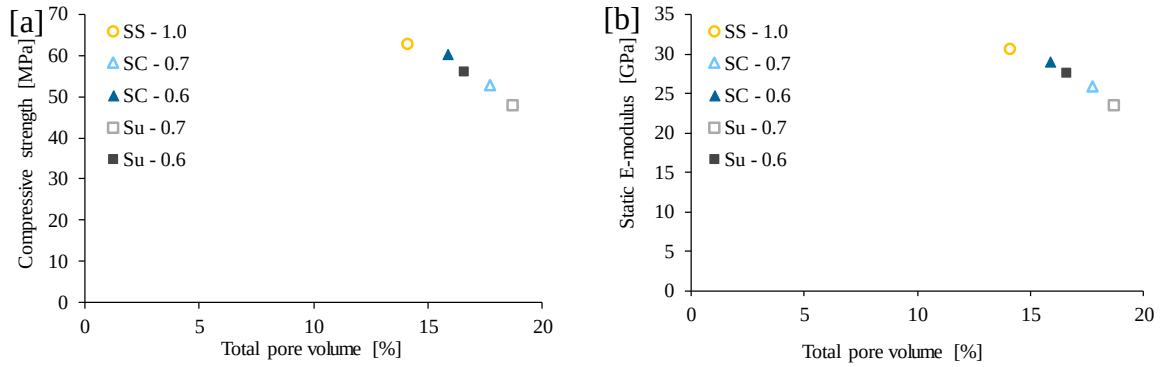

Figure 5.24: Total pore volume derived from MIP method V_s compressive strength [a] and static E-modulus [b] of AASF samples at 7 days.

5.8 Conclusions

In this chapter, the effect of the incorporation of sodium carbonate and sodium sulfate on the microstructure of the sodium silicate-activated slag/fly ash cements was experimentally investigated. The reaction products, chemical bonds, mineral composition of the reaction products and the pore structure were characterized for the studied AASF cements. Based on the experimental results, the following conclusions can be drawn:

- The XRD and FTIR results show that Al-substituted C-S-H type gel is the main reaction product in all investigated AASF cements. Also, the FTIR spectrum after deconvolution demonstrated that a stable three-dimensional structured N-A-S-H type is formed in all studied AASF cements. Hydrotalcite is observed as the main secondary reaction product in all studied AASF cements.
- The incorporation of sodium carbonate resulted in the formation of carbonate phases like calcite, gaylussite, and pirssonite. In the sample with sodium sulfate, no crystalline sulfate phases like ettringite or calcium-aluminum-sulfate-hydrate (C-A-S-H type gels) are observed.
- The sulfate ions provided from the activating solution have limited contribution in the reaction process and mostly remained as free sulfate ions in the pore solution.
- The partial substitution of sodium silicate with sodium carbonate and sodium sulfate results in (N,C)-A-S-H gel with higher Ca/Si ratio and lower Al/Si ratio. Moreover, the alkalis (Na^+) integrated into the (N,C)-A-S-H gel are significantly reduced with incorporation of sodium carbonate and sodium sulfate solution.

- A good linear correlation was observed between the concentration of OH^- ions in the pore solution and the TGA bound water content and the isothermal calorimetry heat release. This finding suggests that a decrease in OH^- ions is correlated to dissolution kinetics, thus reaction kinetics in studied AASF cements.
- The incorporation of sodium carbonate and sodium sulfate makes the pore structure of sodium silicate-activated samples coarser.

Chapter 6

Autogenous shrinkage

6.1 Introduction

This chapter describes the basic mechanism of autogenous shrinkage in AASF through an interlinked assessment of reaction kinetics, reaction chemistry, and microstructure development reported in previous chapters. In addition, the capillary tension caused by self-desiccation is calculated by using measured internal relative humidity and surface tension of the pore solutions, in order to elucidate the relationship between the capillary tension in the pore fluid and the autogenous shrinkage in AASF.

Firstly, the chemical shrinkage of AASF pastes measured using the dilatometry method is described and linked to the reaction kinetics. Secondly, various methods to estimate 'Time-zero', defined as the time for the start of autogenous shrinkage measurements, are elaborated and then the effect of type and concentration of alkaline solutions on the autogenous shrinkage starting from 'time-zero' is described. Thirdly, internal relative humidity and surface tension of the extracted pore solutions are determined as inputs to calculate the capillary tension in the pore fluid. After that, the autogenous shrinkage caused by the self-desiccation mechanism is modelled and discussed. Finally, based on the resulting correlations, new models are developed for predicting autogenous shrinkage of AASF cements. Also, existing empirical shrinkage models for traditional OPC-based materials are evaluated for the prediction of autogenous shrinkage in AASF cements. Summary of the main conclusions is given at the end of the chapter.

6.2 Chemical shrinkage

As explained in Chapter 2, chemical shrinkage is defined as the volume reduction associated to the formation of reaction products that occupy less volume than the initial reaction reactants. The results of the chemical shrinkage of the AASF paste samples, measured with the

dilatometry method, are shown in Fig. 6.1. The measured chemical shrinkage of all AASF samples after 7 days is in between 20-35 mm^3 per gram of initial binder. Previous studies [294, 108] on OPC-based materials have reported that the chemical shrinkage of traditional Portland cement paste with a water-to-binder ratio of 0.5 is around 55-60 mm^3/g of binder at 7 days. This suggests that the measured chemical shrinkage of AASF pastes is lower (~50%) than that of OPC pastes. The lower chemical shrinkage in studied AASF paste may be due to lower rate of reaction during early-hours and formation of dense microstructure, which lower penetration of the solution into the sample to compensate the chemical shrinkage. Lower chemical shrinkage values for AASF cements were also reported by other researchers [25, 165].

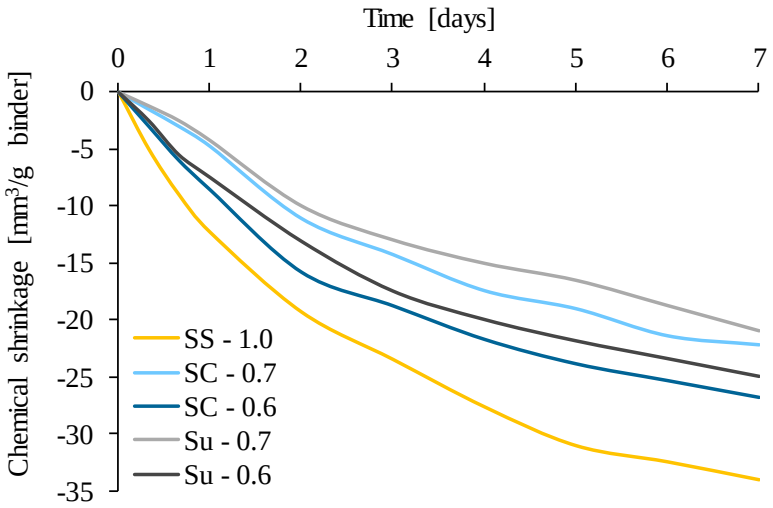

Figure 6.1: Chemical shrinkage of AASF paste, derived from the dilatometry method (negative values indicates shrinkage).

Samples activated with only sodium silicate (SS-1.0) have higher chemical shrinkage compared to the samples with sodium carbonate (SC) and sodium sulfate (Su). This is most likely due to a higher rate of reaction in the samples activated with sodium silicate, as a consequence of higher concentration of OH^- ions, as explained in Chapter 4 and Chapter 5. Moreover, the presence of more aqueous silicates in SS-1.0 contributes to a higher rate of silica polycondensation reaction [242] and results in the formation of dense reaction products that occupy only a small fraction of the original solid volume. On the other hand, incorporation of sodium carbonate forms mesoporous hydroxysodalite ($Na_8Al_6Si_6O_{24}(OH)_2(H_2O)_2$) at early ages (see XRD results in Chapter 5), which may have a larger or similar molar volume than that of original reactants [295] and results in lower chemical shrinkage. Samples with sodium carbonate have higher chemical shrinkage compared to the samples with sodium sulfate at the

same Na_2O concentration (Fig. 6.1). This is attributed to higher rate of reaction in the samples with sodium carbonate due to the formation of calcite as nucleation sites to precipitate more C-A-S-H type gels. Moreover, the formation of carbonate phases increases the concentration of OH^- ions in the pore solution (as explained in Chapter 5) and leads to an increase in the rate of dissolution kinetics and thus amount of reaction products formation with time. The chemical shrinkage of AASF pastes increases with increase in concentration (Na_2O) of the activator due to a higher rate of reaction as shown in Fig. 4.2 (Chapter 4).

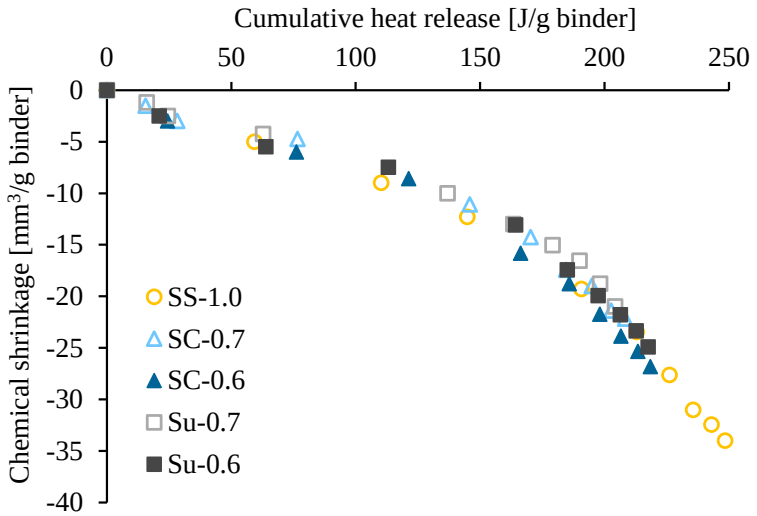

Figure 6.2: Comparison between chemical shrinkage and cumulative heat release, up to 7 days.

For alkali-cements activated with different type and concentration of alkaline solutions, the chemical shrinkage can be the consequence of the combination of two phenomena: reaction degree and modification of reaction products. On one hand, acceleration of AASF hydration due to increase in OH^- and Na_2O concentration induces an increase of the chemical shrinkage. One the other hand, the formation of reaction products with different molecular weights and densities can also induce different chemical shrinkage. For example, the formation of hydroxysodalite in samples with sodium carbonate lowers the chemical shrinkage as explained above. This latter effect can be quantified by relating the measured chemical shrinkage with the cumulative heat release. It can be seen that the difference in the magnitude of chemical shrinkage samples at same amount of heat release is only marginal for the studied AASF pastes (Fig. 6.2). This confirms that the measured chemical shrinkage in the studied AASF cements is mainly attributed to the reaction kinetics effect rather than phase assemblage at early ages.

6.3 Autogenous shrinkage

As defined in Chapter 2, the autogenous shrinkage refers to the macroscopic volume reduction of sealed cementitious materials without moisture loss to the environment. The linear autogenous shrinkage of AASF mortar samples measured using the corrugated tube method, immediately after mixing (10 min after addition of alkaline solution) is shown in Fig. 6.3. The initial sharp increase of the autogenous shrinkage (until knee point) is entirely attributed to the chemical shrinkage, as the material is still in the fluid state. This volume change does not induce any internal stresses leading to cracking. After the knee point a solid skeleton is formed and this restrains the external volume change (autogenous shrinkage) caused by chemical shrinkage, resulting in the formation of internal voids and air-solution menisci [122, 136]. As reaction proceeds, water/solution in bigger pores inside the matrix is consumed and discharged first [145]. This process is called self-desiccation, which is reflected by internal a drop in the relative humidity.

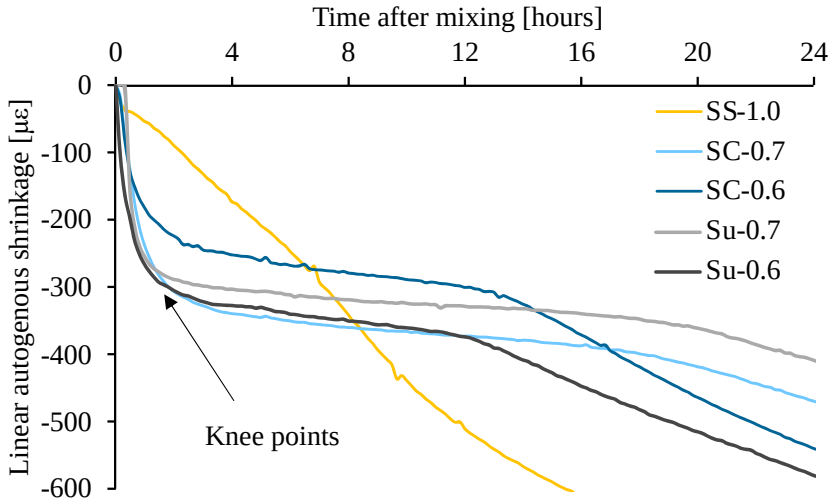

Figure 6.3: Autogenous shrinkage of AASF mortar samples, from the time of mixing.

6.3.1 Time-Zero (t_0)

"Time-zero" is defined as the time when the paste or matrix forms a solid skeleton to enable tensile stress transfer. Interpreting autogenous shrinkage as from time-zero is interesting, since only this autogenous shrinkage induces stresses under restraint conditions and causes cracking in cementitious materials. Therefore, the accurate determination of 'time-zero' is critical to understand the autogenous shrinkage behavior and cracking potential of AASF cements.

The three different approaches that have been commonly reported in literature to determine time-zero are: (i) the final setting time obtained from standard Vicat needle test [296], (ii) the time where the slope of autogenous shrinkage changes or knee point [146], and (iii) the onset of internal relative humidity drop [155]. The autogenous shrinkage of the AASF mortar samples, plotted starting from the Vicat final setting time, is shown in Fig. 6.4. Choosing the final setting time as time-zero, the autogenous shrinkage of AASF samples increases with increase in silica-content (SS-1.0) and alkali-content (SC-0.6 & Su-0.6) of the activator.

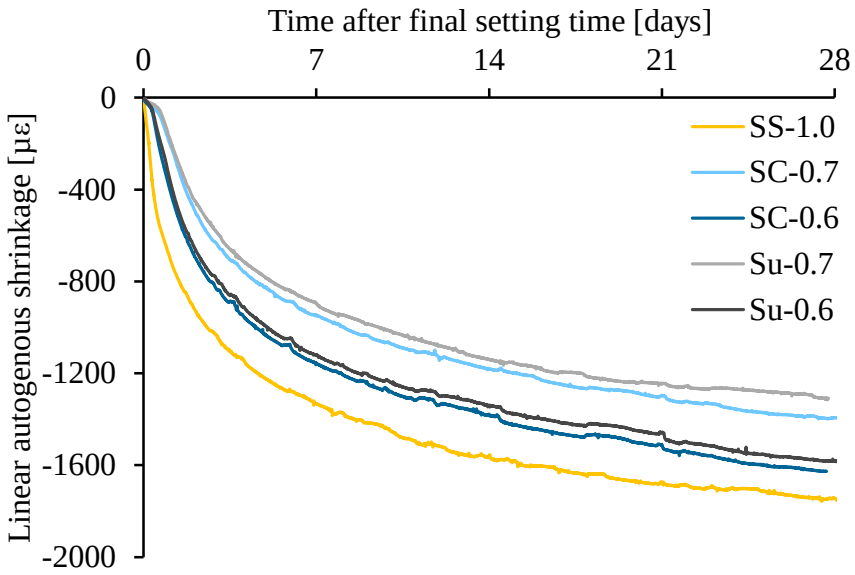

Figure 6.4: Autogenous shrinkage of AASF mortar samples, plotted as from Vicat final setting time.

As explained above, from the time of formation of the solid skeleton, the chemical shrinkage is transferred into internal voids and results in self-desiccation causing autogenous shrinkage. Thus, a change in slope is expected in the autogenous shrinkage curves after the formation of self-supporting solid skeleton, as autogenous shrinkage starts changing form the function of chemical shrinkage to self-desiccation. The time corresponding to a change in slope or knee point of the autogenous shrinkage curves for the studied AASF mixes is given in Table. 6.1. No significant difference is observed between the Vicat final setting time and knee point of the autogenous shrinkage curves for the studied AASF mixes. These results suggest that the final setting time obtained from Vicat needle test can accurately correspond to time-zero, i.e. when the solid skeleton forms.

Table 6.1: Comparison between the Vicat final setting time and knee point of the autogenous shrinkage curves.

Mix ID	SS-1.0	SC-0.7	SC-0.6	Su-0.7	Su-0.6
Vicat final setting time [min]	90	180	230	220	310
Knee point [min]	95	195	245	220	305

Since defining setting time from Vicat test method is based on arbitrary thresholds, many researchers [151, 153, 152] have argued the reliability of using Vicat final setting time as the time-zero. On the other hand, some studies have reported that the precise measurement of internal RH drop, which is associated to the self-desiccation process, is a more appropriate approach to define time-zero than using Vicat final setting time. However, the internal RH approach is not considered in this study due to the negative influence of bleeding and condensation process, occurring in the studied AASF mixes, on the accuracy of time-zero values. Actually, the measured internal RH using Rotronic probes (as explained in Chapter 3) is only the real-time change in RH on the top layer of specimen. Therefore, a thin layer of water/solution remaining on the top surface of the specimen during bleeding affects the RH measurements and postpones the time-zero value in the studied AASF mixes. Therefore, the Vicat final setting time, which corresponds well with the knee point of the autogenous shrinkage, is used as "time-zero" in this study.

As shown in Fig. 6.4, the sodium silicate-activated samples (SS-1.0) shrink rapidly after final setting time, reaching around 650 με at 1 day and around 1750 με at 28 days. This magnitude of shrinkage in SS-1.0 is substantial higher than that of OPC mortar with water-to-binder ratio of 0.5 (85 με at 1 day) [108]. This observation is consistent with previous studies [129, 130, 131, 132, 133, 134], which reported that sodium silicate-activated slag exhibit around 6-10 times higher autogenous shrinkage than the Portland cement. However, with incorporation of sodium carbonate (SC-0.6) and sodium sulfate (Su-0.6) solutions, the autogenous shrinkage of sodium silicate-activated mortar samples reduces to around 50% at 1 day and around 15% at 28 days. The decrease in concentration of sodium carbonate (SC-0.7) and sodium sulfate (Su-0.7) leads to a further reduction in autogenous shrinkage to around 75% at 1 day and around 20% at 28 days. Also, the results show that samples with sodium sulfate have slightly lower autogenous shrinkage compared to samples with sodium carbonate of the same concentration.

It is apparent from XRD and FTIR results (Chapter 5) that there is no formation of expansive phases like ettringite crystals in samples with sodium sulfate (Su). This indicates that compensation of autogenous shrinkage with formation of the expansive phase ettringite is limited in hybrid sodium silicate and sodium sulfate activating systems. This is in contrast to ordinary Portland cement [94, 95] and only sodium sulfate activated slag [69, 68], where the formation of expansive ettringite can benefit the autogenous shrinkage at early hours. These findings imply that the lower autogenous shrinkage in samples with sodium sulfate is mainly attributed to self-desiccation process associated to reaction kinetics, rather than the phase assemblages at early ages.

As explained in Chapter 2, evolution of ultrasonic wave velocity in cement and concrete has been commonly used to continuously monitor the percolation of the solid phases which caused dramatic changes in the ultrasonic wave behavior [297, 298, 299, 300, 301]. Longitudinal wave (P-wave) velocity is sensitive to the formation of hydrates and can characterize the very early-age microstructure changes involved with autogenous shrinkage development and self-desiccation process. Therefore, to better understand the autogenous shrinkage in AASF cements, it is compared with ultrasonic measurements as shown in Fig. 6.5. By comparing with ultrasonic P-wave velocity, the evolution of autogenous shrinkage immediately after mixing in AASF cements can be divided into three stages.

As can be seen from Fig. 6.5, the autogenous shrinkage of AASF mortar samples increases rapidly during the first stage. This stage corresponds to the condensation stage in ultrasonic velocity evolution curves, which is assigned to the formation of initial reaction products (Si-Al units) and the condensation reaction between them, simultaneously (as explained in Chapter 4). Thus, the rapid increase in measured autogenous shrinkage during the first stage is completely assigned to the chemical shrinkage due to formation of initial reaction products through condensation reaction. When the slope of the autogenous shrinkage curve starts to change, indicating the final setting time or time-zero, a change in the slope of UPV curves is also observed. As explained in Chapter 4, this change in UPV curves reflects the start of the induction stage, where the formation of new reaction products is temporarily hindered due to the dilution effect and the material undergoes continuous polycondensation reactions at solid-liquid interface to form a more interconnected structure. By comparing with UPV evolution curves, the small increase in autogenous shrinkage during stage II is attributed to the volume changes induced by polycondensation reaction at solid-liquid interfaces and/or between two adjacent aluminosilicate units and/or low Ca/Si ratio C-A-S-H type gels.

During stage II, the samples activated with SS-1.0 exhibit a higher rate of autogenous shrinkage (Fig. 6.5). This is mainly attributed to the higher degree of polycondensation reaction at solid-liquid interfaces and between two adjacent aluminosilicate units due to the presence of more soluble silicate in the solution. In samples with sodium carbonate and sodium sulfate, no significant change is observed in the rate of autogenous shrinkage during this stage II with increase in concentration of the activating solutions.

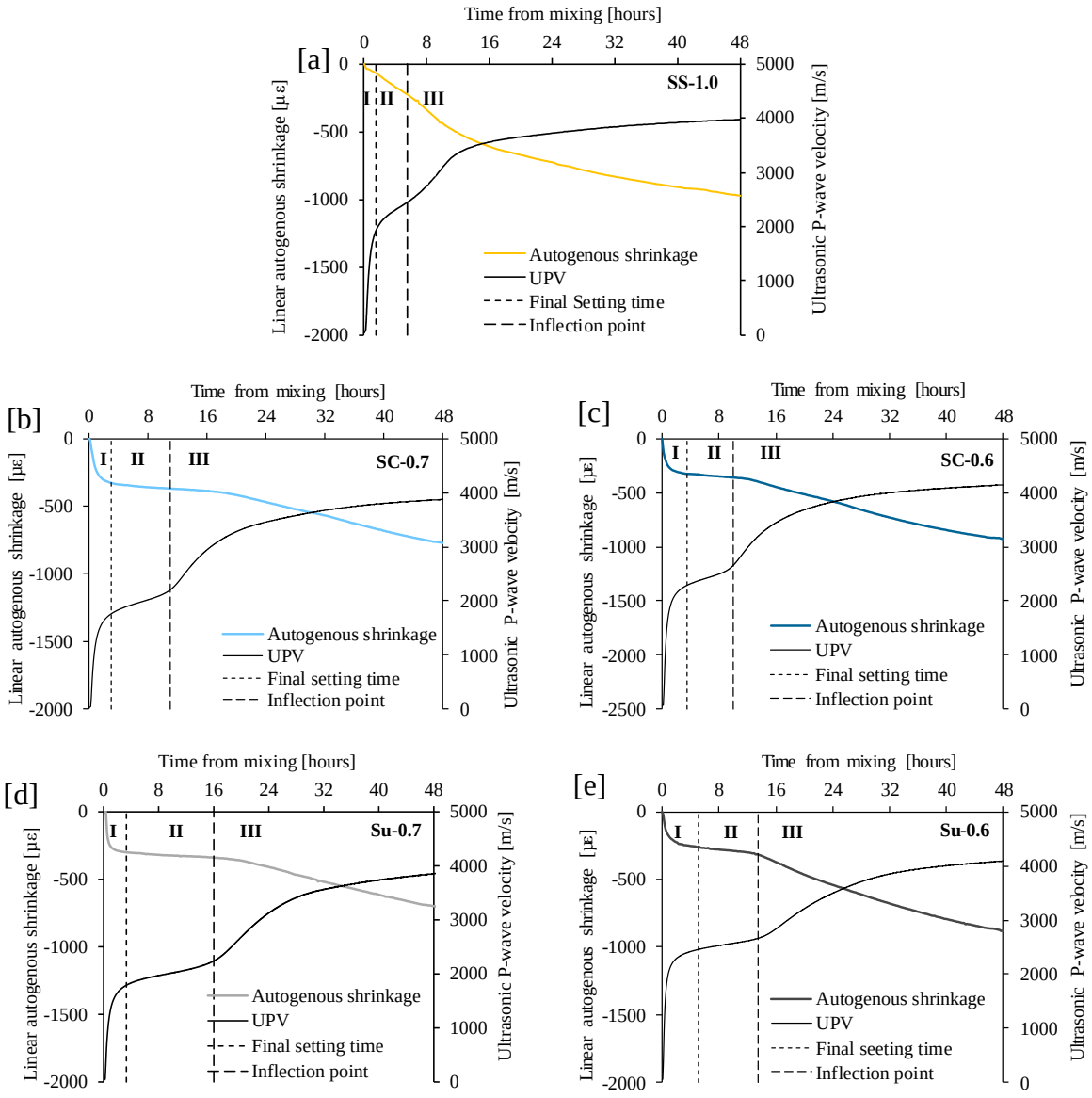

Figure 6.5: Comparison between autogenous shrinkage and ultrasonic P-wave velocity measurements SS-1.0 [a], SC-0.7 [b], SC-0.6 [c], Su-0.7 [d], and Su-0.6 [e].

During stage III, the autogenous shrinkage strongly increases in all studied AASF mortars as shown in Fig. 6.5. In this stage, the ultrasonic velocity strongly increases due to formation of massive reaction products and consequently increase in the volume fraction of connected solids

as explained in Chapter 4. Thus, by comparing with the UPV evolution curves, we can suggest that the autogenous shrinkage during stage III is mainly attributed to the chemical reaction associated with the formation of reaction products and self-drying (i.e. self-desiccation process). In other words, beyond the inflection point or end of stage II, the volume changes caused by the formation of reaction products develop a significant volume of internal voids in the capillary pores, leading to the formation of air-solution menisci, and subsequently undergoes internal pore drying due to consumption of solution for further hydration (i.e. self-desiccation).

6.3.2 Autogenous shrinkage V_s chemical shrinkage

Again, as explained above, the autogenous shrinkage of cementitious materials is defined as the macroscopic volume reduction resulting from the self-desiccation induced by chemical shrinkage. Therefore, relating autogenous shrinkage to chemical shrinkage helps to better understand the shrinkage mechanism in AASF cements.

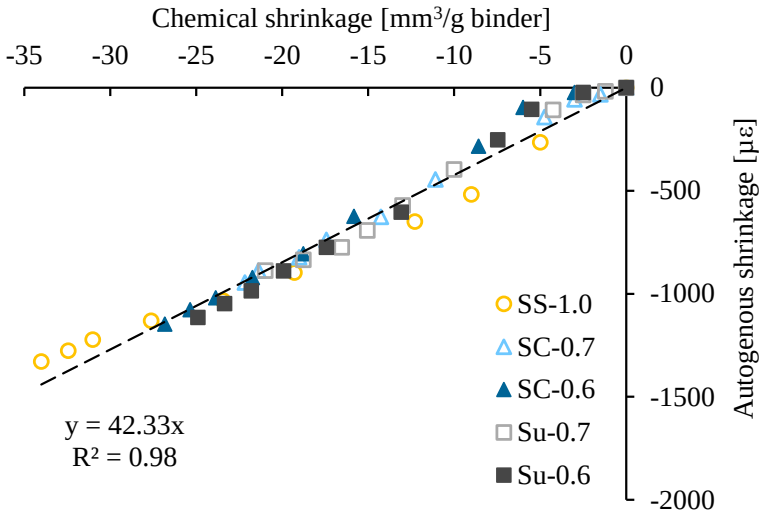

Figure 6.6: Comparison between autogenous shrinkage and chemical shrinkage of AASF samples, after Vicat final setting time or time-zero.

Fig. 6.6 shows the autogenous shrinkage of AASF mortars samples as a function of chemical shrinkage after final setting time. A strong linear correlation between these two indicates that the measured autogenous shrinkage is predominately influenced by chemical shrinkage. In other words, the drop of pore relative humidity (i.e. self-desiccation process), caused by chemical shrinkage is the main driving force for the autogenous shrinkage in AASF. This finding is consistent with some previous studies [163, 164, 166] but contrasts to others [165], which reported that besides the self-desiccation process, a reduction in steric-hydration forces

takes place, due to the consumption of ions from the pore solution attributed to the autogenous shrinkage in AASF cements at early ages.

6.3.3 Autogenous shrinkage V_s cumulative heat release

Fig. 6.2 indicates that the chemical shrinkage has a strong relationship with the cumulative heat release in AASF cements. Thus, the relationship between the cumulative heat release and the autogenous shrinkage can be used to further verify the correlation between chemical shrinkage and autogenous shrinkage in AASF. It can be noticed that at the same amount of cumulative heat release, samples activated with only sodium silicate (SS-1.0) exhibit a higher autogenous shrinkage during early hours compared to the samples with sodium carbonate and sodium sulfate. This can be explained by the higher rate of autogenous shrinkage in SS-1.0 samples due to Si polycondensation reaction at solid-liquid interfaces and/or between two adjacent aluminosilicate units, as explained above, from Fig. 6.5. These results suggest that the autogenous shrinkage in AASF is not completely attributed to the chemical reactions associated with the formation of reaction products and self-drying (self-desiccation). The polycondensation reaction, particularly during the induction period of the UPV curves (i.e. induction period of heat flow curve), also cause a certain amount of autogenous shrinkage in AASF. With the reaction going on, same magnitude of the autogenous shrinkage is observed for all the AASF samples at same amount of cumulative heat release (Fig. 6.7). This indicates that the self-desiccation, associated with the chemical reactions forming reaction products and self-drying, become more dominant in the evolution of autogenous shrinkage over time.

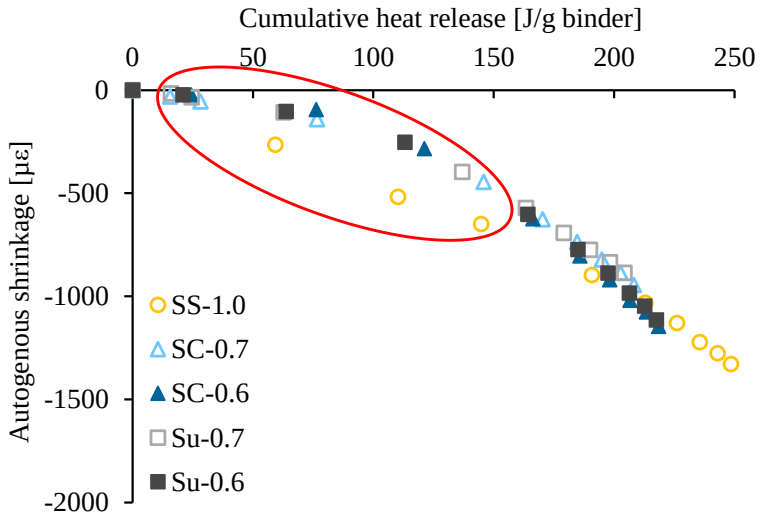

Figure 6.7: Comparison between autogenous shrinkage and cumulative heat release of AASF samples.

6.4 Internal relative humidity

In order to avoid the condensation risk due to significant amount of heat release during the early hours, the internal relative humidity (RH) is measured from approximately 10 hours after mixing and plotted in Fig. 6.8. The results show that samples activated with only sodium silicate (SS-1.0) show lower internal relative humidity. A higher rate of reaction in SS-1.0 results in a higher consumption of solution from pores to form reaction products and leads to a lower RH. Similarly, the increase in concentration of sodium carbonate (SC-0.6) and sodium sulfate (Su-0.6) results in a lower RH due to higher rate of reaction. These internal RH measurements are corresponding well with the calorimetry and TGA results. This measured internal RH is a combination of the RH drop due to dissolved salts in the pore solution *(RH_s)* and the RH drop due to air-solution menisci formation *(RH_k)* or self-desiccation [302, 139].

$$RH = RH_s \,.\, RH_k \tag{6.1}$$

$$RH_s = \frac{n_{H_2O}}{n_{solution}} \tag{6.2}$$

The ions dissolved in the pore solution, especially the alkalis and hydroxyl ions, reduce the water activity and consequently the internal RH. According to Raoult's law [139], the effect of dissolved ions on RH_s can be expressed with Eq. (6.2). n_{H_2O} is the mole fraction of water in the pore solution and $n_{solution}$ is the total number of moles in the solution.

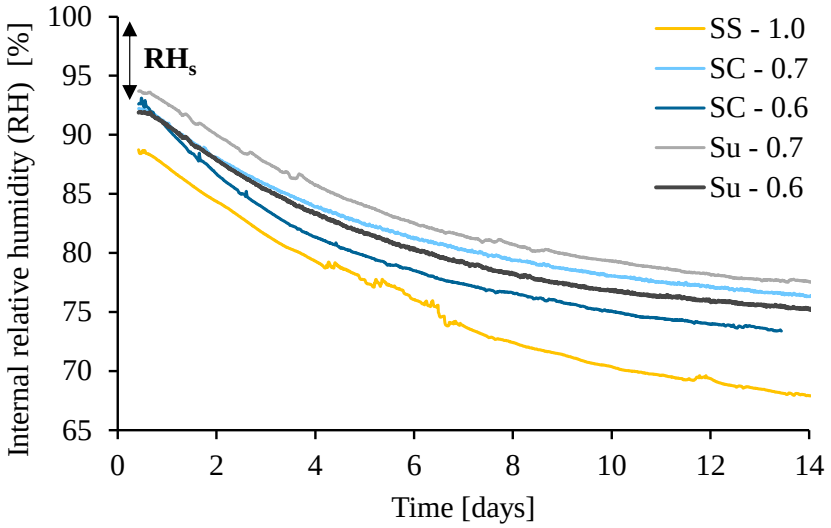

Figure 6.8: Measured internal relative humidity (RH) of AASF mortar samples.

Table 6.2: RHs [%] of pore solutions extracted from AASF mortar samples, measured by using Rotronic station probes.

Mix	14 Hour	1 Day	3 Days	7 Days
SS - 1.0	90	91.4	91.8	92.0
SC - 0.7	92.9	93.5	94.5	95.3
SC - 0.6	92.5	93.3	93.7	94.3
Su - 0.7	91.8	92.4	93.0	94.7
Su - 0.6	91.1	91.6	92.3	93.3

The measured RH_s values of the pore solutions extracted from AASF mortar samples at different curing ages are given in Table. 6.2. As expected, the RH_s values are much lower than 100% due to the presence of Na^+ and OH^- ions [303, 304]. The results show that the RH_s values of the extracted pore solution increases over time. From ICP-OES resulted explained in Chapter 5, it is clear that the dissolved ions in the pore solution are continuously consumed in the formation of reaction products and can lead to an increase of the water activity (RH_s values) of the pore solution. The RH_s values are lower for samples activated with SS-1.0 due to the presence of more Na^+ and OH^- ions at all ages. Similarly, the increase in concentration of sodium carbonate (SC-0.6) and sodium sulfate (Su-0.6) results in lower RH_s values (Table. 6.2). These results are in agreement with the pore solution composition results explained in Chapter 5. With the measured RH in the mortar samples and RH_s in the pore solution, the RH drop due to self-desiccation (RH_k), named as autogenous relative humidity in this study, can be calculated by using Eq. (6.3) [139].

$$RH_k = \frac{RH}{RH_s} \tag{6.3}$$

RH is the measured relative humidity of the mortar, RH_s is the measured relative humidity of the pore solution (Table. 6.2) and RH_k is the calculated autogenous relative humidity. Fig. 6.9 shows the RH drop due to the formation of air-solution menisci (RH_k), which reflects the self-desiccation process. The significant drop in RH_k over time manifests that the self-desiccation is one of main driving forces for autogenous shrinkage in AASF cements. The results show that samples activated with sodium silicate (SS-1.0) have lower autogenous RH (RH_k) compared to those samples with sodium carbonate and sodium sulfate. These results indicate that samples activated with SS-1.0 have higher degree of self-desiccation and this can lead to

a higher autogenous shrinkage. With increasing concentration of sodium carbonate and sodium sulfate, the autogenous RH (RH_k) decreases, indicating that the self-desiccation process increases with increase in concentration of the activator. At the same concentration, samples with sodium carbonate have lower RH_k values compared to samples with sodium sulfate, indicating a higher degree of self-desiccation and this can result in a higher autogenous shrinkage in samples with sodium carbonate than samples with sodium sulfate at the same concentration. These results correspond well the measured autogenous shrinkage results.

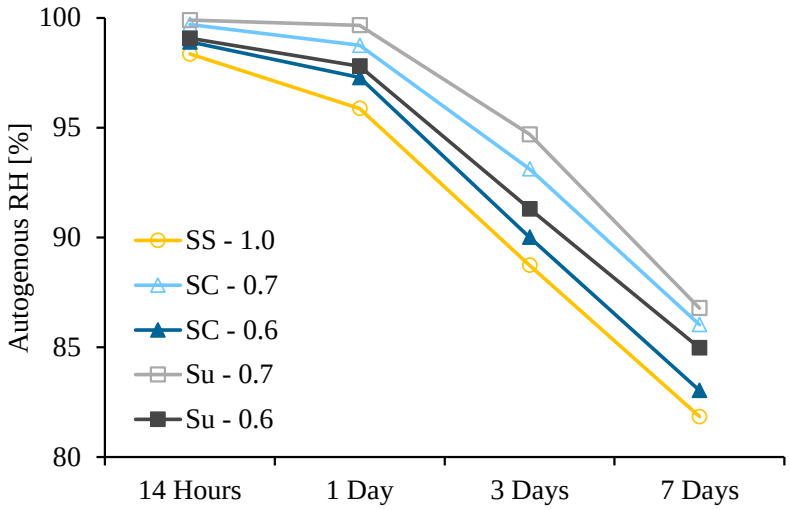

Figure 6.9: Calculated autogenous RH (RH_k) of AASF mortar samples.

Fig. 6.10 shows the measured autogenous shrinkage of the AASF mortar samples (started as from Vicat final setting time, plotted in Fig. 6.4 as a function of the calculated autogenous RH (RH_k). The results show that the autogenous shrinkage of all AASF mortar samples follows a similar trend with decreasing autogenous RH (RH_k). Interestingly, the autogenous shrinkage of sodium silicate-activated samples at the same RH_k values (i.e. at same self-desiccation) changes significantly with incorporation of sodium carbonate and sodium sulfate. This difference between the autogenous shrinkage of only sodium silicate-activated samples and the samples with sodium carbonate and sodium sulfate can be attributed to the difference in stiffness development and pore size distribution. The different capillary tension in pore fluids and the resistance to deformation or elastic modulus of mortars can result in different autogenous shrinkage at the same RH_k. Nevertheless, there is an overall good linear correlation between the calculated autogenous RH (RH_k) and the measured autogenous shrinkage (Fig. 6.11). These findings confirm that reduction in the pore humidity (i.e. self-desiccation) is the

main driving force from approximately 10-15 hours after mixing for autogenous shrinkage in AASF, like in OPC-based materials [122].

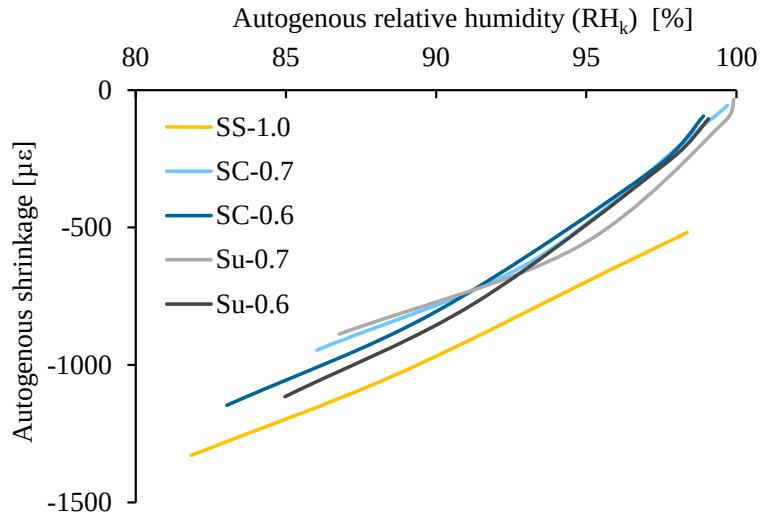

Figure 6.10: Autogenous shrinkage as a function of autogenous RH (RH_k) or self-desiccation.

6.5 Surface tension

The surface tension of the pore solution extracted from AASF mortar samples was measured using a Pendant drop tensiometer and the results are shown in Fig. 6.11. The measured surface tension of the pore solution in AASF varies from 45 mN/m to 65 mN/m, which is much lower than of the water (~72 mN/m).

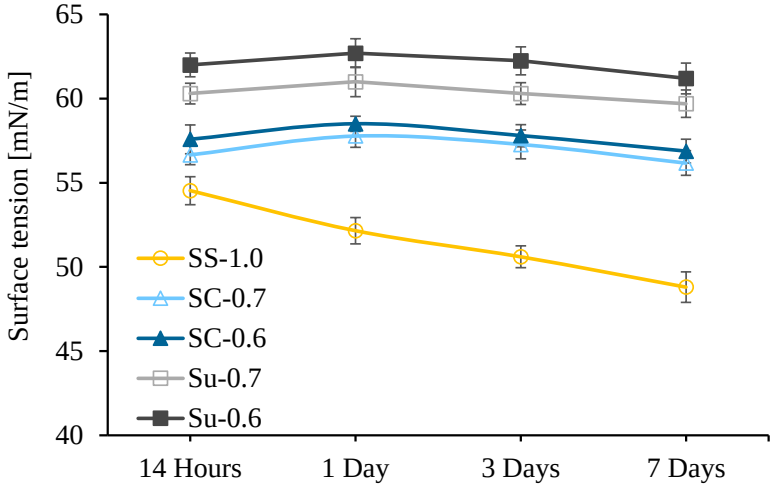

Figure 6.11: Surface tension of the pore solutions extracted from AASF mortars.

In samples activated with sodium silicate (SS-1.0), the surface tension of the extracted pore solution decreases with curing time, while in samples with sodium carbonate and sodium sulfate the surface tension increases slightly during first 24 hours and later decreases with time (Fig. 6.11). One would expect that a high amount of OH^- ions (pH value) in the samples activated with SS-1.0 enhance the dissolution of slag and increases the concentration of dissolved ions in the pore solution, which leads to a higher surface tension [305]. However, the samples with sodium carbonate and sodium sulfate show a higher surface tension at all ages (Fig. 6.11) probably due to the presence of more CO_3^{2-} and SO_4^{2-} ions in the pore solution that are not likely to be involved in the reaction process. This can be supported from the pore solution data explained in Section 5.5, which demonstrated that most of the CO_3^{2-} and SO_4^{2-} ions remain in the pore solution as free ions. The results in Fig. 6.11 show that increase in the concentration of sodium carbonate and sodium sulfate solutions, increases the surface tension of the pore solution. This is due to the fact that an increase in concentration (Na_2O) of the activator enhances the depolymerization of the slag and increases the concentration of dissolved ions in the pore solution, which leads to higher surface tension. Regardless of the concentration, samples with sodium sulfate show higher surface tension than the samples with sodium carbonate.

6.6 Modelling autogenous shrinkage caused by self-desiccation

As explained in Chapter 2, the autogenous shrinkage due to change in internal relative humidity, i.e. self-desiccation, has been typically attributed to three mechanisms, including capillary pressure in the pore fluid, disjoining pressure, and change in the surface tension of the solid gel particles [139]. Among these, the capillary pressure associated with the formation of air-solution menisci and the internal relative humidity drop are considered to be primarily responsible for autogenous shrinkage at moderate to high relative humidity (>75%) [139]. An internal RH drop reduces the disjoining pressure and causes shrinkage. However, the range of relative humidity responsible for disjoining pressure is quite in debate [144]. On the other hand, the change in surface tension mechanism is mostly prominent at lower relative humidity because, above a certain relative humidity (>40%), the solid particles are covered with the absorbed water layers and as a result the surface tension cannot vary significantly when relative humidity changes. Since the measured relative humidity is above 80% (Fig. 6.9), the capillary pressure mechanism is discussed further and linked to the observed autogenous shrinkage in the studied AASF mortar samples.

After ‘time-zero’, as a consequence of chemical reaction, empty voids start to be created and occupied with gas or air in the capillary pores. As reaction proceeds, the internal RH drops gradually by consuming solution from capillary pores and this decreases the curvature radius of the air-solution menisci. Consequently, hydrostatic tensile stress is created in the pore fluid to maintain equilibrium between the empty pores formed by the consumption of solution in the reaction and the solution that is left over. Under equilibrium conditions, capillary tension in the liquid phase is counterbalanced by compressive stresses of the surrounding solid particles. This compressive stress will result in a macroscopic volume reduction, called as autogenous shrinkage. The magnitude of capillary tension in the pore fluid can be calculated by using Laplace equation (Eq. 6.4) [139].

$$P_{cap} = -\frac{2.\gamma}{r} \tag{6.4}$$

Where P_{cap} is the capillary tension in the pore fluid, γ is surface tension of the pore solution experimentally measured in this study (see section 6.5), and r is capillary radius at the menisci curvature (Kelvin radius). The Kelvin radius can be calculated by using the Kelvin equation (Eq. 6.5), in which the influence of both RH drop; due to dissolved salts (RH_s) and air-solution menisci formation (RH_k) are taken into account:

$$r = \frac{2.\gamma.V_m}{\ln\left(\frac{RH}{RH_s}\right).R.T} \tag{6.5}$$

R is the universal gas constant (8.314 J/mol k), T is the absolute temperature (293.15 K), V_m is the molar volume of the pore solution (18.02 cm^3/mol), RH is the measured relative humidity, and RH_s is the relative humidity of the pore solution (Table 6.2). The calculated Kelvin radius for the studied AASF mortar samples are given in Table. 6.3.

Table 6.3: Calculated Kelvin radius (nm) for the studied AASF samples.

Mix ID	14 Hours	1 Day	3 Days	7 Days
SS-1.0	48.00	16.50	5.50	3.10
SC-0.7	86.10	52.60	8.80	4.85
SC-0.6	71.20	29.50	7.60	4.20
Su-0.7	163.90	103.95	15.20	6.00
Su-0.6	104.30	46.75	11.85	5.60

Based on the above equation, the calculated Kelvin radius primarily depends on the change in internal relative humidity and the pore solution chemistry (surface tension), rather than pore size distribution. These results show that small changes in the internal RH are accompanied by a significant change in the Kelvin radius. Samples activated with sodium silicate (SS-1.0) have a lower Kelvin radius at early ages compared to those samples with sodium carbonate (SC) and sodium sulfate (Su). The reason for this is that samples activated with SS-1.0 have higher rate of reaction (See Fig. 4.2) and consequently this decreases the internal RH (see Fig. 6.8). Similarly, the increase in concentration of sodium carbonate and sodium sulfate activator results in a lower calculated Kelvin radius due to a higher rate of reaction and lower internal RH (Table. 6.3). Regardless of concentration (Na_2O), the samples activated with sodium carbonate (SC) have a lower Kelvin radius compared to those samples with sodium sulfate (Su). This can primarily be explained by a higher rate of reaction and lower RH (Fig. 6.9). Furthermore, a lower surface tension of the pore solutions in samples with sodium carbonate is also responsible for a lower Kelvin radius.

Using above calculated Kelvin radius as input, the capillary tension in the pore fluid is calculated by using Eq. 6.4 and plotted in Fig. 6.12. From Eq. 6.4, we can clearly observe that the surface tension of the pore solution and the Kelvin radius are the two critical parameters for the capillary tension developed in the pore fluid. A smaller Kelvin radius leads to the generation of higher capillary tension in the pore fluid, which puts the surrounding matrix under great compression and expected to generate large autogenous shrinkage. Accordingly, the samples activated with sodium silicate (SS-1.0) having higher capillary tension in the pore fluid resulted in a greater autogenous shrinkage as shown in Fig. 6.4. Regardless of the concentration (Na_2O), samples with sodium carbonate have higher capillary tension in the pore fluid and are expected to generate a larger autogenous shrinkage compared to samples with sodium sulfate (Su). However, samples activated with Su-0.6 have higher autogenous shrinkage than the samples with SC-0.7 as shown in Fig. 6.4. This can be attributed to the difference in volume fraction of pores with Kelvin radius. The MIP and nitrogen absorption results (Chapter 5) reveal that samples activated with Su-0.6 exhibit a finer pore structure and this consequently causes higher capillary tension in the pore structure; which would explain the cause of higher autogenous shrinkage in Su-0.6 compared to the SC-0.7.

Since capillary tension in the pore fluid is recognized as the direct driving force for autogenous shrinkage in AASF cements, investigating their correlation is meaningful. Fig. 6.13 shows the correlation between the calculated capillary tension in the pore fluid and the measured

autogenous shrinkage for the studied AASF samples. An error in the linear equation (R^2=0.83) is mainly attributed to the ability to resist deformation under internal stresses (capillary tension in the pore fluid). In other words, the elastic modulus increases as the reaction proceeds (see Fig. 4.17) and this would result in a decreasing rate of the autogenous shrinkage with increasing capillary tension in the pore solution over time.

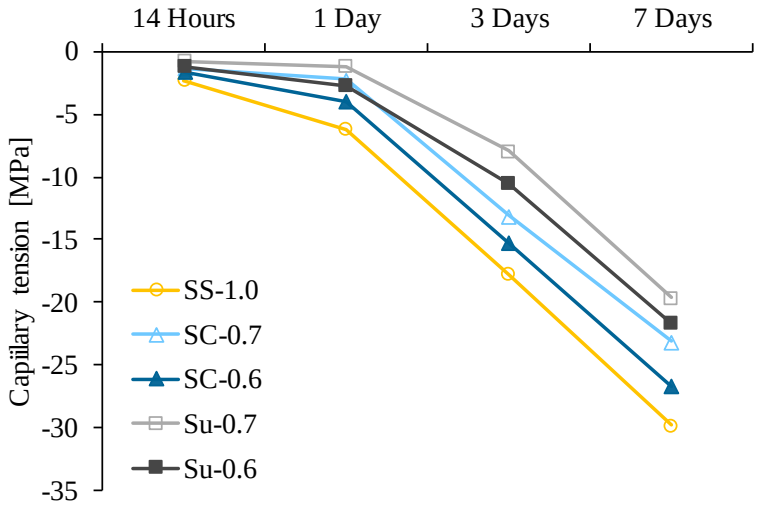

Figure 6.12: Calculated capillary tension in the pore fluid of AASF samples.

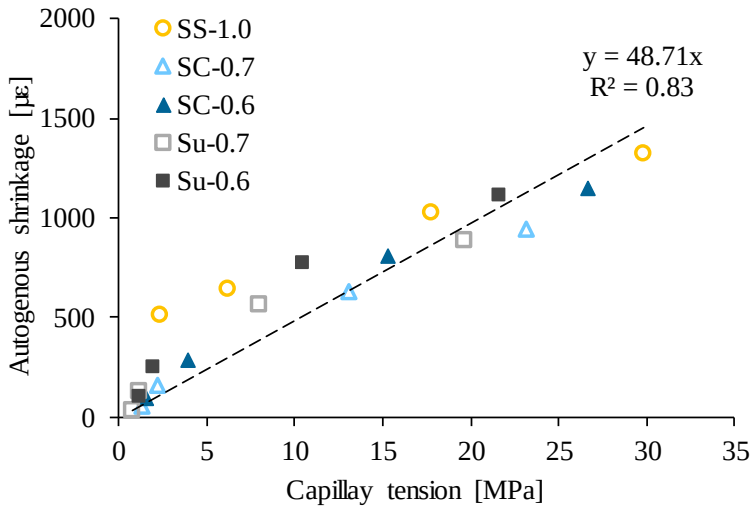

Figure 6.13: Comparison between calculated capillary tension in the pore fluid and measured autogenous shrinkage.

Calculated autogenous shrinkage: Since cementitious materials are not an ideally elastic material, the measured autogenous deformation (ε_{auto}) under internal stress (capillary tension) may include two parts: an elastic deformation (ε_e) and time-dependent deformation or creep (ε_c) (Eq. 6.6).

$$\varepsilon_{auto} = \varepsilon_e + \varepsilon_c \tag{6.6}$$

$$\varepsilon_e = \frac{S.P_{cap}}{3}\left[\frac{1}{K_p} - \frac{1}{K_s}\right] \tag{6.7}$$

The autogenous shrinkage of a partially saturated porous elastic medium due to internal stress (capillary tension in the pore fluid) is calculated using the Biot-Bishop model (Eq. 6.7) [145, 139]. ε_e is the elastic deformation, S is the saturation fraction, P_{cap} is the capillary tension in the pore fluid (Fig. 6.12), K_p is the bulk modulus of AASF mortar ($K_p = E_s/3(1-\upsilon)$), where E_s is the static elastic modulus experimentally measured in this study (Fig. 4.17), υ is the Poisson's ratio for which a constant value of 0.15 is adopted, K_s is the bulk modulus of the solid skeleton, assumed constant to 44 GPa in this study as taken from literature [133].

Calculated saturation degree (S):

The degree of saturation is calculated as the ratio between the evaporable water content and the total permeable pore space in the AASF mortar samples (Eq. 6.8). The evaporable water content and the total amount of open porosity are measured as explained in Chapter 3.

$$S = \frac{V_{ew}}{V_{pt}} \tag{6.8}$$

The degree of saturation calculated from the moisture content and the permeable porosity of sealed mortar samples is shown in Fig. 6.14. The results show that samples activated with only sodium silicate (SS-1.0) have a lower saturation degree compared to the samples with sodium carbonate and sodium sulfate. Also, the increasing concentration of sodium carbonate and sodium sulfate solution (SC-0.6 & Su-0.6) shows lower saturation degree. These results are in agreement with calorimetry and TGA results, which showed that an increase in silica content (SS-1.0) and concentration of the activator (SC-0.6 & Su-0.6) enhance the reactivity of AASF samples and reduce the evaporable water content. Moreover, samples with higher rate of reactivity result in higher chemical shrinkage and this leads to higher pore volume. This can also partly explain the reason for lower saturation degree in samples with sodium silicate and higher concentration of sodium carbonate and sodium sulfate solutions.

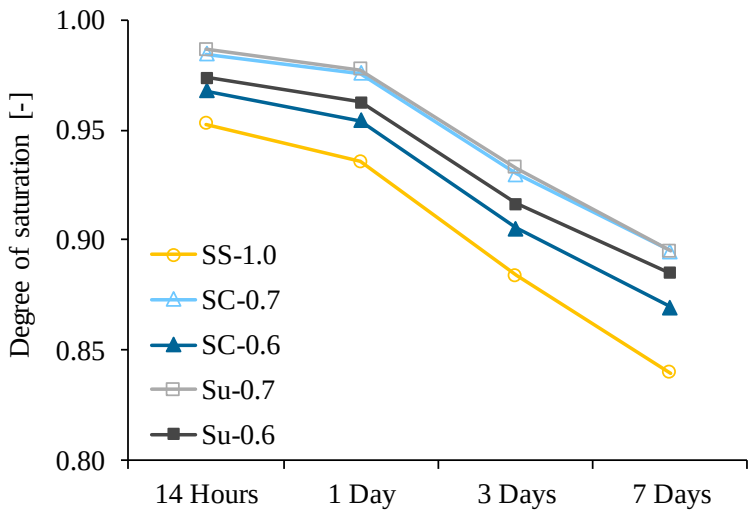

Figure 6.14: Degree of saturation in the AASF mortar samples.

The calculated elastic-part of the autogenous shrinkage calculated using Biot-Bishop model (Eq. 6.7) is shown in Fig. 6.15. As observed, these calculated elastic strain values are substantially smaller than the measured autogenous strain values. This difference between the calculated elastic strains and the measured autogenous strains is mainly attributed to the time-dependent deformations or creep effect that is not accounted in this calculation (Eq. 6.6-6.7). The calculated strain values in the samples activated with sodium silicate are around 190 με and 380 με at 1 day and 7 days, respectively. These values are about 3.5 times lower than the measured autogenous strain values. One the other hand, the calculated elastic strain values for SC-0.7, SC-0.6, Su-0.7, and Su-0.6 at 1 day are around 180 με, 175 με, 125 με and 140 με, respectively, which are approximately 1-1.5 times lower than the measured autogenous strain values. This striking finding indicates that the partial substitution of sodium silicate by sodium carbonate and sodium sulfate signifiantly reduces the viscoelastic effect or creep-part of the auotogenous shirnkage at early ages. Similarly, at 7 days, the calculated strain values in samples with sodium carbonate and sodium sulfate are approximately 2.0-3.0 times lower than the measured autogenous strain values.

Meanwhile, by comparing the calculated elastic strain values between the studied AASF samples, it can be seen that the incoporation of sodium carbonate and sodium sulfate does not induce much effect on the elastic deformation of the sodium silicate-activated samples. These results suggest that the viscoelastic or creep-part of the autogenous shirnkage plays an important role in the autogenous shirnkage of AASF cements.

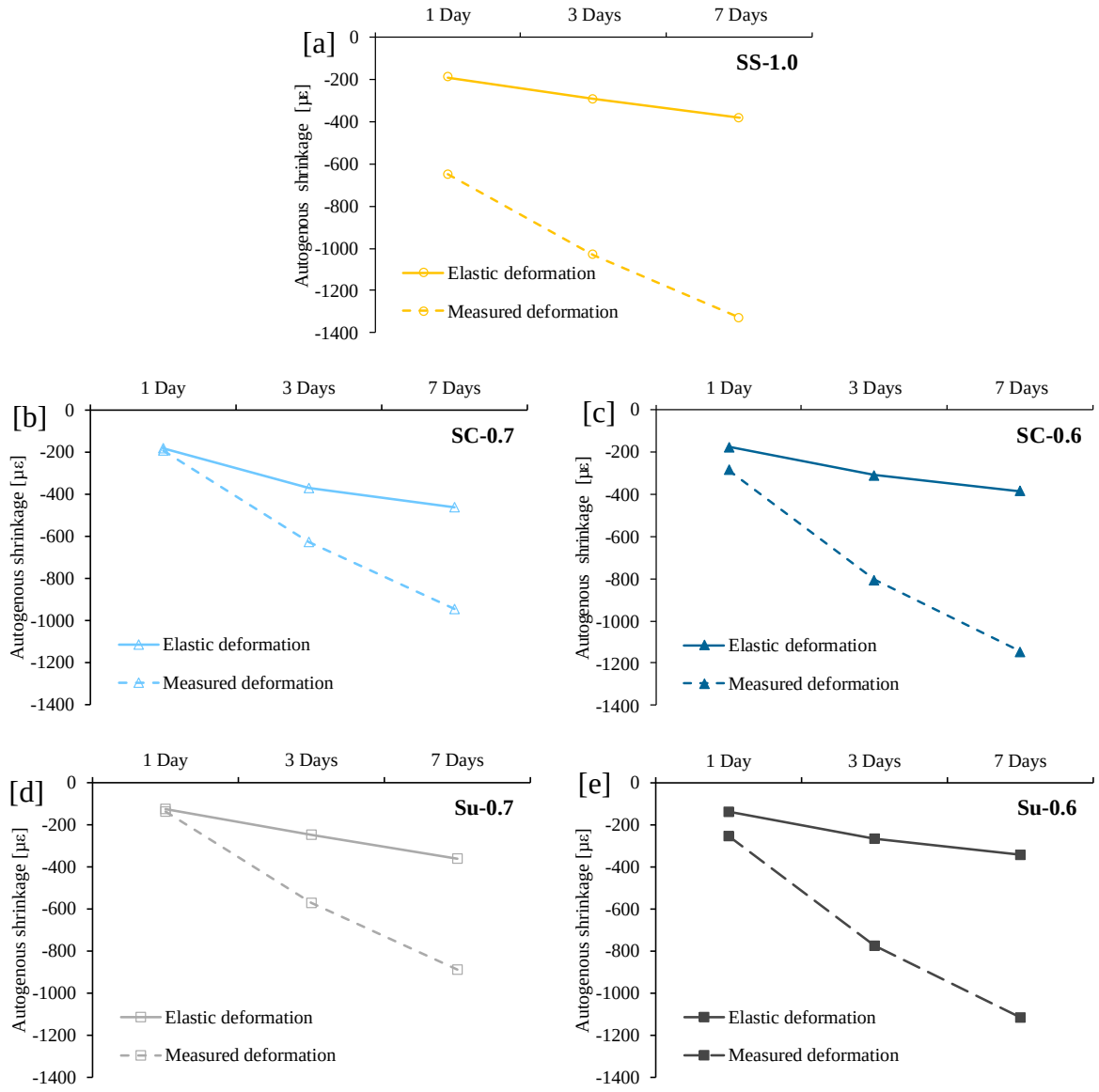

Figure 6.15: Comparison between calculated shrinkage and measured autogenous shrinkage SS-1.0 [a], SC-0.7 [b], SC-0.6 [c], Su-0.7 [d], and Su-0.6 [e].

Recent studies [293, 173, 174] have reported that the viscoelastic behavior of cementitious materials is primarily associated with the movement of C-A-S-H particles under local stresses. Considerably higher viscoelastic effects in sodium silicate activated samples (SS-1.0) can be attributed to the formation of more deformable or unstable C-A-S-H gel. Previous studies [24, 132] have suggested that the presence of alkali cations (Na^+) in C-A-S-H is more likely to cause a viscoelastic effect in alkali-activated slag systems. The incorporation of alkalis into the C-A-S-H gel can reduce the stacking regularity of C-A-S-H gel layers and makes it easier to collapse or redistribute under internal stress [24]. As evidenced in Table. 5.3 (Chapter 5), more sodium is incorporated into the gel structure of sodium silicate activated samples (SS-1.0) which are

expected to show a higher viscous shrinkage at early ages. A recent work [306] has also reported that the stability of C-A-S-H type gel structure decreases significantly when the Na/Ca ratio exceeds 0.11. It can be observed from Table. 5.3 that the samples activated with SS-1.0 have Na/Ca ratio of around 1.3-1.70 (>0.11). This indicates that a more unstable C-A-S-H type gel is formed in samples activated only sodium silicate (SS-1.0) and this leads to a higher viscoelastic deformation under internal load (capillary tension). On the other hand, samples with sodium carbonate and sodium sulfate have a Na/Ca ratio of 0.01-0.005 (<0.11). This implies that the addition of sodium carbonate and sodium sulfate improves the stability of C-A-S-H and this reduces the viscoelastic effect compared to only sodium silicate activated systems. Nevertheless, further experimental investigation on basic creep is needed to understand the pronounced viscoelastic behavior of the AASF cements.

In addition, the viscoelastic properties are subjected to aging, defined as the change in the gel structures over time due to continuous reaction and polycondensation of the silica network [307]. The unchanged wavenumber of Si-O-T bond in the FTIR spectrum suggests that the Si polycondensation is limited by its chain structure after 15 hours (i.e. after induction period of UPV and calorimetry curves) in studied AASF. In other words, the two silicon molecules at the end chain of the adjacent C-A-S-H can undergo linear polycondensation and results in microstructure arrangement. Previous studies [308, 309, 310] using ^{29}Si NMR demonstrated that hydrated gel with low Ca/Si ratio favors a higher degree of Si polycondensation. It is observed from Table. 5.3 that the Ca/Si ratio of the reaction products in samples activated with sodium silicate (SS-1.0) are lower than that of the reaction products of the samples with sodium carbonate and sodium sulfate. This implies that the reaction products in sample activated with sodium silicate (SS-1.0) have a higher degree of Si-polycondensation, and thus higher viscoelastic effect associated to the rearrangement of C-A-S-H gels.

At a high RH, the disjoining pressure acting in small gaps (<30 nm) between the particles is also identified as the main governing mechanism [311]. The presence of more OH^- ions in the pore solution depresses the solubility of Ca^{2+} ions and influences the ionic strength, proportional to the square root of the valence of the ionic species [311]. As the ionic strength of the pore solution decreases with an increase in OH^- ions, the double layer electrostatic repulsive forces increase, and this leads to more deformable C-A-S-H structures. Thus, samples activated with sodium silicate, having a higher concentration of OH^- ions (Table. 3.3), may result in the formation of more deformable C-A-S-H gel than in samples with sodium carbonate and sodium sulfate. Further study is needed to support this.

6.7 Predication of autogenous shrinkage in AASF cements

6.7.1 Predication from compressive strength and bound water content

The above predicted shrinkage using the Biot-Bishop model assumes that autogenous shrinkage has a mechanical response under internal applied stresses known as capillary tension. This capillary tension approach is considered as more appropriate as it includes both a mechanical and a thermodynamic basis. However, this approach requires more input which is difficult to measure such as internal relative humidity, pore solution chemistry, and bulk modulus of matrix and solid skeleton (C-A-S-H gel). Moreover, the predicted shrinkage using Biot-Bishop model approach can only explain the elastic-shrinkage part in the total autogenous shrinkage and ignores the visco-elastic or creep part. Therefore, in this section, new models are developed based on the experimentally measured correlations for predicting autogenous shrinkage in the AASF cements.

It is well known that the compressive strength is the commonly used mechanical property to characterize the resistance of the material under external compressive loading. Meanwhile, the capillary tension in the pore fluid induced by self-desiccation results in a macro-volume reduction (autogenous shrinkage) by generating an internal prestress in compression between surrounding solids. Exploring the relation between the measured compressive strength and the autogenous shrinkage is definitely helpful for researcher and engineering to estimate the autogenous shrinkage easily for alkali-cements (Fig. 6.16). Eurocode 2 [209] suggests a correlation between the compressive strength and the autogenous shrinkage for OPC-based materials, and the validation of this model for alkali-cement is discussed in section 6.7.3.

By considering that the autogenous shrinkage of AASF cements is mainly attributed to the self-desiccation process, which is associated to the drop of internal RH by liquid consumption during the hydration reaction, the correlation between autogenous shrinkage and hydration degree is meaningful and contributes to the fast estimation of autogenous shrinkage (Fig. 6.17).

In Fig. 6.16 and Fig. 6.17, it is clearly seen that the measured autogenous shrinkage has a good correlation with both compressive strength and bound water content results, up to 28 days, for the studied AASF samples. Based on these correlations, two approaches are suggested for prediction of the autogenous shrinkage in AASF systems using parameters like compressive strength and bound water content, which are easy to be measured.

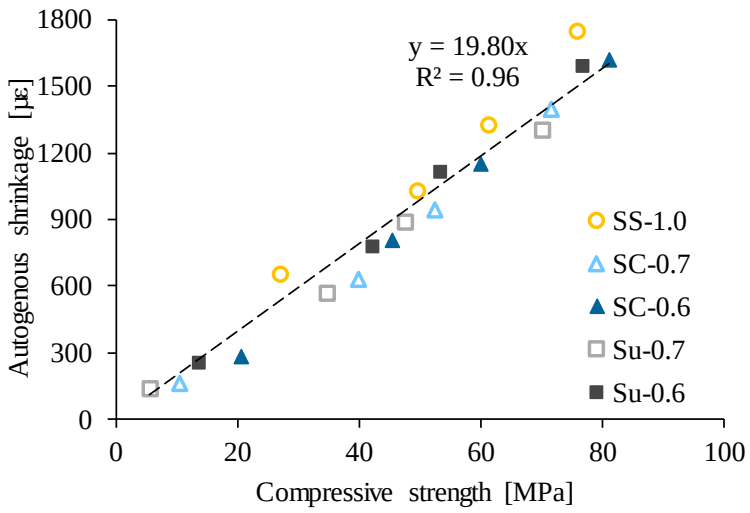

Figure 6.16: Comparison between compressive strength and measured autogenous shrinkage for AASF samples.

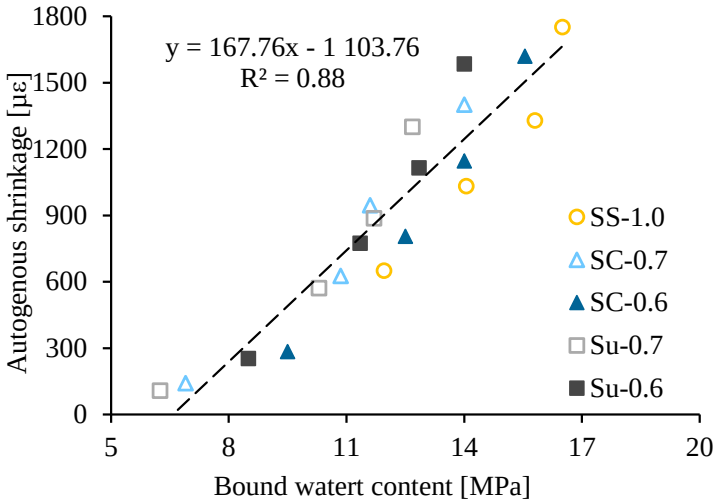

Figure 6.17: Comparison between bound water content and measured autogenous shrinkage for AASF samples.

As illustrated from Fig. 6.16 and Fig. 6.17, the autogenous shrinkage of AASF systems can be expressed as a function of compressive strength and bound water content:

$$\varepsilon_{auto}(t) = 19.80.f_c(t) \quad (6.9)$$

$$\varepsilon_{auto}(t) = 167.75.W_b(t) - 1103.75 \quad (6.10)$$

Where ε_{auto} [με] is the autogenous shrinkage of mortar samples, f_c [MPa] is the measured compressive strength of mortar samples, W_b [%] is the chemical bound water content (weight

loss between 30 °C to 600 °C) measured using TGA. The compressive strength and bound water content as a function of time can be modeled using exponential fitting functions (Eq. 6.11-6.12).

$$f_c(t) = f_{c,\infty} \cdot \exp\left(-\left[\frac{\tau}{t}\right]^{\beta}\right) \quad (6.11)$$

$$W_b(t) = W_{b,\infty} \cdot \exp\left(-\left[\frac{\tau}{t}\right]^{\beta}\right) \quad (6.12)$$

In the above exponential equations, $f_c(t)$ and $W_b(t)$ are the compressive strength and bound water content values at time *t*, respectively, $f_{c,\infty}$ and $W_{b,\infty}$ are the ultimate compressive strength and bound water content values at infinite time. In this study, the ultimate compressive strength is taken as the measured strength value at 28 days (Fig. 4.11), while the ultimate bound water content is taken as the measured value at 180 days (Fig. 5.2). τ and β are the time and shape parameters respectively. Parameters of this fitting models for the studied AASF mixes are given in Table. 6.4.

Table 6.4: Parameters of the exponential fitting model for compressive strength and bound water content in the studied AASF samples.

Mix	From compressive strength model			From bound water content model		
	$f_{c,\infty}$ [MPa]	τ	β	$W_{b,\infty}$ [%]	τ	β
SS-1.0	76.00	1.06	0.88	17.80	0.20	0.56
SC-0.7	71.80	1.87	1.04	15.65	0.71	0.62
SC-0.6	81.16	1.51	0.88	15.98	0.21	0.60
Su-0.7	70.18	2.30	1.07	14.90	0.71	0.69
Su-0.6	77.00	1.81	0.93	16.00	0.39	0.58

The comparison between the measured and predicted autogenous shrinkage using compressive strength and bound water content parameters is given in Fig. 6.18. The predicted autogenous shrinkage with both approaches corresponds well with the measured autogenous shrinkage. The compressive strength approach predicts the autogenous shrinkage of SS-1.0 quite well at early ages (Fig. 6.18a). However, after 7 days, significant deviation is observed between predicted and experimentally measured results. This error can be attributed to the reduced strength of matrix due to the formation of microcracks induced by large autogenous shrinkage.

On the other hand, the relative error on the predicted autogenous shrinkage by bound water content and compressive strength reaches in average ± 5% during early ages (< 7 days) in samples with sodium carbonate and sodium sulfate. This error is probably attributed to sampling methodology and TGA bound water calculation. Overall, both compressive strength and bound water content can be considered as good predictors for autogenous shrinkage in AASF cements.

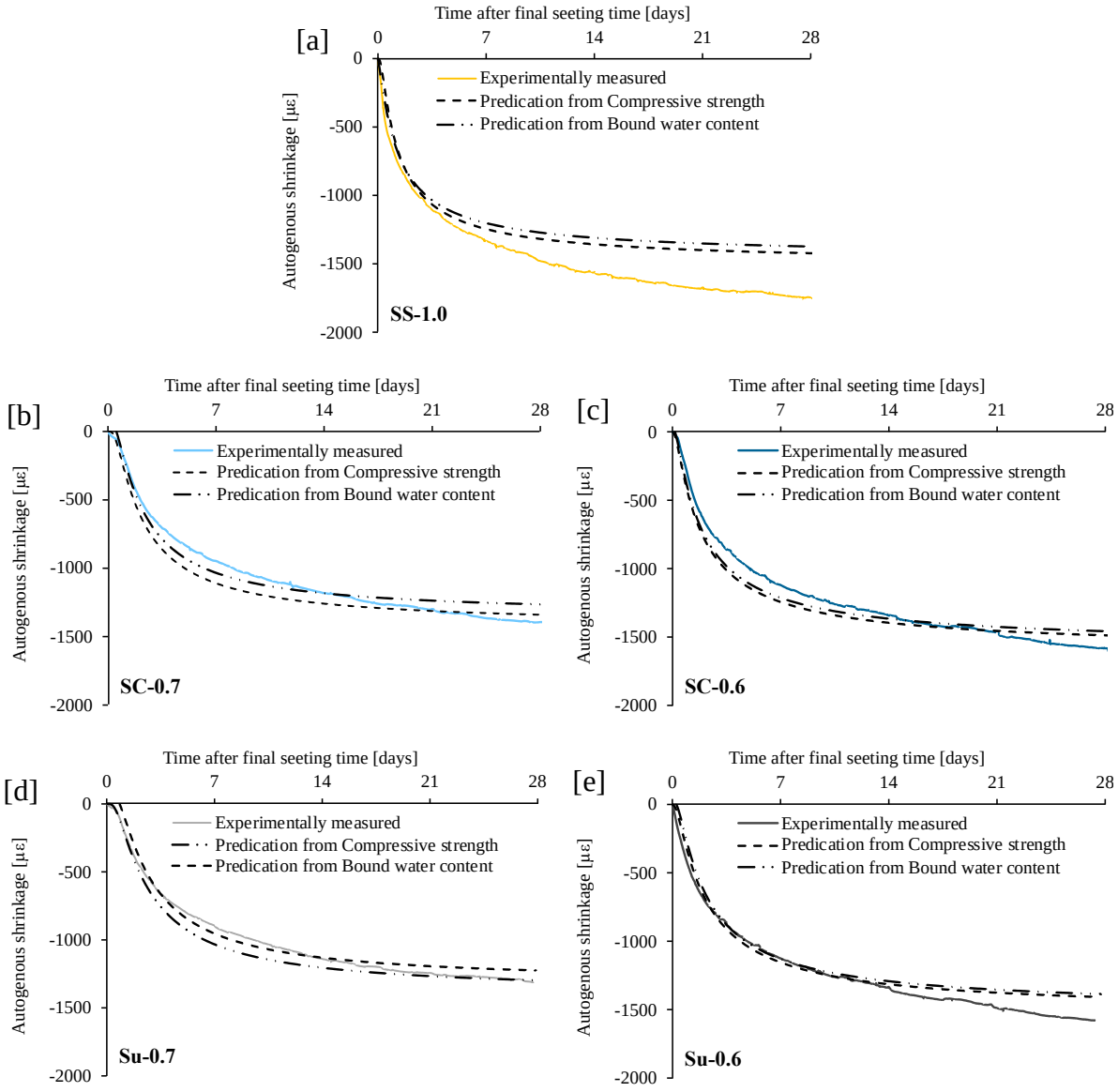

Figure 6.18: Predicted autogenous shrinkage from compressive strength and bound water content in AASF samples activated with SS-1.0 [a], SC-0.7 [b], SC-0.6 [c], Su-0.7 [d], and Su-0.6 [e].

6.7.2 Prediction from ultrasonic P-wave velocity (UPV) measurements

UPV testing is a well-established non-destructive testing method used to monitor the setting behavior and the mechanical properties of the cementitious materials. From a particle point of view, exploring a relation between autogenous shrinkage and ultrasonic measurements is definitely beneficial for engineers to estimate the autogenous shrinkage at various ages quickly and easily in actual projects. Fig. 6.19 shows the correlation between measured UPV values and autogenous shrinkage of AASF mortar samples, up to 7 days.

With increasing the ultrasonic P-wave velocity measurements, the autogenous shrinkage strains of AASF increases gradually over time. Due to the chemical reaction or hydration and drop of internal relative humidity, self-desiccation is induced and causes autogenous shrinkage. When the reaction is going on, the density of the matrix increases due to the formation of reaction products and this leads to an increase in the ultrasonic P-wave velocity. An exponential function is utilized to predict the autogenous shrinkage of AASF cements based on the results of ultrasonic measurements, as given in Eq. 6.13.

$$\varepsilon_{auto} = 0.59.\, exp^{(0.002.V_p)} \tag{6.13}$$

Where, ε_{auto} is the autogenous shrinkage and V_p is the ultrasonic P-wave velocity of the AASF mortar samples.

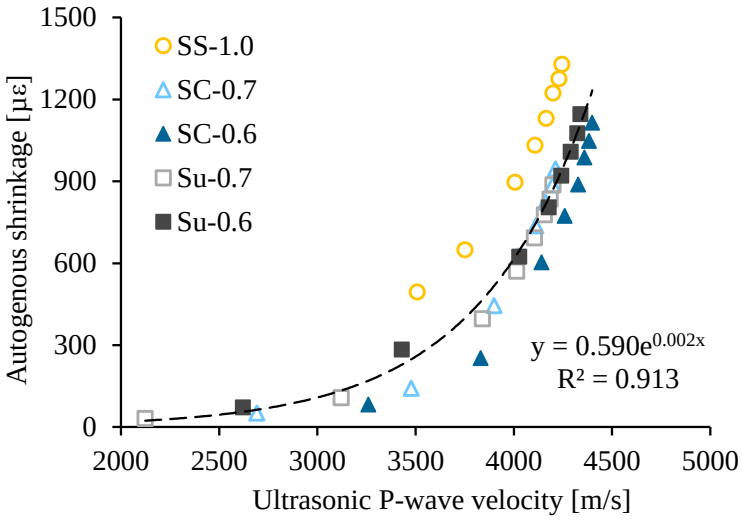

Figure. 6.19: Correlation between the measured autogenous shrinkage and ultrasonic P-wave velocity of mortar samples.

Fig. 6.20 presents the comparison between measured and predicted autogenous shrinkage strains of AASF mortar samples, up to 7days. As observed, the deviation between measured and predicted strains values for the studied AASF mortar samples is rather small for all studied AASF samples expected from SS-1.0. The large deviation in the samples activated with SS-1.0 may be attributed to its large autogenous shrinkage behavior, which influences the evolution of the ultrasonic measurements due to loss of contact between the probes and the sample (as explained in Chapter 4). Nevertheless, the results suggest that the proposed model using ultrasonic P-wave velocity measurements could be utilized to predict the autogenous shrinkage with an error in average less than +8% for the AASF cements.

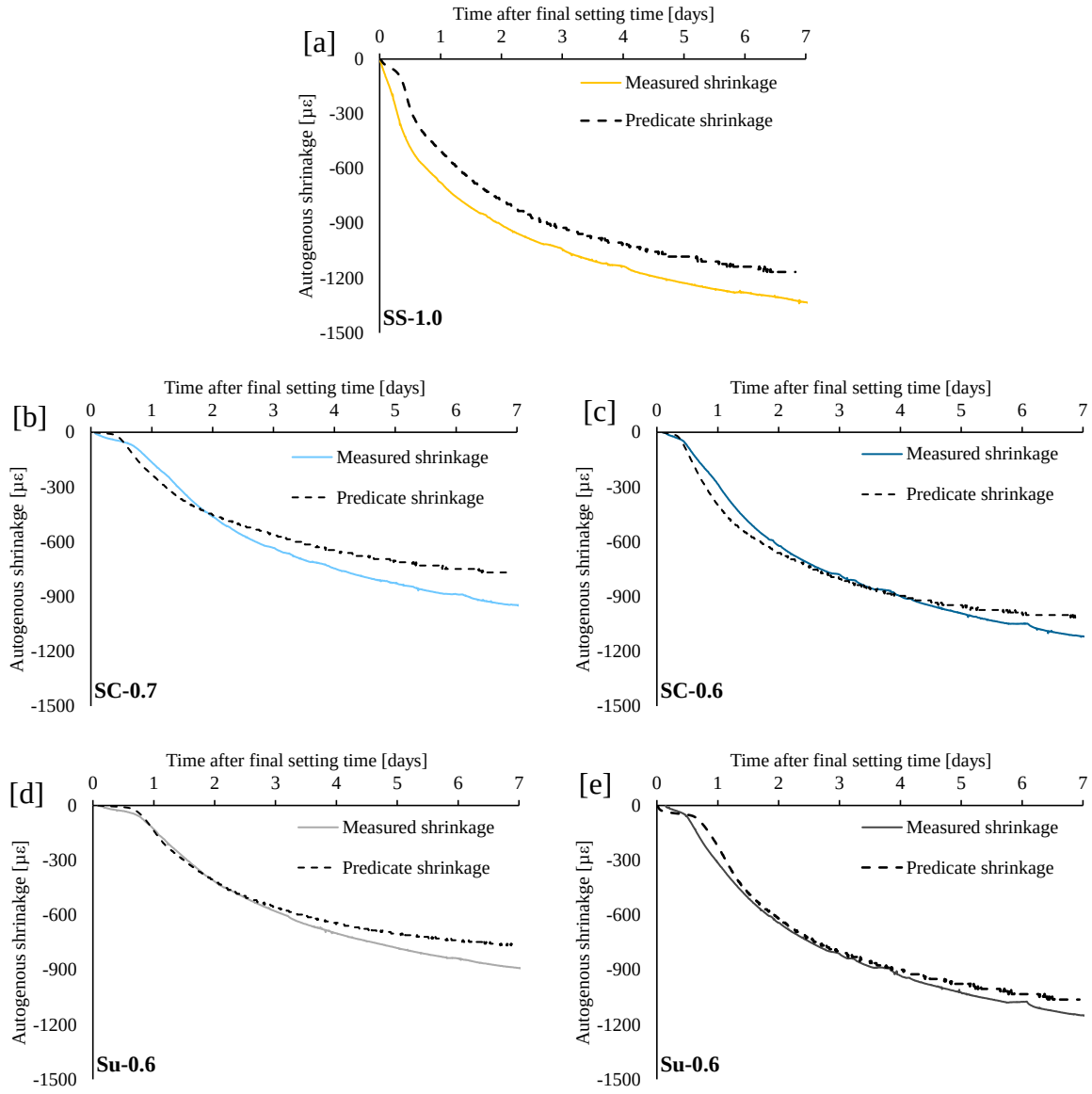

Figure 6.20: Predicted autogenous shrinkage from ultrasonic measurements in AASF samples activated with SS-1.0 [a], SC-0.7 [b], SC-0.6 [c], Su-0.7 [d], and Su-0.6 [e].

6.7.3 Prediction from existing models of OPC-based materials

To estimate the autogenous shrinkage in OPC-based materials, two different empirical formulas are reported in different standard codes using parameters as compressive strength and internal RH:

Eurocode 2 [209]

$$\varepsilon_{auto}(t) = 2.5.(f_c - 10).\left[1 - exp\left(-0.2.\sqrt{t}\right)\right] \quad (6.14)$$

ACI 209 [312]

$$\varepsilon_{auto}(t) = 780.\left(\frac{t}{35+t}\right).(1.4 - 0.01RH) \text{ when } 40 \leq RH \leq 80 \quad (6.15)$$

$$\varepsilon_{auto}(t) = 780.\left(\frac{t}{35+t}\right).(3.0 - 0.03RH) \text{ when } 80 < RH \leq 100 \quad (6.16)$$

ε_{auto} is the autogenous shrinkage, f_c is the compressive strength at 28 days, RH is the internal relative humidity, and t is the time in days. Fig. 6.21 shows the predicted autogenous shrinkage using above empirical formulas for the studied AASF samples. As observed, the autogenous shrinkage predicted using Eurocode 2 and ACI 209 models deviate significantly from the experimentally measured results shown in Fig. 6.4, both at early ages and later ages. These findings indicate that the empirical models developed for predicting autogenous shrinkage in OPC-based materials are not applicable for the AASF cements.

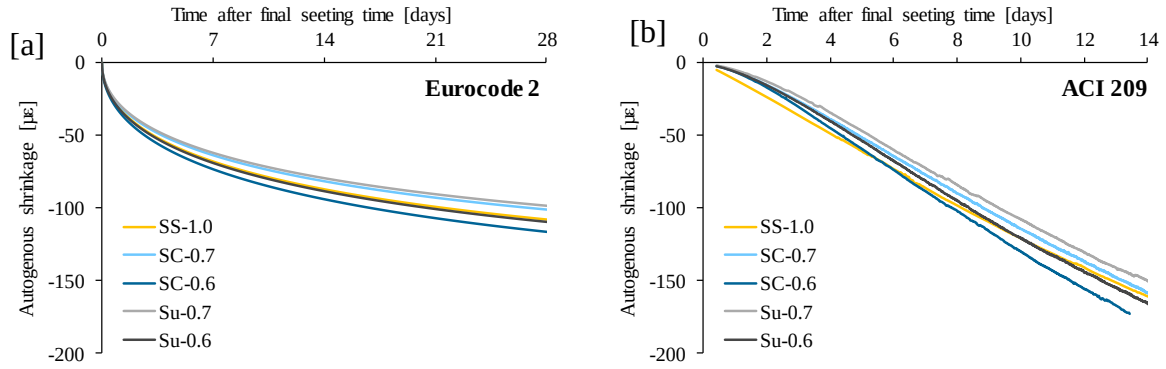

Figure 6.21: Predicted autogenous shrinkage from Eurocode 2 [a] and ACI 209 [b].

6.8 Conclusions

In this chapter, the basic mechanism of autogenous shrinkage in AASF cements is explored through an interlink assessment of reaction kinetics, reaction products, reaction chemistry, pore structure and stiffness development. The influence of the incorporation of sodium carbonate

and sodium sulfate on the autogenous shrinkage of sodium silicate-activated samples was investigated. The capillary tension in the pore fluid is calculated and related to the measured autogenous shrinkage, in order to understand the influential role of self-desiccation on the autogenous shrinkage in AASF. Based on the experimental results, the following conclusions can be drawn:

- The partial substitution of sodium silicate with sodium carbonate and sodium sulfate significantly reduces the autogenous shrinkage, particular at early ages. Approximately 50-75% reduction in the autogenous shrinkage is obtained during the first 24 hours when sodium carbonate and sodium sulfate solution are incorporated.
- The chemical shrinkage is mainly attributed to the reaction degree rather than the phase assemblage in the studied AASF samples.
- Besides the self-desiccation process, the Si polycondensation reaction at the solid-liquid interface is also responsible for a certain amount of the autogenous shrinkage, particularly in the induction stage of the UPV curves or heat flow curves.
- With incorporation of sodium carbonate and sodium sulfate, the chemical shrinkage decreases, and the pore structure of sodium silicate-activated samples becomes coarser due to a decrease in rate of reaction. As a result, the self-desiccation process and the capillary tension in the pore fluid decrease and this results in a lower autogenous shrinkage.
- Increasing the concentration of sodium carbonate and sodium sulfate solutions results in higher autogenous shrinkage due to the increase of the self-desiccation process and the capillary tension in the pore fluid.
- Capillary stress in the pore fluid induces both the elastic deformation and the time-dependent creep or viscoelastic deformation. In which, the viscoelastic deformation under capillary stress is more dominant in the autogenous shrinkage of AASF cement.
- Samples activated with only sodium silicate exhibit a pronounced viscoelastic deformation due to the incorporation of more alkali-cations (Na^+) into C-A-S-H gel. The partial substitution of sodium silicate with sodium carbonate and sodium sulfate significantly reduces the intake of alkali-cations into the gel structure and improves the stability of the reaction products. As a result, the creep-part of the autogenous shrinkage associated to the movement of C-A-S-H under internal pressure is reduced remarkably when sodium carbonate and sodium sulfate solution is incorporated.

- Partial substitution of sodium silicate with sodium sulfate does not lead to formation of expansive phases like ettringite to compensate the autogenous shrinkage in AASF cements.
- Predicting models using parameters like compressive strength, TGA bound water content and ultrasonic P-wave velocity are found to be applicable to predict autogenous shrinkage in the studied AASF cements accurately, regardless of type and concentration of activator.
- Models developed for predicting autogenous shrinkage in OPC-based materials are not applicable for AASF cements.

Chapter 7

Autogenous shrinkage cracking tendency

7.1 Introduction

The use of alkali-activated slag (AAS) has gained popularity since it has been reported that they develop superior or comparable engineering properties to OPC-based materials. Moreover, they have low environmental footprints. However, the marketability and acceptance of alkali-activated slag in the construction industry are hindered mostly due to the concerns related to uncertainties in their long-term durability performance as a consequence of early-age shrinkage cracking [189, 15]. The results from the previous chapter manifested that the studied alkali-activated slag/fly-ash (AASF) mixes have pronounced autogenous shrinkage during the first days after casting which is expected to cause severe cracking problems under restrained conditions. On the other hand, it has been reported that high autogenous shrinkage itself is not necessarily the main factor explaining the high cracking tendency under restraint condition. Some other factors can also influence the cracking potential during early ages, including restraint degree, time-dependent properties of the material such as tensile strength and elastic modulus, and stress relaxation [313, 314]. Among these, stress relaxation or creep effect is reported as an important parameter that needs to be considered in predicting the shrinkage induced stresses and further to evaluate the cracking potential in elements under restraint condition [315]. Nevertheless, very few studies have reported the combined effect of autogenous shrinkage, stress relaxation, tensile strength and stiffness development on the cracking tendency of alkali-activated cements [189]. In this chapter, an attempt has been made using a ring test to determine the stress relaxation parameter and study the cracking potential of AASF cements.

First, the time-dependent properties of the AASF mortar samples are computed from experimentally measured values using the exponential fitting functions. Secondly, stresses including both theoretical elastic stresses and actual residual stresses in restrained mortar rings

are quantified by using the measured inner steel ring strains. Thirdly, the creep related stress relaxation is evaluated by comparing the calculated theoretical elastic stress and actual residual stress to better understanding the cracking resistance of AASF mortars. Finally, the cracking potential is measured as a function of time by relating the actual residual stress developed in the mortar ring due to restrained autogenous shrinkage and the time-dependent tensile strength of the material.

7.2 Restrained ring test

Autogenous shrinkage in hardening concrete can result in the development of residual tensile stresses if deformations are restrained. Restraint in concrete is an unavoidable issue and can be internally and externally based on its origin, i.e. due the concrete itself or its surroundings. Internal restraint in autogenous shrinkage can be contributed from reinforcement, aggregates, and anhydrous cement particles, while the external restraint mainly arises from the adjacent structures. If residual tensile stresses developed due to restraint of autogenous shrinkage exceed the tensile strength of concrete, cracking occurs and can cause serious threat to materials and structural durability through service life. Two testing methods have been developed to assess the cracking potential of concrete under restraint conditions, as reported in a recent review paper [316]. Some studies utilize either Active-restraint [317, 318], in which a hydraulic or electric force is applied to restrain the volume changes in concrete or Passive-restraint [319, 320], which provides rigid restraint in concrete to limit the volume changes. Among these two methods, Passive-restraint with a ring test is a commonly used method to assess the concrete potential for shrinkage cracking due to its simplicity in interpreting data and cost effectiveness compared to the Active-restraint test method.

The American Society of Testing Material (ASTM C1581) [321] recommends a ring test with specific dimensions to estimate the early-age cracking tendency of cement-based materials under restraint shrinkage conditions. Many researchers have been quantifying the potential of shrinkage cracking in cementitious materials by using a ring test with different dimensions, other than ASTM standard ring [316, 322]. Furthermore, several modifications have been implemented to the standard ring test, such as pressurizing ring to fully restrain the shrinkage in concrete [323]. Eccentric and elliptic ring tests were employed to investigate the early-age shrinkage cracking more effectively, since these geometries have the ability to generate higher concentration of residual tensile stresses and thus increase the cracking sensitivity of concrete at early ages [322, 324]. Although the procedure of ring test to restraint shrinkage in concrete

is similar in each of these approaches, the ring geometry and boundary conditions have significant influence on quantifying the potential of shrinkage cracking in concrete [325, 326].

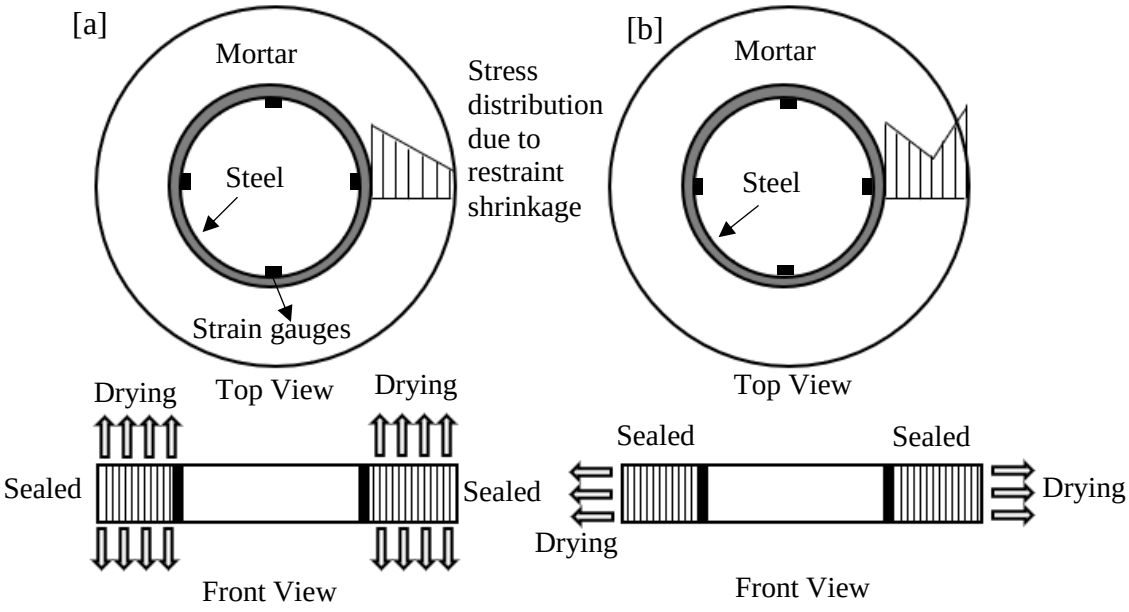

Figure 7.1: Restrained ring test: Stress distribution based on the boundary conditions; autogenous condition and/or drying from top and bottom [a], drying from outer circumference [b] [327, 328].

According to ASTM C1581 [321] and AASHTO PP34-99 [329] standards, the ring test basically consists of two rings including a concrete ring and a steel ring. The shrinkage of the concrete ring is restrained by the steel ring and induces stresses in the concrete ring and surface pressure on the outer surface of the restraining steel ring. The resultant deformations in the steel ring are measured by using four strain gauges attached to the inner side of the steel ring as shown in Fig. 7.1. The sudden drop in the steel ring deformation indicates the formation of a macro-crack or visible crack in the concrete ring. The age of macro-cracking in the concrete under restraint is mainly dependent on the restrained ring dimension and tensile stress distribution over the cross section in the concrete ring. If the concrete ring is completely sealed (autogenous shrinkage) or circumference shrinkage is uniform in radial direction, the maximum circumference stress occurred at the inside of the concrete ring and decreases along the radius (Fig. 7.1a) [327, 328]. If concrete dries from the outer circumference (drying shrinkage), the shrinkage occurs non-uniformly in a radial direction and develops eigenstresses by moisture gradient, making stress analysis more difficult. In this case, the maximum circumference stress or hoop stress can occur at the inner side or outer side of the concrete ring as shown in Fig. 7.1b [327, 328]. To overcome this issue, it is suggested to dry concrete ring

from top and bottom [330, 331]. As a result, the moisture gradient will become uniform along the radial direction of the specimen and therefore the maximum hoop stresses occur at the inner side of the steel ring. In this case, the maximum hoop stresses developed due to restrained autogenous shrinkage can be computed from the measured steel ring deformations.

7.3 Time-dependent properties

7.3.1 Tensile strength

In literature, it has been reported that there is a linear correlation between the uniaxial tensile strength (also known as direct tensile strength) and the splitting tensile strength for hardened concrete [332, 209]. It is generally accepted that these relationships are also valid for early-age measurements [333]. Due to difficulty in measuring the direct tensile strength, which is an important parameter that influences the cracking potential of materials, such relationships are very useful for the characterization of the tensile behavior of materials with simple test such as brazilian test or splitting tensile test.

$$f_{ct} = 0.9.f_{ct,sp} \tag{7.1}$$

In this study, the direct tensile strength (f_{ct}) is calculated from the splitting tensile ($f_{ct,sp}$) results (Fig. 4.15) using Eq. 7.1, according to EN 1992-1-1 [209] and plotted in Fig. 7.2.

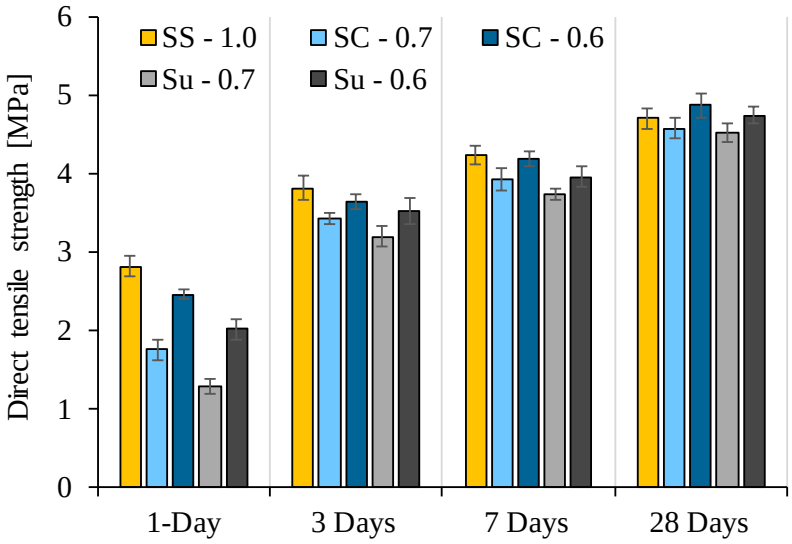

Figure 7.2: Calculated direct tensile strength of AASF mortar samples.

The time-dependent direct tensile strength of AASF mortar samples is modeled using an exponential fitting function (Eq. 7.2) and plotted in Fig. 7.3.

$$f_{ct}(t) = F_{ct,\infty} \cdot \exp\left(-\left[\frac{\tau}{t}\right]^{\beta}\right) \quad (7.2)$$

$F_{ct}(t)$ is direct tensile strength at time t and $f_{ct,\infty}$ is the "ultimate" value for the direct tensile strength, referred as the 28 days value in this study, τ and β are the time and shape parameters, respectively.

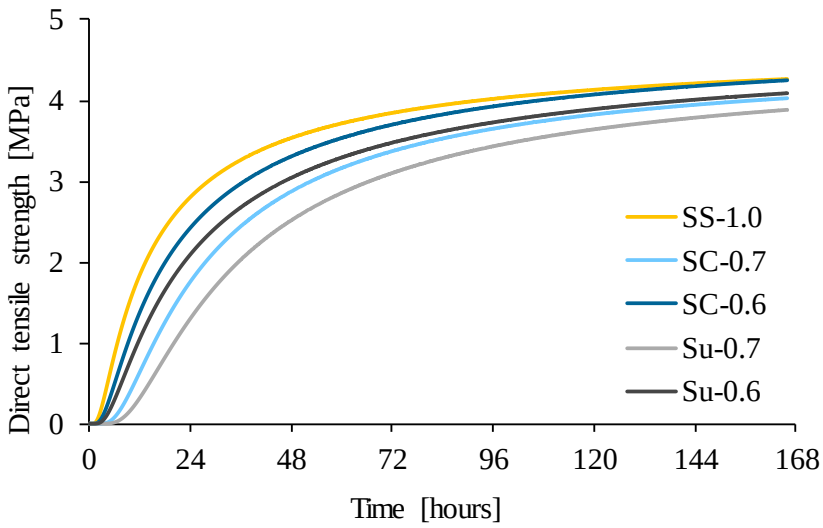

Figure 7.3: Time-dependent direct tensile strength.

7.3.2 Static elastic modulus

The static elastic modulus is an essential parameter, required to quantify the cracking potential of AASF mortar samples under restrained conditions. In this study, the time-dependent static modulus of elasticity is calculated from the dynamic elastic modulus, which is continuously monitored from the ultrasonic measurements. The static elastic modulus (E_s) of the AASF mortar samples is calculated from the dynamic elastic modulus (E_d) by using Eq. (7.3), derived from Fig. 4.23 and plotted in Fig. 7.4.

$$E_s(t) = 1.15\,(E_d) - 16.50 \quad (7.3)$$

7.3.3 Free autogenous shrinkage

The linear autogenous strain measured from corrugated polyethylene tubes (reported in Chapter 6) is considered as the free autogenous shrinkage in the present study. The early-age autogenous shrinkage recorded starting from final setting time for the studied AASF mortars is shown in Fig. 7.5. To summarize, samples activated with sodium silicate (SS-1.0) have

higher autogenous shrinkage compared to those samples with sodium carbonate (SC) and sodium sulfate (Su). This is mainly attributed to the formation of a dense microstructure in samples with high silica content, leading to higher capillary stress, and consequently to higher autogenous shrinkage related to self-desiccation (Chapter 6). Also, the increase in autogenous shrinkage with increase in concentration of activator is associated to a higher degree of reaction and a denser matrix formation. At the same concentration (Na_2O), samples with sodium carbonate have slightly higher autogenous shrinkage compared to samples with sodium sulfate due to acceleration of reaction kinetics with formation of calcite as explained in Chapter 4.

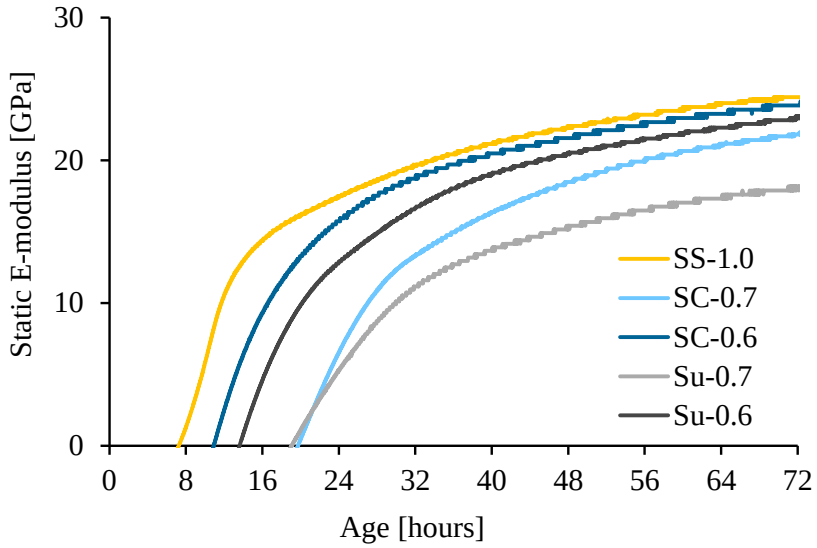

Figure 7.4: Time-dependent static elastic modulus of the AASF mortar samples.

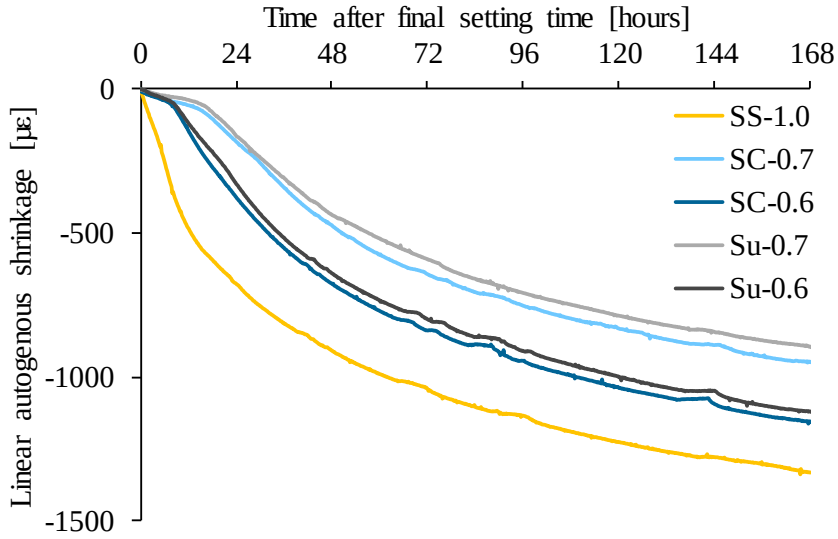

Figure 7.5: Early-age free autogenous shrinkage of AASF mortar samples.

7.4 Measured inner steel ring strains

The strain, which develops in the inner steel ring due to restrained autogenous shrinkage, is continuously monitored by using ring test detailed in Fig. 3.10 (Chapter 3). The average inner steel ring strains are shown in Fig. 7.6. All results are plotted from the time of final setting, derived from standard Vicat needle test (Fig. 4.8). The inner steel ring strains are close to zero during early hours for samples with sodium carbonate (SC) and sodium sulfate (Su). For example, in samples activated with SC-0.7 and Su-0.7 the inner steel ring starts to deform at approximately 22 hours (Fig. 7.6). However, in samples activated with only sodium silicate (SS-1.0) the first strains are measured at only 6 hours. Thereafter the inner steel strains rapidly increase with curing age. These results imply that the activator used in the AASF mortars follows this order in stiffness development at early hours: sodium silicate > sodium carbonate > sodium sulfate. These results are in agreement with the static elastic modulus results derived from the ultrasonic measurements (Fig. 7.4).

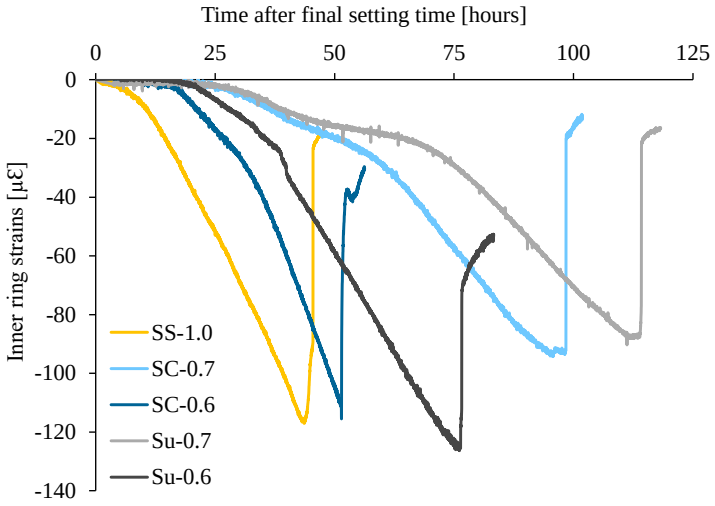

Figure 7.6: Measured strains in the restrained inner steel ring.

The rate of strain development due to restrained autogenous shrinkage in sodium silicate-activated samples is significantly reduced with incorporation of sodium carbonate and sodium sulfate solutions as shown in Fig. 7.6. Samples with sodium carbonate result in a higher rate of strain development compared to the samples with sodium sulfate at the same concentration.

The observed sudden change in the measured steel strains can be attributed to the age of cracking in the restrained ring specimens. The partial substitution of sodium silicate with sodium carbonate and sodium sulfate prolonged the time of cracking in AASF mortars (Fig.

7.7). At equal replacement of sodium silicate with sodium carbonate and sodium sulfate, the improvement in the cracking resistance is higher for the samples with sodium sulfate. This is expected due to a reduced elastic modulus (Fig. 7.4), which delays the development of restraint stresses and thus age of cracking. The results also show that with a decrease in the concentration (Na_2O) of sodium carbonate and sodium sulfate solutions, the time of cracking is delayed (Fig. 7.7). This is the result of the decrease in autogenous shrinkage rate and elastic modulus in samples with lower concentration of sodium carbonate (SC-0.7) and sodium sulfate (Su-0.7) solutions.

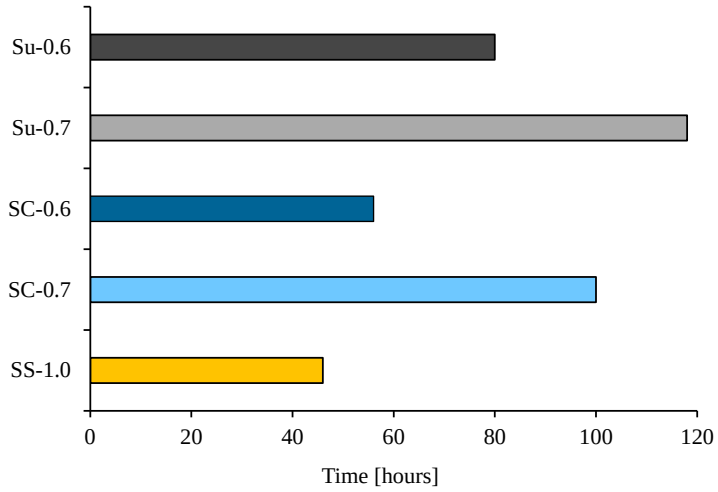

Figure 7.7: Age of macro-cracking or visible crack in AASF mortar samples.

The maximum strains at the age of cracking increased with the increase in concentration (Na_2O) or decrease in alkali-modulus of the activator. For example, the absolute value of the strain in the restrained steel ring at the age of cracking is around 90-95 με for samples activated with SC-0.7 and Su-0.7 (Fig.7.6). These values increased to around 115-125 με with increasing the concentration of the sodium carbonate (SC-0.6) and sodium sulfate (Su-0.6) solutions.

Fig. 7.8 shows the measured strains in the restrained inner steel ring as a function of cumulative heat release. The measured strain developed in the restrained steel ring is nearly zero although the cumulative heat release increases continuously at early ages. This implies that significant amount of heat is released before the development of sufficient stiffness or elastic modulus which is required to restrain the autogenous shrinkage. Nevertheless, it can be noticed that the cumulative heat release at the age of cracking is almost similar (160-180 J/g) for all studied AASF mixtures.

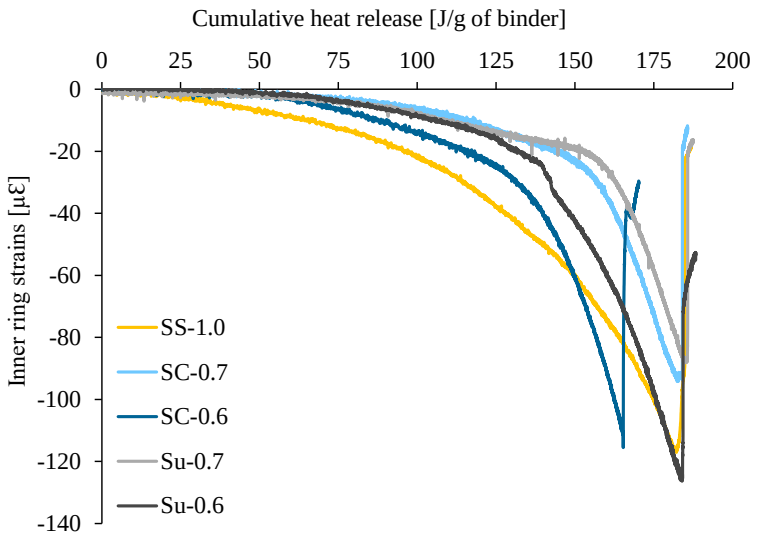

Figure 7.8: Measured strains in the restrained steel ring against cumulative heat release.

7.5 Quantitative analysis of the restrained ring test

Due to restraint, the autogenous shrinkage induces an internal tensile stress and leads to cracking if these stresses exceed the tensile strength of the mortar as explained above. There are two stress quantities that are important, the actual residual stress (σ_{act}) and the theoretical-elastic stress (σ_{ela}). The actual residual stress (σ_{act}) occurs if mortar deformation is restraint by the inner steel ring while the theoretical elastic stress (σ_{ela}) occurs if the mortar deformation is purely elastic or without any restraint effect from the inner steel ring on the mortar deformation (i.e. creep related stress relaxation is not consider). Comparison between the actual residual stress (σ_{act}) and the theoretical elastic stress (σ_{ela}) provides an information about the stress relaxation that influences the cracking potential of the material.

7.5.1 Determination of the actual residual tensile stress

The measured strains in the restrained steel ring can be used to compute the residual tensile stresses in the mortar by assuming the elastic behavior of mortar [315, 327, 334, 335]. To do this the restraint ring test is separated as the mortar cylinder pressurized at the inner surface and a steel cylinder with equal and opposite pressurized at outer surfaced as shown in Fig. 7.9 [327]. For developing the same amount of strains as those obtained in the restraint inner steel ring, the corresponding pressure (termed as actual pressure (P_{act})) is generated on the mortar ring, as expressed in Eq. (7.4) [336].

$$P_{act} = -\varepsilon_{st}.E_{st}.\frac{(R_{os}^2 - R_{is}^2)}{2.R_{os}^2} \quad (7.4)$$

R_{is} and R_{os} are the inner and outer radius of the inner steel ring; ε_{st} is the mean strain in the restraint inner steel ring, measured continuously by using strain gauges mounted at the inside of the steel ring (με); E_{st} is the elastic modulus of the steel (E_{st} = 150 GPa).

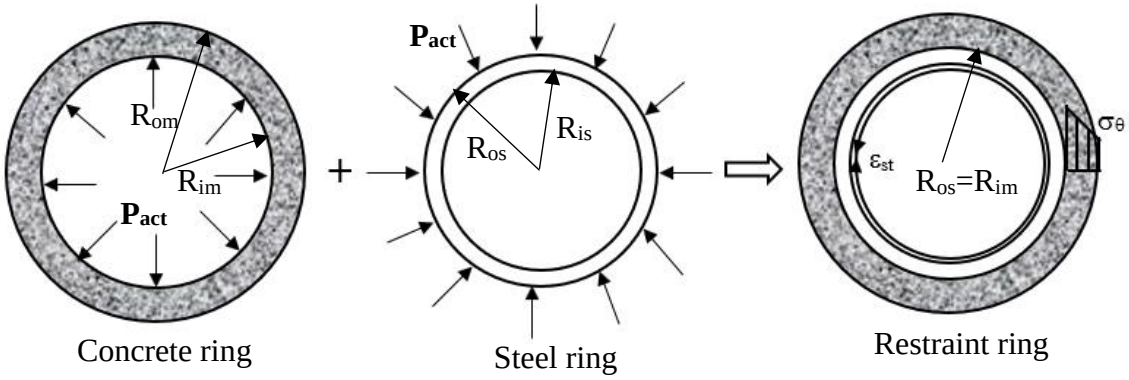

Figure 7.9: Scheme of restraint ring test [327].

$$\sigma(r) = P_{act} \cdot \left[\frac{\frac{1}{R_{om}^2} + \frac{1}{r^2}}{\frac{1}{R_{im}^2} - \frac{1}{R_{om}^2}}\right] \quad (7.5)$$

A thick-wall solution is commonly applied to evaluate the tensile stresses in an elastic pressurized ring, in contrast to the thin-wall solution which neglects the fact that the circumference or hoop stress is not constant along the radial direction [337]. Moreover, it has been reported that a cylinder is considered to be thick, if the ratio of ring thickness to the inner radius is greater than 1/20 [338]. Since this is the case for the restraint ring setup used in this study, a thick-wall solution is applied to analyze the stress distribution in the pressurized rings. By considering the mortar ring as a thick-wall cylinder under pressure (P_{act}) with inner and outer radius of R_{im} and R_{om}, the circumferential or hoop stress at any radius (r) of the ring can be calculated using Eq. (7.5) [339].

In case of autogenous shrinkage, the maximum hoop stress occurs at the inner radius of the mortar ring (R_{im}) and it is proportional to the measured strains in the steel ring [327, 328]. The maximum hoop stress at the inner radius (r = R_{im}) can be calculated by using Eq. (7.6). Substituting Eq. (7.4) in Eq. (7.6) provides the maximum hoop stress or actual residual stress at the inner radius of the mortar ring, as shown in Eq. (7.7).

$$\sigma(r = R_{im}) = \sigma_{act,max} = P_{act} \cdot \left[\frac{R_{im}^2 + R_{om}^2}{R_{om}^2 - R_{im}^2}\right] \quad (7.6)$$

$$\sigma_{act,max} = -\varepsilon_{st}.E_{st}.\frac{(R_{os}^2 - R_{is}^2)}{2.R_{os}^2}.\left[\frac{R_{im}^2 + R_{om}^2}{R_{om}^2 - R_{im}^2}\right] \quad (7.7)$$

The actual residual stresses that were calculated using Eq. (7.7) for the investigated AASF mortar samples are shown in Fig. 7.10. It is evident from Fig. 7.10 that the partial substitution of sodium silicate with sodium carbonate and sodium sulfate decreases the rate of residual tensile stress of the mortar ring. This decrease in stress level is attributed to the fact that incorporation of sodium carbonate and sodium sulfate reduces the rate of autogenous shrinkage and stiffness development of sodium silicate-activated samples (Fig. 7.4 & Fig. 7.5). Similarly, samples activated with sodium sulfate have lower rate of residual stresses compared to the samples activated with sodium carbonate at the same concentration, as shown in Fig. 7.10. Also, the results show that the actual residual stress decreases with increase in alkali-modulus from 0.6 to 0.7 or decrease in concentration (Na_2O) of sodium carbonate and sodium sulfate activators. These results suggest that both the concentration and nature of anions present in the activating solution affect the actual residual tensile stress in the restraint AASF mortar ring.

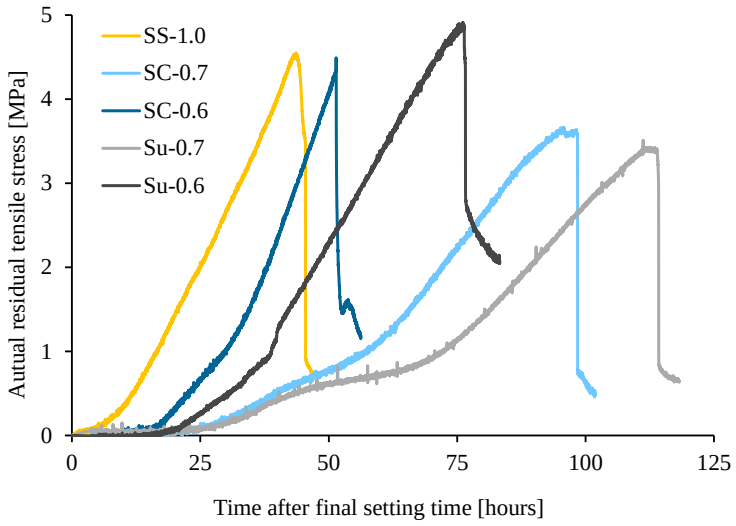

Figure 7.10: Actual residual stresses developed in AASF mortar rings.

7.5.2 Determining the theoretical elastic stress

As explained above, the theoretical elastic stress occurs if the mortar is deformed purely elastically or if no creep occurs. In this study, the theoretical elastic stress in the mortar ring is

calculated with 'shrinkage-fit' approach as suggested in previous studies [327, 334, 335] (Fig. 7.11). It is assumed that no gap exists between the steel and mortar ring before mortar starts shrinking, i.e. the boundary condition $R_{os} = R_{im}$ is valid as shown in Fig. 7.11a. To compute the theoretical elastic stress which develops in the mortar ring due to shrinkage without any restraint effect, it is assumed that the inner steel ring is temporary removed and allows the mortar ring to shrink freely, as shown in Fig. 7.11b. The magnitude of radial displacement U_{free} of the unrestrained mortar ring can be calculated by using Eq. (7.8) in which ε_{auto} is the measured autogenous shrinkage strain (Fig. 7.5) and R_{im} is the inner radius of the mortar ring.

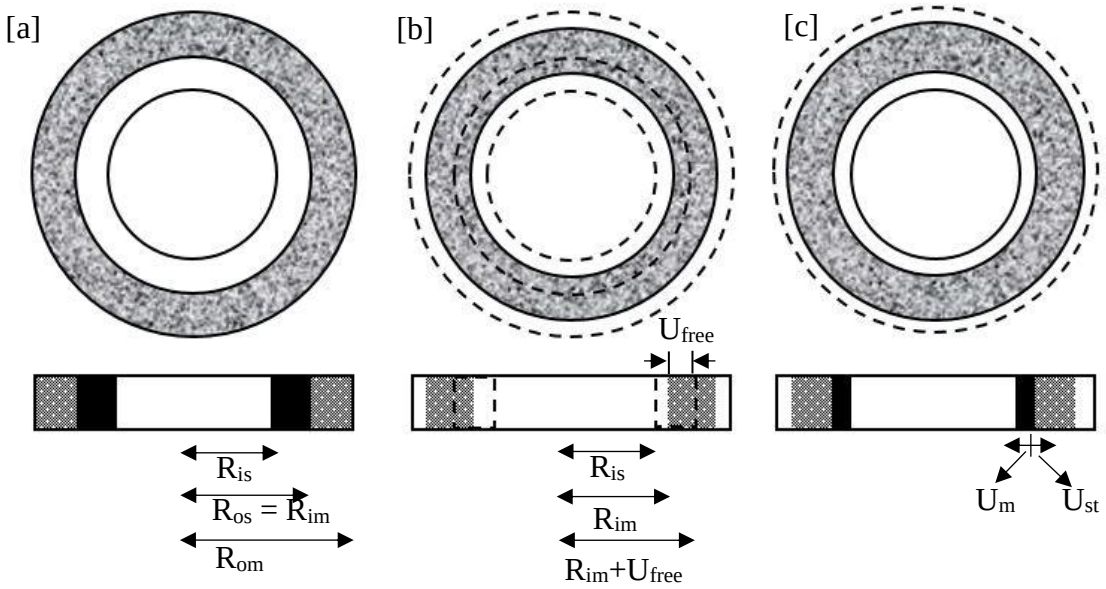

Figure 7.11: Scheme of the ring to determine the theoretical-elastic stress; initial condition without shrinkage [a]; allowing mortar to shrinkage without restraint [b]; elastic deformation to satisfy boundary conditions [c].

$$\left|U_{free}\right| = R_{im} \cdot \varepsilon_{auto} \tag{7.8}$$

A 'shrinkage-fit' approach is applied to account the mismatch between the inner radius of the mortar ring (R_{im}+U_{free}) and outer radius of inner steel ring (R_{os}) by assuming a pressurizing force (P_{ela}) at the interface between steel and mortar ring [327, 340]. This interface pressure (P_{ela}) will compress the steel ring U_{st} by acting from the outside and expand the mortar ring U_m by acting from the inside, until the boundary conditions $R_{os} = R_{im}$ remain valid (Fig. 7.11c). The elastic deformation of the steel ring U_{st} and mortar ring U_m due to interfacial pressure P_{ela} can be calculated from Eq. (7.9) and Eq. (7.10). The sum of these displacements should equal to the free displacement U_{free}, Eq. (7.11), to satisfy the original boundary.

$$U_{st} = -P_{ela}.\left[\frac{R_{os}^2[(1+v_s).R_{is}^2 + (1-v_s).R_{os}^2]}{E_{st}.R_{os}.(R_{os}^2 - R_{is}^2)}\right] \quad (7.9)$$

$$U_m = P_{ela}.\left[\frac{R_{im}^2[(1+v).R_{om}^2 + (1-v).R_{im}^2]}{E_s.R_{im}.(R_{om}^2 - R_{im}^2)}\right] \quad (7.10)$$

$$U_{free} = U_{st} - U_m \quad (7.11)$$

E_{st} and v_s are the elastic modulus and Poisson's ratio of the steel, respectively (v_s = *0.25;* E_{st} = *150 GPa);* E_s and v are the static elastic modulus and Poisson's ratio of the mortar, respectively (v = *0.15).* The static elastic modulus of the mortar samples (E_s) evolves with time were calculated from ultrasonic measurements (Fig. 7.4) to facilitate the computation of the elastic deformations in the mortar ring. Substituting Eq. (7.9-7.11) leads to Eq. (7.12) for computing the increase in elastic pressure due to increase in free shrinkage.

$$\Delta P_{ela} = \frac{-\Delta\varepsilon_{sh}.E_s}{\frac{E_s.[(1+v_s).R_{is}^2 + (1-v_s).R_{os}^2]}{E_{st}.(R_{os}^2 - R_{is}^2)} + \frac{[(1-v).R_{os}^2 + (1+v).R_{om}^2]}{(R_{om}^2 - R_{os}^2)}} \quad (7.12)$$

From the interface pressure (P_{ela}), the maximum theoretical elastic stress due to shrinkage can be calculated by using the stress solution for a thick-wall cylinder under pressure (P_{ela}) as explained above (Eq. 7.13) and plotted in Fig 7.12.

$$\sigma_{ela,max} = P_{ela}.\left[\frac{R_{im}^2 + R_{om}^2}{R_{om}^2 - R_{im}^2}\right] \quad (7.13)$$

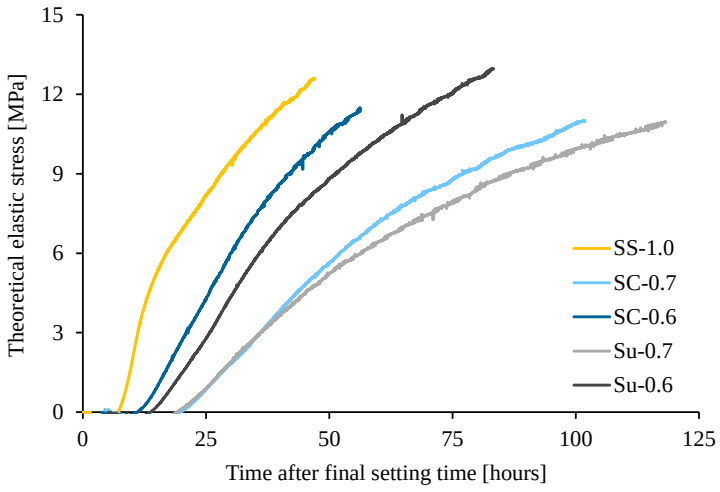

Figure 7.12: Predicted theoretical elastic stresses in the restrained AASF mortar ring.

The theoretical elastic stress essentially depends on the modulus of elasticity and the autogenous shrinkage as per Eq. 7.9-7.12. As a consequence of higher elastic modulus and/or higher autogenous shrinkage, the samples activated with higher silica content (SS-1.0) and alkali-content (SC-0.6 & Su-0.6) lead to much higher theoretical elastic stresses (Fig. 7.12). Similarly, samples with sodium carbonate (SC) resulted higher level of elastic stresses than samples with sodium sulfate (Su) at the same concentration.

7.5.3 Degree of restraint

The degree of restraint depicts how two elastic bodies are restrained by each other when a force (*P*) acts in between them. For the restrained ring tests, the degree of restraint can be expressed by the ratio of prevented to free radial displacement of the mortar rings (Eq. 7.14).

$$\varphi = \frac{U_{free} - U_{st}}{U_{free}} \times 100\% \qquad (7.14)$$

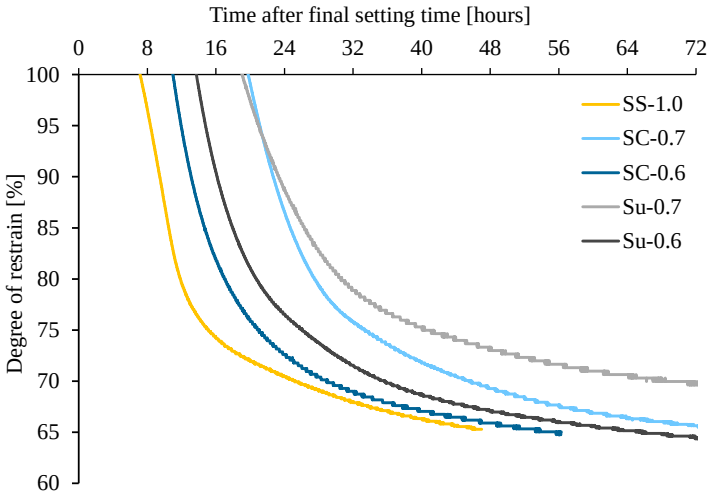

Figure 7.13: Calculated degree of restraint.

The computed degree of restraint for the studied AASF mortars up to first 72 hours is illustrated in Fig. 7.13. As observed, the degree of restraint decreases over time due to increase in stiffness development of the AASF mortar samples, as shown in Fig. 7.4. The restraint degree in samples activated with only sodium silicate (SS-1.0) decreases with higher rate and reaches to around 65% at the age of cracking (~45 hours). Reflecting to the slower development of elastic modulus, the restraint degree for samples with sodium carbonate and sodium sulfate decreases slowly during early hours and ends around 65-70% at 48 hours. With decreasing concentration (Na_2O) of sodium carbonate and sodium sulfate solutions, the restraint degree of sodium

silicate-activated samples increases (Fig. 7.13). Samples with sodium carbonate exhibit a different restraint degree compared to samples with sodium sulfate at the same concentration, as the stiffness development or elastic modulus of the mortar influence the behavior. These results imply that the restraint degree varies proportionally with the elastic modulus of the mortar samples.

7.5.4 Stress relaxation

As tensile stresses are developed in the mortar ring under restraint condition, tensile creep is created and counteracts the shrinkage strains. As a result, some amount of stresses induced by autogenous shrinkage is reduced and this benefits the cracking potential of the material. Thus, the creep related stress relaxation parameter is important for the prediction of actual stresses induced by autogenous shrinkage strains and further to evaluate the risk of cracking.

Once the theoretical-elastic stress is obtained, the stress relaxation defined as time-dependent decrease in stress due to constant deformation, can be quantified by calculating the difference between the theoretical-elastic stress and the actual hoop stress [327, 335, 337]. Fig. 7.14 shows the stress relaxation calculated using Eq. (7.15) for the studied AASF mortar samples.

$$Stress\ relaxation\ \sigma_{rel}(t) = \ \sigma_{ela,max}(t) - \sigma_{act,max}(t) \tag{7.15}$$

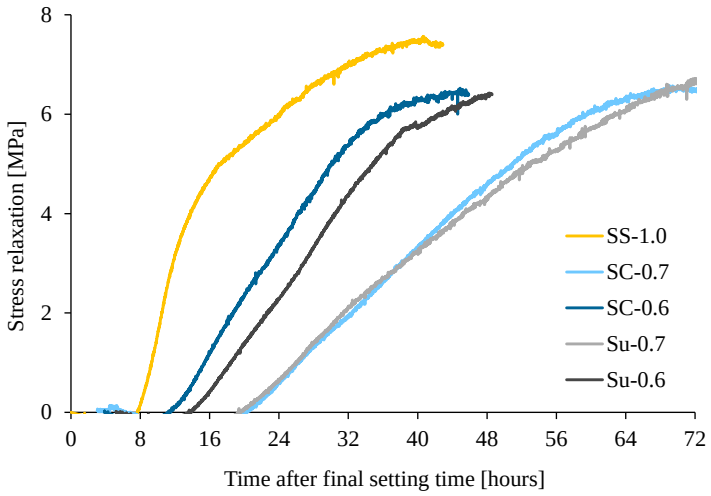

Figure 7.14: Estimated relaxed stress in AASF mortar rings.

As observed, the stress relaxation effect is more pronounced in samples activated only sodium silicate (SS-1.0). Fig. 7.14 also shows that the stress relaxation effect increases with increasing the concentration of sodium carbonate (SC-0.6) and sodium sulfate (Su-0.6) solutions. At equal replacement of sodium silicate by sodium carbonate and sodium sulfate, the samples with

sodium carbonate exhibits slightly higher relaxation than samples with sodium sulfate. Since the creep related stress relaxation is significant for the studied AASF samples, ignoring this effect would introduce a significant error in estimating the stresses induced by autogenous shrinkage and evaluating the cracking resistance at early ages.

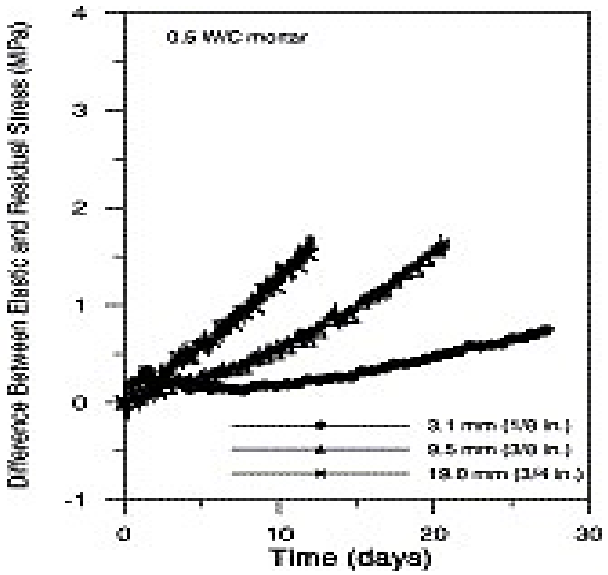

Figure 7.15: Estimated relaxed stress for OPC mortars with water-to-binder ratio of 0.5 [327]

By comparing with OPC mortar samples having a water-to-binder ration of 0.5 [327], the stress relaxation effect is significantly higher for the studied AASF cements (Fig. 7.14 & Fig. 7.15). Nevertheless, further investigation with the more standard creep or relaxation measurements is required to support this observation.

The creep factor calculated using Eq. (7.16) for a time interval from 0 to 24 hours is illustrated in Fig. 7.16. The creep factor indicates the level of stress eliminated in pure elastic behavior by relaxation or creep effect. The sample activated with sodium silicate (SS-1.0) has a creep factor of around 0.75 at the age of 24 hours. This indicates that 75% of the stresses induced by the elastic deformation are eliminated by stress relaxation effect. Incorporation of sodium carbonate and sodium sulfate in the activating solutions increases the creep factor during first 24 hours of sodium silicate-activated samples (Fig. 7.16). Also, the results show that the creep factor increases further with decreasing concentration of sodium carbonate (SC-0.7) and sodium sulfate (Su-0.7) solutions. Regardless of the concentration of the activator, samples with sodium sulfate demonstrated higher relaxation of elastic stress than the samples with sodium carbonate.

$$Creep\ factor\ \emptyset(t) = \frac{\sigma_{rel}(t)}{\sigma_{ela,max}(t)} \tag{7.16}$$

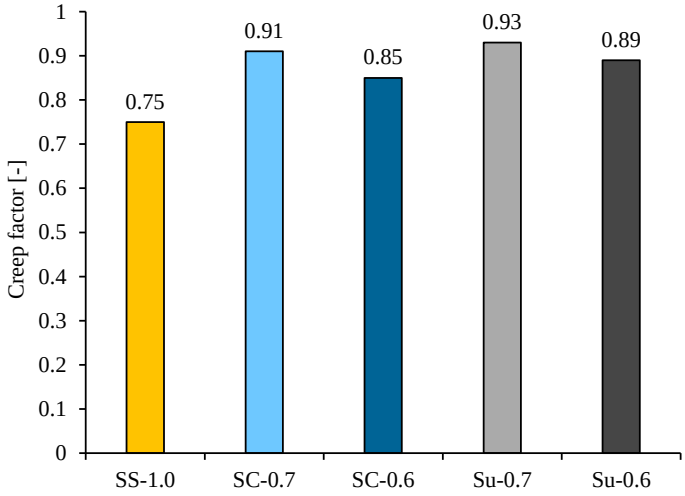

Figure 7.16: Creep factor up to the age of 24 hours.

7.5.5 Cracking potential

The autogenous shrinkage cracking potential of AASF mortar samples is simply computed by relating the actual residual stresses developed due to restrained autogenous shrinkage and the tensile strength development (Eq. 7.17). Fig. 7.17 shows the calculated autogenous shrinkage cracking potential of the studied AASF samples as a function of time. From Fig. 7.17, it is evident that the cracking potential ratio of AASF mortar samples decreases with decreasing the concentration of sodium carbonate and sodium sulfate solutions. This is explained by the fact that samples incorporated with sodium carbonate (SC-0.7) and sodium sulfate (Su-0.7) have lower autogenous shrinkage (Fig. 6.4) and lower elastic modulus or degree of restrain (Fig. 4.17).

$$Cracking\ potential = \frac{\sigma_{act,max}(t)}{f_{ct}(t)} \tag{7.17}$$

When the cracking potential is simply quantified as ratio between the residual tensile stress and the direct tensile stress, the theoretical cracking is expected to occur at ratio 1.0. Fig. 7.17 shows that the samples with low concentrated sodium carbonate (SC-0.7) and sodium sulfate (Su-0.7) crack when the cracking potential ratio is close to 1.0, as excepted. While in samples activated with only sodium silicate (SS-1.0) and samples with higher concentrated sodium carbonate (SC-0.7) and sodium sulfate (Su-0.7) solutions, the cracking potential ratio exceeds

1.0 as shown in Fig. 7.17. Although the reason for this is not clearly understood, it could be related to overestimation of the actual residual tensile stresses at the inner radius of mortar ring.

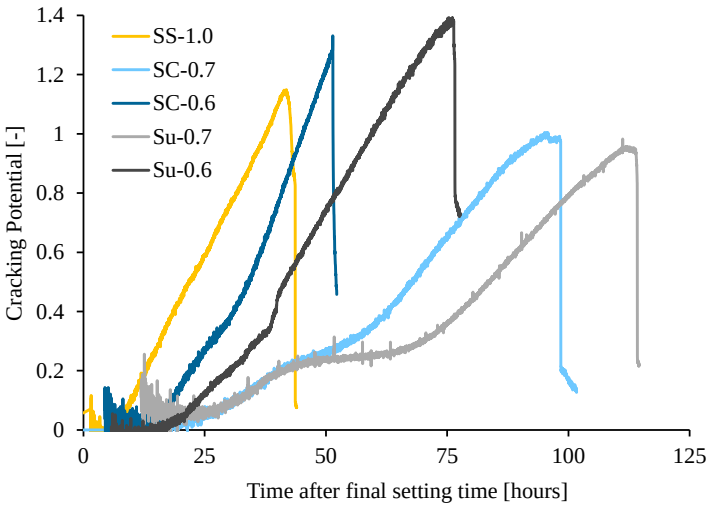

Figure 7.17: Cracking potential of AASF mortar samples.

As mentioned above, the inner steel ring strains are converted to residual tensile stresses in the mortar ring under the assumption of an elastic non-linear distribution of stress along the radial direction of the mortar ring. However, due to the strong stress relaxation or creep effect observed in the studied AASF samples (Fig. 7.14), it is not reasonable to consider that the residual tensile stress distribution along the radius is like in purely elastic material, i.e. maximum stress occurs at inner radius and decreases gradually towards outer radius. Large deformations resulting from creep effect can lead to redistribution of the residual tensile stresses along the radius of the mortar ring. Therefore, the maximum residual tensile stress at the inner radius of mortar ring computed from elastic solution is expected to be overestimated. Thus, the cracking potential obtained using the calculated maximum residual tensile stress (Eq. 7.17) may be considerably overestimated. Additional measurements are needed to quantify the redistribution of residual tensile stresses due to relaxation or creep effect. Moreover, other factors like loading rate and formation of early age microcracks can also affects the splitting tensile strength results, and thus cracking potential.

7.6 Conclusions

In this chapter, the influence of the incorporation of sodium carbonate and sodium sulfate on the cracking tendency of sodium silicate-activated samples is investigated using ring test. The actual residual tensile stress, theoretical-elastic stress, and creep related to stress relaxation are

quantified for better understanding the cracking resistance of AASF mortar samples under restrained autogenous conditions. Based on the above discussion, the following conclusions can be drawn:

- The time of cracking in sodium silicate-activated samples is prolonged significantly with incorporation of sodium carbonate and sodium sulfate solutions. Decreasing the concentration (Na_2O) of incorporated activators delays further the time of cracking in sodium silicate-activated samples. In comparison, incorporating sodium sulfate has much better cracking resistance than sodium carbonate.
- The partial substitution of sodium silicate with sodium carbonate and sodium sulfate reduces the rate of strain development in the restrained steel ring. Samples with sodium sulfate have lower strain rate compared to samples with sodium carbonate of the same concentration.
- Both the residual tensile stress developed due to restrained autogenous shrinkage and the theoretical-elastic stress developed under elastic deformation of sodium silicate-activated samples are substantially reduced with incorporation of sodium carbonate and sodium sulfate solutions. This is due to the fact that the partial substitution of sodium silicate with sodium carbonate and sodium sulfate reduces the stiffness development and rate of autogenous shrinkage as concluded in the previous chapter.
- The degree of restraint is reduced over time for all studied AASF mortar samples as stiffness development increases with curing age. With incorporation of sodium carbonate and sodium sulfate, the restraint degree of sodium silicate-activated samples increases.
- With incorporation of sodium carbonate and sodium sulfate solutions, the creep factor of the sodium silicate-activated samples increases during the interval from 0-24 hours. The creep factor increases further with decreasing the concentration of incorporated activators. Samples with sodium sulfate have a higher creep factor than samples with sodium carbonate of the same concentration.
- The cracking potential ratio decreases with decreasing the concentration of sodium carbonate and sodium sulfate solutions.

Chapter 8

Mitigation of autogenous shrinkage by elevated curing temperature

8.1 Introduction

It is evident from Chapter 6 and Chapter 7 that the investigated AASF cements cured at 20°C suffer from large autogenous shrinkage and consequently have higher cracking tendency under restrained conditions. The effect of curing temperature has been extensively studied in OPC-based materials and reported that a high curing temperature result in the formation of coarse microstructure (i.e. reduced capillary stress) and lead to lower autogenous shrinkage. However, the effect of curing temperature on autogenous shrinkage and how it is connected to the reaction kinetics and microstructure development is not well reported in the literature of AASF systems. On the other hand, recent studies [132, 182] have reported that elevated curing temperature can effectively reduce the drying shrinkage of alkali-activated slag cements due to the reduction in deformability of the reaction products. In this context, a high curing temperature may also reduce the autogenous shrinkage in AASF systems, since the viscoelastic deformation, associated to the rearrangement of C-A-S-H gel under internal stress, is more dominant in the autogenous shrinkage, as observed in Chapter 6. Nevertheless, this hypothesis has not been evaluated before.

First, the influence of curing temperature on compressive strength development, Vicat setting times, and autogenous shrinkage of AASF samples is explained. Secondly, the effect of curing temperature on reaction kinetics, reaction products and microstructure development is discussed and then linked to the autogenous shrinkage behavior in AASF. Afterwards, the stiffness development of the mortar samples is measured for a better understanding of the curing temperature effect on the autogenous shrinkage, since it also depends on the level of compressibility under capillary stress in the pore fluid. Finally, the capillary tension caused by

self-desiccation is calculated by using the experimentally measured internal relative humidity as an input in order to elucidate the relationship between the capillary tension in the pore fluid and the autogenous shrinkage in AASF. The main conclusions are summarized at the end of this chapter.

8.2 Compressive strength

Fig. 8.1 shows the compressive strength development of the studied AASF samples cured at 20°C and 40°C. The strength values in samples cured at 40°C are significantly higher than those observed in samples cured at 20°C at all ages. Regardless of the curing temperature, the incorporation of sodium carbonate and sodium sulfate solutions significantly reduces the compressive strength of sodium silicate activated samples at early hours (≤24hours). This is explained by the fact that the partial substitution of sodium silicate with sodium carbonate and sodium sulfate reduce the concentration of OH^- ions in the solution. As a consequence, the dissolution kinetics of the slag/fly ash particles decreases and results in the formation of lower amounts of reaction products. However, after 3 days, the compressive strength is greatly improved and shows comparable strength values to samples activated with SS-1.0 at both 20°C and 40°C (Fig. 8.1).

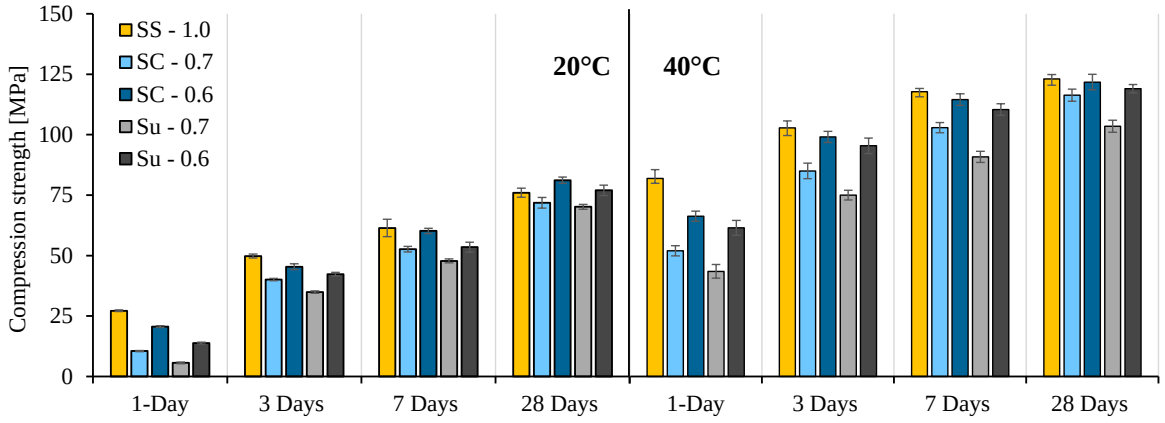

Figure 8.1: Compressive strength of AASF mortar samples at 20°C and 40°C.

At 20°C, the compressive strength of samples with sodium carbonate and sodium sulfate at 1 day is around 7.5-20 MPa. These strength values are considerably lower than Portland cement (around 20-25 MPa) at water-to-binder ratio of 0.5 [10]. Samples cured at 40°C gain substantial strength during the first 24 hours, which gradually increases over time up to 28 days as shown in Fig. 8.1. These results suggest that curing at evaluated temperature (40°C) helps to overcome the slower strength development of samples with sodium carbonate and sodium sulfate during

early ages and shows comparable or even better strength values than OPC-based materials. Regardless of the curing temperature, the increase in concentration or alkali-content (Na_2O) of the sodium carbonate and sodium sulfate solutions results in higher compressive strength at all curing ages.

8.3 Vicat setting time and autogenous shrinkage

The Vicat setting time of the AASF pastes at 20°C and 40°C is presented in Fig. 8.2. The initial and final setting time of AASF is notably affected by the curing temperature. Both initial and final setting time decrease significantly as the curing temperature increases from 20°C to 40°C. Regardless of the curing temperature, the initial setting time of sodium silicate-activated samples increases slightly with incorporation of sodium carbonate and sodium sulfate. The final setting time, however, increases greatly for samples with sodium carbonate and sodium sulfate as shown in Fig. 8.2.

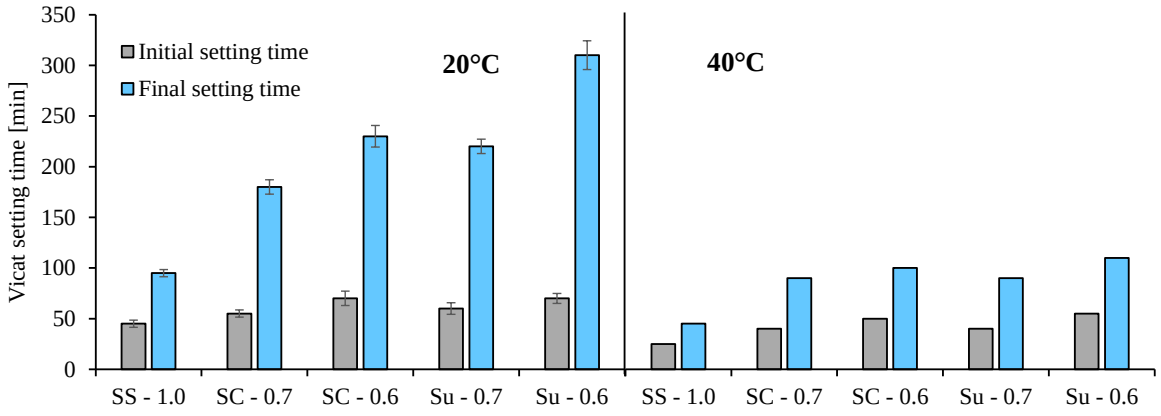

Figure 8.2: Vicat setting times of AASF pastes at 20°C and 40°C.

The measured autogenous shrinkage of AASF mortar samples, plotted starting from the final setting time obtained from standard Vicat needle test method is shown in Fig. 8.3. As explained in Chapter 6, the Vicat final setting time is considered as ‘time-zero’ for autogenous shrinkage in AASF samples. It is evident from Fig. 8.3 that the partial substation of sodium silicate with sodium carbonate and sodium sulfate significantly reduces the autogenous shrinkage of AASF samples, regardless of the curing temperature (20°C & 40°C). Also, the samples with a higher concentration (Na_2O) of sodium carbonate (SC-0.6) and sodium sulfate (Su-0.6) solutions shrink more compared to the samples with SC-0.7 and Su-0.7, respectively.

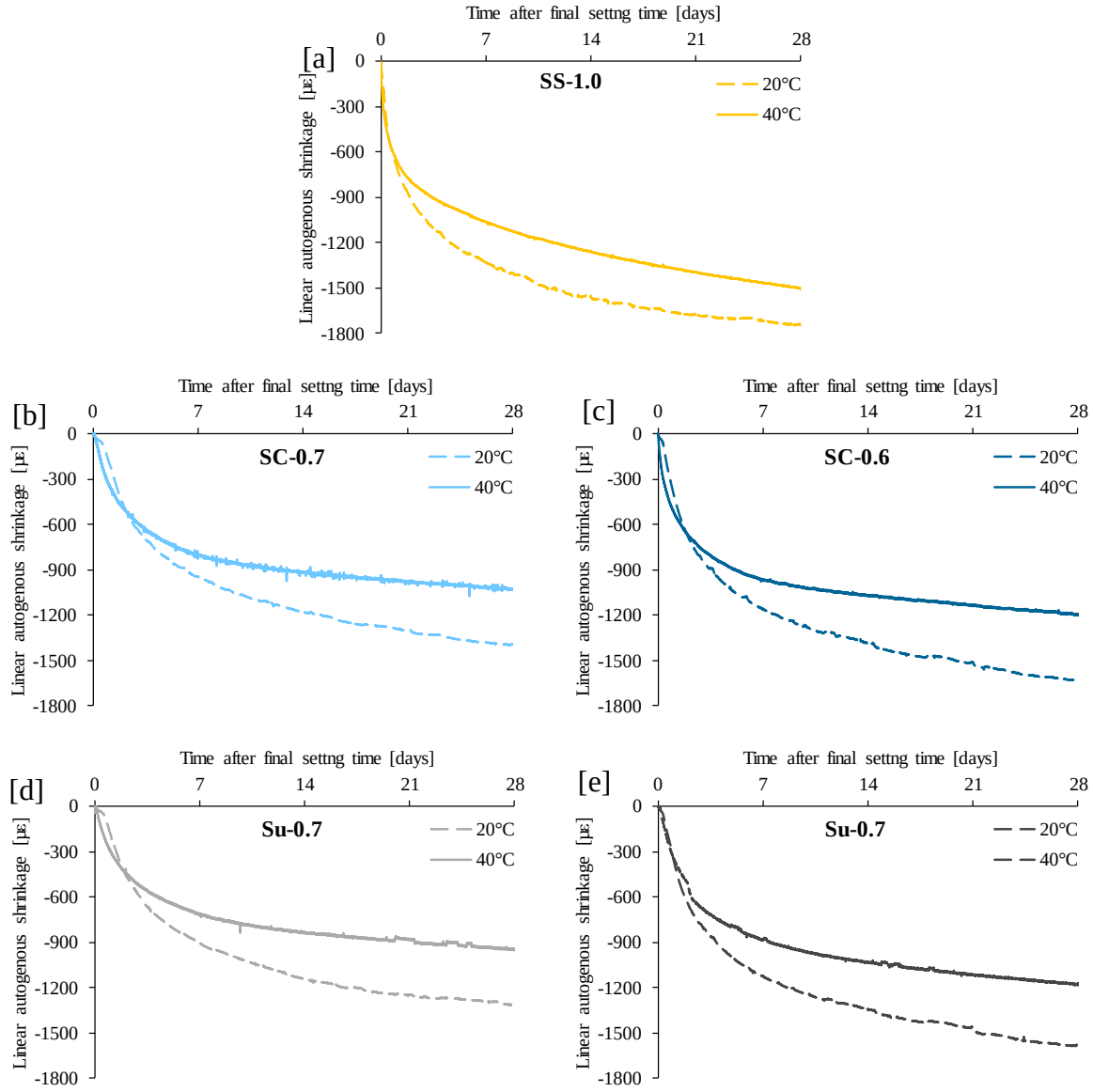

Figure 8.3: Autogenous shrinkage starting from the Vicat final setting time for SS-1.0 [a], SC-0.7 [b], SC-0.6 [c], Su-0.7 [d], and Su-0.6 [e] at both 20°C and 40°C.

At 40°C, the autogenous shrinkage during early hours evolves faster than at 20°C. However, as from 3 days the autogenous shrinkage in samples at 40°C slows down as shown in Fig. 8.3. The ultimate autogenous shrinkage strain value at 28 days of sodium silicate-activated sample (SS-1.0) decreases by approximately 15% when increasing the curing temperature from 20°C to 40°C. However, for samples with sodium carbonate and sodium sulfate, the autogenous shrinkage strain values at 40°C are approximately 25-30% lower than for samples cured at 20°C. These results suggest that elevated curing temperature (40°C) can be effectively used as a mitigation strategy to control autogenous shrinkage of AASF cements.

8.4 Reaction kinetics

8.4.1 Isothermal calorimetry

The calorimetric heat release curves during the first 48h of AASF pastes at 20°C and 40°C are shown in Fig. 8.4. At 40°C, the calorimetric response shows a similar trend with two characteristic peaks as described for samples cured at 20°C. The first peak can be attributed to the wetting and dissolution of slag/fly ash particles and formation of initial reaction complexes with the dissolved species. The second peak can be attributed to the formation of reaction products as a result of reaction between the dissolved ions and/or the anions present in the activator. The induction period between the first dissolution peak and the second acceleration peak can be attributed to the time required to reach a critical concentration of dissolved ions to form reaction products.

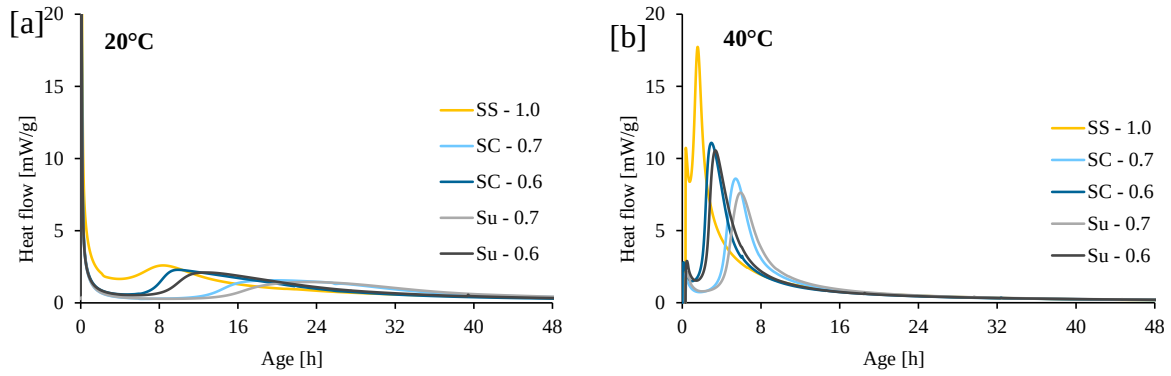

Figure 8.4: Heat flow curves of the AASF paste samples at 20°C [a] and 40°C [b].

Increasing curing temperature from 20°C to 40°C reduces the time of appearance of the acceleration peak and increases the peak intensity by approximately five times. These results indicate that the increasing curing temperature to 40°C greatly accelerates the reactivity of AASF cements. In other words, curing at 40°C provides an energy necessary to overcome the barrier effect that arises from the precipitation of reaction products on the particle surface and enhances the formation of reaction products by increasing the solubility and diffusivity [341, 56]. Similar to 20°C, an increase in sodium carbonate and sodium sulfate (SC-0.6 & Su-0.6) concentration results in a shorter induction period and an intense and sharp acceleration peak at 40°C. This suggests that the formation of the reaction products is accelerated with an increase in concentration of the activator, regardless of curing temperature.

The cumulative heat release of the AASF pastes at 20°C and 40°C is shown in Fig. 8.5. The longer induction period in samples activated with SC-0.7 and Su-0.7 is represented by a

relatively slow increase in the heat release between the initial rise and later rise. By comparing the cumulative heat release at 20°C and 40°C, it is observed that the cumulative heat release significantly increases during early hours with an increase in curing temperature. As shown in Fig. 8.6, the compressive strength has a good correlation with the cumulative heat release until 7 days. A similar correlation is also observed for samples cured at 20°C (Chapter 4). This suggests a way to predict the early age compressive strength, by using the parameter cumulative heat release in AASF cements, regardless of the curing temperature.

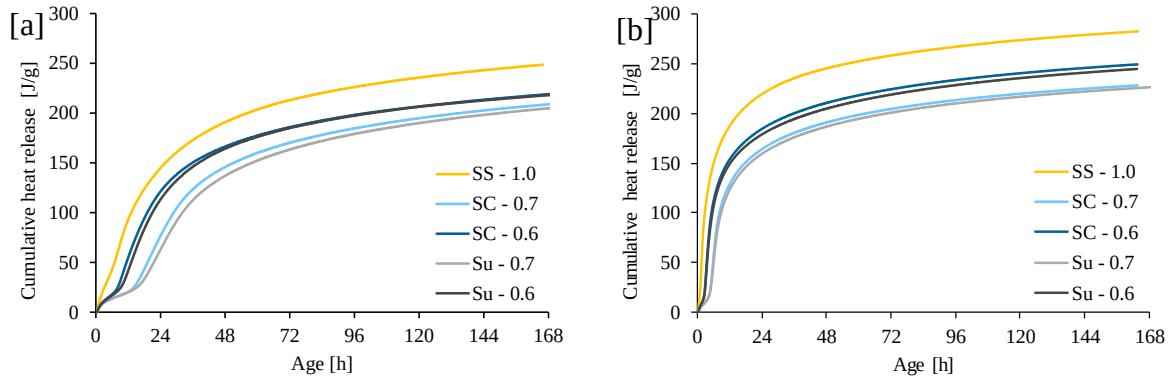

Figure 8.5: Cumulative heat release of the AASF paste samples at 20°C [a] and 40°C [b].

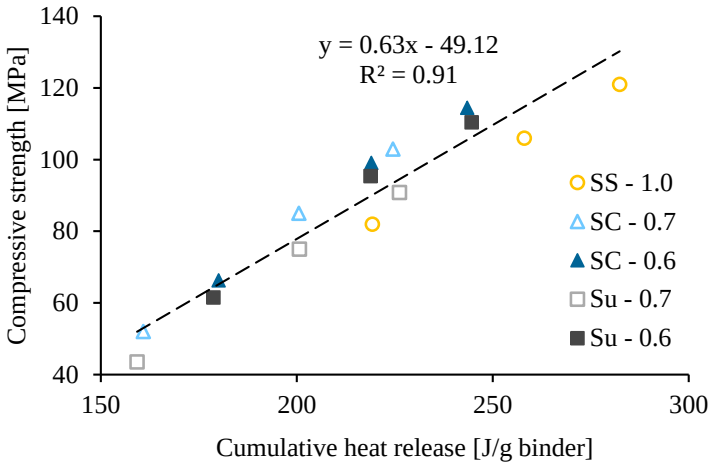

Figure 8.6: Comparison between the compressive strength and cumulative heat release of the AASF samples at 40°C, up to 7 days.

8.4.2 Thermogravimetric analysis

Fig. 8.7 shows the bound water content of AASF samples cured at 20°C and 40°C, at different curing ages. The results show that at 20°C the bound water content of sodium silicate-activated samples is significantly reduced when sodium carbonate and sodium sulfate solutions are incorporated. However, with increasing curing temperature from 20°C to 40°C, the bound

water content in samples with sodium carbonate and sodium sulfate increases significantly during the first 24 hours, indicating the formation of larger amount of reaction products. This can explain the higher rate of strength development during early hours in samples with sodium carbonate and sodium sulfate cured at 40°C as shown in Fig. 8.1.

After 3 days, the increase in curing temperature shows negligible influence on the reactivity of AASF cements (Fig. 8.7). This is probably due to the formation of thicker hydrated rim around the slag particles and suppressing the reactivity of slag during the diffusion-control reaction stage in samples cured at elevated curing temperature [182]. Thus, the reactivity of AASF samples cured at 40°C slow down with curing time. These results suggest that the degree of reaction does not change with temperature at later ages (28 days).

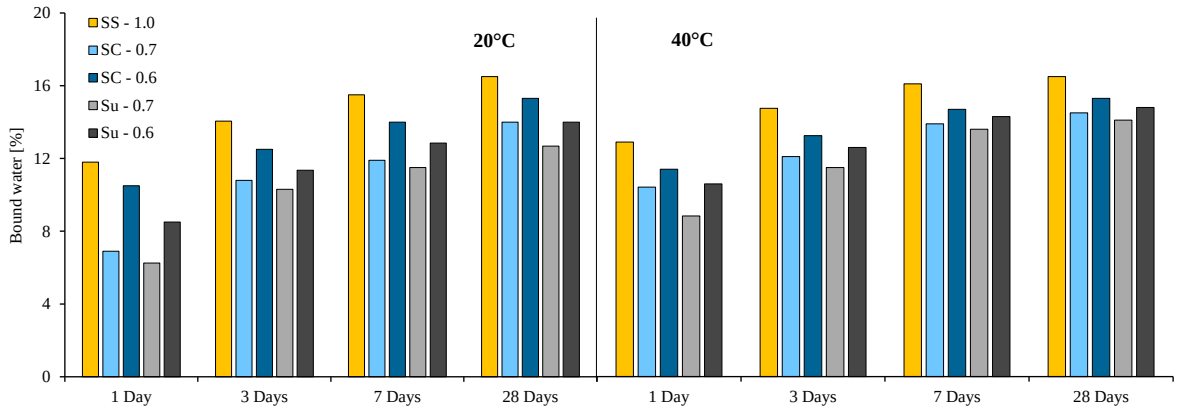

Figure. 8.7: Comparison of the bound water content of the AASF paste samples cured at 20°C and 40°C, calculated based on the weight loss between 30 °C-600 °C.

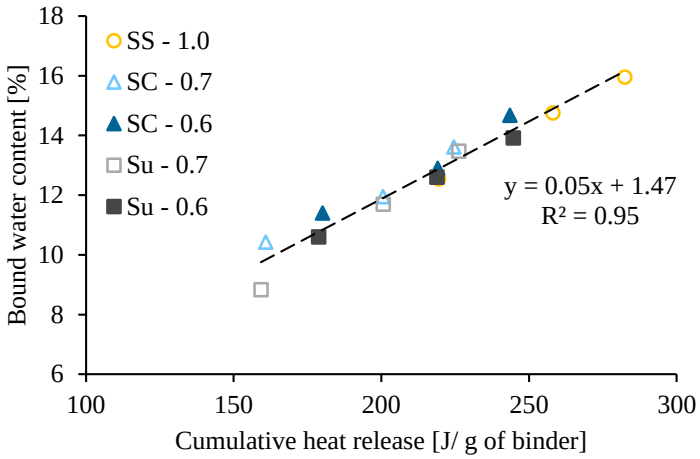

Figure 8.8: Comparison between the cumulative heat release and bound water content of the AASF samples at 40°C, up to 7 days.

Similar to 20°C, the bound water content increases with increase in concentration of sodium carbonate (SC-0.6) and sodium sulfate (Su-0.6). Also, the samples with sodium carbonate result in a slightly higher bound water content than samples with sodium sulfate of the same concentration. This implies that regardless of the curing temperature, samples with sodium carbonate have slightly higher reactivity than samples with sodium sulfate. These results are consistent with the calorimetry heat flow curves (Fig. 8.5) at 40°C. A good correlation exists between the cumulative heat release and the bound water content up to 7 days (Fig. 8.8).

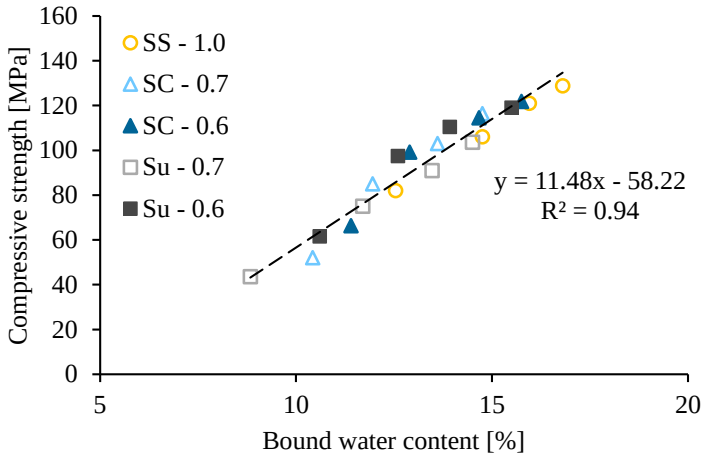

Figure 8.9: Comparison between the compressive strength and bound water content of the AASF samples at 40°C, up to 28 days.

Comparison between the bound water content and the compressive strength of AASF samples cured at 40°C until 28 days is shown in Fig. 8.9. Samples cured at 40°C have a considerable higher strength at and beyond 3 days, although the bound water content is only marginally increased. This can be attributed to other factors influencing the compressive strength development, such as pore size distribution and microstructure development. Nevertheless, there is an overall good correlation between the bound water content and compressive strength of AASF cements cured at 40°C (Fig. 8.9).

8.5 Characterization of reaction products

8.5.1 XRD analysis

Fig. 8.10 illustrates X-ray diffractograms of AASF pates after 1 day of curing at 20ºC and 40ºC, respectively. Regardless of activator type and curing temperature, all the studied AASF pastes shows diffraction peaks at around 2θ = 29º and 49º, which can be attributed to the formation

of C-A-S-H type gels [68, 37, 92]. By comparing the XRD patterns at 20ºC and 40ºC, it can be seen that the peak of this C-A-S-H type gels become sharper and more intense with increasing curing temperature, implying that crystallinity of this main reaction product increases at this temperature (40°C).

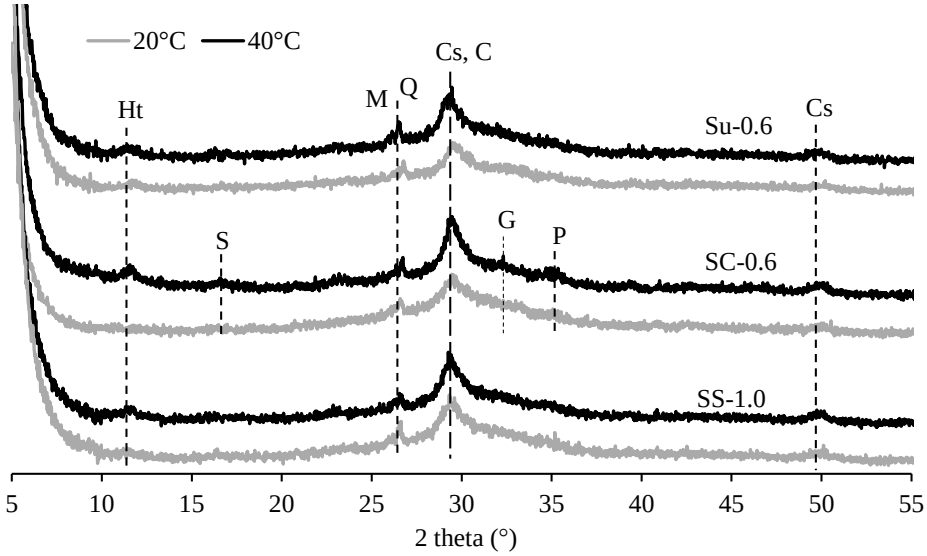

Figure 8.10: XRD patterns of the AASF samples after 1-day cured at 20°C and 40°C, Key: Ht- Hydrotalcite, Cs – calcium silicate hydrate type gels, C – Calcite, S – Hydroxysodalite, G – Gaylussie, P – Pirssonite, M – Mullite, Q – Quartz.

Regardless of the curing temperature, the samples with sodium carbonate forms carbonate phases like calcite, gaylussite and pirssonite. However, in samples with sodium sulfate, no ettringite or other crystalline sulfate phases like of sodium calcium aluminum sulfate hydrate (N-C-A-S-H) are observed at 40°C, similar to samples cured at 20ºC. Regardless of the nature of anions present in the activator, hydrotalcite phase is observed as the main secondary reaction product in all studied AASF pastes at both 20ºC and 40ºC.

8.5.2 FT-IR analysis

The influence of curing temperature on gel structure in AASF is investigated using FTIR. Fig. 8.11 shows the infrared spectrum of the studied AASF pastes cured at 40ºC. It can be seen that, regardless of type and concentration of the activator, all samples exhibit similar location of transmission bands at 40ºC. Specifically, all samples showed a main transmission band at around 955 cm^{-1}, which is attributed to the asymmetrical stretching vibrations of Si-O terminal bonds in C-A-S-H type gel [271, 39]. The transmission bands centered at 3400 cm^{-1} and 1640

cm^{-1}, presents in all AASF samples, correspond to OH groups in the hydration products [267, 268]. In samples with sodium carbonate, a band at around 1420 cm^{-1} is observed, which is associated to the stretching vibration of O-C-O bonds in carbonates [269]. Similar to 20ºC, the location of the main Si-O-T vibration bonds remains stable at around 955 cm^{-1} with increasing curing time at 40ºC. These results imply that regardless of the curing temperature, the polymerization of hydrated gels formed in AASF is limited to chain reaction.

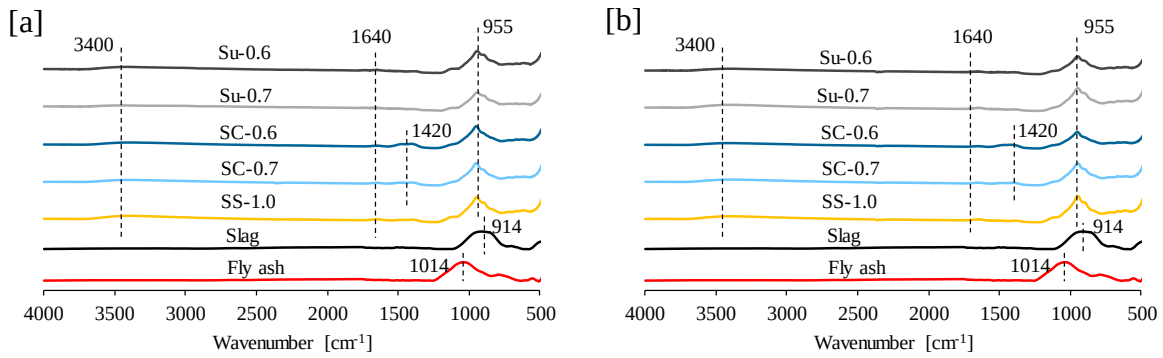

Figure 8.11: FTIR spectrum of AASF paste samples after: (a) 1 day, and (b) 28 days curing at 40ºC.

By comparing the FTIR spectrum at 20ºC (Fig. 5.9) and 40ºC (Fig. 8.11), no significant change in the location of main bands is observed with increasing curing temperature. To better understand the influence of curing temperature on the gel structure of AASF pastes, the FTIR spectrum is deconvoluted in between 600-1200 cm^{-1} and the results are shown in Fig. 8.12. Increasing curing temperature from 20°C to 40°C shows negligible changes in wavenumber of the main Si-O-T band (944 cm^{-1} to 955 cm^{-1}). It is generally reported that a shifting of the wavenumber of the main Si-O-T band represents the polymerization degree (cross-linking) of reaction products, thus the unchanged/or negligible change in wavenumber of the main Si-O-T band indicates that increasing the curing temperature has no influence on the cross-linking polymerization degree of C-A-S-H gel in AASF cements. Meanwhile, the main band of Si-O-T bonds becomes sharper and more intense with increasing curing temperature, indicating the presence of large amounts of the bridging Si-O-T bonds. In other words, an increase in the curing temperature enhances the reactivity or formation of reaction products in AASF cements, which is in agreement with TGA bound water content and calorimetry heat flow results.

The transmission band at around 890 cm^{-1} is associated to the asymmetric vibration of Si-O terminal bonds generated by Q^2 units, the small band at around 835 cm^{-1} is associated to Si-O bonds (Q^1 units). These FTIR results suggest that the reaction products formed in studied AASF

cements are short range C-A-S-H type gels (more Q^2 units), regardless of the curing temperature. The band at 1135 cm^{-1} is related to T-O bonds of quartz in fly ash.

With increasing curing temperature, the intensity of the band at 890 cm^{-1}, associated to Q^2 units (in-chain tetrahedron), is increased, while the intensity of the band at 835 cm^{-1}, associated to Q^1 units (end-chain tetrahedron), is decreased (Fig. 8.12). These results imply that linear polymerization of reaction products is increased with an increase in the curing temperature. This is consistent with previous studies using ^{29}Si NMR [342].

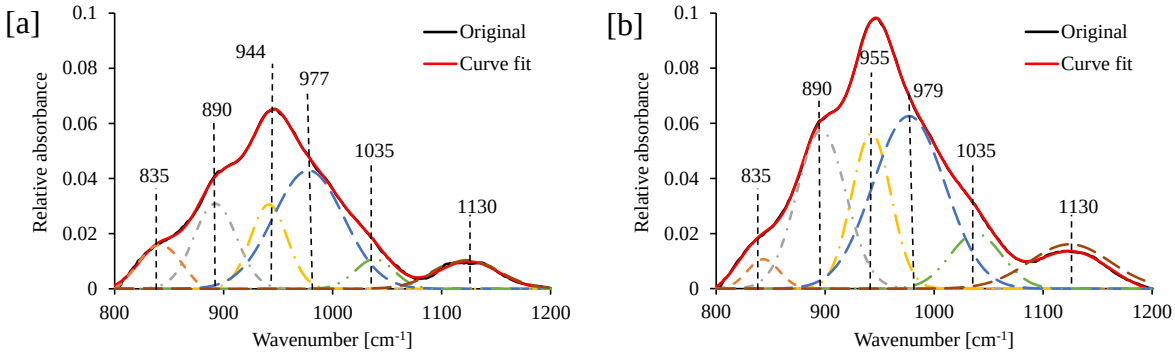

Figure 8.12: Deconvolution FTIR spectra of SS-1.0 sample after 1 day of curing at 20ºC [a] and 40ºC [b].

The spectrum of AASF pastes also shows a very small shoulder at around 1035 cm^{-1}, which can be attributed to the formation of N-A-S-H type gels, as explained in Chapter 5 (Fig. 5.11). As observed, the intensity of this hump associated to N-A-S-H type gels increases with curing temperature. This suggests that the amount of N-A-S-H gels formed during early ages increases with curing temperature. This is due to the fact that the dissolution of fly ash increases at higher temperature and releases more Si and Al ions to facilitate the formation of N-A-S-H type gels. Considering that the FTIR results provide limited information about the quantitative analysis, further study is needed to support this observation.

8.5.3 Pore solution composition

Fig. 8.13 presents the comparison between the concentration of Na, OH^-, Si, Al, CO_3^2, and S ions in the pore solution of AASF pastes cured at 20ºC and 40ºC, respectively. The concentration of Ca ions in pore solutions is not compared in this work since their values are very low in samples cured at 40ºC and become difficult to measure accurately using the ICP-OES technique.

Similar to the samples cured at 20ºC, the concentration of Na ions in the pore solution decreases over time in all AASF samples cured at 40ºC. This is probably due to intake of these ions into C-A-S-H type gels to compensate the charge imbalance created by substitution of Si^{4+} by Al^{+3} at tetrahedral bridging positions and formation of N-A-S-H type gels. On the other hand, the decrease in concentration of OH^- ions in the pore solution is due to the consumption of these ions during the dissolution of slag/fly ash particles and formation of reaction products, as evident from Chapter 5. Fig. 8.13 (a)-(b) shows that the concentration of Na and OH^- ions is significant reduced over time in samples cured at 40°C than in samples cured at 20°C. This is most likely due to consumption of these ions in the dissolution of fly ash and the formation of N-A-S-H type gels.

It can be seen from 8.13 (c) that samples cured at elevated curing temperature (40°C) have higher concentration of Al ions in the pore solution than in samples cured at 20°C at early hours (≤ 24 hours). This may suggest that dissolution of fly ash is enhanced at elevated curing temperature (40°C) and releasing more Al ions into the pore solution at early hours.

It has been reported that solubility of Al ions increases with increase in alkalinity of the solution [74]. In this respect, one would expect that samples activated with SS-1.0, having higher concentration of OH^- ions (~2 times), will have a higher concentration of Al ions in the pore solution than samples with sodium carbonate and sodium sulfate. However, no significant change is observed in the concentration of Al ions between the samples activated with only sodium silicate and samples with sodium carbonate and sodium sulfate at 40°C. This is probably due to consumption of more dissolved Al ions in the formation of Si-Al units. In other words, in samples activated with SS-1.0, having higher silica content, the released Al ions may quickly react with SiO_4^{4-} ions present in the activator and form more Si-Al gels at 40°C.

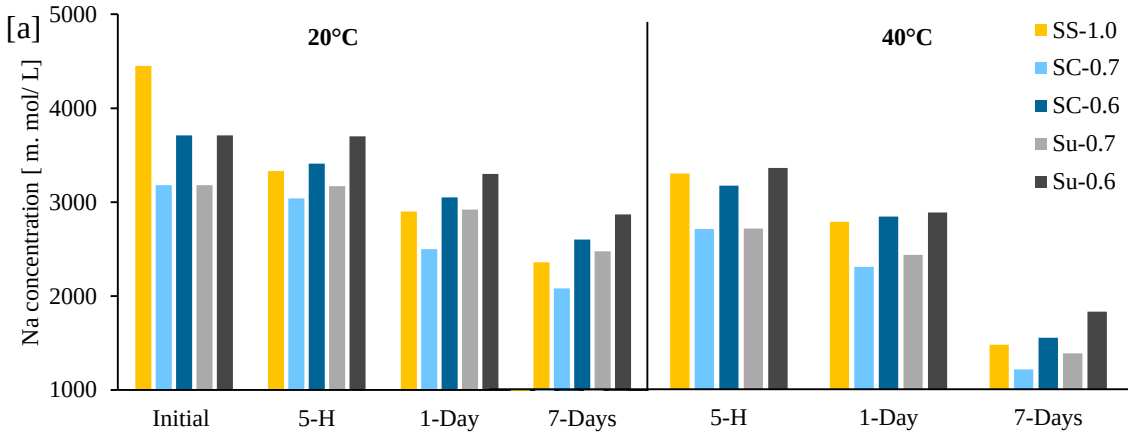

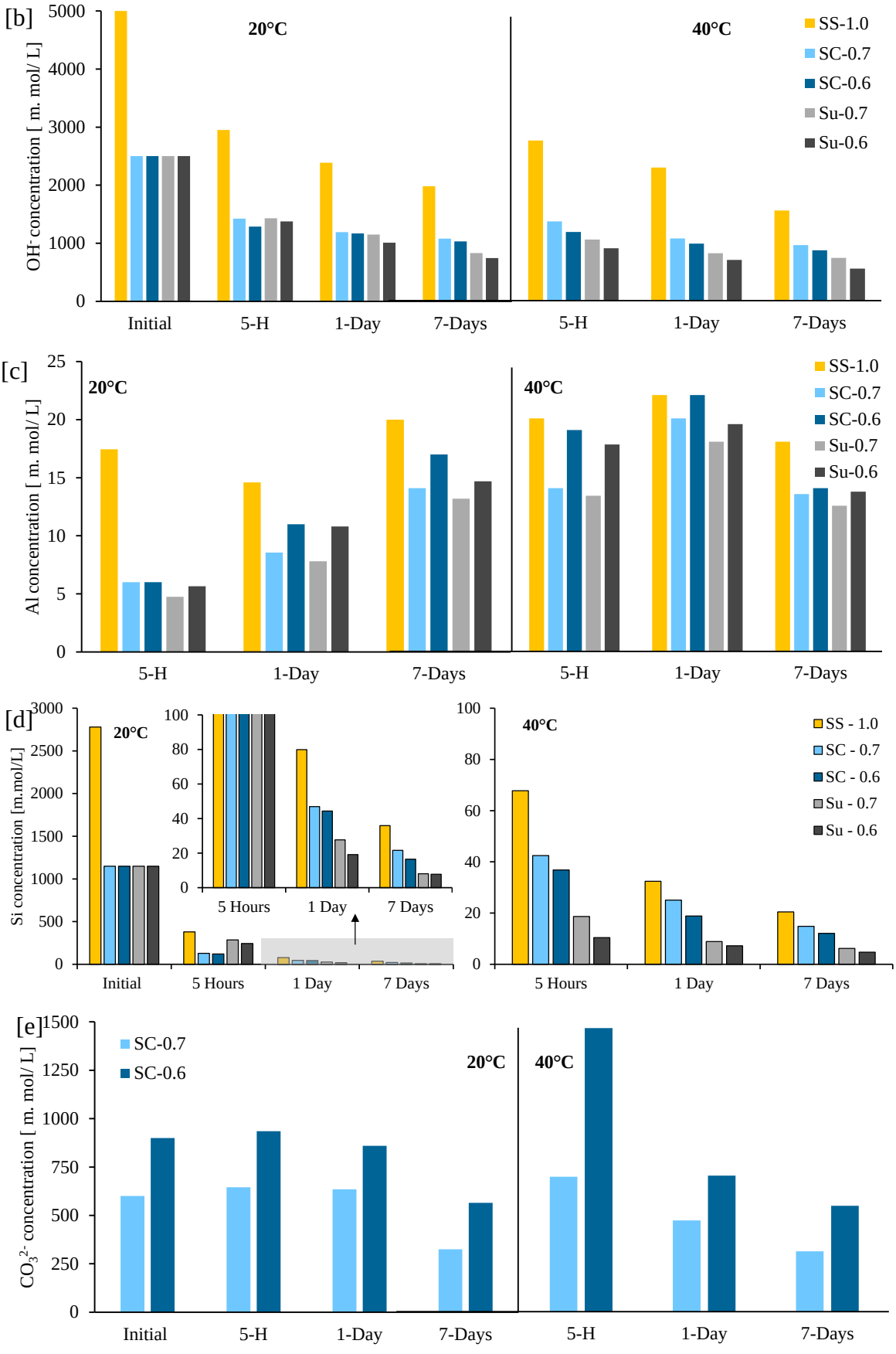
[b]
OH- concentration [m. mol/ L]
20°C
40°C
SS-1.0
SC-0.7
SC-0.6
Su-0.7
Su-0.6
Initial
5-H
1-Day
7-Days
[c]
Al concentration [m. mol/ L]
[d]
Si concentration [m.mol/L]
5 Hours
1 Day
7 Days
SS - 1.0
SC - 0.7
SC - 0.6
Su - 0.7
Su - 0.6
[e]
CO_3^{2-} concentration [m. mol/ L]

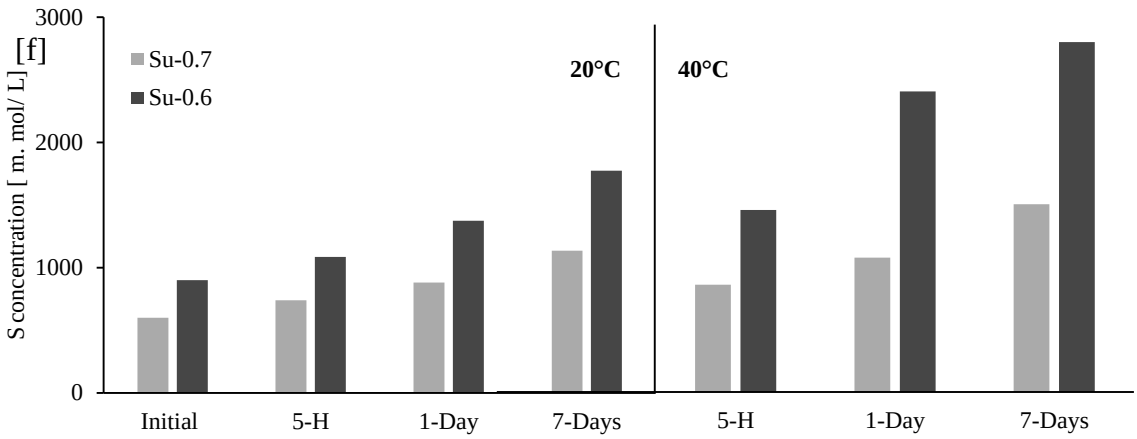

Figure 8.13: Comparing the concentration of (a) Na, (b) OH^- (c) Al, (d) Si, (e) CO_3^{2-}, and (f) S ions in pore solutions of AASF cured at 20ºC and 40ºC; initial concentration values are from alkaline-solutions.

It is observed that the concentration of Si ions in the pore solution is much lower at 40ºC than at 20°C at a given curing time. This indicates that increasing the curing temperature (40°C) either retards the dissolution of slag/fly ash particles or precipitates the reaction products (C-A-S-H and N-A-S-H type gels) much faster by consuming Si ions in the pore solution compared to the samples cured at 20°C. The latter seems to be the case here according to the shorter induction period in calorimetry heat flow curves and TGA bound water content results. In other words, the reactivity of AASF cements increases with increasing curing temperature from 20°C to 40°C.

Regardless of the curing temperature, the concentration of CO_3^{2-} ions in the pore solution increases during the first 5 hours of reaction and then decrease gradually over time due to the formation of carbonate phases as evident from XRD results (Fig. 8.10). However, in samples with sodium sulfate, the concentration of S ions increases with time at both 20°C and 40°C. These results indicate that regardless of the curing temperature, SO_4^{2-} ions provided from the activating solution have limited contribution in the formation of reaction products.

8.6 Characterization of pore structure

8.6.1 MIP

The pore size distribution and the pore size proportion at 3 days and 7 days are presented in Fig. 8.14 and Table. 8.1, respectively. These MIP results reveal that all studied AASF cements are highly mesoporous at 40°C. The total pore volume decreases and the percentage of the mesopore volume in the total pore volume increases from 3 to 7 days, indicating the formation

of a denser matrix with refined pore structure over time. The MIP results show that incorporation of sodium carbonate and sodium sulfate coarsen the pore structure of sodium silicate activated samples at 40°C. The total pore volume decreases also with an increase in sodium carbonate and sodium sulfate concentrations. Comparison of the pore size distribution between samples cured at 20°C (Fig. 5.21) and 40°C (Fig. 8.14) reveals that an increasing curing temperature results in the formation of a denser microstructure at early ages (≤7 days). It should be noted that the samples with sodium carbonate (SC-0.7) have higher porosity, although they have higher rate of reaction compared to the samples with sodium sulfate (Su-0.7). This is probably due the formation of mesoporous hydroxysodalite in samples with sodium carbonate.

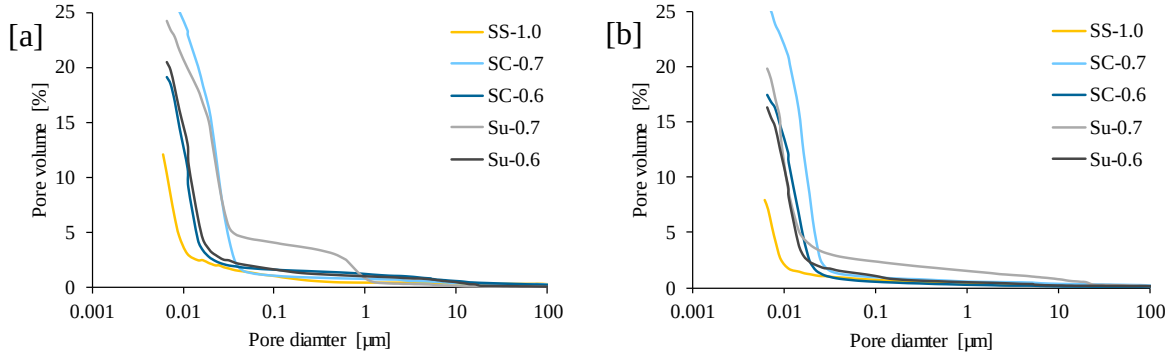

Figure 8.14: Pore size distribution of AASF pastes at 3 days [a] and 7 days [b].

Table 8.1: Pore size proportions for AASF pastes at 3 and 7 days, derived from MIP.

Mix ID	**Mesopore volume/Total volume [%]**		**Total Pore volume [%]**	
	[<50 nm]		[100µm-6nm]	
	3 days	7 days	3 days	7 days
SS-1.0	88.50	89.50	12.00	8.00
SC-0.7	86.25	95.67	27.50	25.40
SC-0.6	90.60	96.10	19.10	17.50
Su-0.7	82.00	86.80	21.00	16.50
Su-0.6	90.30	91.70	20.41	16.20

8.6.2 Nitrogen absorption test

As mentioned in Chapter 5, the nitrogen absorption test is used to further investigate the gel pores that are beyond the detection limit of the MIP test. The pores detected using N_2 absorption

are of sizes in between 1.4nm and 30 nm. Fig. 8.15 shows the N_2 absorption isotherms, corresponding to the volume of gel pores, and the differential curves of AASF paste samples cured at 40°C. The differential curves of the pore size distribution show one main peak around 1.4-10 nm, corresponding to the gel pores [293]. As curing age increases, the quantity of absorbed N_2, as well as the amplitude of the main peak increase, indicating the formation of a dense matrix with refined pore structure over time.

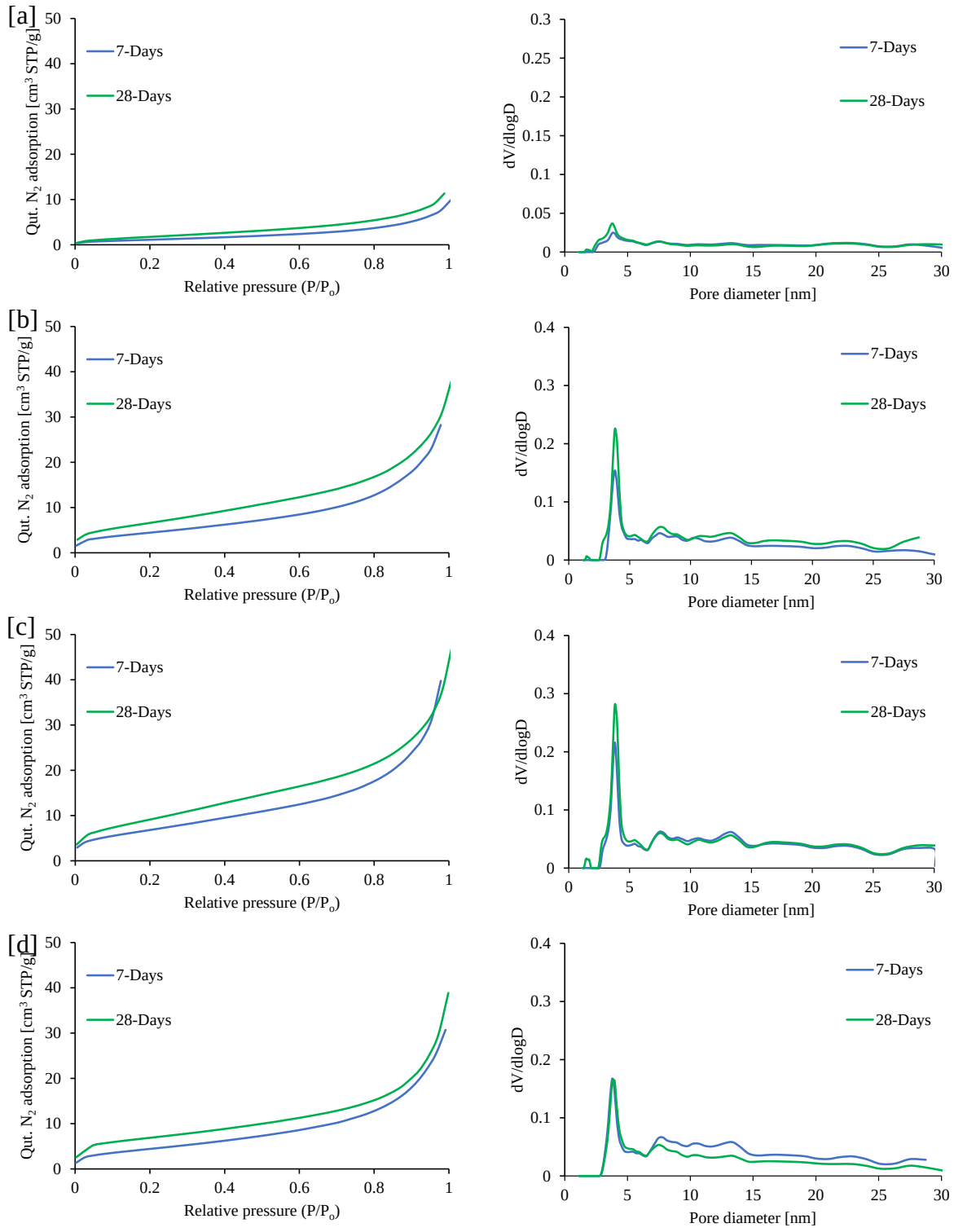

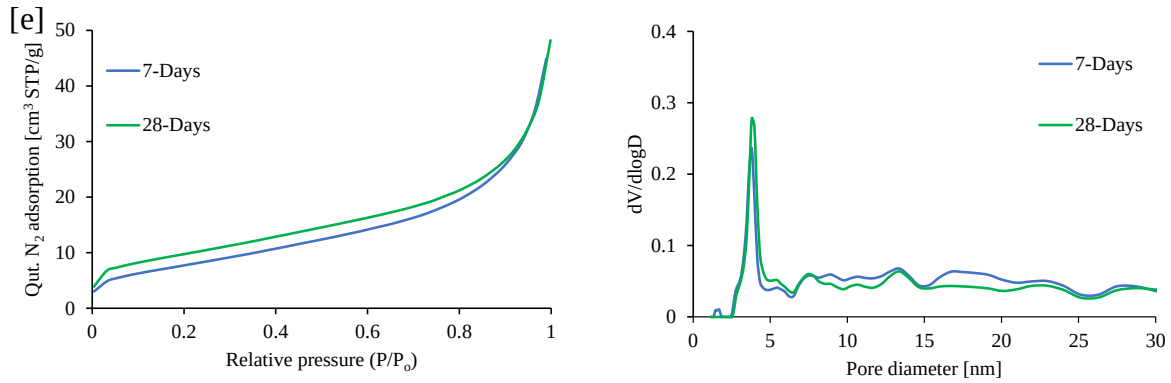

Figure 8.15: N_2 absorption isotherms (left) and differential curves (right) of the AASF pastes activated with SS-1.0 [a], SC-0.7 [b], SC-0.6 [c], Su-0.7 [d], and Su-0.6 [e].

Similar to 20°C, the volume of gel pores increases with increasing of the concentration of sodium carbonate (SC-0.6) and sodium sulfate (Su-0.6) solutions at 40°C. This is mainly due to a higher reactivity in samples activated with SC-0.6 and Su-0.6, and thus formation of a larger amount of hydration products. Similarly, samples with sodium carbonate have a slightly higher volume of gel pores than samples with sodium sulfate of the same concentration. It should be noted that the samples activated with sodium silicate (SS-1.0) show a lower volume of gel pores compared to samples with sodium carbonate and sodium sulfate, although it has higher reactivity. This is probably due to the formation of dense C-A-S-H type gels and this creates low accessibility of the gel pores for nitrogen molecular.

By comparing the N_2 absorption isotherms in samples cured at 20°C (Fig. 5.22) and 40°C (Fig. 8.15), it can be seen that the quantity of absorbed N_2 for samples cured at 40°C is higher at 7 days and lower at 28 days than the quantity of samples cured at 20°C. These results confirm that samples cured at 40°C have higher reactivity during early ages but decelerate with time due to formation of dense hydrated rims around slag/fly ash particles.

8.7 Internal relative humidity

The measured internal relative humidity (RH) of AASF mortar samples cured at 40°C from 14 hours to 14 days is shown in Fig. 8.16. Independent from curing temperature, type and concentration of activator have no significant influence on the measured internal RH during early hours. However, at later ages, the sample activated with a high silica content (SS-1.0) shows lower internal RH. Also, the increase in concentration of sodium carbonate and sodium sulfate results in lower internal RH as shown in Fig. 8.16. By comparing with samples cured at 20°C, it is observed that internal RH of samples cured at 40°C starts to drop significantly at

early ages. Higher reaction rate in samples at 40°C results in higher consumption of solution during the first few days of the reaction and leads to a significant drop in the internal RH.

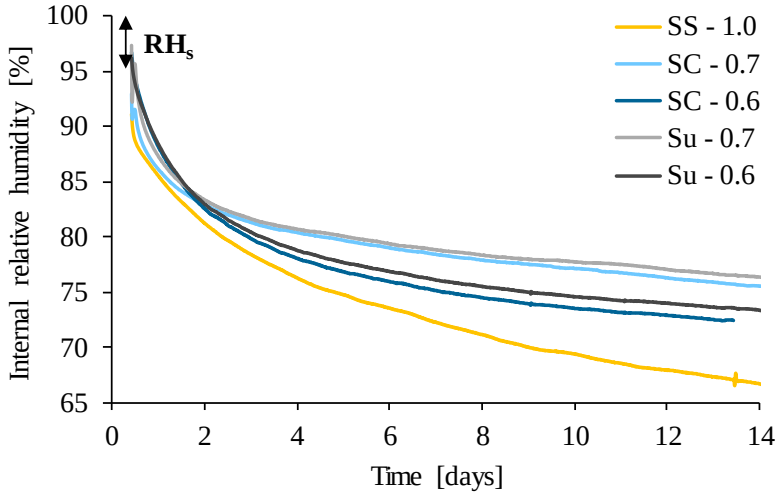

Figure 8.16: Measured internal relative humidity of AASF mortar samples at 40°C.

Table 8.2: Measured RHs [%] of pore solutions extracted from AASF samples cured at 40°C.

Mix ID	1 day	3 days	7 days
SS-1.0	90.10	91.20	91.95
SC-0.7	91.45	92.25	93.50
SC-0.6	91.75	92.15	93.35
Su-0.7	91.25	92.10	94.45
Su-0.6	90.95	92.45	94.00

As explained in Chapter 5, this measured RH is a combination of both the RH drop in the pore solution due to the presence of dissolved salts (RH_s) and the RH drop due to air-solution menisci formation or self-desiccation (RH_k) [343, 139]. The RH_s at different curing ages is given in Table. 8.2. As expected, the RH_s values are lower in samples activated with only sodium silicate (SS-1.0) due to its high alkalinity and consequently this results in more dissolved ions in the pore solution. Similarly, samples activated with a higher concentration of sodium carbonate (SC-0.6) and sodium sulfate (SS-0.6) have lower RH_s values due to the presence of more Na^+ ions in the pore solution. With this measured total RH in mortar and RH_s in pore solution, the RH drop due to self-desiccation (RH_k), named as autogenous relative humidity in this study, is calculated as explained in Chapter 5 and the results are shown in Fig. 8.17.

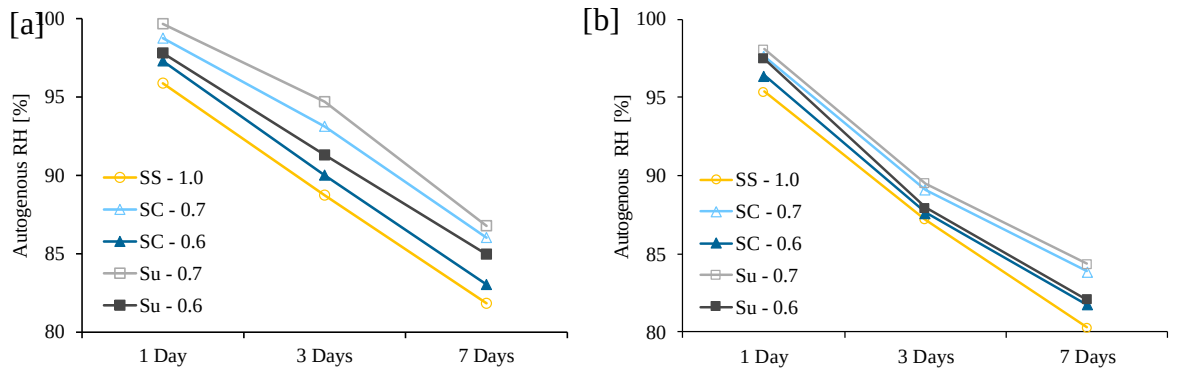

Figure 8.17: Calculated autogenous relative humidity *(RH_k)* of AASF mortar samples at 20°C [a] and 40°C [b].

The results show that the calculated autogenous RH (RH_k) values decrease with increasing silica content (SS-1.0) and concentration of sodium carbonate (SC-0.6) and sodium sulfate (Su-0.6) solutions, indicating the increase in self-desiccation process. By comparing RH_k values of samples cured at 20°C and 40°C, it is concluded that the self-desiccation process is enhanced with increase in curing temperature at early ages (≤7 days).

8.8 Elastic modulus

The elastic modulus of the AASF mortar samples cured at 20°C and 40°C is shown in Fig. 8.18. At early ages, the elastic modulus of sodium silicate activated samples significantly decreases with incorporation of sodium carbonate and sodium sulfate, regardless of the curing temperature. However, at later ages, the elastic modulus of SC-0.6 and Su-0.6 is nearly the same compared to SS-1.0. Curing at 40°C significantly improves the stiffness development at early ages compared to samples cured at 20°C due to the enhanced reaction rate.

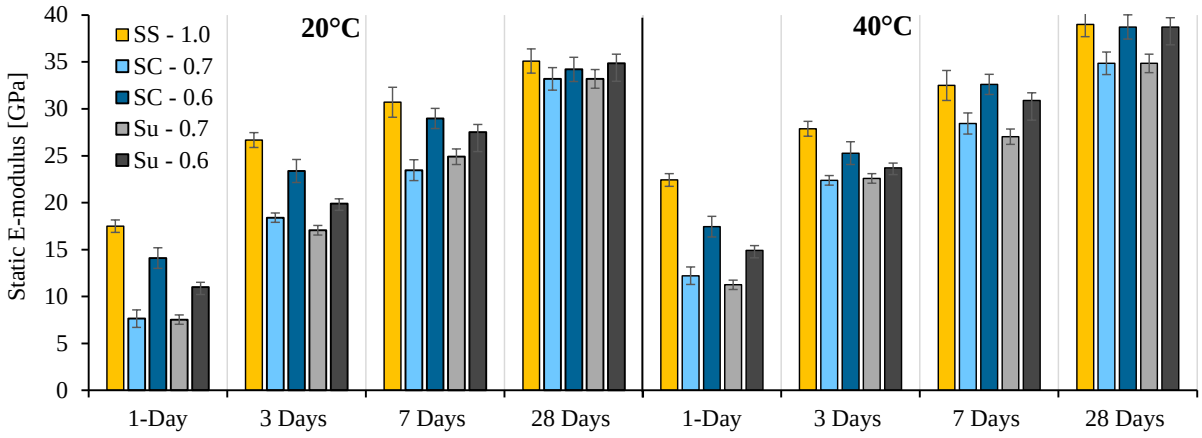

Figure 8.18: Measured static elastic modulus of AASF mortar samples cured at 20°C and 40°C.

8.9 Effect of curing temperature on autogenous shrinkage

To better understand the influence of curing temperature on autogenous shrinkage of alkali-activated slag-fly ash cements, first the reaction products, reaction kinetics, and microstructure development are discussed.

Influence of curing temperature on the reaction products, reaction kinetics, and pore structure development:

The XRD results together with the FTIR analysis reveal that Al-substituted C-S-H type gel predominate with more Q^2 units and three-dimensional structure N-A-S-H type gel are the main reaction products formed in studied AASF cements, regardless of curing temperature. It is apparent from XRD results that the crystallinity of hydrated C-A-S-H type gels is considerably increased with increasing curing temperature from 20°C to 40°C. Also, the FTIR spectrum after deconvolution (Fig. 8.12) demonstrated that the formation of N-A-S-H type gels increases with increasing curing temperature. This is most likely due to enhanced reactivity of fly ash during early ages at 40°C. This can be supported from the pore solution composition results given in Fig. 8.13. It can be seen from Fig. 8.13 that the concentration of Na, Si, Al and OH^- ions in the pore solution is more significantly reduced with time in samples cured at 40°C. This substantial reduction is mostly attributed to the dissolution of fly ash and formation of N-A-S-H type gels by consuming Na, Si, Al and OH^- ions in the pore solution [344]. In other words, since the measured OH^- ions concentration in the pore solution indicates a pH value of >13.5 from 1-7 days, the concentration of dissolved Ca^{2+} ions in the pore solution remains very low due to its less solubility at higher alkalinity (pH>12.5) [74]. In the meantime, the concentration of Al and Si ions in the pore solution increases due to enhanced dissolution of fly ash at 40°C [345, 242] and forms more N-A-S-H type gel at early ages. This is in agreement with previous studies [346, 238, 242, 227], which report that the presence of extra Si and Al ions in the pore solution can retard the formation of C-A-S-H type gels favors more N-A-S-H type gels.

It is evident from the XRD results that there is no formation of expansive phases like ettringite to compensate the autogenous shrinkage in samples with sodium sulfate at 20°C and 40°C. This can be further supported from pore solution data, where the concentration of S in the pore solution increases over time (Fig. 8.13f). The increase in S concentration can be explained by higher rate of water molecules consumption in the reaction process than the SO_4^{2-} ions. This may lead to increase the concentration of the solution and results in higher S ions per liter. The pore solution data confirms that sulfate ions provided from the activating solution have limited

contribution in the formation of reaction products and mostly remains as free sulfate ions in the solution, at both 20°C and 40°C.

The calorimetry and TGA bound water content results show that the increasing curing temperature accelerates the rate of reaction during early hours in AASF cements, regardless of type and concentration of the activator. This effect can also be explained through comparing the concentration of OH^- ions in the pore solution of samples cured at 20°C and 40°C (Fig. 8.13b). It is evident from Chapter 5 (Fig. 5.19 & Fig. 5.20) that the reduction in OH^- ions is proportional to dissolution kinetics and consequently the formation of reaction products. It can be seen from Fig. 8.13b that the concentration of OH^- ions in the pore solution is lower in samples cured at 40°C. This confirms that curing at elevated curing temperature (40°C) accelerates the dissolution kinetics of slag/fly ash particles and consequently the precipitation of reaction products (C-A-S-H and N-A-S-H gels) at early ages.

The TGA results (Fig. 8.7) indicate that the reaction rate is suppressed at later ages (>7 days) in samples cured at 40°C. This is most probably due to the formation of a denser hydrated rim around the slag/fly ash particles and a lower concentration of dissolved ions in the pore solution that is required to continue the further reaction process [182]. This effect at 40°C is further supported from the internal RH measurements in Fig. 8.16. It can be seen that the measured internal RH is significantly reduced during early hours, however, at later ages the rate of reduction is slow down, since the drop of internal RH is linearly related to hydration process by consuming solution.

Since the formation of reaction products is accelerated with increase in curing temperature, the microstructure appeared to be refined with higher rate of reaction and results in finer pore structure at early ages.

Influence of curing temperature on autogenous shrinkage of AASF samples:

Similar to samples cured at 20°C, the capillary tension caused by self-desiccation is considered as the main driving force for autogenous shrinkage at 40°C, since the internal relative humidity (Fig. 8.17) is greater than 75% [139].

The drop of the internal RH (i.e. self-desiccation) causes a hydrostatic tensile stress in the pore fluid and it can be calculated by using modified Kelvin equation (Eq.6.4-6.5), as explained in Chapter 6. The measured surface tension of the pore solutions, extracted from samples cured at 40°C, is equal to samples cured at 20°C, with an error not exceeding ±5 $mN.m^{-1}$. The Kelvin radius calculated using Eq. 6.5 for samples cured at 40°C is given in Table. 8.3. By comparing

the calculated Kelvin radius between samples cured at 20°C and 40°C, it is observed that increasing curing temperature results in lower calculated Kelvin radius at early ages. The reason is that a high curing temperature accelerates the rate of reaction and consequently the self-desiccation process (drop of internal RH) (Fig. 8.17).

Table 8.3: Calculated Kelvin radius [nm] for AASF samples cured at 40°C.

Mix ID	1 day	3 days	7 days
SS-1.0	13.35	4.50	2.75
SC-0.7	30.75	6.50	4.20
SC-0.6	20.50	5.50	3.70
Su-0.7	39.10	6.90	4.60
Su-0.6	30.52	6.20	61.20

The calculated capillary tension in the pore fluids using Kelvin radius and surface tension of the pore solution as inputs is shown in Fig. 8.19. From the Laplace equation (Eq. 6.4), a small Kelvin radius is expected to generate the high capillary tension in the pore fluid, and this causes a large autogenous shrinkage. However, samples cured at 40°C, having a higher capillary tension in the pore fluid, show a lower autogenous shrinkage (Fig. 8.3). This can be attributed to the different resistance of deformation (elastic modulus) under similar capillary tension in the pore fluid. At early ages, the elastic modulus of samples cured at 40°C is higher compared to the samples at 20°C. Because of the high elastic modulus or the restraint effect of the solid skeleton rapidly formed at early ages, the samples cured at 40°C exhibit a lower autogenous shrinkage even with higher capillary tension in the pore fluid. This effect is supported by a poor linear correlation (R^2=0.58) between the capillary tension in the pore fluid and the autogenous shrinkage of AASF mortar samples (Fig. 8.20). However, only the elastic modulus may not fully explain the significant reduction (15-30%) of autogenous shrinkage at 40°C. It is therefore suspected that other factors may also influence the autogenous shrinkage at elevated curing temperatures as explained below.

By comparing the calculated capillary tension in the pore fluid (Fig. 8.19) with the measured autogenous shrinkage (Fig. 8.3), it is observed that the magnitude of autogenous shrinkage differs significantly with incorporation of sodium carbonate and sodium sulfate, although there is only a small change of capillary tension in the pore fluid. Previous studies have reported that the volume fraction of pores with Kelvin radius is another important factor that effects

autogenous shrinkage in cementitious materials [145, 139]. The MIP results reveal that the partial substitution of sodium silicate with sodium carbonate and sodium sulfate coarsen the pore structure and consequently causes lower capillary tension in the pore structure. This would explain the cause of reduction of autogenous shrinkage in sodium silicate activated samples when sodium carbonate and sodium sulfate is incorporated at 40°C. A similar effect is observed in sampled cured at 20°C.

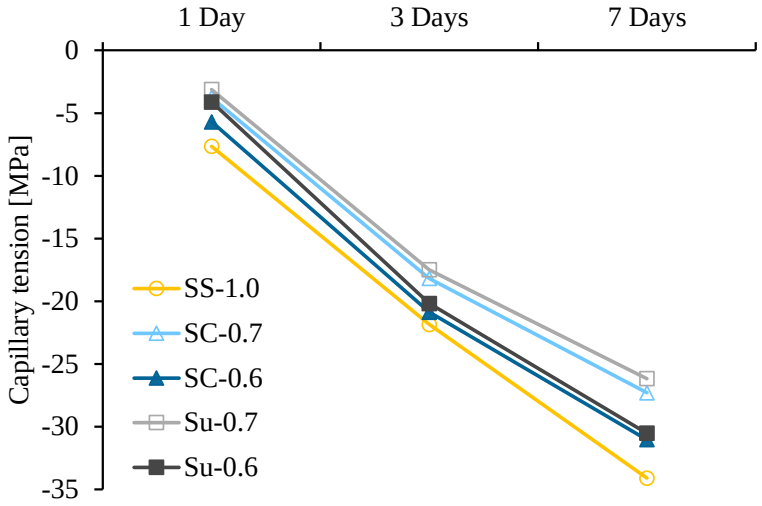

Figure 8.19: Calculated capillary tension in pore fluid of AASF mortar samples cured at 40°C.

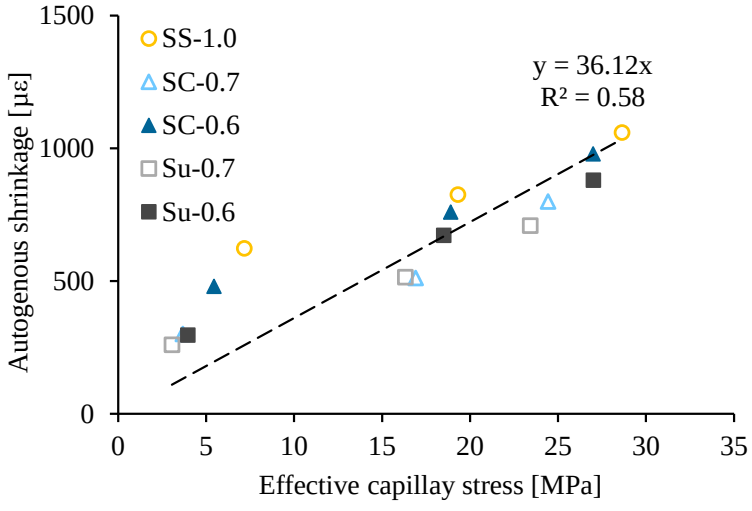

Figure 8.20: Comparison between calculated capillary tension in the pore fluid and measured autogenous shrinkage.

Calculated autogenous shrinkage: As explained in Chapter 6, the autogenous shrinkage in cementitious materials includes both elastic and visco-elastic deformations (Eq. 8.1). The linear

autogenous shrinkage (elastic) in AASF mortars can be calculated using Biot-Bishop model (Eq. 8.2) [144, 139].

$$\varepsilon_{auto} = \varepsilon_e + \varepsilon_c \tag{8.1}$$

$$\varepsilon_e = \frac{S.P_{cap}}{3}\left[\frac{1}{K_p} - \frac{1}{K_s}\right] \tag{8.2}$$

ε_{auto} is the linear autogenous shrinkage, S is the saturation fraction experimentally measured in this study (Table. 8.4), P_{cap} is capillary tension (Fig. 8.19), K_p is the bulk modulus of AASF mortar ($K_p = E/3(1-\nu)$), where E is the static elastic modulus experimentally measured in this study (Fig. 8.18), υ is the Poisson's ratio and a constant value of 0.15 is adopted [208], K_s is the bulk modulus of the solid skeleton, assumed constant to 44 GPa from literature [133]. The comparison between the measured and the calculated autogenous shrinkage of AASF mortars is shown in Fig. 8.21.

Table 8.4: Saturation degree [-] for AASF samples cured at 40°C.

Mix ID	1 day	3 days	7 days
SS-1.0	0.85	0.82	0.79
SC-0.7	0.87	0.84	0.82
SC-0.6	0.85	0.83	0.80
Su-0.7	0.89	0.86	0.83
Su-0.6	0.87	0.84	0.80

The calculated autogenous shrinkage is much smaller than the measured autogenous shrinkage as shown in Fig. 8.21. This difference can be attributed to the viscoelastic behavior (creep) associated to the movement of C-A-S-H globules under internal pressure [347, 348, 24], which is neglected in the Biot-Bishop model (Eq. 8.1). By comparing Fig. 6.15 and Fig. 8.21, it observed that both elastic deformation and visco-elastic deformation under capillary tension are reduced with increasing curing temperature (40°C).

The reduction in elastic-deformation can be attributed to the higher elastic modulus or stiffness development in samples cured at 40°C (Fig. 8.18). However, the reduction in viscoelastic deformation can be explained by the combination of two reasons. Previous studies [132, 24] have demonstrated that the viscoelastic behavior in AASF is primarily attributed to the

incorporation of alkali cations (Na^+) into C-A-S-H gel, which destabilizes the nanostructure of C-A-S-H gel and makes it easier to collapse or redistribute under internal stress. On the other hand, it has been reported that the number of possible alkali (Na^+) sites is limited with increase in crystallinity of the C-A-S-H type gel [349]. Therefore, at a high curing temperature (40°C), resulting in the formation of more crystalline C-A-S-H gel, the incorporation of the alkali cations into C-A-S-H gel can be reduced and results in lower viscoelastic deformation. Secondly, the formation of larger amounts of 3D structured N-A-S-H type gels due to an enhanced reactivity of fly ash in samples cured at 40°C may reduce the shrinkage C-A-S-H type gels. Moreover, as a consequence of deceleration in the hydration process, the self-desiccation (i.e. drop of internal RH) is reduced and results in lower autogenous shrinkage at later ages in samples cured at 40°C

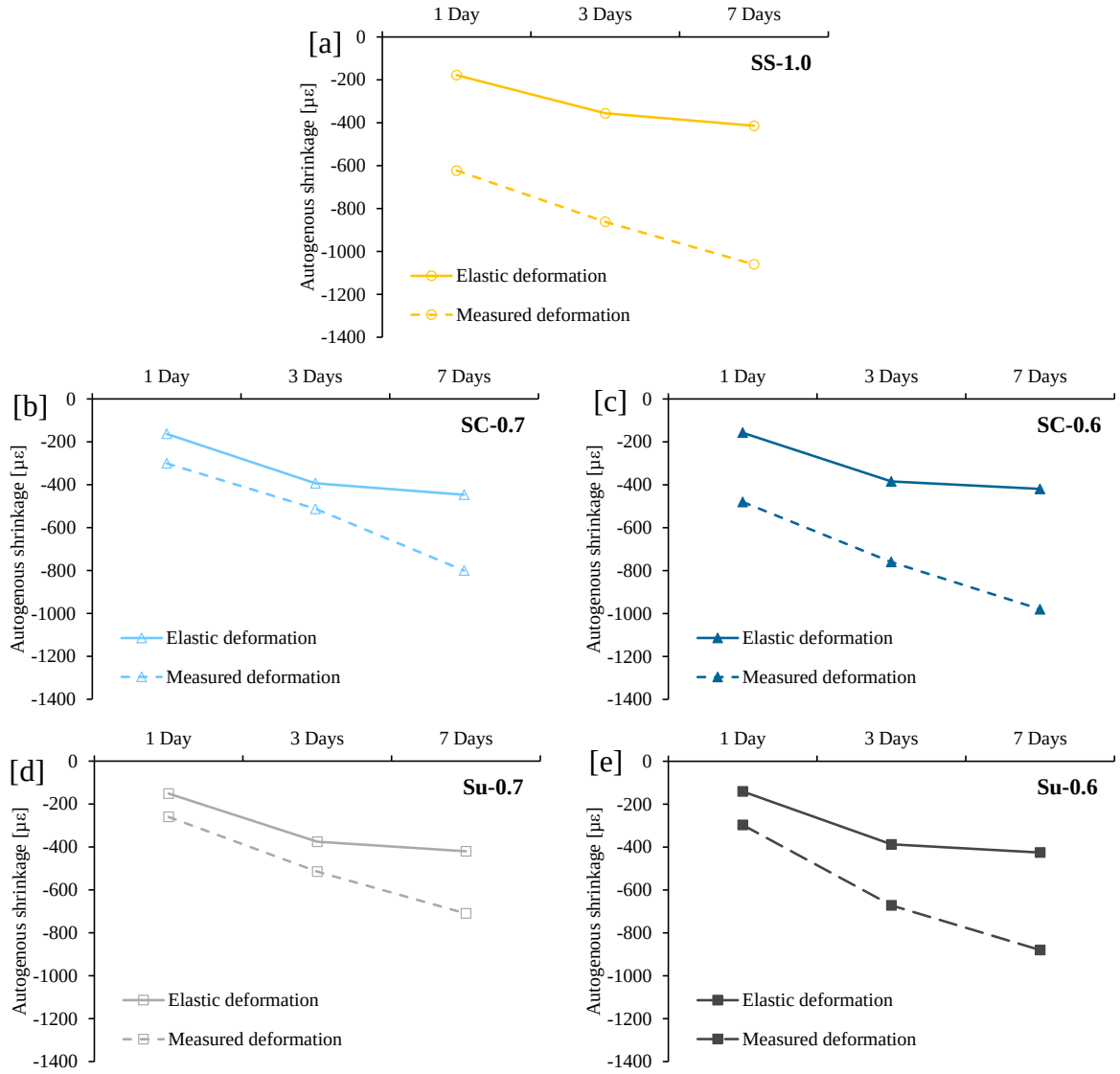

Figure 8.21: Comparison between calculated shrinkage and measured autogenous shrinkage SS-1.0 [a], SC-0.7 [b], SC-0.6 [c], Su-0.7 [d], and Su-0.6 [e].

8.10 Prediction of autogenous shrinkage

As explained in Chapter 6, there is a lack of agreement on the autogenous shrinkage predicted from the capillary tension approach using Biot-Bishop model since it could explain only the elastic-deformation and ignores the creep deformation and other mechanisms like disjoining pressure that causes autogenous shrinkage at moderate to high RH. Moreover, this approach requires multiple inputs which are difficult to measure.

$$\varepsilon_{auto}(t) = 153.85\big(W_b(t)\big) - 1273. \tag{8.3}$$

$$\varepsilon_{auto}(t) = 12.92.\big(f_c(t)\big) - 442.0 \tag{8.4}$$

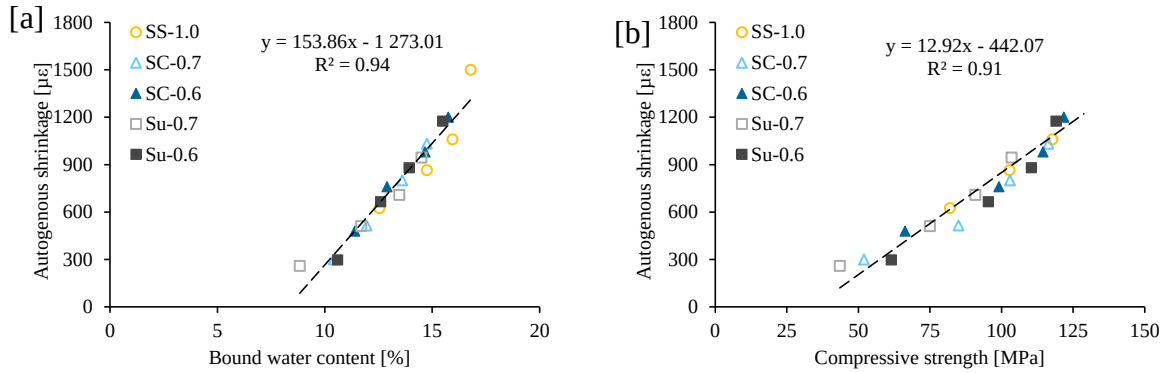

Figure 8.22: Comparison between measured autogenous shrinkage and bound water content [a] and compressive strength [b].

On the other hand, it is confirmed from Chapter 6 that the autogenous shrinkage in AASF cements is a linear function of the volume change of individual constituent (chemical shrinkage) which is dependent of the reaction degree. Therefore, it is suspected that the autogenous shrinkage in AASF cement can be predicted from bound water content, which is used as a relative measure of the reaction degree. A good correlation between bound water content and measured autogenous shrinkage is obtained for AASF cements cured at 40°C (Fig. 8.22a). This confirms that the prediction of autogenous shrinkage using bound water content is reliable at 40°C. Moreover, a good correlation exists between the measured autogenous shrinkage and the compressive strength development up to 28 days (Fig. 8.22b). Therefore, for the purpose of practical use, the autogenous shrinkage in AASF can also be predicted from compressive strength results.

From Fig. 8.23, the autogenous shrinkage of AASF cements at 40°C can be expressed as a function of bound water and compressive strength, as given in Eq (8.3-8.4). The comparison

between measured autogenous shrinkage and predicted autogenous shrinkage using parameters as bound water content and compressive strength is shown in Fig. 8.22. Predicted autogenous shrinkage from bound water content and compressive strength corresponds well the measured autogenous shrinkage for AASF samples cured at 40°C, expect for SS-1.0 samples.

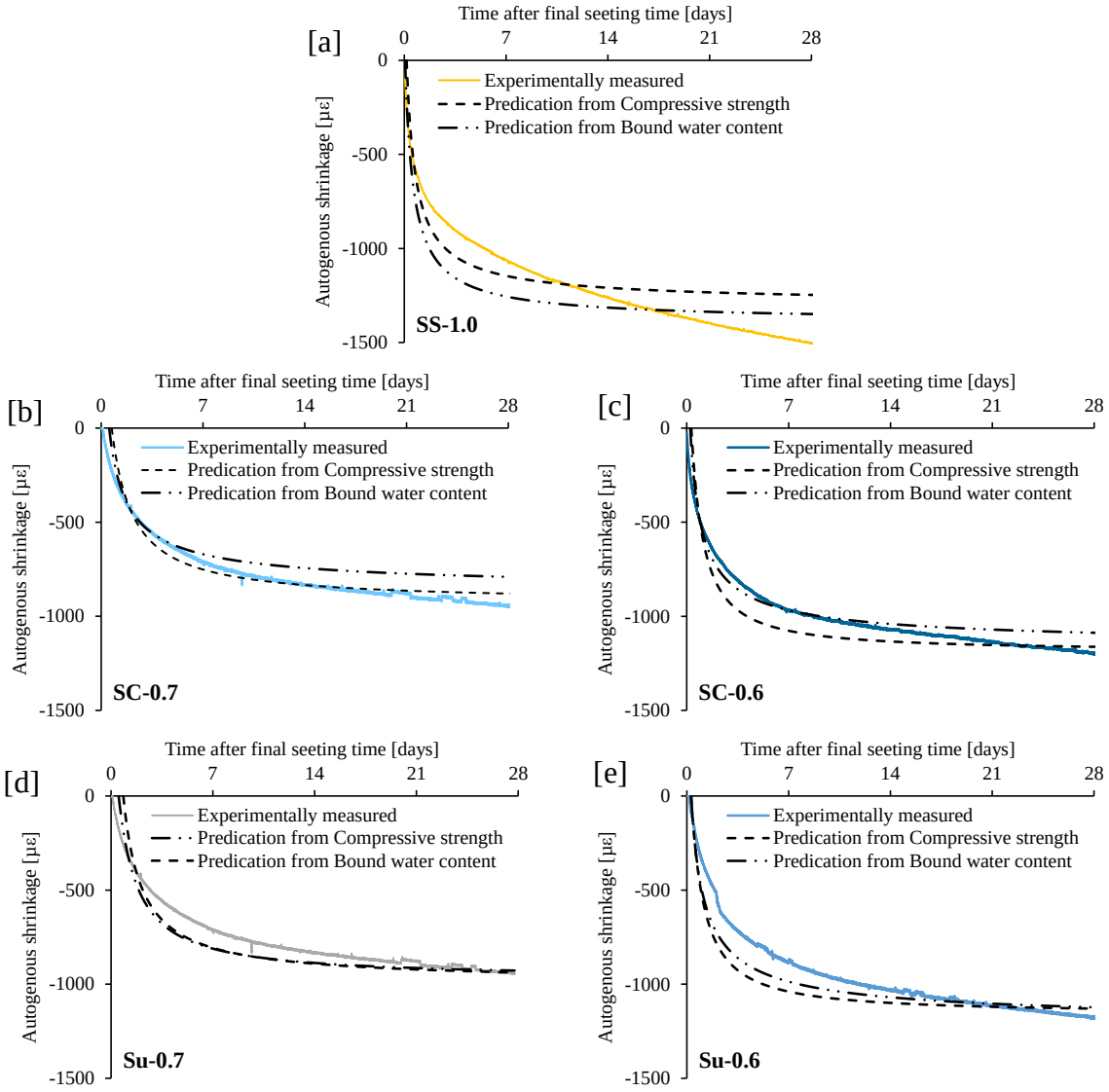

Figure 8.23: Comparison between measured and predicted autogenous shrinkage SS-1.0 [a], SC-0.7 [b], SC-0.6 [c], Su-0.7 [d], and Su-0.6 [e].

8.11 Conclusion

In this chapter, the effect of curing temperature on autogenous shrinkage of AASF samples is investigated. First, the influence of curing temperature on compressive strength, reaction kinetics, reaction products and microstructure development is primarily investigated. These aspects are then linked to the autogenous shrinkage behavior in order to elucidate the influential

role of curing temperature on autogenous shrinkage in AASF cements. Based on the experimental results and discussion, the following conclusions can be drawn:

- The autogenous shrinkage increases significantly with increasing curing temperature from 20°C to 40°C during early hours. However, after 3 days, the rate of autogenous shrinkage decreases with increasing curing temperature. The ultimate autogenous shrinkage at 28 days decreases by approximately 15-30% for the studied AASF samples with increasing the curing temperature from 20°C to 40°C.
- Increasing curing temperature greatly accelerates the reactivity of AASF at early hours, but later decelerated.
- C-A-S-H and N-A-S-H type gels are the two main reaction products formed in studied AASF systems, regardless of the curing temperature. FTIR results show that the increase in curing temperature enhances the linear polymerization of Si in C-A-S-H gel, but no influence on the cross-linking polymerization was observed with increase in curing temperature.
- The formation of 3D N-A-S-H type gels increases with increase in curing temperature.
- The elastic-part of the autogenous shrinkage decreases with increase in curing temperature. This is mainly due to the restrained effect of the matrix (high elastic modulus), which is rapidly formed at early ages.
- Increase in curing temperature enhances the crystallinity of C-A-S-H gels and reduces creep-part or viscoelastic deformation of the hydrated gels under capillary stress. Moreover, the formation of more 3D-structured N-A-S-H type gels restrain the deformability of C-A-S-H gels and results in lower autogenous shrinkage at 40°C.
- The self-desiccation process is decelerated over time due to decrease in rate of reaction and consequently the autogenous shrinkage is reduced at later ages in samples cured at 40°C.

Chapter 9

Conclusion

9.1 General conclusions

Alkali-activated cement is considered to be a promising eco-friendly alternative to Ordinary Portland Cement (OPC). In addition to its eco-friendly performance, the alkali-activated cements synthesized with blast furnace slag and fly ash offers several potential advantages as compared to OPC, including higher rate of strength development and good resistance to chemical and fire attacks. Despite these advantages, the acceptance and application of the alkali-activated slag/fly ash (AASF) cements in construction industry is hampered by concerns related to their quick setting process and large shrinkage deformations.

Sodium silicate (SS) is the most widely used activator in AASF cements that show comparable or even better strength properties to Portland cement. However, these cements set rather quickly due to presence of soluble SiO_4^{4-}, which renders them unsuitable for concrete applications. Also, the sodium silicate activation of slag and fly ash systems exhibits a considerably higher autogenous shrinkage (~6-10 times) than OPC. Furthermore, the production process of sodium silicate solution is expensive with high environmental impact. Meanwhile, samples activated with sodium carbonate (SC) and sodium sulfate (Su) generates longer setting (>3-5 days), slower strength development, and comparable shrinkage deformations to OPC. Hybrid or blended activators, therefore, can counterbalance the shortcoming of each activator and create a good balance between mechanical properties, cost, and environmental impact. Nevertheless, the effect of using hybrid activators on alkali-activated cements has not been investigated yet. Therefore, the main objective of this research is to assess the effect of hybrid activators (SS+SC or SS+Su) on the early-age structural development of alkali-activated slag/fly ash cements (AASF) causing setting and the autogenous shrinkage.

Carbon footprint:

In comparison to the traditional OPC mortar samples, the AASF samples activated with only sodium silicate reduce the CO_2 equivalent GHG emission to around 35%. The partial substitution of sodium silicate with sodium carbonate and sodium sulfate further reduce the CO_2 equivalent GHG emission to around 65-70% when compared to the OPC-mortar samples.

Proposed reaction mechanism from ultrasonic measurements:

By comparing the ultrasonic P-wave velocity with the isothermal calorimetry heat flow curves, the reaction mechanism of studied AASF systems could be described in five main stages as shown in Fig. 9.1.

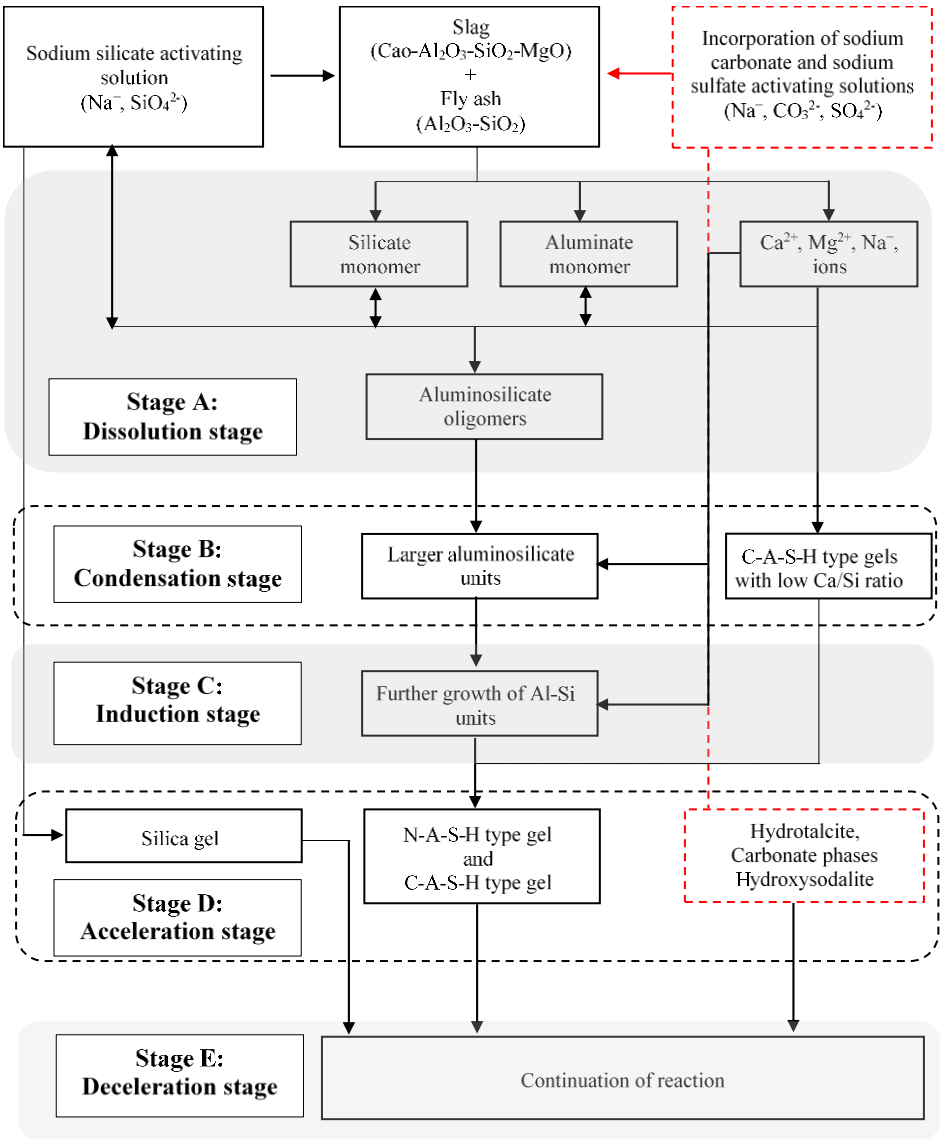

Figure 9.1: Schematic outline of the reaction mechanism involved in studied AASF systems based on UPV and heat flow measurements.

Stage A (~ <1 hours):

- Dissolution and hydrolysis of slag/fly ash simultaneous - forms aluminosilicate oligomers and/or monomers in solution.

Stage B (~ 1-3 hours):

- Aluminosilicate oligomers and/or monomers in solution undergoes condensation reactions and form large aluminosilicate structural units near the slag/fly ash particle surface.
- Formation of initial reaction products from the reaction between dissolved Ca^{2+} ions and anions present in the activator (SiO_4^{4-}, CO_3^{2-} and SO_4^{2-}).

Stage C (~ 3-16 hours):

- Polycondensation reaction at solid-liquid interface and/or between initial formed reaction products.

Stage D (~ 16-24 hours):

- Intense hydration and rapid formation of reaction products.

Stage E (~ >24 hours)

- Ongoing reaction.

Reaction kinetics:

The effect of incorporation of the sodium carbonate and sodium sulfate on the reaction kinetic of sodium silicate-activated samples was studied by isothermal calorimetry heat flow curves and bound water content measured from thermogravimetry analysis.

- With partial substitution of sodium silicate with sodium carbonate and sodium sulfate, the reaction rate decreases due to decrease in alkalinity (OH^- ions) of the solution. In samples with sodium carbonate and sodium sulfate, the rate of reaction increases with increase in concentration or alkali-content of the activator.
- **Role of anions (CO_3^{2-} and SO_4^{2-}) on the reaction kinetics:**
  In samples with sodium carbonate, the initially dissolved Ca^{2+} ions react with CO_3^{2-} ions in the activating solution to produce calcite. On the one hand, the formation of these phases consumes a large amount of dissolved Ca^{2+} ions and accelerate the dissolution of slag to provide more reactive ions to continue further reaction process.

On the other hand, the formation of calcite can act as a nucleation sites for the formation of C-A-S-H type gels and accelerate the reactivity in AASF systems. Moreover, the formation of calcite from the chemical reaction between dissolved Ca^{2+} ions and CO_3^{2-} ions releases OH^- ions into solution and enhances the reactivity of AASF systems.

In samples with sodium sulfate, the sulfate ions provided from the activating solution have limited influence on the reaction process and mostly remains as free ions in the pore solution.

As a result, the samples with sodium carbonate have higher rate of reactivity than those samples with sodium sulfate at the same concentration.

Setting and hardening behavior:

The setting process of the AASF paste samples was continuously monitored from ultrasonic P-wave velocity measurements and compared with standard Vicat needle test method. The effect of incorporation of sodium carbonate and sodium sulfate on the strength and stiffness development were experimentally measured on the mortar samples. The main conclusions are summarized as follows:

- The partial substitution of sodium silicate with sodium carbonate and sodium sulfate activators has no noticeable effect on the initial setting time, while the final setting time increases significantly.
- Comparative assessment of ultrasonic measurements with Vicat setting times and calorimetry heat flow curves shows that condensation reaction between the aluminosilicate units formed near the particle surface is most likely responsible for setting rather than the formation of C-A-S-H type gels.
- **Role of anions (CO_3^{2-} and SO_4^{2-}) on the setting process**

  The CO_3^{2-} and SO_4^{2-} ions in the pore solution, which are likely not involved in the formation of reaction products during early hours, are assumed to decelerate the condensation reaction between adjacent aluminosilicate units and lead to longer setting times. With increase in the concentration of sodium carbonate and sodium sulfate solutions, the setting times of AASF samples were further delayed due to increase in the amounts of the CO_3^{2-} and SO_4^{2-} ions in the pore solution.
- The incorporation of sodium carbonate and sodium sulfate significantly reduces the early-age strength and stiffness development of the sodium silicate-activated samples,

but strongly increases at later ages (≥ 3days) and shows comparable or even better strength and stiffness values than only sodium silicate-activated samples.

- The strength and stiffness development of the AASF samples can be predicted from the ultrasonic measurements on the mortar samples.

Characterization of solid phases and pore structure:

The reaction products of the AASF samples were characterized by thermogravimetry (TG), X-ray diffraction (XRD), Attenuated Total Reflectance FTIR spectrometry, and field emission gun electron probe micro-analyzer (FEM EPMA). The pore structure of the AASF paste samples was examined by using mercury intrusion porosimetry (MIP) and nitrogen adsorption test. The main conclusions are summarized as follows:

- The main reaction products in AASF samples are the Al-substituted C-A-S-H type gel (predominate with more Q^2 units) and the N-A-S-H type gel, regardless of type and concentration of the activator. Hydrotalcite is observed as the main secondary reaction product in all the AASF samples.
- **Role of anions (CO_3^{2-} and SO_4^{2-}) on the formation of reaction products**
  In samples with sodium carbonate, the CO_3^{2-} ions provided from the activating solution react with dissolved Ca^{2+} and Na^+ ions to produce carbonate phases like calcite, gaylussite, and pirssonite. The formation of hydroxysodalite phase is also identified in hybrid sodium silicate and sodium carbonate activation due to saturation of silicate and alumina species, as dissolved Ca^{2+} ions react with CO_3^{2-} ions rather than silicates to form C-A-S-H type gel.
  The presence of SO_4^{2-} ions in the activating solution does not lead to the formation of ettringite or any other crystalline sulfate phases.
- Incorporation of sodium carbonate and sodium sulfate solutions has limited influence on the gel structure of the main reaction products.
- The partial substitution of sodium silicate with sodium carbonate and sodium sulfate increases the Ca/Si ratio of (N,C)-A-S-H gel.
- Also, the Na/Si and Na/Ca ratio of the (N,C)-A-S-H gel in sodium silicate-activated samples is significantly reduced with incorporation of sodium carbonate and sodium sulfate solutions.
- In the pore solution of AASF samples activated with only sodium silicate, the concentration of the Na, Si, and Al ions decreases significantly with curing time.

However, with the incorporation of sodium carbonate and sodium sulfate, the level of decrease of these ions in the pore solution is reduced, indicating the formation of reaction products that consuming these ions is slowed down (i.e. lower rate of reaction).

- The porosity of sodium silicate-activated samples decreases when sodium carbonate and sodium sulfate solutions are incorporated. Samples with sodium carbonate exhibit a higher volume of mesopores compared to samples activated with only sodium silicate due to the formation of hydroxysodalite phase.

Autogenous shrinkage:

The autogenous shrinkage of the AASF mortar samples was experimentally measured and then related to the reaction kinetic, reaction chemistry and microstructure development to explore its basic mechanism. The main conclusions regarding the influence of incorporating sodium carbonate and sodium sulfate on autogenous shrinkage of sodium silicate activated AASF samples are summarized as follows:

- The partial substitution of sodium silicate with sodium carbonate and sodium sulfate reduces the autogenous shrinkage by around 50-75% during the first 24 hours and around 15-20% at the age of 28 days.
- Capillary stress induced by self-desiccation is the main driving force for the autogenous shrinkage in AASF. Besides this self-desiccation process, the Si polycondensation reaction at solid-liquid interface also induces a certain amount of autogenous shrinkage, especially during the induction period of heat flow or UPV curves.
- Viscoelastic or creep-part of the autogenous shrinkage, associated to the rearrangement and reorganization of C-A-S-H gels under internal stress, is the main governing part of the autogenous shrinkage in AASF.
- **Role of anions (CO_3^{2-} and SO_4^{2-}) on the autogenous shrinkage**

  Incorporation of sodium carbonate and sodium sulfate reduces the chemical shrinkage of sodium silicate activated samples due to the decrease in rate of reaction rather the phase assemblage.

  As a result of the decrease in chemical shrinkage and formation of coarser pore structure, the capillary stress in the pore fluid caused by self-desiccation is reduced and results in lower autogenous shrinkage for samples with sodium carbonate and sodium sulfate.

The partial substitution of sodium silicate with sodium carbonate and sodium sulfate substantial reduces the Si polycondensation reaction at solid-liquid interface due to decrease in soluble silicate in solution and results in a lower rate of autogenous shrinkage during the induction period of heat flow or UPV curve.

The incorporation of sodium carbonate and sodium sulfate substantial reduces the viscoelastic deformation of sodium silicate activated samples and results in a lower autogenous shrinkage.

- The autogenous shrinkage of the studied AASF systems can be accurately predicted from the compressive strength, bound water content, and ultrasonic P-wave velocity measurements.

Autogenous shrinkage cracking tendency:

The actual residual stress development and the stress relaxation under restrained autogenous shrinkage condition were quantified by using circular ring test. The potential for the early-age cracking in AASF was then calculated as the ratio of the residual tensile stresses to the tensile strength development. The influence of incorporation of sodium carbonate and sodium sulfate on the cracking potential of sodium silicate activated samples is summarized as follows:

- The partial substitution of sodium silicate with sodium carbonate and sodium sulfate significantly prolongs the time of cracking under restraint autogenous condition in AASF mortar samples.
- At equal replacement of sodium silicate with sodium carbonate and sodium sulfate solutions, the samples with sodium sulfate show higher cracking resistance than samples with sodium carbonate.
- Incorporation of sodium carbonate and sodium sulfate reduces the rate of restrained tensile stress development, as a result of the lower rate of autogenous shrinkage and stiffness development.
- The creep factor of sodium silicate activated samples increases during the first 24 hours with incorporation of sodium carbonate and sodium sulfate solutions.
- The studied AASF mortars have higher level of relaxation or creep effect compared to OPC-based mortars.
- As a consequence of pronounced stress relaxation, the cracking potential calculated as the ratio of residual stress in restrained ring to tensile strength is an appropriate failure criterion for the studied alkali-activated slag/fly ash mortar systems.

Influence of curing temperature:

The influence of curing temperature (20°C and 40°C) on reaction kinetics, reaction products and microstructure development are primarily investigated. These aspects are then linked to the autogenous shrinkage behavior. The main conclusions are summarized as follows:

- An elevated curing temperature can be effectively used as a mitigation strategy to control autogenous shrinkage of AASF cements.
- At high-curing temperature (40°C), the decrease in rate of autogenous shrinkage with time is primarily attributed to the suppression in the self-desiccation process due to decrease in rate of reaction and the formation of matrix with high elastic-modulus or restrain effect at early ages.
- The increase in crystallinity of C-A-S-H gels and formation of more 3D-structured N-A-S-H types are also responsible for a lower rate of autogenous shrinkage in samples cured at 40°C.
- **Role of anions (CO_3^{2-} and SO_4^{2-}) at elevated curing temperature**
  Increasing curing temperature has limited influence in terms of CO_3^{2-} and SO_4^{2-} ions contribution in the reaction process.

"In addition to the reduction of the CO_2 equivalent GHG emission, all the property improvements, such as delay in the setting time, improvement in the strength and stiffness development, reduction in the autogenous shrinkage and the cracking risk, suggest that the partial substitution of sodium silicate with naturally occurring minerals like sodium carbonate and sodium sulfate (hybrid activator) is a very promising way to develop more viable and durable alkali-activated cements".

9.2 Recommendations for future research

The present PhD work was focused on the understanding of setting and autogenous shrinkage behavior of slag/fly ash blends activated with hybrid sodium silicate-based activators through an interlinking assessment of reaction kinetics, reaction chemistry, and microstructure development. Based on the obtained results, a number of recommendations could be taken into account in future research.

- In this study, the setting behavior of AASF cements was investigated by comparing the ultrasonic P-wave velocity measurements with the Vicat needle test method. However, the Vicat needle test is developed to monitor the setting time of OPC-based materials, in which the 'nucleation and topotactic growth' of C-S-H gel is the basic mechanism resulting setting time. On the other hand, it is postulated in literature that 'through-solution' precipitation is more predominant in sodium silicate-based activated slag/fly ash systems to transform from a liquid precursor to a solid gel (setting time). Despite these differences in the microstructure development between alkali-activated cements and OPC, it is necessary to explore whether the traditional methods like Vicat needle test can be applied to alkali-activated cements.
- The nano-and microstructural evolution should be study in depth by using ^{27}Al and ^{29}Si NMR and SEM/ESEM analyses in order to well understand the setting and hardening behavior of the AASF cements.
- The kinetics of the reactions should be further study by using advanced quantification techniques:
    - Selective dissolution method.
    - Since the reaction products formed in studied AASF systems are highly X-ray amorphous, Partial or No Known Crystal Structures (PONKCS) analysis is recommended to distinguish and separately quantify both amorphous reaction products and precursors.
    - Back-scattered electron scanning electron microscopy (BSE-SEM) images combined with chemical Energy Dispersive X-ray spectrometry (EDX).
- From FTIR results, we observed that both C-A-S-H and N-A-S-H type gels were the main reaction products in the studied AASF. However, many researchers have been arguing the co-existence of these two gels in high slag/fly ash ratio blends activated at highly alkaline environment. Therefore, further study using advance techniques like ^{27}Al and ^{29}Si NMR is needed to confirm the co-existence of C-A-S-H and N-A-S-H type gels in studied AASF at 20°C.
- With respect to the scope of this thesis, several extensions on the autogenous shrinkage behavior of AASF could be taken into account in future research:
    - As hydration is an exothermic reaction (from Chapter 4), the temperature variation plays a major role in the autogenous internal stress development. In order to characterize the importance of these deformations regarding self-

desiccation deformation, a decoupling of autogenous and thermal shrinkage should be performed by considering a coefficient of thermal expansion (CTE).

  - From results in Chapter 6, it is clear that the viscoelastic behavior or creep-part plays an important role in autogenous shrinkage of AASF systems. To explain the scientific reasoning and mechanisms behind the pronounced viscoelastic deformations in AASF, the C-A-S-H phase needs to be further investigated.
  - The role of disjoining pressure on the autogenous deformation should be considered since it has been reported that at high to moderate RH, the disjoining pressure may also contribute to autogenous deformation in cementitious materials.

- In this study, only the autogenous shrinkage of AASF cements was investigated. But it is necessary to investigate all other shrinkage deformations like drying shrinkage and carbonation shrinkage to understand which shrinkage deformation is more dominant in total shrinkage deformation, and which one is at the origin of shrinkage micro-cracking.
- The autogenous shrinkage of AASF samples in concrete scale also needs to be investigated, because concrete is the final product used in real structures. Additionally, the mechanical bonding between the aggregates and the matrix is very important for the assessment of the engineering properties in concrete scale.
- Creep behavior (both basic and drying) of the AASF cements needs to be studied.
- It is highly recommended to take into account the influence of S ions on the microstructure changes of C-A-S-H gel, since their content in the pore solution is markedly high as shown in Table. 5.2.
- Durability properties such as carbonation resistance, sulfate resistance, freeze-thaw resistance, chloride ingress, acid resistance, etc., should be investigated to get complete picture of the performance of the studied AASF.

Appendix A

Technical datasheets

This appendix contains the technical datasheets of the sodium silicate activating solutions, fly ash, and river sand.

Gute Chemie abcr

Specification

Product name:	**Sodium silicate; water glass, 39-40% silicates in water**
Product no.:	**AB100652**
CAS no.:	**[1344-09-8]**

Test	**Specification**
Solids content	35.8% approx.
Na_2O SiO_2	8.3% approx. 27.5% approx.
pH	11.3 approx.
Viscosity	100 mPa·s approx.
Weight ratio (SiO_2 : Na_2O)	3.3 approx.
Mol ratio (SiO_2 : Na_2O)	3.4 approx.
Specific weight	1.37 g/cm^3 approx.

Dipl. Ing. Ute Eschrig
Product Safety Manager

Phone +49 (0)721 95061 46
Fax +49 (0)721 95061 33
u.eschrig@abcr.de

Karlsruhe, 14.11.2016

BauMineral KraftWerkstoffe

PRODUCT DATA SHEET

EFA-Füller® HP

Fly ash according to DIN EN 450-1 – For concrete according to DIN 1045-2

The fly ash **EFA-Füller® HP from the power plant Heyden of Uniper Kraftwerke GmbH** is a fine-grained pozzolanic binder that consists mainly of SiO_2 and Al_2O_3. The content of reactive SiO_2 is at least 25 % by mass. It is a type II concrete addition according to DIN 1045-2: Plain, reinforced and pre-stressed concrete structures – Part 2: Specification, properties, production and conformity of concrete – Application document for use with DIN EN 206-1.

In combination with DIN EN 206-1 DIN 1045-2 regulates the use of **EFA-Füller® HP** as follows:

- paragraph 5.2.5.2.2:
  - minimum cement content
  - maximum permissible water/cement ratio
  - sulphate resistance
  - combined use with aggregates sensitive to alkalis
- paragraph 5.2.5.2.4: the common use of **EFA-Füller® HP** and microsilica
- paragraph 5.3.2: the limits for the fine grain content < 0.125 mm
- paragraph 5.3.4: the use of **EFA-Füller® HP** in subaqueous concrete

The use of **EFA-Füller® HP** in bored cast-in-place piles according to DIN EN 1536 and cast-in-situ concrete diaphragm walls according to DIN EN 1536 is regulated by addendum to the enclosure for parts 2.1/2 and 2.1/6 of "Musterliste der Technischen Baubestimmungen". According to this paragraphs paragraph 5.3.4 from DIN 1045-2 has to be used for these concretes.

Advantages of **EFA-Füller® HP**:

- cement reduction
- reduction of water demand
- improved workability of fresh concrete including pumping capability
- increased compactability of fresh concrete
- reduction of the hydration temperature, e.g. for mass concrete

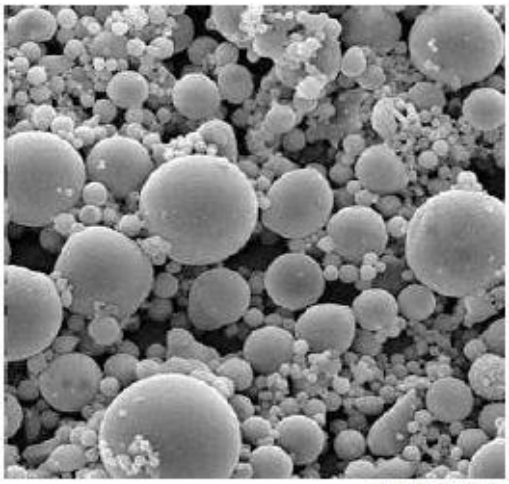

scale: 1000:1

- reduced efflorescence of the concrete
- increased resistance to chemical attacks on concrete, e.g. Sulphate, chloride, sea water

CHARACTERISTIC VALUES

Loss on ignition: category A	≤ 5 % by mass
Fineness > 45 µm	20 ± 10 % by mass
Na_2O equivalent *	2.95 % by mass
Bulk density (DIN EN 459 part 2) *	1,11 t/m³
Particle density	2.32 ± 0.20 t/m³

* average of the year 2015

PARTICLE SIZE DISTRIBUTION *

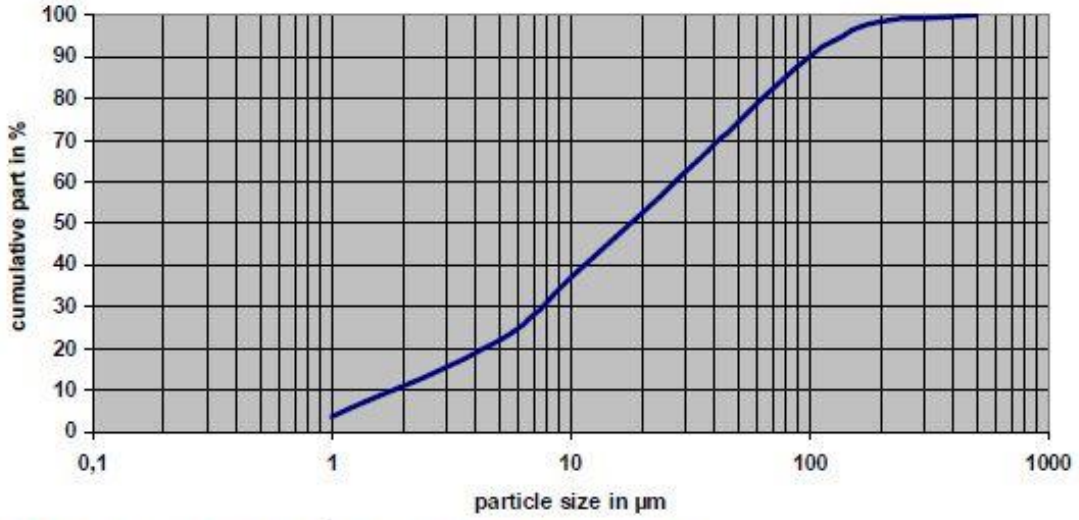

STRENGTH DEVELOPMENT * (according to DIN EN 196 part 1)

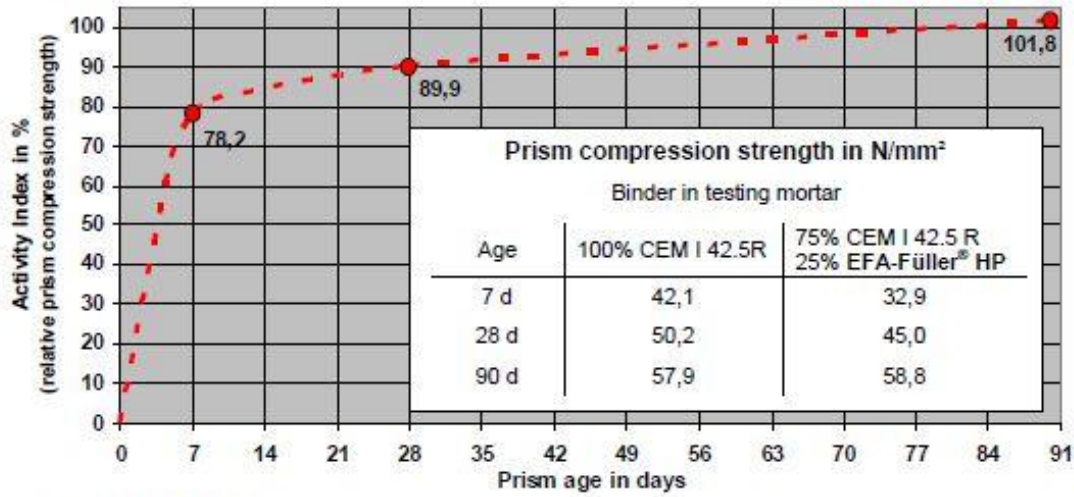

Prism compression strength in N/mm²

Binder in testing mortar

Age	100% CEM I 42.5R	75% CEM I 42.5 R 25% EFA-Füller® HP
7 d	42,1	32,9
28 d	50,2	45,0
90 d	57,9	58,8

* average of the year 2015

BauMineral

Werk Heyden

Z-3.31-1792

MPA NRW.

EFA-Füller® HP

Fly ash according to DIN EN 450-1

CE

0432 - CPR - 00112-01

External control and certification
Materialprüfungsamt
Nordrhein-Westfalen (MPA)
Marsbruchstraße 186
44287 Dortmund

BauMineral GmbH
Hiberniastraße 12
45699 Herten
Germany
Phone: +49 (0) 23 66/509-0
Fax: +49 (0) 23 66/509-285

Building material testing laboratory
(Internal quality control)

Internet: www.baumineral.de
E-Mail: baumineral@baumineral.de

Version: 10/2016

PRESTATIEVERKLARING BFCV-A2-002

COECK
innovative building material partner

Producent - distributeur:
Coeck NV - De Laetstraat 6 - 2845 Niel - België
Tel. +32 3/880.75.00 - Fax. +32 3/880.75.10

CE

Jaar van de markering: 13
Systeem 2+

Product **Rivierzand 0/4**

Toepassing: Zand voor bereiding van beton en mortel voor bouwwerken, wegen en andere civieltechnische werken.

Essentiële kenmerken	**Prestaties**		**Geharmoniseerde technische specificaties**
Korrelgroep	0-8		NEN-EN 12620:2002 + A1:2008 NEN-EN 13139:2002 + C1:2006
Categorie korrelverdeling	$G_{NR}90$		
	ISO 565:1990 R20	Grenzen [%]	
	11,2 8 5,6 4 2 1 0,250 0,125	100 - 100 97 - 100 88 - 100 82 - 99 73 - 93 58 - 78 0 - 20 0 - 3	
Korrelvorm	Ecs<30		
Waterabsorptie	≤ 0,5%		
Deeltjesdichtheid	2,60 ± 0,07 (Mg/m³)		
Schelpgehalte	SC_{10}		
Hoeveelheid fijne deeltjes < 63 µm	F3		
Weerstand tegen verbrijzeling	LA_{NR}		NEN-EN 12620:2002 + A1:2008
Weerstand tegen afslijten	$M_{DE}NR$		
Weerstand tegen polijsten	PSV_{NR}		
Weerstand tegen afslijten van het korreloppervlak	AAV_{NR}		
Weerstand tegen afslijten door spijkerbanden	AN_{NR}		
Bestanddelen in grove gerecyclede toeslagmaterialen	NR		
Chloridegehalte	≤ 0,005%		NEN-EN 12620:2002 + A1:2008 NEN-EN 13139:2002 + C1:2006
In zuur oplosbaar sulfaat	AS0,2		
Totaal zwavelgehalte	Voldoet (<1%)		
Gehalte aan in water oplosbaar sulfaat van gerecyclede toeslagmaterialen	SS_{NR}		NEN-EN 12620:2002 + A1:2008
Bindings- en verhardingsvertraging	Voldoet		NEN-EN 12620:2002 + A1:2008 NEN-EN 13139:2002 + C1:2006
Invloed op bindtijd van cement (gerecyclede toeslagmaterialen)	A_{NR}		NEN-EN 12620:2002 + A1:2008
Gehalte aan carbonaten	≤ 0,2% m/m		
Volume stabiliteit	NPD		NEN-EN 12620:2002 + A1:2008 NEN-EN 13139:2002 + C1:2006
Bestanddelen die de vormvastheid van luchtgekoelde hoogovenslak beïnvloeden	NR		NEN-EN 12620:2002 + A1:2008
Vrijkomende gevaarlijke bestanddelen	NPD		NEN-EN 12620:2002 + A1:2008 NEN-EN 13139:2002 + C1:2006
Vorst/dooi bestandheid	F_{NR}		
ASR gevoeligheid	Niet gevoelig		

De aangemelde certificatie-instantie IKOB-BKB (nr 0957) heeft onder systeem 2+ de initiële inspectie van de productie-installatie en van de productiecontrole in de fabriek uitgevoerd en zal tevens de permanente bewaking, beoordeling en evaluatie van de productiecontrole op zich nemen. Op basis daarvan is het conformiteitscertificaat voor de productiecontrole in de fabriek verstrekt.
De prestaties van het omschreven product zijn conform de aangegeven prestaties. Deze prestatieverklaring wordt verstrekt onder de exclusieve verantwoordelijkheid van de fabrikant. Ondertekend voor en namens de distributeur.

Ludo Coeck
Gedelegeerd Bestuurder

Robert Coeck
Gedelegeerd Bestuurder

Appendix B

Screening mix compositions

In the appendix, a bottom-up approach is adopted based on the Vicat setting times, isothermal calorimetry heat evolution curves, and strength development to determine the optimum mix composition for alkali-actiavted slag/fly ash blend cements. For this study, the classified fly ash with a mean diameter of 20 μm and ground granulated blast furnace slag were used as primary materials. Various combination of activators with different concentrations were tested and most ideal activator combinations are selected for further studies. A bottoum-up approach is shown in Fig. B.1

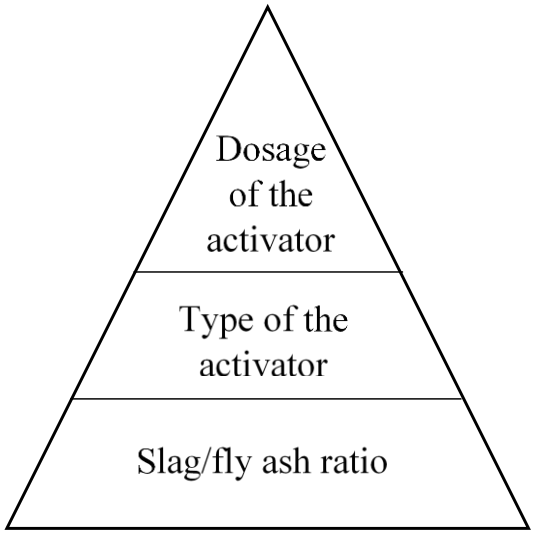

Figure B.1: A bottom-up approach for developing optimal mix compositions.

B.1 Effect of slag/fly ash ratio

First, the optimum synthesis of slag/fly ash blended system is determined based on the screening test results. Sodium silicate solution with alkali-modulus (M_s) of 1.25 and alkali-content of 7.5% was used as the activating solution.

Vicat setting times:

The Vicat setting times of alkali-activated slag/fly ash pastes (AASF) are shown in Fig. B.2. It can be seen that both initial and final setting times of AASF pastes significantly increases with increasing the fly ash replacement content.

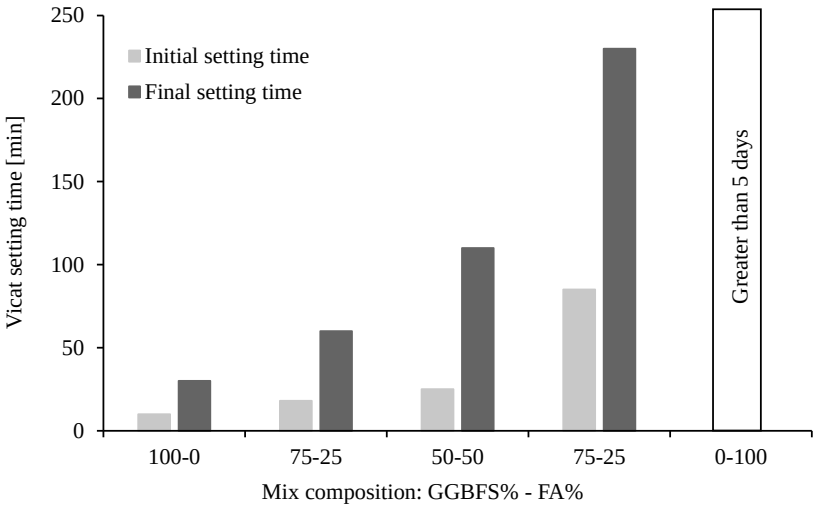

Figure B.2: Effect of slag/fly ash ratio on Vicat setting times.

Calorimetry heat flow curves:

The heat flow of slag/fly ash blends activated with sodium silicate of alkali-modulus 1.25 up to 72 hours is shown in Fig. B.3. Increasing fly ash content shows considerably longer induction periods due to its low reactivity and it may mainly act as an inert material and has a negative contribution to the further reaction between alkalis and slag particles.

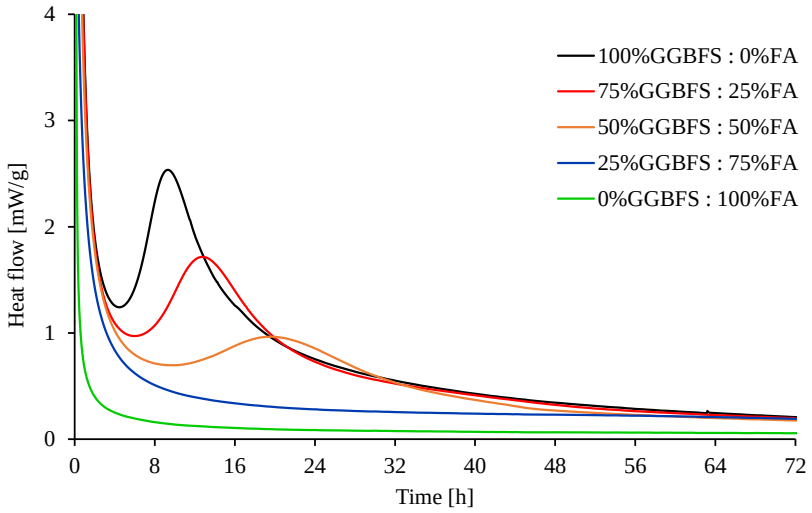

Figure B.3: Heat evolution rate of AASF pastes.

The cumulative heat evolutions of slag/fly ash blends activated with a sodium hydroxide and sodium silicate are shown in Fig. B.4. The first dramatic increase is associated with the initial wetting and dissolution of slag and fly ash in the alkali solutions; followed by moderate increase corresponding to the induction period; the further increase is assigned to the

acceleration stage. The heat of hydration decreases with increase in fly ash content ash as shown in Fig. B.4.

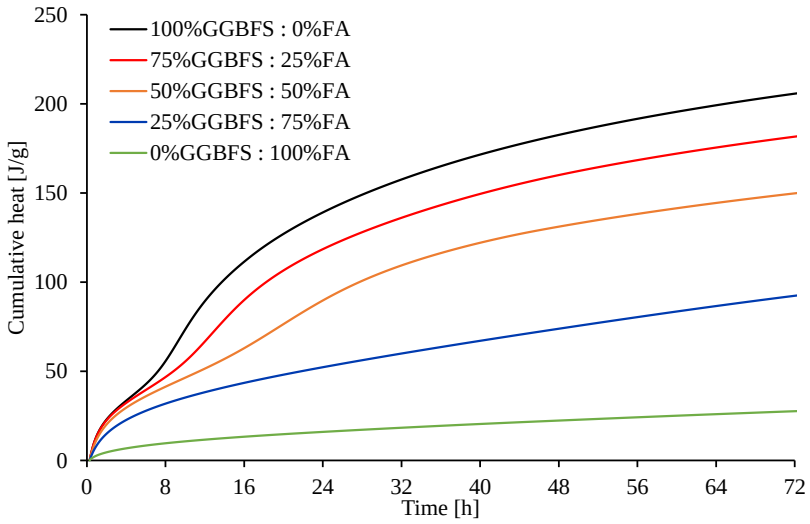

Figure B.4: Cumulative heat release of AASF pastes.

Compressive strength:

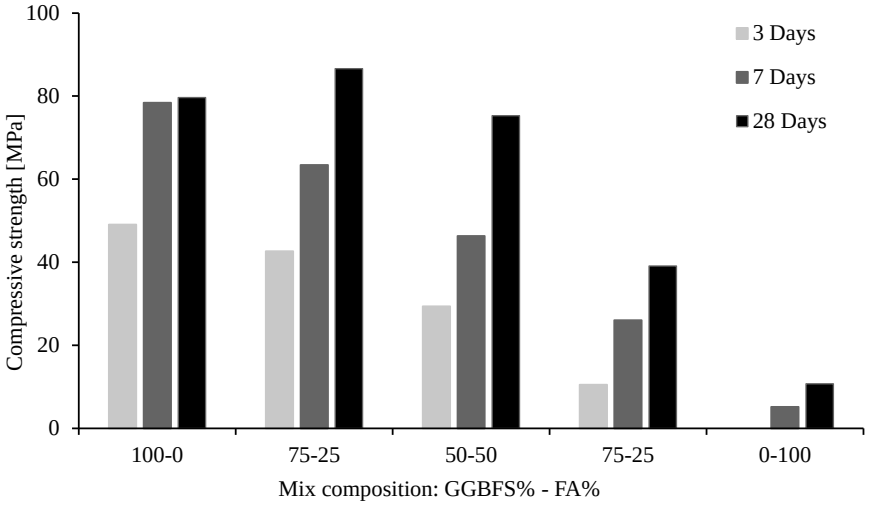

Figure B.5: Compressive strength development of AASF mortar samples.

One of the key factors affecting the strength of the alkali-activated slag/fly ash blend system is the amount of CaO. This arises because the presence of high amount of CaO improves the compactness of the microstructure by forming the C-S-H gel. As a result, an increase in the amount of GGBFS was followed with the increase in strength properties with respect to curing age (Fig. B.5). However, the strength development of AASF with 100% slag levels off between 7 and 28 days and show lower strength when compared to 75% GGBFS-25% FA at the age of

28 days. The reason is likely due to the development of micro-cracks caused by large autogenous shrinkage strains (Fig. B.5). Moreover, the high strength with 25% FA replacement is due to the formation of highly cross-linked structures of the reaction products caused by the presence of Al supplied by fly ash dissolution.

Autogenous shrinkage:

Early-age autogenous shrinkage deformation is a physico-chemical phenomenon resulted from the chemo-mechanical and hydro-mechanical interactions within the hardening cementitious matrix. The chemo-mechanical deformation known as Le Chatelier contraction (chemical shrinkage) developed due to the negative balance between the absolute density of hydrates and those of cementitious materials and solution, while the hydro-mechanical deformation, known as self-desiccation shrinkage, results from the development of internal stresses within the matrix due to the consumption of pore solution by hydration.

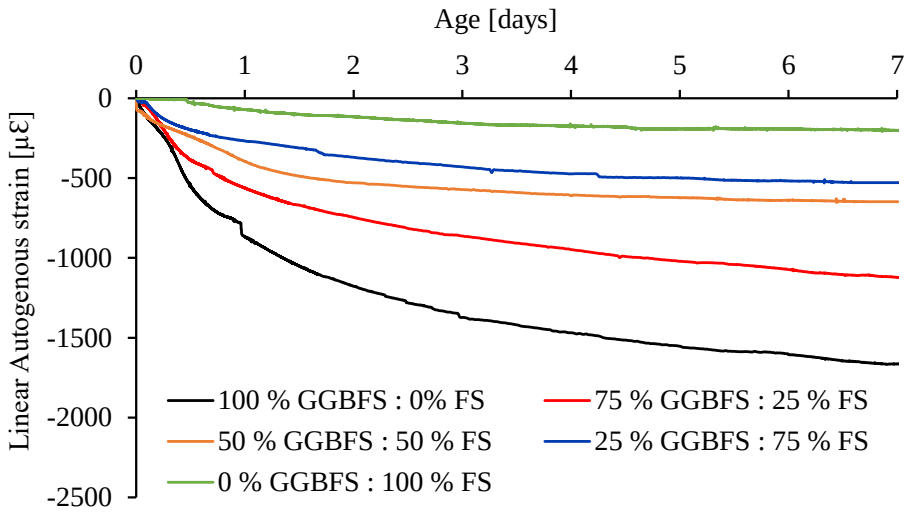

Figure B.6: Autogenous shrinkage of AASF mortar samples.

Fly ash contains more inactive minerals and also its active constituents are mainly hollow glass spheres, which are not as reactive as glassy phase of slag at early ages. As a result, the reactivity of alkali-activated slag/fly blend systems decreases with increase in fly ash content as shown in Fig. B.3 and thus the autogenous deformation related to the chemical shrinkage decreases with increases in fly ash content. In addition to this, with increase in the fly ash content and decrease in slag content, the concentration Ca^{+2} ions decrease and contributes to the formation of less C-A-S-H gel. This may result in formation of less dense matrix and lower mesopore volume, which is related to self-desiccation resulting from a decrease in the relative humidity

of the capillary pores. Thus, the autogenous shrinkage related to self-desiccation decreases with increases in fly ash as shown in Fig. B.6.

B.2 Effect of type and concentration of the activator

Based on the above results, slag to fly ash ratio at 80:20 vol% was selected to screen the type and dosage of activators. Screening tests were performed on different type of activator with different concentrations given in Table. B.1.

Table B.1: Mix proportions of alkali-activated slag/fly ash blends.

Mix ID	**Sodium Silicate**		**Sodium hydroxide**	**Sodium Carbonate**	**Sodium Sulfate**	**Modulus M_s= (SiO_2/Na_2O)**
	SiO_2 [%]	Na_2O [%]	Na_2O [%]	Na_2O [%]	Na_2O [%]	
SS-1.5	12.0	8.0	-	-	-	1.50
SS-1.25	10.0	8.0	-	-	-	1.25
SS-1.00	8.0	8.0	-	-	-	1.00
SS+SC-0.7	4.0	4.0	-	1.70	-	0.7
SS+SC-0.6	4.0	4.0	-	2.70	-	0.6
SS+SC-0.5	4.0	4.0	-	4.00	-	0.5
SS+Su-0.7	4.0	4.0	-	-	1.70	0.7
SS+Su-0.6	4.0	4.0	-	-	2.70	0.6
SS+Su-0.6	4.0	4.0	-	-	4.00	0.5
SH+SC-6%	-	-	3.0%	3.0%	-	-
SH+SC-9%	-	-	3.0%	6.0%	-	-
SH+SC-6%	-	-	3.0%	-	3.0%	-
SH+SC-9%	-	-	3.0%	-	6.0%	-

Vicat setting times:

The Vicat setting time of alkali-activated slag/fly ash blends (AASF) with different type and concentrations are shown in Fig. B.7. The Vicat setting time results imply that the activator used in AASF cements follow this order in setting time:

Sodium silicate < Sodium silicate + sodium carbonate < Sodium silicate + Sodium sulfate < Sodium hydroxide + sodium carbonate < Sodium hydroxide + sodium sulfate.

The results of samples activated with only sodium carbonate and sodium sulfate are presented since there does not setting behavior even after 5 days after casting. With increasing silicate content or alkali-modulus from 1.0 to 1.5, the setting time decreases. While with increasing concentration of sodium carbonate and sodium sulfate, the Vicat setting time increases.

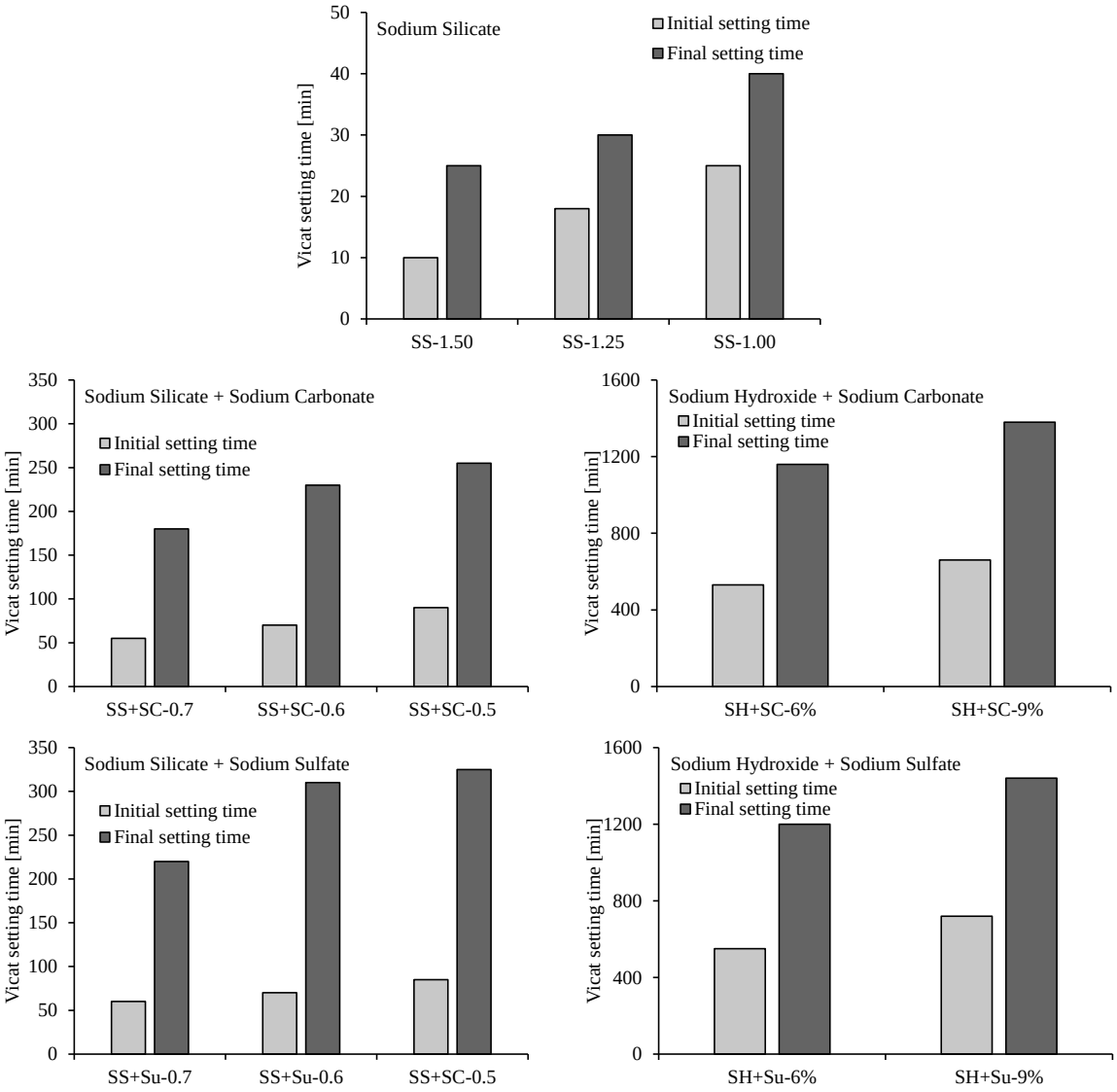

Figure B.7: Effect of type and concentration on Vicat setting times of AASF pastes.

Calorimetry heat flow curves:

The heat evolution of alkali-activated slag/fly ash blended cements activated with different alkaline solution given in Table. B.1 are shown in Fig. B.8.

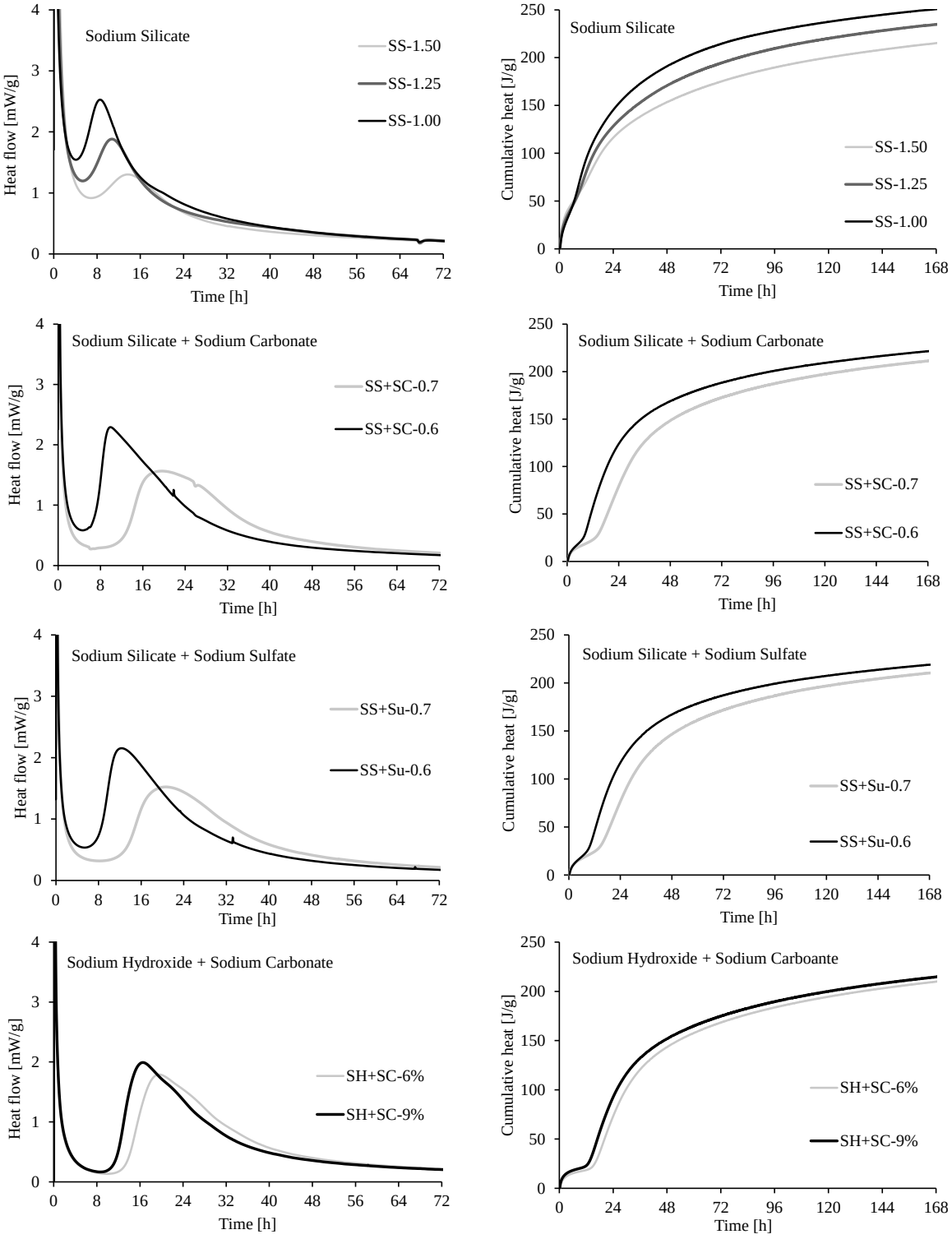

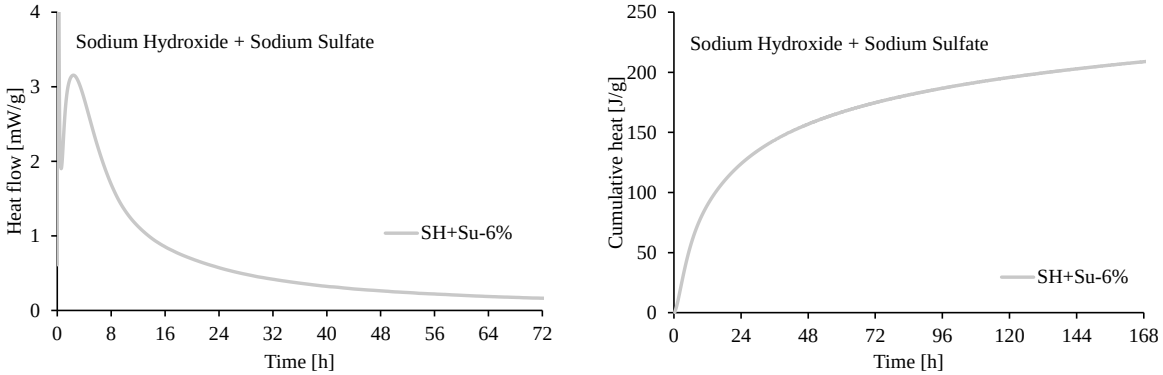

Figure B.8: Effect of type and concentration on heat evolution of AASF pastes.

Samples activated with sodium silicate shows higher rate of reaction. With incorporating sodium carbonate and sodium sulfate, the rate of reaction decreases due to decrease in alkalinity of the solution. In comparison, samples activated with combination of sodium silicate and sodium carbonate results higher rate of reaction than samples combined with sodium hydroxide. The samples activated with hybrid sodium hydroxide and sodium sulfate shows shorter induction as shown in Fig. B.8.

It can be seen that increasing the silica content or alkali-modulus from 1.0 to 1.5 decreases the rate of reaction. This can be explain by the fact that increasing silica concentration led to a higher degree of polymerization reaction in the alkaline solution and forms more trimer units rather than monomer and dimer units. The formation of monomer or dimer can directly react with dissolved ions and form reaction products casing setting and strength development, while the trimer units reacted very slowly and retard the degree of reaction. The increase in concentration (Na_2O) of sodium carbonate and sodium sulfate results in higher rate of reaction.

Compressive strength:

The compressive strength of alkali-activated slag/fly ash mortar samples activated with different type and concentration of activators are shown in Fig. B.9. It can be seen that samples activated with sole sodium silicate shows higher compressive strength development compared to all other activators. With incorporating sodium carbonate and sodium sulfate, the compressive strength of sodium silicate-activated samples decreases significantly during first 24 hours. However, at and beyond 3 days, the compressive strength strongly improves and shows comparable or even better results than sole sodium silicate-activated samples. While in samples activated with hybrid sodium hydroxide and sodium silicate, the strength values are significantly lower than the samples activated with sole sodium silicate.

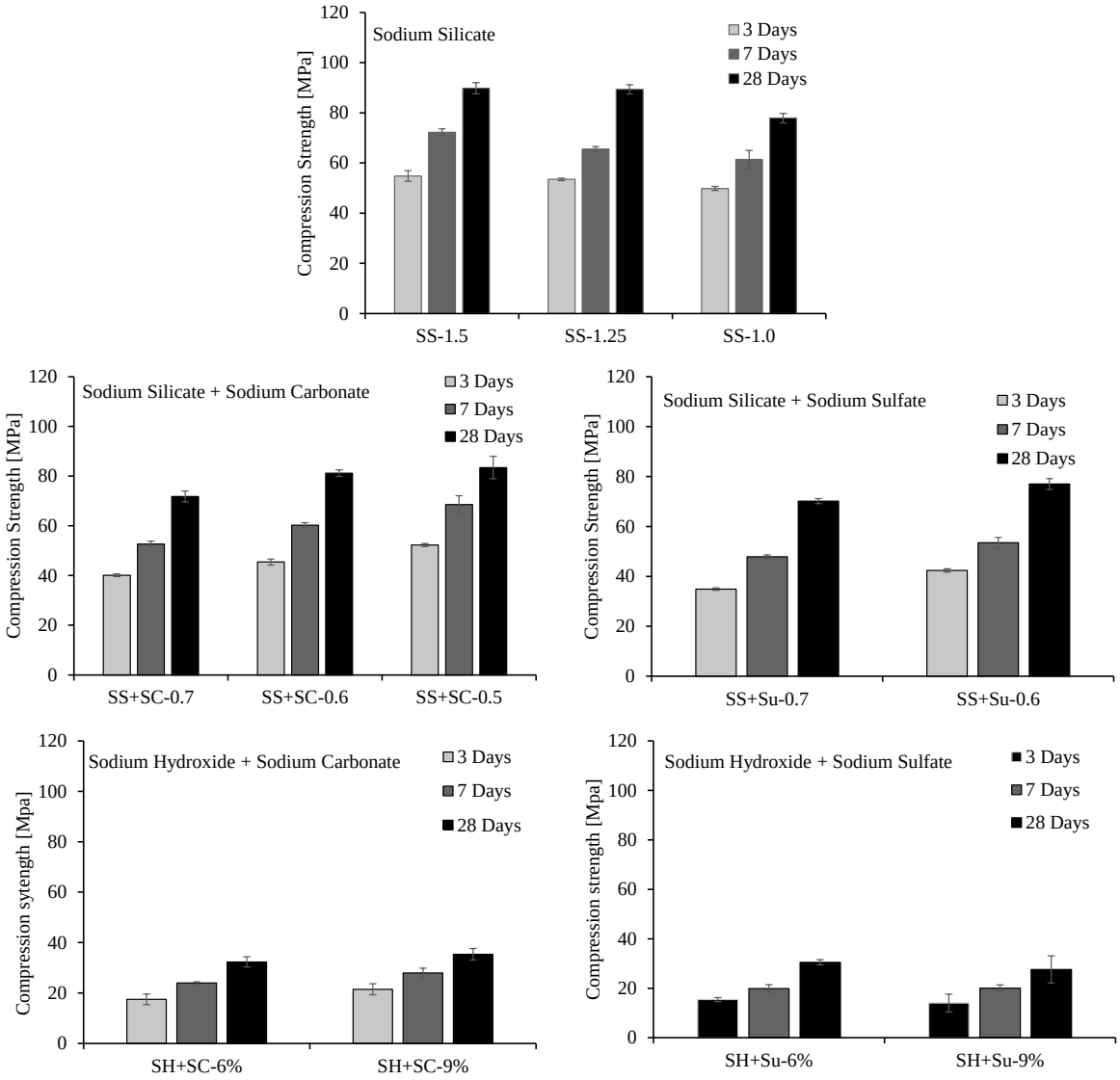

Figure B.9: Effect of type and concentration on compressive strength of AASF pastes.

It can be seen that with increasing concentration of silica content or alkali-modulus from 1.0 to 1.5, the compressive strength increases, although the rate of reaction decreases as shown in Fig. B.8. This can be attributed to the other factor influencing the compressive strength development, such as pore size distribution and microstructure development. While with increasing the concentration or alkali-content of the sodium carbonate and sodium sulfate solutions, the compressive strength increases due to higher rate of reaction.

Appendix C

Repeatability of the isothermal calorimetry

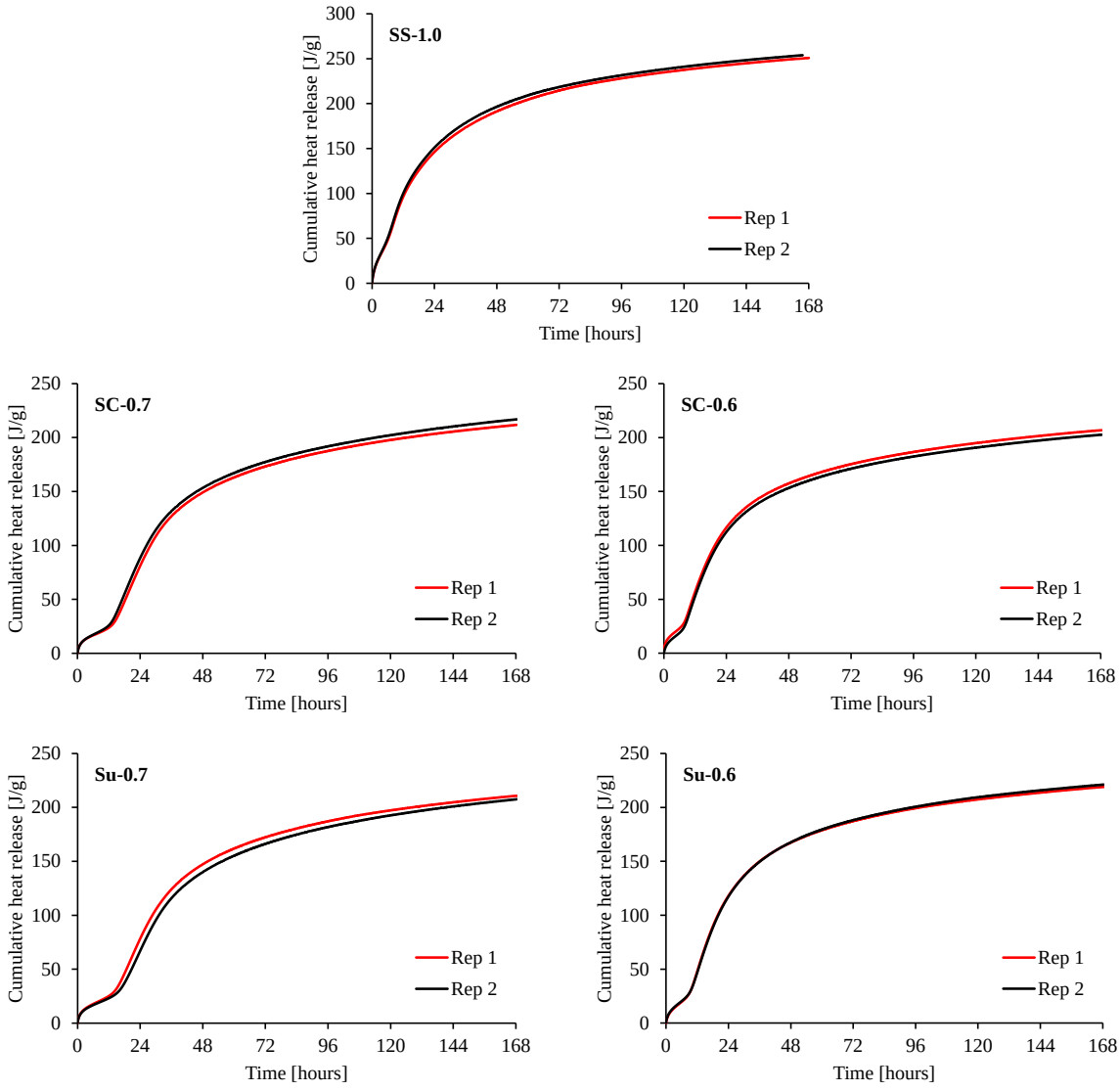

Figure C.1: Repeatability of the isothermal calorimetry heat flow curves.

Repeatability of the autogenous shrinkage

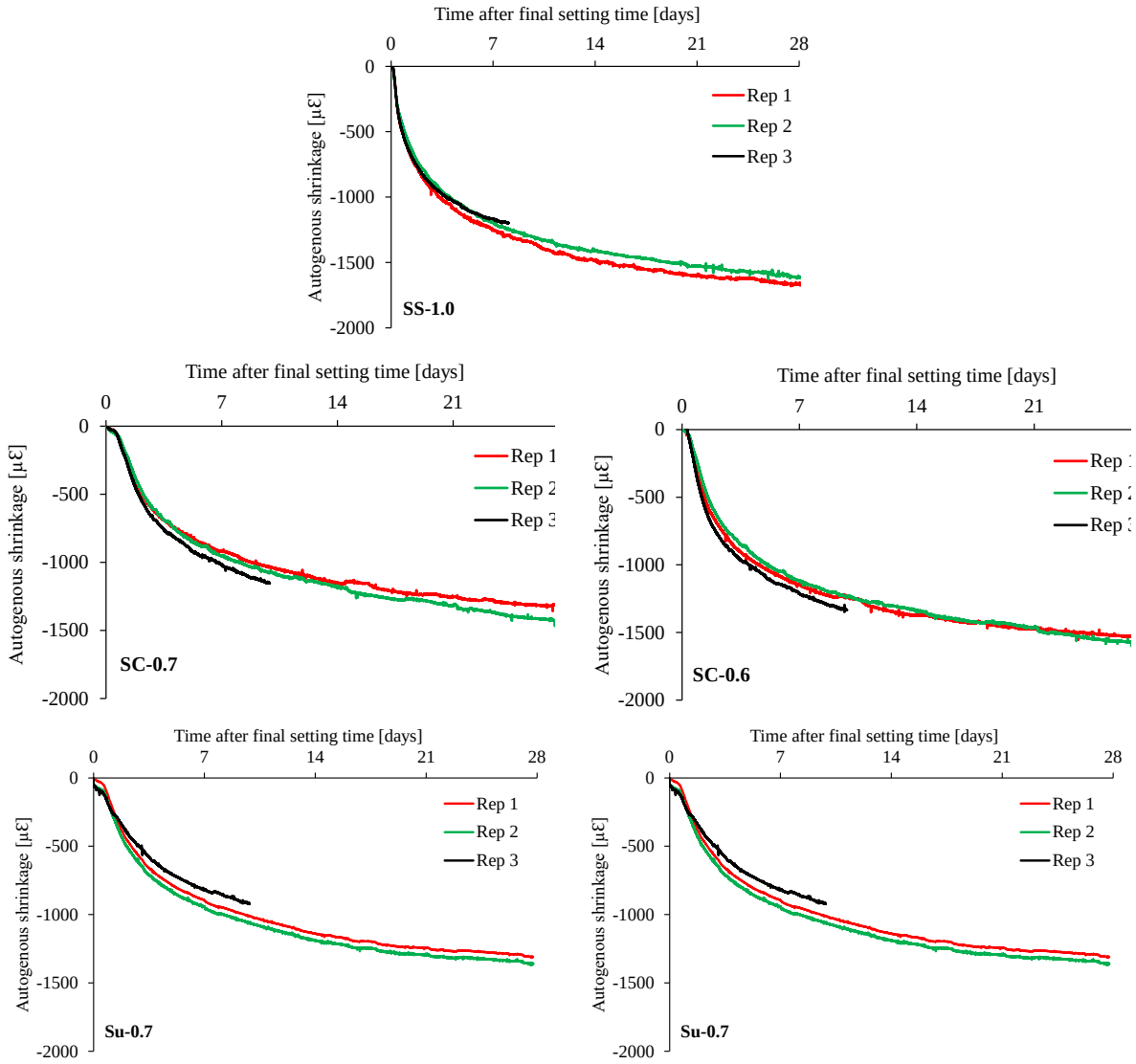

Figure C.2: Repeatability of the autogenous shrinkage of AASF mortar samples.

Appendix D

Gel molecular structures

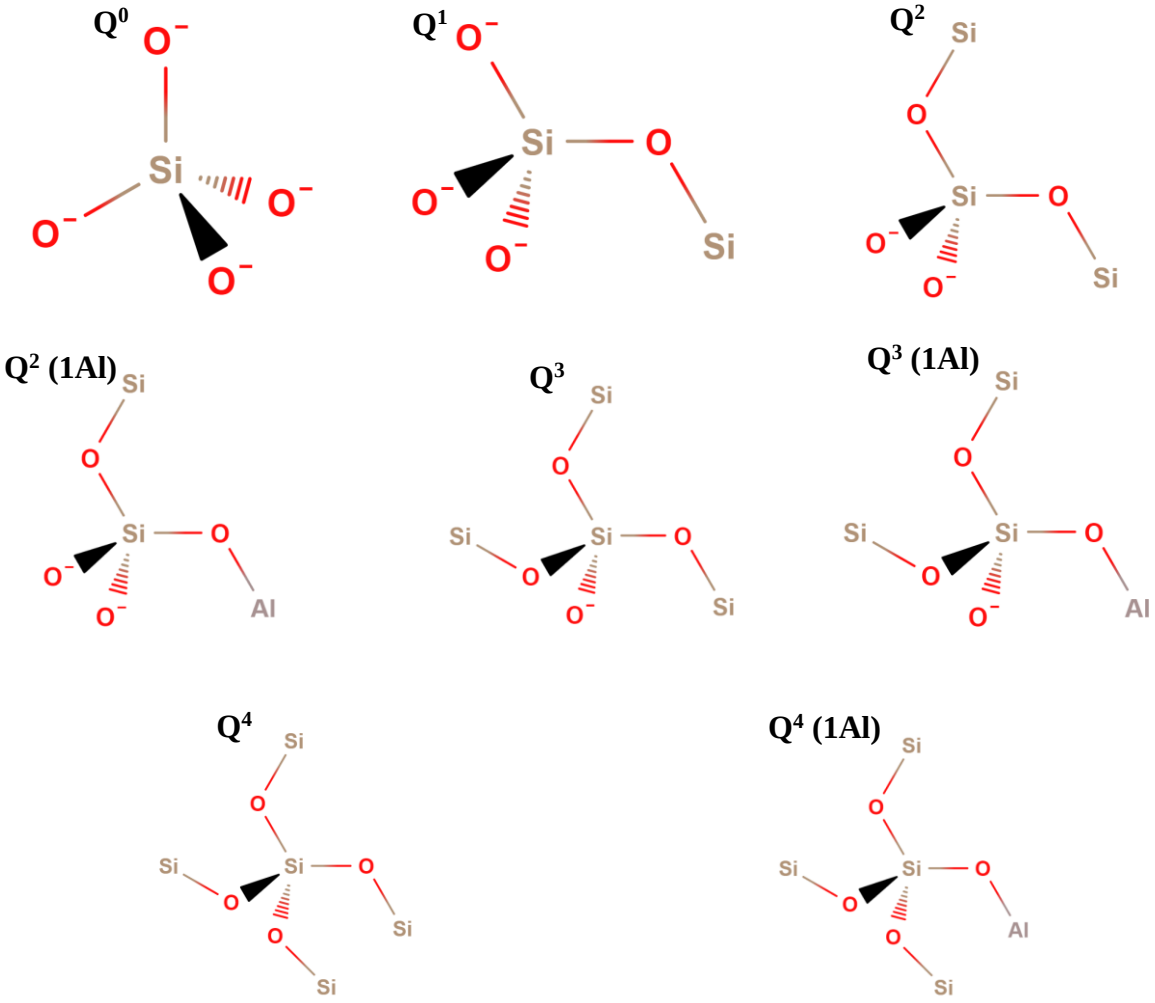

Gel molecular structures based on connectivity of silicate sites in the alkali-activated materials.

Bibliography

[1] M. Schneider, "The cement industry on the way to a low-carbon future," *Cement and concrete Research,* vol. 124, 2019.

[2] OECD/IEA and CSI, "Low-carbon Transition in the Cement Industry: Technology," International Energy Agency, IEA, Paris, 2018.

[3] R. M. Andrew, "Global CO2 emissions from cement production," *Earth System Science Data,* vol. 10, pp. 195-217, 2018.

[4] Z. He, X. Zhu, J. Wang, M. Mu and Y. Wang, "Comparison of CO2 emissions from OPC and recycled cement production," *Construction and Building Materials,* vol. 211, pp. 965-973, 2019.

[5] M. Schneider, M. Romer, M. Tschudin and H. Bolio, "Sustainable cement production—present and future," *Cement and Concrete Research,* vol. 41, no. 7, pp. 642-650, 2011.

[6] UN Environment, K. L. Scrivener, V. M. John and E. M. Gartner, "Eco-efficient cements: Potential economically viable solutions for a low-CO2 cement-based materials industry," *Cement and Concrete Research,* vol. 114, pp. 2-26, 2018.

[7] S. A.Miller, A. Horvath and P. J.Monteiro, "Readily implementable techniques can cut annual co2 emissions from the production of concrete by over 20%,," *Environmental Research Letters,* vol. 11, no. 7, 2016.

[8] D. N. Huntzinger and T. D. Eatmon, "A life-cycle assessment of portland cement manufacturing: comparing the traditional process with alternative technologies," *Journal of Cleaner Production,* vol. 17, no. 7, pp. 668-675, 2009.

[9] B. Lothenbach, K. Scrivener and R.D. Hooton, "Supplementary cementitious materials," *Cement and Concrete Research,* vol. 41, no. 12, pp. 1244-1256, 2011.

[10] S. Joseph, R. Snellings and Ö. Cizer, "Activation of Portland cement blended with high volume of fly ash using Na2SO4," *Cement and Concrete Composites,* vol. 104, 2019.

[11] J. L. Provis, "Alkali activated materials," *Cement and Concrete Research,* vol. 114, pp. 40-48, 2018.

[12] A. Palomo, P. Krivenko, I. Garcia-Lodeiro, E. Kavalerova, O. Maltseva and A. Fernandez-Jimenez, "A review on alkali activation: new analytical perspectives," *Materiales de la Construcción,* vol. 64, 2014.

[13] C. Shi, A. Fernández-Jiménez and A. Palomo, "New cements for the 21st century: the pursuit of an alternative to Portland cement," *Cement and Concrete Research,* vol. 41, pp. 750-763, 2011.

[14] J. L. Provis, A. Palomo and C. Shi, "Advances in understanding alkali-activated materials," *Cement and Concrete Research,* vol. 78A, pp. 11-125, 2015.

[15] P. Awoyera and A. Adesina, "A critical review on application of alkali activated slag as a sustainable composite binder," *Case Studies in Construction Materials,* vol. 11, 2019.

[16] K. Yang, J. Song and Keum-Il Song, "Assessment of CO2 reduction of alkali-activated concrete," *Journal of Cleaner Production,* vol. 39, pp. 265-272, 2013.

[17] L. K. Turner and F. G. Collins, "Carbon dioxide equivalent (CO2-e) emissions: A comparison between geopolymer and OPC cement concrete," *Construction and Building Materials,* vol. 43, p. 125130, 2013.

[18] W. Chen and H. J. H. Brouwers, "The hydration of slag. Part 1: Reaction models for alkali-activated slag," *Journal of Materials Science,* vol. 42, pp. 428-443, 2007.

[19] T. Bakharev, J. G. Sanjayan and Y. Cheng, "Alkali activation of Australian slag cements," *Cement and Concrete Research,* vol. 29, pp. 113-120, 1999.

[20] D. M. Roy, W. Jiang and M.R Silsbee, "Chloride diffusion in ordinary, blended, and alkali-activated cement pastes and its relation to other properties," *Cement and Concrete Research,* vol. 30, pp. 1879-1884, 2000.

[21] A. M. Rashad, "A comprehensive overview about the influence of different additives on the properties of alkali-activated slag-A guide for Civil Engineer.," *Construction and Building Materials.,* vol. 47, pp. 29-55, 2013.

[22] G. Fang, W. K. Ho, W. Tu and M. Zhang, "Workability and mechanical properties of alkali-activated fly ash-slag concrete cured at ambient temperature," *Construction and Building Materials,* vol. 172, pp. 476-487, 2018.

[23] M. Palacios, P. F. G. Banfill and F. Puertas, "Rheology and setting of alkali-activated slag pastes and mortars: effect of organic admixture," *ACI Materials Journal,* vol. 105, pp. 140-148, 2016.

[24] H. Ye and A. Radlińska, "Shrinkage mechanisms of alkali-activated slag," *Cem. Concr. Res,* vol. 88, pp. 126-135, 2016.

[25] C. Cartwright, F. Rajabipour and A. Radlińska, "Shrinkage Characteristics of Alkali-Activated Slag Cements," *Journal of Materials in Civil Engineering,* vol. 27, no. 7, 2015.

[26] S.-D. Wang, X.-C. Pu, K.L. Scrivener and P.L. Pratt, "Alkali-activated slag cement and concrete: a review of properties and problems," *Advance Cement Research* , vol. 7, pp. 93-102, 1995.

[27] J. G. Jang, N.K. Lee and H.K. Lee, "Fresh and hardened properties of alkali-activated fly ash/slag pastes with superplasticizers," *Construction and Building Materials,* vol. 50, pp. 169-176, 2014.

[28] C. Shi, D. Roy and P. Krivenko, Alkali-Activated Cements and Concretes, Newyork, USA: Tayler & Francis , 2006.

[29] J. L. Provis and J. S. J. van Deventer, Alkali-activaed materials - RILEM state of the art, pringer Science & Business Media, 2013.

[30] F. Pacheco-Torgal, J. Labrincha, C. Leonelli, A. Palomo and P Chindaprasit, Handbook of Alkali-Activated Cements, Mortars and Concretes, Elsevier, 2014.

[31] C. Li, H. Sun and L. Li, "A review: The comparison between alkali-activated slag (Si + Ca) and metakaolin (Si + Al) cements," *Cement and Concrete Research,* vol. 40, no. 9, pp. 1341-1349, 2010.

[32] X. Hu, C. Shi, Z. Shi and L. Zhang, "Compressive strength, pore structure and chloride transport properties of alkali-activated slag/fly ash mortars," *Cement and Concrete Composities,* vol. 104, 2019.

[33] N. R. Rakhimova and R. Z. Rakhimov, "Reaction products, structure and properties of alkali-activated metakaolin cements incorporated with supplementary materials – a review," *Journal of Materials Research and Technology,* vol. 8, no. 1, pp. 1522-1531, 2019.

[34] S. Aydın and B. Baradan, "Effect of activator type and content on properties of alkali-activated slag mortars," *Composites Part B: Engineering,* vol. 57, pp. 166-172, 2014.

[35] A. Gruskovnjak, B. Lothenbach, L. Holzer, R. Figi and F. Winnefeld, "Hydration of alkali-activated slag: comparison with ordinary Portland cement," *Advances in Cement Research,* vol. 18, no. 3, pp. 119-128, 2006.

[36] S. Wang and K. L. Scrivener, "Hydration products of alkali activated slag cement," *Cement and Concrete Research,* vol. 25, no. 3, pp. 561-571, 1995.

[37] J. I. Escalante-García, A.F. Fuentes, A. Gorokhovsky, P. E. Fraire-Luna and G. Mendoza-Suarez, "Hydration Products and Reactivity of Blast-Furnace Slag Activated by Various Alkalis," *J. American Ceramic Society,* vol. 86, no. 12, pp. 2148-2153, 2003.

[38] F. Puertas, A. Fernández-Jiménez and M.T Blanco-Varela, "Pore solution in alkali-activated slag cement pastes. Relation to the composition and structure of calcium silicate hydrate," *Cement and Concrete Research,* vol. 34, no. 1, pp. 139-148, 2004.

[39] F. Puertas, M. Palacios, H. Manzano, J.S. Dolado, A. Rico and J. Rodríguez, "A model for the C-A-S-H gel formed in alkali-activated slag cements," *J. European Ceramic Society,* vol. 31, no. 12, pp. 2043-2056, 2011.

[40] P. Faucon, A. Delagrave, C. Richet, J. M. Marchand and H. Zanni, "Aluminum Incorporation in Calcium Silicate Hydrates (C−S−H) Depending on Their Ca/Si Ratio," *J. Phys. Chem. B,* vol. 103, no. 37, pp. 7796-7802, 1999.

[41] M. D. Andersen, Hans J. Jakobsen and J. Skibsted, "Incorporation of Aluminum in the Calcium Silicate Hydrate (C−S−H) of Hydrated Portland Cements: A High-Field 27Al and 29Si MAS NMR Investigation," *Inorg. Chem,* vol. 42, no. 7, pp. 2280-2287, 2003.

[42] J. L. Provis and J. S. J. van Deventer , Geopolymers: Structures, Processing, Properties and Industrial Applications, Woodhead Publishing Series in Civil and Structural Engineering, 2009.

[43] A. Fernández-Jiménez, A. Palomo and M. Criado, "Microstructure development of alkali-activated fly ash cement: a descriptive model," *Cement and Concrete Research,* vol. 35, no. 6, pp. 1204-1209, 2005.

[44] S. K. Nath, S. Maitra, S. Mukherjee and Sanjay Kumar, "Microstructural and morphological evolution of fly ash based geopolymers," *Construction and Building Materials,* vol. 111, no. 15, pp. 758-765, 2016.

[45] B. Walkley, R. San Nicolas and .et. all, "Phase evolution of C-(N)-A-S-H/N-A-S-H gel blends investigated via alkali-activation of synthetic calcium aluminosilicate precursors," *Cement and Concrete Research,* vol. 89, pp. 120-135, 2016.

[46] I. Garcia-Lodeiro, A. Palomo, A. Fernández-Jiménez and D.E. Macphee, "Compatibility studies between N-A-S-H and C-A-S-H gels. Study in the ternary diagram Na2O–CaO–Al2O3–SiO2–H2O," *Cement and Concrete Research,* vol. 41, no. 9, pp. 923-931, 2011.

[47] C. K. Yip, G.C. Lukey and J.S.J. van Deventer, "The coexistence of geopolymeric gel and calcium silicate hydrate at the early stage of alkaline activation," *Cement and Concrete Research,* vol. 35, no. 9, pp. 1688-1697, 2005.

[48] S. Puligilla and P. Mondal, "Co-existence of aluminosilicate and calcium silicate gel characterized through selective dissolution and FTIR spectral subtraction," *Cement and Concrete Research,* vol. 70, pp. 39-49, 2015.

[49] Z. Giergiczny, "Fly ash and slag," *Cement and Concrete Research,* vol. 124, 2019.

[50] C. Shi and J. Qian, "High performance cementing materials from industrial slags — a review," *Resources, Conservation and Recycling,* vol. 29, no. 3, pp. 195-207, 2000.

[51] J. Chang, "A study on the setting characteristics of sodium silicate-activated slag pastes," *Cement and Concrete Research,* vol. 33, no. 7, pp. 1005-1011, 2003.

[52] EUROPEAN COMMITTEE FOR STANDARDIZATION, EN 450-1: Fly ash for concrete. Definition, specifications and conformity criteria, 2012.

[53] M. Nedeljkovic, "Carbonation mechanism of alkali-activated fly ash and slag materials," PhD thesis, TU Delf, Netherland , 2019.

[54] A. Fernández-Jiménez and A. Palomo, "Composition and microstructure of alkali activated fly ash binder," *Cement and Concrete Research,* vol. 35, no. 10, pp. 1984-1992, 2005.

[55] J. Van Jaarsveld, J. Van Deventer and G. Lukey, "The characterisation of source materials in fly ash-based geopolymers," *Materials Letters,* vol. 57, no. 7, pp. 1272-1280, 2003.

[56] V. Živica, "Effects of type and dosage of alkaline activator and temperature on the properties of alkali-activated slag mixtures," *Construction and Building Materials,* vol. 21, no. 7, pp. 1463-1469, 2007.

[57] V. Glukhovsky, G. Rostovskaja and G. Rumyna, "High strength slag-alkaline cements," in *Proceedings of the,* Paris, 1980.

[58] A. Fernández-Jiménez, A. Palomo and M. Criado, "Alkali activated fly ash binders. A comparative study between sodium and potassium activators," *Mater. Construcc,* vol. 56, no. 281, 2006.

[59] A. R. Brough and A. Atkinson, "Sodium silicate-based, alkali-activated slag mortars: Part I. Strength, hydration and microstructure," *Cement and Concrete Research,* vol. 32, no. 6, pp. 865-879, 2002.

[60] A. Fernández-Jiménez, F. Puertas, I. Sobrados and J. Sanz, "Structure of calcium silicate hydrates formed in alkaline activated slag. Influence of the type of alkaline activator," *J. American Ceramic Society,* vol. 86, no. 3, pp. 1389-1394, 2003.

[61] Y. Ma, J. Hu and G. Ye , "The effect of activating solution on the mechanical strength, reaction rate, mineralogy, and microstructure of alkali-activated fly ash," *Journal of Materials Science,* vol. 47, pp. 4568-4578, 2012.

[62] P. Duxson, J. L. Provis and et. all., "Understanding the relationship between geopolymer composition, microstructure and mechanical properties," *Colloids and Surfaces A: Physicochemical and Engineering Aspects,* vol. 269, no. 1-3, pp. 47-58, 2005.

[63] S. D. Wang, K. L. Scrivener and P. Pratt, "Factors affecting the strength of alkali-activated slag," *Cement and Concrete Research,* vol. 31, no. 9, pp. 1033-1043, 1994.

[64] X. Ke, S. A. Bernal and J. L. Provis, "Controlling the reaction kinetics of sodium carbonate-activated slag cements using calcined layered double hydroxides," *Cement and Concrete Research,* vol. 81, pp. 24-37, 2016.

[65] S. A. Bernal, J. L. Provis, R. J. Myers, R. San Nicolas and J. S. J. van Deventer , "Role of carbonates in the chemical evolution of sodium carbonate-activated slag binders," *Materials and Structures,* vol. 48, pp. 517-529, 2015.

[66] B. Akturk, S. Nayak, S.M.ASCE, S. Das, A.M.ASCE and A. B. Kizilkanat, "Microstructure and Strength Development of Sodium Carbonate–Activated Blast Furnace Slags," *Journal of Materials in Civil Engineering,* vol. 31, no. 11, 2019.

[67] A. F. Abdalqader, F. Jin and A. Al-Tabbaa, "Development of greener alkali-activated cement: utilisation of sodium carbonate for activating slag and fly ash mixtures," *Journal of Cleaner Production,* vol. 113, pp. 66-75, 2016.

[68] A. M. Rashad, Y. Bai, P.A.M. Basheer, N.B. Milestone and N.C. Collier, "Hydration and properties of sodium sulfate activated slag," *Cem. Concr. Compo,* vol. 37, pp. 20-29, 2013.

[69] N. Mobasher, S. A. Bernal and J. L. Provis, "Structural evolution of an alkali sulfate activated slag cement," *J. Nucle. Mater,* vol. 468, pp. 97-104, 2016.

[70] A. Fernández-Jiménez and F. Puertas, "Effect of activator mix on the hydration andstrength behaviour of alkali-activated slag cements," *Adv. Cem. Res,* vol. 15, no. 3, pp. 129-136, 2003.

[71] S. A. Bernal, J. S. J. van Deventer, R. S. Nicolas and J. L. Provis, "Alkali-activated slag cements produced with a blended sodium carbonate/sodium silicate activator," *Adv. Cem. Res,* vol. 28, no. 4, pp. 262-273, 2016.

[72] A. Fernández-Jiménez and F. Puertas, "Setting of alkali-activated slag cement. Influence of activator nature," *Advances in Cement Research,* vol. 13, no. 3, pp. 115-121, 2001.

[73] F. Puertas and M. Torres-Carrasco, "Use of glass waste as an activator in the preparation of alkali-activated slag. Mechanical strength and paste characterisation," *Cement and Concrete Research,* vol. 57, pp. 95-104, 2014.

[74] S. Song and H. M Jennings, "Pore solution chemistry of alkali-activated ground granulated blast-furnace slag," *Cement and Concrete Research,* vol. 29, no. 2, pp. 159-170, 1999.

[75] A. Fernández-Jiménez, J.G. Palomo and F. Puertas, "Alkali-activated slag mortars: Mechanical strength behaviour," *Cement and Concrete Research,* vol. 29, no. 8, pp. 1313-1321, 1999.

[76] A. Palomo, M.W. Grutzeck and M.T. Blanco, "Alkali-activated fly ashes: A cement for the future," *Cement and Concrete Research,* vol. 29, no. 8, pp. 1323-1329, 1999.

[77] B. C. Mclellan, R.P. Williams, J. Lay, A. Van Riessen and G.D. Corder, "Costs and carbon emissions for geopolymer pastes in comparison to ordinary Portland cement," *Journal of Cleaner Production,* vol. 19, no. 9-10, pp. 1080-1090, 2011.

[78] C. Ma, B. Zhao, L. Wang, G. Long and Y. Xie, "Clean and low-alkalinity one-part geopolymeric cement: Effects of sodium sulfate on microstructure and properties," *Journal of Cleaner Production,* vol. 252, 2020.

[79] C. Ma, G. Long, Ye. Shi and Y. Xie, "Preparation of cleaner one-part geopolymer by investigating different types of commercial sodium metasilicate in China," *Journal of Cleaner Production,* vol. 201, no. 10, pp. 636-647, 2018.

[80] R. A. Robayo-Salazar, J. M. Mejía-Arcila and R. M. Gutiérrez, "Eco-efficient alkali-activated cement based on red clay brick wastes suitable for the manufacturing of building materials," *Journal of Cleaner Production,* vol. 166, pp. 242-252, 2017.

[81] A. J. Moseson, D. E. Moseson and M. W. Barsoum, "High volume limestone alkali-activated cement developed by design of experiment," *Cement and Concrete Composites,* vol. 34, no. 3, pp. 328-336, 2012.

[82] O. Burciaga-Díaz and J. Iván Escalante-García, "Structure, Mechanisms of Reaction, and Strength of an Alkali-Activated Blast-Furnace Slag," *J. American Ceramic Scociety,* vol. 96, no. 12, pp. 3939-3948, 2013.

[83] P. Duxson and J. L. Provis, "Designing Precursors for Geopolymer Cements," *J. American Ceramic Society,* vol. 91, no. 12, pp. 3864-3869, 2008.

[84] A. Fernandez-Jimenez and F. Puertas, "Alkali-activated slag cements: Kinetic studies," *Cement and Concrete Research,* vol. 27, no. 3, pp. 359-368, 1997.

[85] O. Mikhailova, A. del Campo, P. Rovnanik, J.F. Fernández and et. all, "In situ characterization of main reaction products in alkali-activated slag materials by Confocal Raman Microscopy," *Cement and Concrete Composites,* vol. 99, pp. 32-39, 2019.

[86] H. Stade, "on the reaction of CASH (di, poly) with alkali hydroxides," *Cement and Concrete Research,* vol. 19, pp. 802-810, 1989.

[87] S. Yoon Hong and F.P Glasser, "Alkali sorption by C-S-H and C-A-S-H gels: Part II. Role of alumina," *Cement and Concrete Research,* vol. 32, no. 7, pp. 1101-1111, 2002.

[88] J. Schneider, M.A Cincotto and H. Panepucci, "29Si and 27Al high-resolution NMR characterization of calcium silicate hydrate phases in activated blast-furnace slag pastes," *Cement and Concrete Research,* vol. 31, no. 7, pp. 993-1001, 2001.

[89] S. A. Bernal, J. L. Provis and et. all, "Gel nanostructure in alkali-activated binders based on slag and fly ash, and effects of accelerated carbonation," *Cement and Concrete Research,* vol. 53, pp. 127-144, 2013.

[90] M. Palacios and F. Puertas, "Effect of Carbonation on Alkali-Activated Slag Paste," *J. American Cermamic Society,* vol. 89, no. 10, pp. 3211-3221, 2006.

[91] B. Lothenbach and A. Gruskovnjak, "Hydration of alkali-activated slag: thermodynamic modelling," *Advances in Cement Research,* vol. 19, no. 2, pp. 81-92, 2007.

[92] M. Ben Haha, B. Lothenbach, G. Le Saout and F. Winnefeld, "Influence of slag chemistry on the hydration of alkali-activated blast-furnace slag — Part I: Effect of MgO," *Cement and Concrete Research,* vol. 41, no. 9, pp. 955-963, 2011.

[93] F. Bonk, J. Schneider, M. Alba Cincotto and H. Panepucci, "Characterization by Multinuclear High-Resolution NMR of Hydration Products in Activated Blast-Furnace Slag Pastes," *J. American Ceramic Society,* vol. 86, no. 10, pp. 1712-1719, 2003.

[94] X. Yuan, W. Chen, Zhe-an Lu and H. Chen, "Shrinkage compensation of alkali-activated slag concrete and microstructural analysis," *Const. Build. Mater,* vol. 66, no. 15, pp. 422-428, 2014.

[95] B. Yuan, Q. L. Yu and H. J. H. Brouwers, "Phase modification induced drying shrinkage reduction on Na2CO3 activated slag by incorporating Na2SO4," *Mater. Struct,* vol. 50, no. 5, p. 220, 2017.

[96] J. L. Provis, P. Duxson, J.S.J. Van Deventer and G.C. Lukey, "The Role of Mathematical Modelling and Gel Chemistry in Advancing Geopolymer Technology," *Chemical Engineering Research and Design,* vol. 83, no. 7, pp. 853-860, 2005.

[97] L. Weng and K. Sagoe-Crentsil, "Dissolution processes, hydrolysis and condensation reactions during geopolymer synthesis: Part I—Low Si/Al ratio systems," *Journal of Materials Science,* vol. 42, pp. 2997-3006, 2007.

[98] N. K. Lee and H.K. Lee, "Setting and mechanical properties of alkali-activated fly ash/slag concrete manufactured at room temperature," *Construction and Building Materials,* vol. 47, pp. 1201-1209, 2013.

[99] I. Ismail, S. A. Bernal, J. L. Provis and et. al. , "Influence of fly ash on the water and chloride permeability of alkali-activated slag mortars and concrete," *Construction and Building Materials,* vol. 48, pp. 1187-1201, 2013.

[100] A. Palomo, A. Fernández-Jiménez, G. Kovalchuk, L. M. Ordoñez and M. C. Naranjo , "Opc-fly ash cementitious systems: study of gel binders produced during alkaline hydration," *Journal of Materials Science,* vol. 42, pp. 2958-2966, 2007.

[101] I. García-Lodeiro, A. Fernández-Jiménez and A. Palomo, "Variation in hybrid cements over time. Alkaline activation of fly ash–portland cement blends," *Cement and Concrete Research,* vol. 52, pp. 112-122, 2013.

[102] I. García-Lodeiro, A. Fernández-Jiménez, A. Palomo and D. E. Macphee, "Effect of Calcium Additions on N–A–S–H Cementitious Gels," *J. American Ceramic Society*, vol. 93, no. 7, pp. 1934-1940, 2010.

[103] M. Ben Haha, G. Le Saout, F. Winnefeld and B. Lothenbach, "Influence of activator type on hydration kinetics, hydrate assemblage and microstructural development of alkali activated blast-furnace slags," *Cement and Concrete Research,* vol. 41, no. 3, pp. 301-310, 2011.

[104] B. S. Gebregziabiher, R.Thomas and S. Peethamparan, "Very early-age reaction kinetics and microstructural development in alkali-activated slag," *Cement and Concrete Composites,* vol. 55, pp. 91-102, 2015.

[105] G. Saout, H.M. Ben, F. Winnefeld and B. Lothenbach, "Hydration degree of alkali-activated slags: a 29Si NMR study," *J. Am. Ceram. Soc.,* vol. 94, no. 12, pp. 4541-4547, 2011.

[106] X. Gao, Q.L. Yu and H.J.H. Brouwers, "Apply 29Si, 27Al MAS NMR and selective dissolution in identifying the reaction degree of alkali activated slag-fly ash composites," *Ceramics International,* vol. 43, no. 15, pp. 12408-12419, 2017.

[107] J. Carette, "Towards Early Age Characterisation of Eco-Concrete Containing Blast-Furnace Slag and Limestone Filler," PhD Thesis, ULB, Brussels, Belgium , 2015.

[108] C. Van Bunderen, "Experimental analysis and numerical modelling of concrete recycling flash calcined dredging sediments," PhD Thesis, KU Leuven, Leuven, 2020.

[109] A. Buchwald, R. Tatarin and D. Stephan , "Reaction progress of alkaline-activated metakaolin-ground granulated blast furnace slag blends," *Journal of Materials Science,* vol. 40, no. 20, pp. 5609-5617, 2009.

[110] R. Cao, S. Zhang, N. Banthia, Y. Zhang and Z. Zhang, "Interpreting the early-age reaction process of alkali-activated slag by using combined embedded ultrasonic measurement, thermal analysis, XRD, FTIR and SEM," *Composites Part B: Engineering,* vol. 186, p. 107840, 2020.

[111] W. Wang, H. Wang and M. Lo, "The fresh and engineering properties of alkali activated slag as a function of fly ash replacement and alkali concentration," *Construction and Building Materials,* Vols. 224-229, p. 84, 2015.

[112] M. Nedeljković, Z. Li, and G. Ye, "Setting, Strength, and Autogenous Shrinkage of Alkali-Activated Fly Ash and Slag Pastes: Effect of Slag Content," *Materials* , p. 11(11), 2018.

[113] M. Chi and Y. Chun Liu, "Effects of Fly Ash/Slag Ratio and Liquid/Binder Ratio on Strength of Alkali-Activated Fly Ash/Slag Mortars," *Applied Mechanics and Materials*, vol. 337, pp. 50-54, 2013.

[114] A. M. Humad1, A. Kothari1, J.L. Provis and A. Cwirzen, "The Effect of Blast Furnace Slag/Fly Ash Ratio on Setting, Strength, and Shrinkage of Alkali-Activated Pastes and Concretes," *Front. Mater*, vol. 6, 2019.

[115] H. Jansson and L. Tang, "Parameters Influencing the Initial Setting Time of Alkali-activated Ground Granulated Blast Furnace Slag Materials," *Norsk Betongforening*, vol. 52, 2015.

[116] J. J Chang, "A study on the setting characteristics of sodium silicate-activated slag pastes," *Cement and Concrete Research*, vol. 33, no. 7, pp. 1005-1011, 2003.

[117] X. Chen, A. Sutrisno and L. J. Struble, "Effects of calcium on setting mechanism of metakaolin-based geopolymer," *Journal of the American Ceramic Society*, vol. 101, no. 2, pp. 957-968, 2018.

[118] X. Chen, A. Sutrisno, L. Zhu and L. J. Struble, "Setting and nanostructural evolution of metakaolin geopolymer," *Journal of the American Ceramic Society*, vol. 100, no. 5, pp. 2285-2295, 2017.

[119] P. Suraneni, S. Puligilla, Eric H. Kim and et al, "Monitoring setting of geopolymers," *Adv Civil Eng Mater*, vol. 177, no. 3, 2014.

[120] J. W. Bullard, H.M. Jennings, R. A. Livingston and et. all, "Mechanisms of cement hydration," *Cement and Concrete Research*, vol. 41, no. 12, pp. 1208-1223, 2011.

[121] E. Tazawa, Autogenous shrinkage of concrete, London and New York: E&F SPON, 1998.

[122] P. Lura, "Autogenous Deformation and Internal Curing of Concrete," Delft University of Technology , Nertherland, 2003.

[123] T. C. Powers and T. L Brownyard, "Studies of the Physical Properties of Hardened Portland Cement Paste," *J Amer Concr Inst*, vol. 43, 1948.

[124] H. J. H. Brouwers and W. Chen, " Reaction Models for Alkali-Activated Slags," *ACI-Symposium Paper,* vol. 221, pp. 303-318, 2004.

[125] J. J. Thomas, A. J. Allen and H. M. Jennings, "Density and water content of nanoscale solid C–S–H formed in alkali-activated slag (AAS) paste and implications for chemical shrinkage," *Cement and Concrete Research,* vol. 42, no. 2, pp. 337-383, 2012.

[126] L. Wu, N. Farzadnia, C. Shi, Z. Zhang and H. Wang, "Autogenous shrinkage of high performance concrete: A review," *Construction and Building Materials,* vol. 149, pp. 62-75, 2017.

[127] D. Shen, J. Jiang, M. Zhang, P. Yao and G. Jiang, "Tensile creep and cracking potential of high performance concrete internally cured with super absorbent polymers at early age," *Constr. Build. Mater,* vol. 165, pp. 451-461, 2018.

[128] P. Lura, O. M. Jensen and J. Weiss, "Cracking in cement paste induced by autogenous shrinkage," *Mater. Struct,* vol. 42, no. 8, pp. 1089-1099, 2009.

[129] M. Palacios and F. Puertas, "Effect of superplasticizer and shrinkage-reducing admixtures on alkali-activated slag pastes and mortars," *Cem. Concr. Res,* vol. 35, pp. 1358-1367, 2005.

[130] M. Palacios and F. Puertas, "Effect of shrinkage-reducing admixtures on the properties of alkali-activated slag mortars and pastes," *Cem. Concr. Res,* vol. 37, pp. 691-702, 2007.

[131] B. Yuan, Q.L. Yu, E. Dainese and H.J.H. Brouwers, "Autogenous and drying shrinkage of sodium carbonate activated slag altered by limestone powder incorporation," *Constr. Build. Mater,* vol. 153, pp. 459-468, 2017.

[132] H. Ye and A. Radlińska, "Shrinkage mitigation strategies in alkali-activated slag," *Cem. Concr. Res,* vol. 101, pp. 131-143, 2017.

[133] Z. Li, M. Nedeljković, B. Chen and G. Ye, "Mitigating the autogenous shrinkage of alkali-activated slag by metakaolin," *Cem. Concr. Res,* vol. 122, pp. 30-41, 2019.

[134] A. R. Sakulich and D. P. Bentz, "Mitigation of autogenous shrinkage in alkali activated slag mortars by internal curing," *Mater. Struct,* vol. 46, no. 8, pp. 1355-1367, 2013.

[135] O. M. Jensen and P. F. Hansen, "Autogenous Deformation and RH-Change in Perspective," *Cement and Concrete Research,* vol. 31, pp. 1859-1865, 2001.

[136] N. Gowripalan, "Autogenous Shrinkage of Concrete at Early Ages," in *25th Australasian Conference on Mechanics of Structures and Materials*, 2019.

[137] V. Mechtcherine and L. Dudziak, "Effects of Superabsorbent Polymers on Shrinkage of Concrete: Plastic, Autogenous, Drying," in *Application of Super Absorbent Polymers (SAP) in Concrete Construction*, RILEM State of the Art Reports, 2011, pp. 63-98.

[138] E. E. Holt, "Early age autogenous shrinkage of concrete," Technical Research Centre of Finland (VTT), Finland, 2001.

[139] P. Lura, O. Mejlhede Jensen and K. van Breugel, "Autogenous shrinkage in high-performance cement paste: An evaluation of basic mechanisms," *Cement and Concrete Research*, vol. 33, no. 2, pp. 223-232, 2003.

[140] Z. Jun, H. Dongwei and C. Haoyu, "Experimental and Theoretical Studies on Autogenous Shrinkage of Concrete at Early Ages," *J. Materials in Civil Eng*, vol. 23, no. 3, pp. 312-320, 2011.

[141] J. Hagymassy, J. R. Brunauer and R. S. Mikhail, "Pore structure analysis by water vapor adsorption," *J. Colloid and Interface Science*, vol. 29, no. 3, pp. 485-491, 1969.

[142] T. C. Powers, "Mechanisms of shrinkage and reversible creep of hardening cement paste," in *Int. Symp. Structure of Concrete and its behaviour under load, Cem. & Concr. Ass*, London, 1965.

[143] L. Barcelo, M. Moranville and B. Clavaud, "Autogenous shrinkage of concrete: a balance between autogenous swelling and self-desiccation," *Cement and Concrete Research*, vol. 35, no. 1, pp. 177-183, 2005.

[144] C. Hua, P. Acker and A. Ehrlacher, "Analyses and models of the autogenous shrinkage of hardening cement paste: I. Modelling at macroscopic scale," *Cement and Concrete Research*, vol. 25, no. 7, pp. 1457-1468, 1995.

[145] H. Ye and A. Radlinska, "A review and comparative study of existibg shrinkage prediction models for portalnd and non-portland cementitious materials," *Adv. Cem. Res*, 2016.

[146] G. Saru, P. Lura and J. Weiss, "A discussion of analysis approaches for determining ‘time-zero’ from chemical shrinkage and autogenous strain measurements in cement paste," in *International RILEM Conference on volume changes of hardening concrete: testing and mitigation, RILEM Publications S.A.R.L*, Denmark, 2006.

[147] J. Weiss, "Experimental determination of the ‘time-zero’ t0 (maturity-zero M0).," in *Early Age Cracking in Cementitious Systems. RILEM Report 25 of RILEM Technical Committee TC 181-EAS*, France, 2003.

[148] K. M. Lee, S.H. Lee and G.Y. Kim, "Autogenous shrinkage of concrete containing granulated blast-furnace slag," *Cement and Concrete Research,* vol. 36, no. 7, pp. 1279-1285, 2006.

[149] ASTM INTERNATIONAL STANDARDS, ASTM C1698 - 19 Standard Test Method for Autogenous Strain of Cement Paste and Mortar, 2019.

[150] T. A. Hammer and Bjøntegaard, "Testing of autogenous deformation (AD) and thermal dilation (TD) of early age mortar and concrete-Recommended test procedure," in *International RILEM Conference on volume changes of hardening concrete: testing and mitigation, RILEM Publications S.A.R.L.*, Denmark, 2006.

[151] Y. Ma, X. Yang, J. Hu, Z. Zhang and H. Wang, "Accurate determination of the “time-zero” of autogenous shrinkage in alkali-activated fly ash/slag system," *Composites Part B: Engineering,* vol. 177, no. 15, p. 107367, 2019.

[152] C. W. Miao, Q. Tian, W. Sun and J.P. Liu, "Water consumption of the early-age paste and the determination of “time-zero” of self-desiccation shrinkage," *Cem. Concr. Res,* vol. 37, no. 11, pp. 1496-1501, 2007.

[153] M. Chang-wen, T. Qian, S. Wei and L. Jia-ping, "Water consumption of the early-age paste and the determination of “time-zero” of self-desiccation shrinkage," *Cement and Concrete Research,* vol. 37, pp. 1496-1501, 2007.

[154] A. Darquennes, Stéphanie Staquet, M. Delplancke-Ogletree and B. Espion, "Effect of autogenous deformation on the cracking risk of slag cement concretes," *Cement and Concrete Composite,* vol. 33, pp. 368-379, 2011.

[155] H. Huang and G. Ye, "Examining the “time-zero” of autogenous shrinkage in high/ultra-high performance cement pastes," *Cem. Concr. Rese,* vol. 97, pp. 107-114, 2017.

[156] P. Lura and O. M. Jensen , "Measuring techniques for autogenous strain of cement paste," *Materials and Structures,* vol. 40, pp. 431-440, 2007.

[157] Ø Bjøntegaard, T.A Hammer and E. J Sellevold, "On the measurement of free deformation of early age cement paste and concrete," *Cement and Concrete Composites,* vol. 26, no. 5, pp. 427-435, 2004.

[158] Z. Hu, C. Shi , Z. Cao, Z. Ou, D. Wang, Z. Wu and L. He, "A review on testing methods for autogenous shrinkage measurement of cement-based materials," *Journal of Sustainable Cement-Based Materials,* vol. 2, pp. 161-171, 2013.

[159] O. M. Hensen and P.F. Hansen, "A dilatometer for measuring autogenous deformation in hardening Portland cement paste," *Materials and Structures,* vol. 28, no. 7, pp. 406-409, 1995.

[160] B. Delsaute, "New approach for Monitoring and Modelling of the Creep and Shrinkage behaviour of Cement Pastes Mortars and Concretes since Setting Time," PhD thesis ULB-Brussels, Belgium, 2017.

[161] N. Marjanović, M. Komljenović, Z. Baščarević, V. Nikolić and R. Petrović, "Physical–mechanical and microstructural properties of alkali-activated fly ash–blast furnace slag blends," *Ceramics International,* vol. 41, no. 1, pp. 1421-1435, 2015.

[162] M. Chi and R. Huang, "Binding mechanism and properties of alkali-activated fly ash/slag mortars," *Construction and Building Materials,* vol. 40, pp. 291-298, 2013.

[163] D. B. Kumarappa, S. Peethamparan and M. Ngami, "Autogenous shrinkage of alkali activated slag mortars: Basic mechanisms and mitigation methods," *Cem. Concr. Res,* vol. 109, pp. 1-9, 2018.

[164] A. A. M. Neto, M. A. Cincotto and W. Repette, "Drying and autogenous shrinkage of pastes and mortars with activated slag cement," *Cem. Concr. Res,* vol. 38, no. 4, pp. 565-574, 2008.

[165] Z. Li, T. Lu, X. Liang, H. Dong and G. Ye, "Mechanisms of autogenous shrinkage of alkali-activated slag and fly ash pastes," *Cement and Concrete Research,* vol. 135, 2020.

[166] F. Collins and J.G. Sanjayan, "Effect of pore size distribution on drying shrinking of alkali-activated slag concrete," *Cem. Concr. Res,* vol. 30, pp. 1401-1406, 2000.

[167] N. K. Lee, J.G. Jang and H.K. Lee, "Shrinkage characteristics of alkali-activated fly ash/slag paste and mortar at early ages," *Cement and Concrete Composites,* vol. 53, pp. 239-248, 2014.

[168] H-J. Kim, M. Tafesse, H. K. Lee and H-Ki Kim, "Incorporation of CFBC ash in sodium silicate-activated slag system: Modification of microstructures and its effect on shrinkage," *Cement and Concrete Research,* vol. 123, 2019.

[169] H. Ye, C. Cartwright, F. Rajabipour and A. Radlińska, "Understanding the drying shrinkage performance of alkali-activated slag mortars," *Cem. Concre. Compos,* vol. 76, pp. 13-24, 2017.

[170] J. Ma and F. Dehn, "Shrinkage and creep behavior of an alkali-activated slag concrete," *Struct. Concr,* vol. 18, pp. 801-810, 2017.

[171] G. Fang, H. Bahrami and M. Zhang, "Mechanisms of autogenous shrinkage of alkali-activated fly ash-slag pastes cured at ambient temperature within 24 h," *Construction and Building Materials,* vol. 171, pp. 377-387, 2018.

[172] Y. Ma and G. Ye, "The shrinkage of alkali activated fly ash," *Cement and Concrete Research,* vol. 68, pp. 75-82, 2015.

[173] H. M. Jennings, "Refinements to colloid model of C-S-H in cement: CM-II," *Cement and Concrete Research,* vol. 38, pp. 275-289, 2008.

[174] J. J. Thomas and H. M. Jennings, "A colloidal interpretation of chemical aging of the C-S-H gel and its effects on the properties of cement paste," *Cement and Concrete Research,* vol. 36, pp. 30-38, 2006.

[175] V. Šmilauer, P. Hlaváček, F. Škvára, R. Šulc, L. Kopecký and J. Němeček, "Micromechanical multiscale model for alkali activation of fly ash and metakaolin," *J. Mater. Sci,* vol. 46, pp. 6545-6555, 2011.

[176] W. Tu, Y. Zhu, G. Fang, X. Wang and M. Zhang, "Internal curing of alkali-activated fly ash-slag pastes using superabsorbent polymer," *Cement and Concrete Research,* vol. 116, pp. 179-190, 2019.

[177] M. Hojati and A. Radlin´ ska, "Shrinkage and strength development of alkali-activated fly ash-slag binary cements," *Construction and Building Materials,* vol. 150, pp. 808-816, 2017.

[178] Z. Li, M. Nedeljkovic, Y. Zuo and G. Ye, "Autogenous shrinkage of alkali-actiavted slag-fl ash pastes," in *Proceedings of the 5th International Slag Valorisation Symposium*, Leuven , 2017.

[179] X. Gao, "Alkali activated slag-fly ash binders," PhD thesis, TU Eindgoven, 2017.

[180] S. Fang, E. Siu Shu Lam, B. Li and B. Wu, "Effect of alkali contents, moduli and curing time on engineering properties of alkali activated slag," *Construction and Building Materials,* vol. 249, 2020.

[181] S. Uppalapati and Ö. Cizer, "Early-age properties of alkali-activated slag/fly ash blends," in *2nd International RILEM/COST Conference on Early Age Cracking and Serviceability in Cement-based Materials and Structures - EAC2*, Brussels, 2017.

[182] T. Bakharev, J.G. Sanjayan and Y. Cheng, "Effect of elevated temperature curing on properties of alkali-activated slag concrete," *Cement and Concrete Research*, vol. 29, pp. 1619-1625, 1999.

[183] F. Jin, K. Gu and A. Al-Tabbaa, "Strength and drying shrinkage of reactive MgO modified alkali-activated slag paste," *Construction and Building Materials*, vol. 51, pp. 395-404, 2014.

[184] A. M. Humad, K. Habermehl-Cwirzen and A.Cwirzen, "Effects of Fineness and Chemical Composition of Blast Furnace Slag on Properties of Alkali-Activated Binder," *Materials*, vol. 12, no. 20, p. 3447, 2019.

[185] Z. Li, W. Zhang, R. Wang, F. Chen, X. Jia and P. Cong, "Effects of Reactive MgO on the Reaction Process," *Materials*, 2019.

[186] S. A. Bernal, R. San Nicolas and et. al., "MgO content of slag controls phase evolution and structural changes induced by accelerated carbonation in alkali-activated binders," *Cement and Concrete Research*, vol. 57, pp. 33-43, 2014.

[187] M. Ben Haha, B. Lothenbach, G. Le Saout and F. Winnefeld, "Influence of slag chemistry on the hydration of alkali-activated blast-furnace slag — Part II: Effect of Al2O3," *Cement and Concrete Research*, vol. 42, no. 1, pp. 74-83, 2012.

[188] R. Tänzer, A. Buchwald and D. Stephan , "Effect of slag chemistry on the hydration of alkali-activated blast-furnace slag," *Materials and Structures*, vol. 48, pp. 629-641, 2015.

[189] F. Collins and J.G Sanjayan, "Cracking tendency of alkali-activated slag concrete subjected to restrained shrinkage," *Cement and Concrete Research*, vol. 30, no. 5, pp. 791-798, 2000.

[190] F. Rifai, A. Darquennes, B. Muzeau, L. Stefan and F. Benboudjema, "Early-age cracking tendency of Alkali-activated slag binders compared to Ordinary Portland Cement," in *SynerCrete'18 International Conference on Interdisciplinary Approaches for Cement-based Materials and Structural Concrete*, unchal, Madeira Island, Portugal , 2018.

[191] S. Oh and Y. Cheol Choi, "Superabsorbent polymers as internal curing agents in alkali activated slag mortars," *Construction and Building Materials,* vol. 159, pp. 1-8, 2018.

[192] B. Vafaei, K. Farzanian and A. Ghahremaninezhad, "The influence of superabsorbent polymer on the properties of alkali-activated slag pastes," *Construction and Building Materials,* vol. 236, 2020.

[193] Z. Li, M. Wyrzykowski, H. Dong, José Granja, M. Azenha, P. Lura and G. Ye, "Internal curing by superabsorbent polymers in alkali-activated slag," *Cement and Concrete Research,* vol. 135, 2020.

[194] C. Song, Y. Cheol Choi and S. Choi, "Effect of internal curing by superabsorbent polymers – Internal relative humidity and autogenous shrinkage of alkali-activated slag mortars," *Construction and Building Materials,* vol. 123, pp. 198-206, 2016.

[195] L. Coppola, D. Coffetti, E. Crotti, S. Candamano, F. Crea, G. Gazzaniga and T. Pastore, "The combined use of admixtures for shrinkage reduction in one-part alkali activated slag-based mortars and pastes," *Construction and Building Materials,* vol. 248, 2020.

[196] X. Zhu, D. Tang, K. Yang, Z. Zhang, Q. Li, Q. Pan and C. Yang, "Effect of Ca(OH)2 on shrinkage characteristics and microstructures of alkali-activated slag concrete," *Construction and Building Materials,* vol. 175, pp. 467-482, 2018.

[197] T. Bakharev, J. Sanjayan and Y.-B. Cheng, "Effect of admixtures on properties of alkali-activated slag concrete," *Cement and Concrete Research,* vol. 30, pp. 1367-1374, 2000.

[198] EUROPEAN COMMITTEE FOR STANDARDIZATION , EN 196-2 Method of testing cement - Part-2: Chemical analysis of cement, 2013.

[199] ACTIVE STANDARD ATSM C618, Standard Specification for Coal Fly Ash and Raw or Calcined Natural Pozzolan for Use in Concrete, 2019.

[200] R. Siddique and M. I. Khan, "Supplementary cementing materials," *Springer Science & BusinessMedia,* 2011.

[201] EUROPEAN COMMITTE FOR STANDARDIZATION , EN 196-6 Methods of testing cement - Part 6 : Determination of fineness,, 2010.

[202] EUROPEAN COMMITTE FOR STANDARDIZATION , EN 1097-5 Tests for mechanical and physical properties of aggregates - Part 6 : Determination of particle density and water absorption, 2013.

[203] EUROPEAN COMMITTEE FOR STANDARDIZATION, EN 12620 Agrgregates for concrete, 2013.

[204] EUROPEAN COMMITTEE FOR STANDARDIZATION, EN 933-1 Tests for geometrical properties of aggregates - Part 1: Determination of paricle size distribution - Sieving method, 2012.

[205] EUROPEAN COMMITEE FOR STANDARDIZATION , EN 196-3 Methods of testing cement - Part 3: Determination of setting times and soundness, 2016.

[206] EUROPEAN COMMITTEE FOR STANDARDIZATION, EN 196-1 Methods of testing cement Part - 1: Deterimination of strength, 2015.

[207] EUROPEAN COMMITTEE FOR STANDARIZATION , EN 12504-4 Testing concrete - Part 4: Deteremintion of ultrasonic pulse velcoity, 2004.

[208] R. J. Thomas and S. Peethamparan, "Alkali-activated concrete: Engineering properties and stress–strain behavior," *Construction and Building Materials,* vol. 93, pp. 49-56, 2015.

[209] EUROPEAN COMMITTEE FOR STANDARDIZATION, EN 1992-1-1 (Eurocode 2): Design of concrete structures - Part 1-1: General rules and rules for building, 2005.

[210] EUROPEAN COMMITTEE FOR STANDARDIZATION, EN 12390-13 Testing hardened concrete - Part -13: Determination of secant modulus of elasticity in compression, 2013.

[211] EUROPEAN COMMITTEE FOR STANDARDIZATION, B 15-229 Concrete testing - Non-destructive testing - Measurement of sound velocity, 1991.

[212] E. Knapen, O. Cizer, K. Van Balen and D. Van Gemert, "Effect of free water removal from earl-age hydration cement paste on thermal analysis," *Construction and Building Materials,* vol. 23, pp. 3431-3438, 2009.

[213] R. S. Barneyback and S. Diamond, "Expression and analysis of pore fluids from hardened cement pasts and mortars," *Cement and Concrete Research,* vol. 11, pp. 279-285, 1981.

[214] Y. Zuo, M. Nedeljković and G. Ye, "Pore solution composition of alkali-activated slag/fly ash pastes," *Cem. Concr. Res,* vol. 115, pp. 230-250, 2019.

[215] E. Knapen, O. Cizer, K. Van Balen and D. Van Gemert , "Comparison of solvent exchange and vacuum drying techniques to remove free water from early age cement-

based materials," in *2nd International Symposium on Advances in Concrete through Science and Engineering*, Quebec City, Canada, 11-13 September 2006.

[216] S. Luo, Min Liu, Lei Yang and Jindan Chang, "Effects of drying techniques on the crystal structure and morphology of ettringite," *Construction and Building Materials,* vol. 195, no. 20, pp. 305-311, 2019.

[217] R. Snellings, J. Chwast, Ö. Cizer, Nele De Belie, Yuvaraj Dhandapani and et al. , "Hydration stoppage methods for phase assemblage studies of blended cements—results of a round robin test," *Materials and Structures,* pp. 51-111, 2018.

[218] K. Scrivener, R. Snellings and B. Lothenbach, A practical guide to microstructure analysis of cementitious materials, 2016.

[219] J. Landers, G. Yu Gor and A. Neimark, "Density functional theory methods for characterization of porous materials," *Colloids and Surfaces A: Physicochem. Eng. Aspects,* vol. 437, pp. 3-32, 2013.

[220] ASTM INTERNATIONAL STANDARDIZATION, ASTM C1608 - 17 Standard Test Method for Chemical Shrinkage of Hydraulic Cement Paste, 2017.

[221] J. D. Berry, M. J. Neeson, R. R. Dagastine, D. Y. C. Chan and R.F. Tabor, "Measurement of surface and interfacial tension using pendant drop," *Journal of Colloid and Interface Science,* vol. 454, pp. 226-237, 2015.

[222] ASTM INTERNATIONAL STANDARDIZATION, ASTM C642 - 13 Standard Test Method for Density, Absorption, and Voids in Hardened Concrete, 2013.

[223] E. Deir, B. S. Gebregziabiher and S. Peethamparan, "Influence of starting material on the early age hydration kinetics,microstructure and composition of binding gel in alkali activatedbinder systems," *Cement and Concrete Composites,* vol. 48, pp. 108-117, 2014.

[224] S. Chithiraputhiran and N. Neithalath, "Isothermal reaction kinetics and temperature dependence of alkaliactivation of slag, fly ash and their blends," *Construction and Building Materials,* vol. 45, pp. 233-242, 2013.

[225] C. Shi and R. L. Day, "A calorimetric study of early hydration of alkali-slag cements," *Cement and Concrete Research,* vol. 25, no. 6, pp. 1333-1346, 1995.

[226] D. Ravikumar and N. Neithalath, "Reaction kinetics in sodium silicate powder and liquid activated slag binders evaluated using isothermal calorimetry.," *Thermochimica Acta*, vol. 546, pp. 32-43, 2012.

[227] X. Gao, Q.L. Yu and H.J.H. Brouwers, "Reaction kinetics, gel character and strength of ambient temperaturecured alkali activated slag–fly ash blends," *Construction and Building Materials* , vol. 80, pp. 105-115, 2015.

[228] F. U. A. Shaikh and S. W.M. Supit, "Mechanical and durability properties of high volume fly ash (HVFA) concrete containing calcium carbonate (CaCO3) nanoparticles," *Construction and Building Materials* , vol. 70, no. 15, pp. 309-321, 2014.

[229] H. Tan, X. Deng, X. He and et. al, "Compressive strength and hydration process of wet-grinded granulated blast-furnace slag activated by sodium sulfate and sodium carbonate," *Cement and Concrete Composites*, vol. 97, pp. 387-398, 2019.

[230] W. Chen, Y. Li, P. Shen and Z. Shui, "Microstructural Development of Hydrating Portland Cement Paste at Early Ages Investigated with Non-destructive Methods and Numerical Simulation," *Journal of Nondestructive Evaluation*, vol. 32, pp. 228-237, 2013.

[231] G. Trtnik, M. Ivan Valič, F. Kavčič and G. Turk, "Comparison between two ultrasonic methods in their ability to monitor the setting process of cement pastes," *Cement and concrete research*, vol. 39, no. 10, pp. 876-882, 2009.

[232] L. Wang, H.Q. Yang, S.H. Zhou, E. Chen and S.W. Tang, "Mechanical properties, long-term hydration heat, shinkage behavior and crack resistance of dam concrete designed with low heat Portland (LHP) cement and fly ash," *Construction and Building Materials*, vol. 187, pp. 1073-1091, 2018.

[233] N. Robeyst, "Monitoring setting and microstructure development in fresh concrete with the ultrasonic through-transmission method," PhD Thesis, Ghent University, Belgium, 2010.

[234] G. Ye, "Experimental Study and Numerical Simulation of the Development of the Microstructure and Permeability of Cementitious Materials," PhD Thesis, TU Delft, Netherlands, 2003.

[235] S. W. Dean, Richard M. Kmack, K.E. Kurtis and et. al, "Assessment of Air Entrainment in Fresh Cement Paste Using Ultrasonic Nondestructive Testing," *Journal of ASTM International 7,* vol. 1, pp. 1-18, 2010.

[236] J. Zhu, S. Kee, Dongyeop Han and Yi-Te Tsai, "Effects of air voids on ultrasonic wave propagation in early age cement pastes," *Cement and Concrete Research,* vol. 41, no. 8, pp. 872-881, 2011.

[237] G. Trtnik, G. Turk, F. Kavčič and V. Bokan Bosiljkov, "Possibilities of using the ultrasonic wave transmission method to estimate initial setting time of cement paste," *Cement and Concrete Research,* vol. 38, no. 11, pp. 1336-1342, 2008.

[238] D. Krizan and B. Zivanovic, "Effects of Dosage and Modulus of Water Glass on Early Hydration of Alkali-Slag Cements,," *Cement and Concrete Research,* vol. 32, no. 8, pp. 1181-1188, 2002.

[239] P. Duxson, A. Fernández-Jiménez, J. L. Provis, G. C. Lukey, A. Palomo and J. S. J. van Deventer, "Geopolymer technology: the current state of the art," *Journal of Materials Science,* vol. 42, no. 9, pp. 2917-2933, 2007.

[240] D. Hou, H. Ma and Z. Li, "Morphology of calcium silicate hydrate (C-S-H) gel: a molecular dynamic study," *Advances in Cement Research,* vol. 27, no. 3, pp. 135-146, 2015.

[241] M. Yuwei, "Microstructure and Engineering Properties of Alkali Activated Fly Ash -as an environment friendly alternative to Portland cement," PhD Thesis, TU Delft, Netherland, 2013.

[242] S. A. Bernal, J. L. Provis, VolkerRose and R. d. Gutierrez, "Evolution of binder structure in sodium silicate-activated slag-metakaolin blends," *Cement and concrete composites,* vol. 33, no. 1, pp. 46-54, 2011.

[243] K. Xinyuan, Bernal, Susan A and Provis, John L, "Controlling the reaction kinetics of sodium carbonate-activated slag cements using calcined layered double hydroxides," *Cement and Concrete Research,* vol. 81, pp. 24-37, 2016.

[244] M. Neda, S. A. Bernal and J. L. Provis, "Structural evolution of an alkali sulfate activated slag cement," *Journal of Nuclear Materials,* Vols. 97-104, pp. 97-104, 2016.

[245] C. Paglia, F. Wombacher and H. Böhni, "The influence of alkali-free and alkaline shotcrete accelerators within cement systems: I. Characterization of the setting behavior," *Cement and Concrete Research,* vol. 31, no. 6, pp. 913-918, 2001.

[246] C. J. Hampson and J.E. Bailey, "On the structure of some precipitated calcium aluminsulphate hydrates," *J Mater Sci,* vol. 71, pp. 3341-3346, 1982.

[247] H. A. Razak and F. Sajedi, "The effect of heat treatment on the compressive strength of cement-slag mortars," *Materials & Design,* vol. 32, no. 8-9, pp. 4618-4628, 2011.

[248] D. Torréns-Martín and L. Fernández-Carrasco, "Effect of sulfate content on cement mixtures," *Construction and Building Materials,* vol. 48, pp. 144-150, 2013.

[249] S. Wistuba, D. Stephan, G. Raudaschl-Sieber and J. Plank, "Hydration products of two-phase Portland cement clinker doped with Na2O," *Advances in Cement Research,* vol. 19, no. 3, pp. 125-131, 2007.

[250] C. U. Grosse, "Ultrasound through-transmission techniques for quality control of fresh concrete," in *Conference on advanced testing of fresh cementinious materials,* 2008.

[251] H. von Daake and D. Stephan, "Setting of cement with controlled superplasticizer addition monitored by ultrasonic measurements and calorimetry," *Cement and Concrete Composites,* vol. 66, pp. 24-37, 2016.

[252] T. Kamada, S. Uchida and K. Rokugo, "Nondestructive Evaluation of Setting and Hardening of Cement Paste Based on Ultrasonic Propagation Characteristics," *J Adv Concr Technol,* vol. 3, no. 3, pp. 343-353, 2005.

[253] P. Mounanga, V. Baroghel-Bouny, A. Loukili and A. Khelidj, "Autogenous deformations of cement pastes: Part I. Temperature effects at early age and micro–macro correlations," *Cement and Concrete Research,* vol. 36, no. 1, pp. 110-112, 2006.

[254] A. Fernandez-Jimenez A, F. Puertas and A. Artega, "Determination of Kinetic Equations of Alkaline Activation of Blast Furnace Slag by Means of Calorimetric Data," *Journal of Thermal Analysis and Calorimetry,* vol. 52, no. 3, pp. 945-955, 1998.

[255] A. K. Schindler, "Concrete hydration, temperature debelopment and setting at early ages," PhD Thesis, Unverisity of Texas, Austin, 2002.

[256] D. P. Bentza, T. Barrett, I. De la Varga and W. Jason Weiss, "Relating Compressive Strength to Heat Release in Mortars," *Advances in Civil Engineering Materials,* vol. 1, no. 1, p. 14, 2012.

[257] A. Behnood, K. Pin Verian and M.M. Gharehveran, "Evaluation of the splitting tensile strength in plain and steel fiber-reinforced concrete based on the compressive strength," *Construction and Building Materials,* vol. 98, pp. 519-529, 2015.

[258] G. Trtnik, F. Kavčič and G. Turk, "Prediction of concrete strength using ultrasonic pulse velocity and artificial neural networks," *Ultrasonics,* vol. 49, no. 1, pp. 53-60, 2009.

[259] M. Shariq, J. Prasad and A. Masood, "Studies in ultrasonic pulse velocity of concrete containing GGBFS," *Construction and Building Materials,* vol. 40, pp. 944-950, 2013.

[260] T. Yanga, H. Zhua, Z.Zhang, Xuan Gao, C. Zhang and Qisheng Wu, "Effect of fly ash microsphere on the rheology and microstructure of alkaliactivated fly ash/slag pastes," *Cement and Concrete Research,* vol. 109, pp. 198-207, 2018.

[261] O. G. Rivera, W.R. Long, C.A. Weiss, R.D. Moser, B.A. Williams, K. Torres-Cancel, E.R. Gore. and P.G. Allison, "Effect of elevated temperature on alkali-activated geopolymeric binders compared to portland cement-based binders," *Cement and Concrete Research,* vol. 90, pp. 43-51, 2016.

[262] K-Il. Song, J-K. Song, B. Yeon Lee and K-H. Yang, "Carbonation Characteristics of Alkali-Activated Blast-Furnace Slag Mortar," *Advances in Materials Science and Engineering,* p. 11, 2014.

[263] J. Skibsted and M. D. Andersen, "The Effect of Alkali Ions on the Incorporation of Aluminum in the Calcium Silicate Hydrate (C–S–H) Phase Resulting from Portland Cement Hydration Studied by 29Si MAS NMR," *J. Am. Ceram. Soc,* vol. 96, no. 2, pp. 651-656, 2012.

[264] S. Song, D. Sohn, H.M. Jennings and T.O. Mason, "Hydration of alkali-activated ground granulated blast furnace slag," *J Mater Sci,* vol. 35, pp. 249-257, 2000.

[265] I. G. Richardson, A.R. Brough, G.W. Groves and C.M. Dobson, "The characterization of hardened alkali-activated blast-furnace slag pastes and the nature of the calcium silicate hydrate (CSH) phase," *Cem Concr Res,* vol. 24, pp. 813-829, 1994.

[266] X. Ke, S. A. Bernal and J. L. Provis, "Layered double hydroxides modify the reaction of sodium silicate-activated slag cements," *Green Materials,* vol. 7, no. 2, pp. 52-60, 2019.

[267] D. S. Perera, O. Uchida, E. R. Vance and K. S. Finnie, "Influence of curing schedule on the integrity of geopolymers," *J. Mater. Sci,* vol. 42, pp. 3099-3106, 2007.

[268] Y. J. Zhang, Y. L. Zhao, H. H. Li and D. L. Xu, "Structure characterization of hydration products generated by alkaline activation of granulated blast furnace slag," *J. Mater. Sci,* vol. 43, pp. 7141-7147, 2008.

[269] C. K. Huanc and P. F. Kerr, "Infrared study of the carbonate minerals," *Am Miner,* vol. 45, 1960.

[270] P. Yu, R. James Kirkpatrick, B. Poe, P. F. McMillan and X. Cong, "Structure of Calcium Silicate Hydrate (C-S-H): Near-, Mid-, and Far-Infrared Spectroscopy," *J. Am.Ceram.Soc,* vol. 82, no. 3, pp. 742-748, 1999.

[271] Y. Liu, W. Zhu and E-H. Yang, "Alkali-activated ground granulated blast-furnace slag incorporating incinerator fly ash as a potential binder," *Const. Buil. Mater,* vol. 112, pp. 1005-1012, 2016.

[272] X. Gao, Yu. Q.L and Brouwers. H.J.H, "Characterization of alkali activated slag–fly ash blends containing nano-silica," *Contruction and Building Materials,* vol. 98, pp. 397-406, 2015.

[273] I. García-Lodeiro, A. Fernández-Jiménez, M. Teresa Blanco and Angel Palomo, "FTIR study of the sol–gel synthesis of cementitious gels: C–S–H and N–A–S–H," *J. Sol-Gel Sci. Technol,* vol. 45, pp. 63-72, 2008.

[274] A. Fernández-Jiménez and A. Palomo, "Mid-infrared spectroscopic studies of alkali-activated fly ash structure," *Microporous and Mesoporous Mater.,* vol. 86, no. 1-3, pp. 207-2014, 2005.

[275] M. Y A. Mollah, F. Lu and D. L. Cocke, "An X-ray diffraction (XRD) and Fourier transform infrared spectroscopic (FT-IR) characterization of the speciation of arsenic (V) in Portland cement type-V," *Sci. Tot. Enviro,* vol. 224, pp. 57-68, 1998.

[276] R. A. Hanna, P.J. Barrie, C.R. Cheeseman, C.D. Hills, P.M. Buchler and R. Perry, "Solid state 29Si and 27Al NMR and FTIR study of cement pastes containing industrial wastes and organics," *Cem. Concr. Resea,* vol. 25, pp. 1435-1444, 1995.

[277] I. Lecomte, C. Henrist, M. Liégeois, F. Maseri, A. Rulmont and R. Cloots, "(Micro)-structural comparison between geopolymers, alkali-activated slag cement and Portland cement," *J. Euro. Ceram. Soci,* vol. 26, pp. 3789-3797, 2006.

[278] I. G. Lodeiro, A. Fernández-Jimenez, A. Palomo and D.E Macphee, "Effect on fresh C-S-H gels of the simultaneous addition of alkali and aluminium," *Cem. Concr. Res,* vol. 40, pp. 27-32, 2010.

[279] Z. Zhang, H. Wang, J. L. Provis, F. Bullen, A. Reid and Y. Zhu, "Quantitative kinetic and structural analysis of geopolymers. Part 1. The activation of metakaolin with sodium hydroxide," *Thermochimica Acta,* vol. 539, no. 10, pp. 23-33, 2012.

[280] D. Dimas, I. Giannopoulou and D. Panias, "Polymerization in sodium silicate solutions: a fundamental process in geopolymerization technology," *J. Mater. Sci,* vol. 44, no. 14, pp. 3719-3730, 2009.

[281] C. A. Rees, J. L. Provis, G. C. Lukey and J. S.J. van Deventer, "The mechanism of geopolymer gel formation investigated through seeded nucleation," *Colloids Surf. A Physicochem. Eng. Asp,* vol. 318, no. 1-3, pp. 97-105, 2008.

[282] I. Ismail, S. A. Bernal, J. L. Provis, R. S. Nicolas, S. Hamdan and J. S.J. van Deventer, "Modification of phase evolution in alkali-activated blast furnace slag by the incorporation of fly ash," *Cem. Concr. Com,* vol. 45, pp. 125-135, 2014.

[283] S. Hong and F.P Glasser, "Alkali sorption by C-S-H and C-A-S-H gels: Part II. Role of alumina," *Cem. Concr. Res,* vol. 32, no. 7, pp. 1101-1111, 2002.

[284] E. L'Hôpital, B. Lothenbach, K. Scrivener and D.A. Kulik, "Alkali uptake in calcium alumina silicate hydrate (C-A-S-H)," *Cem. Concr. Res,* vol. 85, pp. 122-136, 2016.

[285] Y. Zuo, M. Nedeljković and G. Ye, "Coupled thermodynamic modelling and experimental study of sodium hydroxide activated slag," *Constr. Build. Mater,* vol. 188, no. 10, pp. 262-279, 2018.

[286] S. A. Walling, S. A. Bernal, L. J. Gardner, H. Kinoshita and J. L. Provis, "Blast furnace slag-Mg(OH)2 cements activated by sodium carbonate," *RSC Advances,* vol. 8, no. 41, pp. 23101-23118, 2018.

[287] R. J. Myers, B. Lothenbach, S.A. Bernal and J. L. Provis, "Thermodynamic modelling of alkali-activated slag cements," *Applied Geochemistry,* vol. 61, pp. 233-247, 2015.

[288] R. J. Myers, S. A. Bernal, R. S. Nicolas and J. L. Provis, "Generalized Structural Description of Calcium–Sodium Aluminosilicate Hydrate Gels: The Cross-Linked Substituted Tobermorite Model," *Langmuir,* vol. 29, no. 17, pp. 5294-5306, 2013.

[289] X. Pardal, F. Brunet, T. Charpentier, I. Pochard and A. Nonat, "27Al and 29Si Solid-State NMR Characterization of Calcium-Alumino-silicate-Hydrate," *Inorganic Chemsitry,* vol. 51, no. 3, pp. 1827-1836, 2012.

[290] K. K. Aligizaki, Pore Structure of Cement-Based Materials: Testing, Interpretation and Requirements, CRC Press, 2005.

[291] L. T. Nanganoa, K.J. Mbadcam and S. Kang, "Synthesis of Hydroxy-sodalite from Fine Fractions of Sandy Clay Loam Soil (Natural Aluminosilicate)," *Inter. Jour. Chem. Tech. Res,* vol. 9, no. 6, pp. 725-732, 2016.

[292] J. Rouquerol, F. Rouquerol, P. Llewellyn, G. Maurin and K.S. Sing, Adsorption by Powders and Porous Solids: Principles, Methodology and Applications, Academic press, 2013.

[293] H. M. Jennings, "Colloid model of c- s- h and implications to the problem of creep and shrinkage," *Mater. Struct,* vol. 37, pp. 59-70, 2004.

[294] T. Lu, "Autogenous shrinkage of early age cement paste and mortar," PhD thesis, TU Delft, Netherlands, 2019.

[295] B. Držaj, S. Hocevar and S. Pejovnik, Zeolites: Synthesis, Structure, Technology and Application, Elsevier, 2011.

[296] ASTM INTERNATIONAL STANDARIZATION, ASTM C1698-09: Standard Test Method for Autogenous Strain of Cement Paste and Mortar, 2009.

[297] A. Boumiz, C. Vernet and F. C. Tenoudji, "Mechanical properties of cement pastes and mortars at early ages: Evolution with time and degree of hydration.," *Advanced Cement Based Materials,* vol. 3, no. 3-4, pp. 94-106, 1996.

[298] J. Keating, D.J. Hannant and A.P. Hibbert, "Comparison of shear modulus and pulse velocity techniques to measure the build-up of structure in fresh cement pastes used in oil well cementing," *Cement and Concrete Research,* vol. 19, no. 4, pp. 554-566, 1989.

[299] R. D'Angelo, T. J. Plona, L. M. Schwartz and P. Coveney, "Ultrasonic measurements on hydrating cement slurries: Onset of shear wave propagation," *Advanced Cement Based Materials,* vol. 2, no. 1, pp. 8-14, 1995.

[300] B. Desmet, K. C. Atitung and et al, "Monitoring the early-age hydration of self-compacting concrete using ultrasonic p-wave transmission and isothermal calorimetry," *Materials and Structures,* vol. 44, pp. 1537-1558, 2011.

[301] J. Carette and S. Staquet, "Monitoring the setting process of eco-binders by ultrasonic P-waveand S-wave transmission velocity measurement: Mortar vs concrete," *Construction and Building Materials,* vol. 110, pp. 32-41, 2016.

[302] O. M. Jensen and P. F. Hansen, "Autogenous deformation and change of the relative humidity in silica fume-modified cement paste," *ACI Mater. J,* vol. 93, no. 6, pp. 539-543, 1996.

[303] G. Sant, A. Kumar, C. Patapy, G. Le Saout and K. Scrivener, "The influence of sodium and potassium hydroxide on volume changes in cementitious materials," *Cem. Concr. Res,* vol. 42, no. 11, pp. 1447-1465, 2012.

[304] P. B. Petersen and R. J. Saykally, "On the nature of ions at the liquid water surface," *Annu Rev. Phy. Chem,* vol. 57, pp. 333-64, 2006.

[305] B. D. Kumarappa, S. Peethamparan and N. Margueritte, "Autogenous shrinkage of alkali activated slag mortars: Basic mechanisms and mitigation methods," *Cem. Concr. Res,* vol. 109, pp. 1-9, 2018.

[306] V. O. Özçelik, N. Garg and C. E. White, "Symmetry induced stability in alkali doped calcium-silicate-hydrate," *J. Phys. Chem. C,* vol. 123, pp. 14081-14088, 2019.

[307] Z. C. Grasley and Chin K. Leung, "Desiccation shrinkage of cementitious materials as an aging, poroviscoelastic response," *Cem. Concr. Res,* vol. 41, pp. 77-89, 2011.

[308] G. Constantinides and F-J. Ulm, "The effect of two types of C-S-H on the elasticity of cement-based materials: Results from nanoindentation and micromechanical modeling," *Cem. Concr. Res,* vol. 34, no. 1, pp. 67-80, 2004.

[309] J. Li, Q. Yu, H. Huang and S. Yin, "Effects of Ca/Si Ratio, Aluminum and Magnesium on the Carbonation Behavior of Calcium Silicate Hydrate," *Materials,* vol. 12, no. 8, 2019.

[310] S. Wang and K. L Scrivener, "29Si and 27Al NMR study of alkali-activated slag," *Cement and Concrete Research,* vol. 33, no. 5, pp. 769-774, 2003.

[311] F. Beltzung and F. H. Wittmann, "Role of disjoining pressure in cement based materials," *Cem. Concr. Res,* vol. 35, no. 12, pp. 4364-4370, 2005.

[312] ACI Committee 209, 209.2R-08 Guide for Modeling and Calculating Shrinkage and Creep in Hardened Concrete, ACI, 2008.

[313] A. Bentur and K. Kovler, "Evaluation of early age cracking characteristics in cementitious systems," *Materials and Structures,* vol. 36, no. 3, pp. 183-190, 2003.

[314] H. R. Shah and J. Weiss, "Quantifying shrinkage cracking in fiber reinforced concrete using the ring test," *Materials and Structures,* vol. 39, no. 9, pp. 88-899, 2006.

[315] Y. Gao and P. Han, "Determination of stress relaxation parameters of concrete in tension at early-age by ring test," *Construction and Building Materials,* vol. 41, pp. 152-164, 2013.

[316] J. Xin, G. Zhang, Y. Liu, Z. Wang and Z. Wu, "Evaluation of behavior and cracking potential of early-age cementitious systems using uniaxial restraint tests: A review," *Construction and Building Materials,* vol. 231, 2020.

[317] Y. Wei, S. Liang, W. Guo and W. Hansen, "Stress prediction in very early-age concrete subject to restraint under varying temperature histories," *Cement and Concrete Composites,* vol. 83, pp. 45-56, 2017.

[318] S. Garashi, A. Bentur and K. Kovler, "Autogenous shrinkage and induced restraining stresses in high-strength concretes," *Cement and Concrete Research,* vol. 30, no. 11, pp. 1701-1707, 2000.

[319] A. Williams, A. Markandeya, Y. Stetsko, K. Riding and A. Zayed, "Cracking potential and temperature sensitivity of metakaolin concrete," *Construction and Building Materials,* vol. 120, pp. 172-180, 2016.

[320] A. Markandeya, N. Shanahan, D. Mapa Gunatilake, Kyle A. Riding and A. Zayed, "Influence of slag composition on cracking potential of slag-portland cement concrete," *Construction and Building Materials,* vol. 164, pp. 820-829, 2018.

[321] ASTM INTERNATIONAL STANDARIZATION, ASTM C1581 / C1581M-18a, Standard Test Method for Determining Age at Cracking and Induced Tensile Stress Characteristics of Mortar and Concrete under Restrained Shrinkage, 2018.

[322] F. Kanavaris, M. Azenha, M. Soutsos and K. Kovler, "Assessment of behaviour and cracking susceptibility of cementitious systems under restrained conditions through ring tests: A critical review," *Cement and Concrete Composites,* vol. 95, pp. 137-153, 2019.

[323] V. Lamour, A. Haouas and M. Moranville, "A New Technique for Characterization of Early-age Cracking of mortars," in *In: Advances in Concrete Through Science and Engineering*, 2004.

[324] H. Zhu, H. Li and X. Zhu, "On concrete restrained eccentric ring and squared eccentric ring shrinkage test methods," *Construction and Building Materials,* vol. 84, no. 1, pp. 239-244, 2015.

[325] W. Dong, W. Yuan, X. Zhou and X. Zhao, "Influence of specimen geometries and drying conditions on concrete cracking in restrained elliptical ring tests," *Construction and Building Materials,* vol. 207, no. 20, pp. 273-283, 2019.

[326] W. Dong, X. Zhou, Z. Wu and G. Kastiukas, "Effects of specimen size on assessment of shrinkage cracking of concrete via elliptical rings: Thin vs. thick," *Computers & Structures,* vol. 174, pp. 66-78, 2016.

[327] A. B. Hossain and J. Weiss, "Assessing residual stress development and stress relaxation in restrained concrete ring specimens," *Cement and Concrete Composites,* vol. 26, no. 5, pp. 531-540, 2004.

[328] A. B. Hossain and J. Weiss, "The role of specimen geometry and boundary conditions on stress development and cracking in the restrained ring test," *Cement and Concrete Research,* vol. 36, no. 1, pp. 189-199, 2006.

[329] AASHTO, Standard Practice for Estimating the Crack Tendency of Concrete, PP. 34-99, 2006.

[330] H. Kwon Seung and S. P Shah, "Prediction of Early-Age Cracking of Fiber-Reinforced Concrete due to Restrained Shrinkage," *ACI Materials,* vol. 105, no. 4, pp. 381-389, 2008.

[331] S. H. Kwon and S. P. Shah, "Prediction of shrinkage cracking for fiber-reinforced concrete," in *Proceedings of Concreep 8*, Ise-Shima, Japan, 2008.

[332] INTERNATIONAL FDERATION FOR STRUCTURAL CONCRETE (FID), Model code, 2010.

[333] G. De Schutter and L. Taerwe, "Degree of hydration-based description of mechanical properties of early age concrete," *Materials and Structures,* vol. 29, no. 6, pp. 335-344, 1996.

[334] D. Shen, Z. Feng, P. Zhu, X. Tang and G. Jiang, "Effect of pre-wetted lightweight aggregates on residual stress development and stress relaxation in restrained concrete ring specimens," *Construction and Building Materials,* vol. 258, 2020.

[335] D. Shen, H. Shi, X. Tang, Y. Ji and G. Jiang, "Effect of internal curing with super absorbent polymers on residual stress development and stress relaxation in restrained concrete ring specimens," *Construction and Building Materials,* vol. 120, pp. 309-320, 2016.

[336] J. H. Moon and W.J. Weiss, "Estimating residual stress in the restrained ring test under circumferential drying," *Cement and Concrete Research,* vol. 28, no. 5, pp. 486-496, 2006.

[337] S. Eppers, "Assessing the autogenous shrinkage cracking propensity of concrete by means of the restrained ring test," PhD Thesis, TU Drsden, Dresden, Germany, 2010.

[338] V. Vullo, Circular Cylinders and Pressure Vessels, Springer Science & Business Media, 2013.

[339] C. T. F. Ross, Advanced Applied Stress Analysis. Ellis Horwood Limited, ISBN 130161551, United Kingdom, 1987.

[340] D. Yeol Yoo, Jung-Jun Park, Sung-Wook Kim and Young-Soo Yoon, "Influence of ring size on the restrained shrinkage behavior of ultra high performance fiber reinforced concrete," *Materials and Structures,* vol. 47, pp. 1161-1174, 2014.

[341] B. S. Gebregziabiher, R. J. Thomas and S. Peethamparan, "Temperature and activator effect on early-age reaction kinetics of alkali-activated slag binders," *Constr. Build. Mater,* vol. 113, no. 15, pp. 783-793, 2016.

[342] E. Gallucci, X. Zhang and K.L. Scrivener, "Effect of temperature on the microstructure of calcium silicate hydrate (C-S-H)," *Cem. Concr. Res,* vol. 53, pp. 185-195, 2013.

[343] H. K.-Kamyab, A. C. A. Muller, E. Denarié, E. Brühwiler and K. Scrivener, "Kinetics of mixing-water repartition in UHPFRC paste and its effect on hydration and microstructural development," *Cem. Concr. Res,* vol. 124, p. 105784, 2019.

[344] J. Davidovits, Geopolymer Chemistry & Applications, 4 Th, Institut Géopolymère, Saint-Quentin: France, 2015.

[345] Y. Ma, "Microstructure and Engineering Properties of Alkali Activated Fly Ash," PhD thesis, TU Delft, Netherland, 2013.

[346] N. K. Lee and H.K. Lee, "Reactivity and reaction products of alkali-activated, fly ash/slag paste," *Construction and Building Materials,* vol. 81, pp. 303-312, 2015.

[347] H. Ye, "Creep Mechanisms of Calcium–Silicate–Hydrate: An Overview of Recent Advances and Challenges," *Int. J. Concr. Struc. Mater,* vol. 9, no. 4, pp. 453-462, 2015.

[348] Z. C. Grasley and C. K. Leung, "Desiccation shrinkage of cementitious materials as an aging, poroviscoelastic response," *Cem. Concr. Res,* vol. 41, no. 1, pp. 77-89, 2011.

[349] I. García Lodeiro, D.E. Macphee, A. Palomo and A. Fernández-Jiménez, "Effect of alkalis on fresh C–S–H gels. FTIR analysis," *Cement and Concrete Research*, vol. 39, no. 3, pp. 147-153, 2009.

Curriculum vitae

General Information:

Name	Siva UPPALAPATI
Date of Birth	16th June 1991
Nationality	Indian
Email	uppalapati.shiva@gmail.com

Education:

July 2016 – Present	PhD in Engineering Science, Civil Engineering, KU Leuven, Belgium.
Sep 2012 – Oct 2014	Master of Science in Advanced Computational and Civil Engineering Structural Studies (ACCESS), Technical University Dresden, Germany.
Sep 2008 – March 2012	Bachelor of Technology in Civil Engineering, Acharya Nagarjuna University, India.

Work Experience:

July 2016 – Present	Doctoral Researcher, Civil Engineering, KU Leuven, Belgium.
Dec 2015 – June 2016	Structural Engineer, Nhance Consulting Engineers, Hyderabad, India
April 2014 – March 2015	Research Assistant, Institute of Construction Materials, Technical University Dresden, Germany.

List of publications

Articles in internally peer-reviewed scientific journals

1. **Uppalapati. S**, Vandewalle. L., Cizer.Ö, (2020) "Autogenous shrinkage of slag/fly ash blends activated with hybrid sodium silicate and sodium sulfate at different curing temperatures", ***Construction and Building Materials***, Vol 265, 30, 121276, DOI
2. **Uppalapati. S**, Vandewalle. L., Cizer.Ö, (2021) "Monitoring setting process of alkali-activated slag/fly ash cements by ultrasonic P-wave measurements", ***Construction and Building Materials***, Vol 271, 15, 121592, DOI.
3. **Uppalapati. S**, Cizer.Ö, (2017) "Assessing the Autogenous Shrinkage of Alkali-Activated Slag/Fly Ash Mortar Blends", ***ACI Special publication***, 320, pp-23.1-23.2, Access.
4. Joseph. S., **Uppalapati. S**., Cizer.Ö., (2018) "Instantaneous activation energy of alkali activated materials", ***RILEM Technical letter*** , DOI.

Articles in presented at international conferences and symposia

1. **Uppalapati. S**., Joseph. S., Cizer. Ö, "Autogenous shrinkage and strength development of alkali-activated slag/fly ash mortar blends", 5th International Slag Valorisation Symposium Conference, April 2017, Leuven, Belgium.
2. **Uppalapati. S**., Cizer. Ö., "Early-age properties of alkali-activated slag concrete", 2nd Internal RILEM Conference on Early-age cracking and serviceability in cement-based materials and structures, Sept 2017, Brussels, Belgium.
3. **Uppalapati. S**., Cizer. Ö., "Assessing the autogenous shrinkage of alkali-activated slag fly ash mortar blends", 10th ACI/RILEM international conference on cementitious materials and alternative binders or sustainable concrete conference, Oct 2017, Canada.
4. **Uppalapati. S**., Cizer. Ö., "Reaction kinetics, reaction products and strength development of alkali-activated slag/fly-ash blends": Influence of activator, 15th International Congress on the Chemistry of Cement [ICCC-2019], Prague, Czech Republic, 16 Sep 2019 - 20 Sep 2019.